UNIVERSITY OF CALIFORNIA, SAN DIEGO

Theory of Quantum Control of Spin-Photon Dynamics and Spin Decoherence in Semiconductors

A dissertation submitted in partial satisfaction of the
requirements for the degree Doctor of Philosophy
in
Physics

by

Wang Yao

Committee in charge:

Professor Lu Jeu Sham, Chair
Professor Yeshaiahu Fainman
Professor Michael M. Fogler
Professor Yu-Hwa Lo
Professor Sunil K. Sinha

2006

The dissertation of Wang Yao is approved, and it is acceptable in quality and form for publication on microfilm:

Chair

University of California, San Diego

2006

TABLE OF CONTENTS

LIST OF FIGURES

LIST OF TABLES

ACKNOWLEDGEMENTS

First of all, I would like to thank my advisor, Prof. Lu Sham, for taking me into his group and supporting me through the years. I am very much obliged to his many important ideas, from which the work in this dissertation originated, and his guidance throughout the progress of the work. The weekly discussions with Lu on the research project are always enlightening and inspiring, and I wish I had learned more from his profound knowledge in physics. I also appreciate very much that I was given the opportunities to participate in various conferences and summer school.

I feel very lucky to overlap with Dr. Renbao Liu during his three-year stay in the group. He is always so generous in sharing his knowledge and interesting ideas. I am the one who have benefitted the most from our pleasant collaborations, and I feel I owe much to Renbao. I will remember those luncheons at the fifth floor balcony of Mayer Hall when we discussed physics as well as gossiped other events. One critical step in our research was inspired by such a lunch conversation.

I appreciate the help from Dr. Carlo Piermarocchi and Dr. Pochung Chen when I first joined the group. The collaboration with Dr. Hiroshi Ajiki, when the work in this dissertation was at the rudimentary stage, has prepared me with fundamental knowledge on cavity quantum electrodynamics and basic theoretical tools. I want to thank Hiroshi for those discussions. I would also like to acknowledge very useful discussions with Prof. Yeshaiahu Fainman and Yaoming Shen on semiconductor microcavities. Many thanks to Dr. Semion Saikin, Lukasz Cywinski and Sophia Economou for helpful discussions on problems related to the work in this dissertation.

Finally, I want to express my deepest gratitude to my parents and my wife for their continuous support in pursuing my career goals.

The text of chapter IV, in part, is a reprint of the material as it appears in Wang Yao, Ren-Bao Liu, and L. J. Sham, *Nanodot-Cavity Electrodynamics and Photon Entanglement*, Phys. Rev. Lett **92**, 217402, © 2004 The American Physical Society, where the dissertation author was the first author. The co-authors in this publication directed, supervised, and co-worked on the research which forms the basis of this chapter.

The text of chapter V, in part, is a reprint of the material as it appears in Wang Yao, Ren-Bao Liu, and L. J. Sham, *Theory of Control of the Spin-Photon Interface for Quantum Networks*, Phys. Rev. Lett **95**, 030504, © 2005 The American Physical Society, where the dissertation author was the first author, and Wang Yao, Ren-Bao Liu, and L. J. Sham, *Theory*

of Control of the Dynamics of the Interface between Stationary and Flying Qubits, J. Opt. B.: Quant. Semiclass. Opt. **7**, S318, © 2005 IOP Publishing Ltd, where the dissertation author was the first author. The co-authors in these publications directed, supervised, and co-worked on the research which forms the basis of this chapter.

The text of chapter VI, in part, is a reprint of the material as it appears in Ren-Bao Liu, Wang Yao, and L. J. Sham, *Coherent Control of Cavity Quantum Electrodynamics for Quantum Nondemolition Measurements and Ultrafast Cooling*, Phys. Rev. B **72**, 081306(R), © 2005 The American Physical Society, where the dissertation author was the second author. The co-authors in this publication directed, supervised, and co-worked on the research which forms the basis of this chapter.

The text of chapter VII, in part, is a reprint of the material as it appears in Wang Yao, Ren-Bao Liu, and L. J. Sham, *Theory of Electron Spin Decoherence by Interacting Nuclear Spins in a Quantum Dot*, arXiv preprint cond-mat/0508441, (2005), where the dissertation author was the first author. The co-authors in this preprint directed, supervised, and co-worked on the research which forms the basis of this chapter.

The text of chapter VIII, in part, is a reprint of the material as it appears in Wang Yao, Ren-Bao Liu, and L. J. Sham, *Restoring Coherence Lost to a Mesoscopic Bath*, arXiv preprint cond-mat/0604634, (2006), where the dissertation author was the first author. The co-authors in this preprint directed, supervised, and co-worked on the research which forms the basis of this chapter.

VITA

1979	Born, Changchun, P. R. China
2001	Bachelor of Science in Physics Peking University, Beijing, P. R. China
2001–2002	Teaching Assistant, Department of Physics University of California, San Diego
2002–2006	Research Assistant, Department of Physics University of California, San Diego
2006	Doctor of Philosophy University of California, San Diego

PUBLICATIONS

Wang Yao, Ren-Bao Liu, and L. J. Sham, *Nanodot-Cavity Electrodynamics and Photon Entanglement*, Phys. Rev. Lett **92**, 217402 (2004).

Wang Yao, Ren-Bao Liu, and L. J. Sham, *Theory of Control of the Spin-Photon Interface for Quantum Networks*, Phys. Rev. Lett **95**, 030504 (2005).

Ren-Bao Liu, Wang Yao, and L. J. Sham, *Coherent Control of Cavity Quantum Electrodynamics for Quantum Nondemolition Measurements and Ultrafast Cooling*, Phys. Rev. B **72**, 081306(R) (2005).

Wang Yao, Ren-Bao Liu, and L. J. Sham, *Theory of Control of the Dynamics of the Interface between Stationary and Flying Qubits*, J. Opt. B.: Quant. Semiclass. Opt. **7**, S318 (2005).

Wang Yao, Ren-Bao Liu, and L. J. Sham, *Theory of Electron Spin Decoherence by Interacting Nuclear Spins in a Quantum Dot*, arXiv preprint cond-mat/0508441, (2005).

Wang Yao, Ren-Bao Liu, and L. J. Sham, *Restoring Coherence Lost to a Mesoscopic Bath*, arXiv preprint cond-mat/0604634, (2006).

FIELDS OF STUDY

Major Field: Physics

Studies in Theoretical Condensed Matter Physics.
Professor Lu Jeu Sham

ABSTRACT OF THE DISSERTATION

Theory of Quantum Control of Spin-Photon Dynamics and Spin Decoherence in Semiconductors

by

Wang Yao
Doctor of Philosophy in Physics
University of California, San Diego, 2006
Professor Lu Jeu Sham, Chair

Single electron spin in a semiconductor quantum dot (QD) and single photon wavepacket propagating in an optical waveguide are investigated as carriers of quantum bit (qubit) for information processing. Cavity quantum electrodynamics of the coupled system composed of charged QD, microcavity and waveguide provides a quantum interface for the interplay of stationary spin qubits and flying photon qubits via cavity assisted optical control. This interface forms the basis for a wide range of essential functions of a quantum network, including transferring, swapping, and entangling qubits at distributed quantum nodes as well as a deterministic source and an efficient detector of a single photon wavepacket with arbitrarily specified shape. The cavity assisted optical process also made possible ultrafast initialization and QND readout of the spin qubit in QD. In addition, the strong optical nonlinearity of dot-cavity-waveguide coupled system enables phase gate and entanglement operation for flying single photon qubits in waveguides. The coherence of the electron spin is the wellspring of these quantum applications being investigated. At low temperature and strong magnetic field, the dominant cause of electron spin decoherence is the coupling with the interacting lattice nuclear spins. We present a quantum solution to the coupled dynamics of the electron with the nuclear spin bath. The decoherence is treated in terms of quantum entanglement of the electron with the nuclear pair-flip excitations driven by the various nuclear interactions. A novel nuclear interaction, mediated by virtue spin-flips of the single electron, plays an important role in single spin free-induction decay (FID). The spin echo not only refocuses the dephasing by inhomogeneous broadening in ensemble dynamics but also eliminates the decoherence by electron-mediated nuclear interaction. Thus, the decoherence times for single spin FID and ensemble spin echo are significantly different. The quantum theory of decoherence also leads to a method of coherence recovery of the electron by disentanglement, realized through maneuvering the nuclear bath evolution by control of the electron spin-flip. The studies form the basis to outline the construction of a solid-state quantum network for scalable and distributed processing of quantum information.

I

Introduction

I.A Motivation

With the advance of technologies, novel quantum systems becomes accessible in laboratories, e.g., the microscopic system of atoms in engineered electromagnetic environment (e.g., optical cavity) [1], the mesoscopic system of semiconductor quantum dots [2, 3, 4], and the macroscopic system of Bose-Einstein condensate (BEC) of alkali atoms [5]. Coherent quantum effects have recently been observed in all of these systems, making them well suited for use as quantum logic devices (the analog of classic logic devices, however with operation based on quantum mechanics) [6]. Yet several fundamental questions must be answered before these systems can be used as building blocks for large scale quantum computation. These include: (a) how to control the quantum dynamics in these systems in order to realize the desired quantum logic operations; (b) the origin and mitigation of decoherence processes that can be deleterious to these quantum operations. The focus of this dissertation is placed on these two aspects in the mesoscopic system of semiconductor quantum dots.

Quantum dots formed in III-V semiconductor compounds have featured in numerous recent proposals for quantum computing and information processing [7, 8, 9]. The spin of the single electron localized by the three-dimensional confinement in quantum dots has been considered a promising carrier of quantum bit due to the desired features of stability and long coherence time. The mature semiconductor technology also promises the large scale integration and incorporation with other existing semiconductor devices. The various types of III-V quantum dots under intensive investigations includes the gate defined dot formed on two-dimensional electron gas [9, 10, 11], the GaAs fluctuation dot [4, 12, 13], and In(Ga)As self-assembled dot [14, 15, 16]. Our interests have been focused on the latter two types of dots where arbitrary control of spin dy-

namics for universal information processing may be realized by ultra-fast laser techniques [17, 18]. The ultra-short operation time allows a sufficiently large number of operations before the system lost its quantum coherence. Preliminary experimental efforts have indeed demonstrated the ultra-fast optical control of the quantum dynamics in these dots [4]. Meanwhile, optical studies have also started in parallel on other types of semiconductor nanostructures, e.g., the II-VI core shell quantum dots embedded in ploy methyl methacrylate (PMMA) [19] and the diamond nano-crystals with nitrogen vacancy (NV) centers [20, 21, 22], which have exhibited potentials for quantum applications.

There is an entirely different type of quantum information carrier in semiconductor structures, i.e., single photon wavepacket propagating in optical waveguides. Qubit can be encoded either in the photon number subspace or the polarization subspace of the single photon wavepackets. While the stationary qubit carried by the quantum dot spin is of better stability and addressability, encoding qubit in flying single photons enables the information to be carried over long distance.

As pointed out by DiVincenzo in his seven criteria for the physical implementation of quantum computation [23], the ability for faithful interconversion between flying qubit and stationary qubit can greatly increase the chances for realizing a scalable quantum computer. Semiconductor offers an arena for both types of qubit, i.e., the stationary spin qubit in quantum dot and the flying photon qubit in waveguides. The integration of the spintronic and electronic dynamics with photonic dynamics is made possible through the interface offered by micro-cavity quantum electrodynamics (QED) with quantum dot, which is one of the main focuses of this study. As we will show in this dissertation, micro-cavity QED enables the coherent interplay between the electron spin qubit and the single photon flying qubit as well as the ultra-fast initialization and readout of the spin qubit through photon detection. Together with the optical manipulation of the quantum dot spin established in previous work [8, 17, 18], these form the basis of the construction of an optically controlled spin-based quantum network for scalable and distributed processing of quantum information.

In addition, all-photonics quantum computation is possible provided that efficient two photon universal gates can be realized. The conditional dynamics at the single photon level requires the ultra-large optical nonlinearity which may be provided by the quantum dot micro-cavity QED. Part of our effort has also been along this direction.

A major obstacle to quantum logic is the various decoherence processes in these solid state systems. While decoherence is in general deleterious to quantum operations, fault-tolerant quantum computation is nonetheless possible by quantum error correction [24, 25, 26, 27, 28, 29], provided that the ratio between the decoherence time versus the operation time exceeds some

threshold value. Investigation of the dominant decoherence processes in our system and efficient methods to ameliorate their effects on quantum operation is another major consideration in this dissertation.

I.B Dissertation outline

In Chapter II, we briefly review the electronic and optical properties of quantum dots formed in the III-V semiconductor compounds. The three-dimensional confinement in quantum dots leads to the fully quantized electronic energy levels. As a consequence, quantum dot resembles atom in many ways although it is essentially a mesoscopic system. The atom-like electronic and optical properties is the basis for ultra-fast optical control of the quantum coherent effects in quantum dots, in a similar fashion to the development in atomic physics in the past decades.

In Chapter III, we give a brief review to the various micro-cavity and optical waveguide structures that can now be realized in semiconductors. While micro-cavity and optical waveguide are of important applications in other fields, e.g., optical communication and semiconductor lasers, our focus will be placed on their potential use for strong-coupling cavity quantum electrodynamics with quantum dots and discussion on merits of the various structures are based on this need.

The above two chapters provide the knowledge base on the quantum dot and micro-cavity systems on which we are going to explore the quantum control of the single spin and single photon dynamics.

In Chapter IV, we explore the potential of micro-cavity quantum electrodynamics with quantum dot for realizing conditional dynamics of single photons. Ultra-large optical nonlinearity may arise from the strong coupling of quantum dot exciton with micro-cavity photons. We show a integrated dot-cavity-waveguide structure for realizing a prototype two photon gate for universal quantum information processing, i.e., a phase gate on the polarization qubit. The phase gate structure can also be used to generate polarization entangled photon pairs.

In Chapter V, we investigate the coupled dot-cavity-waveguide structure as the spin-photon interface for solid state quantum networks. Interconversion between the stationary spin qubit and the flying photon qubit is realized through a cavity-assisted Raman process. This Raman process can be made to generate or annihilate an arbitrarily shaped single-photon wavepacket by pulse shaping the controlling laser field. This quantum interface forms the basis for many essential functions of a quantum network, including sending, receiving, transferring, swapping, and entangling qubits at distributed quantum nodes as well as a deterministic source and an efficient detector of a single-photon wavepacket with arbitrarily specified shape and average

photon number.

In Chapter VI, we discuss applications of the coupled dot-cavity-waveguide structure for ultrafast initialization and quantum nondemolition (QND) measurements of the spin qubit in quantum dot. QND measurements and ultrafast cooling of single spins are critical for scalable quantum computation. For such purposes, quantum evolution in a coupled structure of a nanodot, a microcavity, and a waveguide can be coherently controlled to establish efficient quantum pathways connecting in sequence an electron spin, a charged exciton, a cavity photon, and finally a flying photon in the waveguide. As an example of suppressing unwanted dynamics in complex solid-state systems, pulse shaping is employed to switch the nanodot-cavity coupling on demand and to perform robust quantum operation.

In the above three chapters, we focuse on the optical control of the quantum dynamics of single spin and single photon. The efficiency or fidelity of these quantum operations depends critically on the coherence times in the system. The optical relaxation due to spontaneous emission is taken into account and the effect is efficiently ameliorated in the design. The dot-cavity-waveguide coupled structure is an example of engineering the electromagnetic vacuum to guide the spontaneous optical relaxation into the desired quantum channel instead of the deleterious leakage into free space. The electron spin coherence time is assumed to be sufficiently long in the design of quantum optical control. The study in Chapter VII and VIII serves as a foundation for such assumption, where the issues of quantum dot electron spin decoherence and coherence control are addressed.

In Chapter VII, we present a quantum theory of the electron spin transverse decoherence induced by interacting nuclear spins in quantum dot. At low temperature and strong magnetic field, the most relevant relaxation process for electron spin is in the form of transverse decoherence, or pure dephasing, and the mechanism is inferred, by process of elimination through experiments and theoretical arguments, to be the lattice nuclear spins that inevitably exist in the III-V materials. We solve the electron spin decoherence by a nuclear pair-correlation method for the electron-nuclear spin dynamics. The theory incorporates the hyperfine interaction, the intrinsic (both direct and indirect) nuclear interactions, and the nuclear coupling mediated by the hyperfine interaction with the electron in question. The last is shown to be important in free-induction decay (FID) of the single electron spin coherence. The spin echo eliminates the hyperfine-mediated decoherence but only reduces the decoherence by the intrinsic nuclear interactions. Thus, the decoherence times for single spin FID and ensemble spin echo are significantly different.

In Chapter VIII, we present a theory to ameliorate the electron spin transverse decoherence induced by the lattice nuclear spins. In the timescale of interest, the relevant environment

for the electron spin in the host quantum dot is of a mesoscopic size which is composed of the nuclear spins that are in direct contact with the quantum dot electron. The coupled dynamics of the electron and the nuclear bath can be treated as a coherent quantum evolution where the decoherence of the electron spin results from the entanglement with the mesoscopic nuclear bath established by this evolution. This quantum picture of decoherence leads to a theory of coherence recovery of the electron spin by disentanglement, realized though maneuvering the nuclear bath evolution by control of the electron spin.

II

Electronic and Optical Properties of III-V Semiconductor Quantum Dot: A Brief Review

In this chapter, we briefly review an important element that is being investigated for an optically controlled quantum computer: quantum dot in III-V semiconductor structures. The carrier of quantum bit is the spin of the electron confined in singly n-doped quantum dot formed in III-V compounds.

In all the III-V compounds, the top of the valence band occurs at the center of the Brillouin zone (Γ point). For the compounds of our interest, i.e., GaAs, AlGaAs and InAs, the conduction band minimum also occurs at the Γ point (see Fig. II.1) and this leads to direct optical transitions which are advantageous for low-temperature optical controls as phonons are not required for compensating the momentum difference. Two types of MBE grown quantum dot formed in direct bandgap III-V compound offer excellent controllability by ultra-fast optics and are being investigated as building blocks for an optically manipulated quantum computer. The first is referred to as interface fluctuation formed quantum dots in GaAs/AlGaAs quantum well structures [12, 13, 30, 31, 32, 33, 34, 35, 36]. Throughout this dissertation, we will refer them in short as GaAs fluctuation quantum dots. As illustrated in Fig. II.2(a), electrons and holes in these samples are localized in the growth direction (z direction) by growing a low bandgap GaAs layer, with a thickness of tens of $\mathring{A}$, between two higher bandgap $Al_{0.3}Ga_{0.7}As$ layers. Growth interruption at the material interfaces leads to a roughness, usually of one monolayer, that has a lateral length scale sufficient to localize electron-hole pair laterally in the quantum

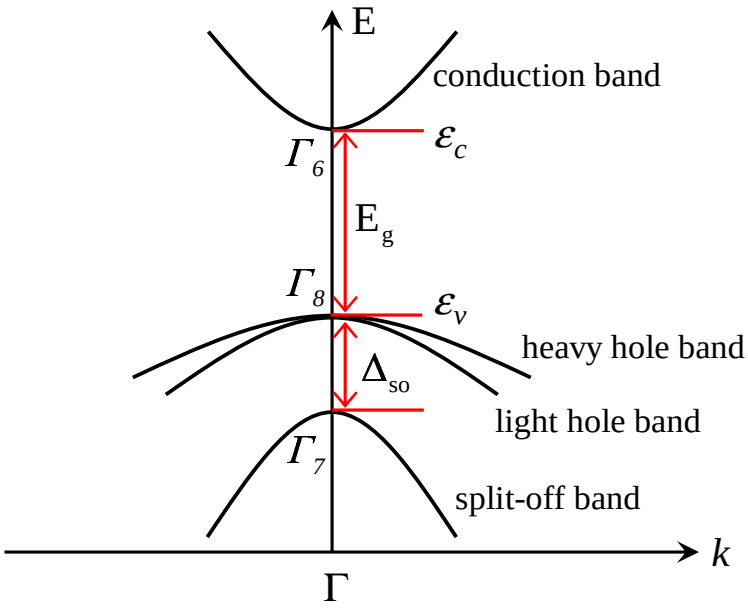

Figure II.1 Bulk band structures of direct bandgap semiconductors.

well. The second type of quantum dot, referred as the InAs self-assembled dots, are formed using the Stranski-Krastanow growth mode which utilizes the strain caused by the lattice mismatch between the InAs QD layer and the GaAs substrate. InAs self-assembles into islands which are primarily in the shape of a pyramid (see Fig. II.2(b)), with a height of tens of $\AA$ and a base size of tens of nanometers [14, 15, 37, 38]. Single conduction band electrons can be incorporated in these quantum dot, e.g., by modulation Si doping in the barriers [39]. The spin of these single electrons will play the critical role as qubit carrier in the optically controlled solid state quantum computation to be discussed in this dissertation.

The confinement principle, energy level structures and optical properties are similar in these two types of quantum dot. The difference lies in the quantitative values of the spatial dimensions, energy scale of confinement potential, electron g factors and the optical transition dipole moments, etc. Below, we will review the electronic and optic properties with the example of GaAs fluctuation quantum dot and the quantitative difference of InAs self-assembled dot will be mentioned when necessary.

II.A Electronic properties

The electronic properties of semiconductor bulk and heterostructures have been extensively discussed in many classical textbooks , e.g., [40, 41]. Here we simply summaries the relevant points to our studies from these discussions.

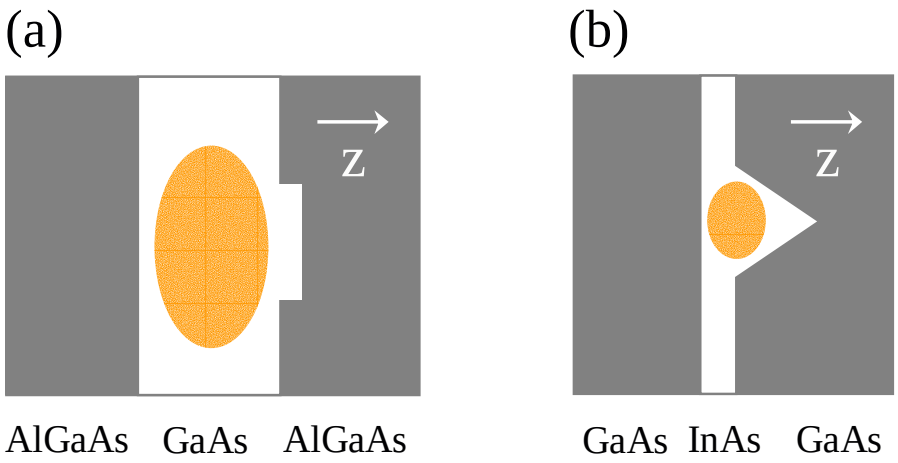

Figure II.2 Illustration of two types of optically controllable quantum dot. The arrow indicate the growth direction (z direction). The ellipse regions show schematically the confinement of electrons in the dot. (a) GaAs fluctuation quantum dot. The dark region is AlGaAs material and the bright region is GaAs material. (b) InAs self-assembled quantum dot. The dark region is GaAs material and the bright region is InAs material.

II.A.1 Bulk properties

For the direct bandgap semiconductors, both the conduction band and the valance band extrema are at the Brillouin zone center (Γ point). For the relevance of the study in this dissertation, of interest are those low-lying states located in the vicinity of conduction and valance band edge. The $\mathbf{k}\cdot\mathbf{p}$ method provides a powerful approach to find these low-lying electronic states. The starting point is the Hamiltonian describing the dynamics of electrons in a semiconductor within the single-particle approximation

$$\left[\frac{p^2}{2m}+V(\mathbf{r})+\frac{\hbar}{4m^2c^2}(\boldsymbol{\sigma}\times\boldsymbol{\nabla}V)\cdot\mathbf{p}\right]\psi_{n\mathbf{k}}(\mathbf{r})=E_{n\mathbf{k}}\psi_{n\mathbf{k}}(\mathbf{r}), \tag{II.1}$$

where m is the free electron mass, $V(\mathbf{r})$ is the periodic crystalline potential and $\mathbf{p}=-i\hbar\boldsymbol{\nabla}$. The third term in the equation represents the spin-orbit coupling. The solution can be written in the Bloch form $\psi_{n\mathbf{k}}(\mathbf{r})=u_{n\mathbf{k}}(\mathbf{r})e^{i\mathbf{k}\cdot\mathbf{r}}$ where $u_{n\mathbf{k}}(\mathbf{r})$ has the same periodicity as the crystal potential, $n=1\cdots\infty$ denotes the band index and $\mathbf{k}$ the crystal momentum. The idea of the $\mathbf{k}\cdot\mathbf{p}$ method is to first solve these equations at the band edge (in this case the Γ point, $\mathbf{k}=0$)

$$\left[\frac{p^2}{2m}+V(\mathbf{r})+\frac{\hbar}{4m^2c^2}(\boldsymbol{\sigma}\times\boldsymbol{\nabla}V)\cdot\mathbf{p}\right]u_{n0}(\mathbf{r})=E_{n0}u_{n0}(\mathbf{r}), \tag{II.2}$$

The solutions $u_{n0}(\mathbf{r})$ form a complete and orthonormal set of basis functions. At the Γ point, the lowest conduction band has an s-like Γ_6 symmetry. Considering the spin, there is a two-fold degeneracy. In absence of the spin-orbit coupling, the top valance band which originate from p-orbital of the onion has a p-like Γ_4 symmetry at the Γ point with a six-fold degeneracy considering

the spin degrees. The spin-orbit coupling lifts the degeneracy and give rise to a quadruplet with Γ_8 symmetry (or total angular momentum $J = 3/2$) and a doublet with Γ_7 symmetry (or total angular momentum $J = 1/2$) as illustrated in Fig. II.1.

Away from the Γ point, the equations for $E_{n\mathbf{k}}$ and $u_{n\mathbf{k}}(\mathbf{r})$ has extra terms containing $\mathbf{k}$

$$\left[\frac{p^2}{2m} + V(\mathbf{r}) + \frac{\hbar^2 k^2}{2m} + \frac{\hbar \mathbf{k}\cdot\boldsymbol{\pi}}{m} + \frac{\hbar}{4m^2c^2}(\boldsymbol{\sigma}\times\boldsymbol{\nabla}V)\cdot\mathbf{p}\right] u_{n\mathbf{k}}(\mathbf{r}) = E_{n\mathbf{k}} u_{n\mathbf{k}}(\mathbf{r}), \tag{II.3}$$

where $\boldsymbol{\pi} \equiv \mathbf{p} + \frac{\hbar}{4mc^2}(\boldsymbol{\sigma}\times\boldsymbol{\nabla}V)$. In the vicinity of the band edge where $|\mathbf{k}|$ is small, we can treat the term $\frac{\hbar\mathbf{k}\cdot\boldsymbol{\pi}}{m}$ as perturbations and solve for $E_{n\mathbf{k}}$ and $u_{n\mathbf{k}}(\mathbf{r})$ from E_{n0} and $u_{n0}(\mathbf{r})$ using either degenerate or nondegenerate perturbation theory.

The conduction band is nondegenerate excluding the spin degrees of freedom. Using the standard nondegenerate perturbation theory, we have

$$u_{c\mathbf{k}}(\mathbf{r}) = u_{c0}(\mathbf{r}) + \frac{\hbar}{m}\sum_{n'\neq c}\frac{\langle u_{c0}|\mathbf{k}\cdot\boldsymbol{\pi}|u_{c0}\rangle}{E_{c0}-E_{n'0}}u_{n'0}(\mathbf{r}), \tag{II.4}$$

and

$$E_{c\mathbf{k}} = E_{c0} + \frac{\hbar^2k^2}{2m} + \frac{\hbar^2}{m^2}\sum_{n'\neq c}\frac{|\langle u_{c0}|\mathbf{k}\cdot\boldsymbol{\pi}|u_{n'0}\rangle|^2}{E_{c0}-E_{n'0}}, \tag{II.5}$$

where we have used the symbol c to denote the lowest conduction band. The term linear in k in the energy correction vanish because we have neglected the small inversion asymmetry in the zinc-blende compound, which is equivalent to assuming the band edge occurs at Γ point. The important result is the effective mass of the conduction band electron

$$\frac{1}{m^*} = \frac{1}{m} + \frac{2}{m^2k^2}\sum_{n'\neq c}\frac{|\langle u_{c0}|\mathbf{k}\cdot\boldsymbol{\pi}|u_{n'0}\rangle|^2}{E_{c0}-E_{n'0}}, \tag{II.6}$$

The matrix element $\langle u_{c0}|\boldsymbol{\pi}|u_{n'0}\rangle$ and the energy separation $E_{c0} - E_{n'0}$ between the two bands c and n' determines the contribution to the correction to m^*. The most important contribution comes from the top Γ_4 valance band where $E_{s0} - E_{n'0}$ is positive. As a consequence, the effective mass of the conduction band electron is less than that of the free electron. In Table. II.1, the effective mass (bulk value) of the conduction band is listed for the relevant III-V compounds.

To apply the $\mathbf{k}\cdot\mathbf{p}$ method to calculate the band dispersion near the edge of the top valance band, a degenerate perturbation theory has to be used. As the spin-orbit coupling split the valance band edge states into quadruplet and doublet with a large splitting of $\sim$ eV, they can be treated separately. The quadruplet $J = 3/2$ band is of our interest. We can write the wave-function as linear combination of the four degenerate states

$$\psi_{\mathbf{k}}(\mathbf{r}) = \sum_{m=-3/2}^{3/2} F_{\mathbf{k}m}e^{i\mathbf{k}\cdot\mathbf{r}}u_{vm0}(\mathbf{r}). \tag{II.7}$$

Table II.1 Band parameters (bulk value) for several direct bandgap III-V compounds at the Γ point [40, 42, 43]. $E_g(\Gamma)$ denotes the energy gap between the top valance band and the lowest conduction band. $\Delta_{\rm so}$ denotes the splitting of Γ_{15} valence band state into Γ_7 and Γ_8 valance bands. m_c is the effective mass of the conduction band. m_{hh} (m_{lh}) is the spherically averaged effective mass of the heavy (light) hole branch of Γ_{8v} bands. m is the mass of free electron. † Extrapolated value from measurement performed on $Al_xGa_{1-x}As$ with x from 0 to 0.21.

	$E_g(\Gamma)$ (eV)	$\Delta_{\rm so}$ (eV)	m_c/m	m_{hh}/m	m_{lh}/m	g_c
GaAs	1.519	0.341	0.067	0.5	0.08	-0.44
InAs	0.45	0.38	0.026	0.4	0.026	-15.0
$Al_{0.3}Ga_{0.7}As$	1.949		0.084	0.575	0.104	0.6 †

The expansion coefficients $F_{\mathbf{k}m}$ are determined from the Luttinger Hamiltonian

$$H_L = \frac{\hbar^2}{2m}\left[\left(\gamma_1 + \frac{5}{2}\gamma_2\right)k^2 - 2\gamma_2(\mathbf{k}\cdot\mathbf{J})^2 + 2(\gamma_3-\gamma_2)(k_x^2J_x^2 + k_y^2J_y^2 + k_z^2J_z^2))\right], \tag{II.8}$$

where the parameters γ_1,γ_2 and γ_3 are known as the Kohn-Luttinger parameters and $\mathbf{J} = (J_x, J_y, J_z)$ is an operator whose effects on the Γ_8 valance band edge states are identical to those of the angular momentum operator on the $J = 3/2$ atomic states. The first two terms in Eqn. (II.8) have spherical symmetry while the last represents the effect of the lower cubic symmetry which will cause warping of the constant energy surfaces in the Brillioun zone. The Luttinger Hamiltonian can also be expressed in matrix form [44]

$$H_L = \begin{bmatrix} P+Q & -S & R & 0 \\ -S^\dagger & P-Q & 0 & R \\ R^\dagger & 0 & P-Q & S \\ 0 & R^\dagger & S^\dagger & P+Q \end{bmatrix}. \tag{II.9}$$

The matrix elements are

$$P = \frac{\gamma_1\hbar^2}{2m}(k_x^2+k_y^2+k_z^2), \tag{II.10}$$

$$Q = \frac{\gamma_2\hbar^2}{2m}(k_x^2+k_y^2-2k_z^2), \tag{II.11}$$

$$S = \frac{\sqrt{3}\gamma_3\hbar^2}{m}k_zk_-, \tag{II.12}$$

$$R = -\frac{\sqrt{3}\hbar^2}{4m}(\gamma_2+\gamma_3)k_-^2 - \frac{\sqrt{3}\hbar^2}{4m}(\gamma_2-\gamma_3)k_+^2, \tag{II.13}$$

where $k_\pm = k_x \pm ik_y$. The basis set for the matrix in Eqn. (II.9) is : $|J = 3/2, J_z = 3/2\rangle$, $|J = 3/2, J_z = 1/2\rangle$, $|J = 3/2, J_z = -1/2\rangle$ and $|J = 3/2, J_z = -3/2\rangle$.

In bulk material, we can always choose the quantization axis for angular momentum $\mathbf{J}$ to be along the direction of the crystal momentum $\mathbf{k}$ and if we neglect the non-spherical terms

in Eqn. (II.8), we obtained the eigenenergies of Eqn. (II.8),

$$E_{\mathbf{k}m} = \begin{cases} \frac{k^2}{2m_{hh}}, & m = \pm\frac{3}{2} \\ \frac{k^2}{2m_{lh}}, & m = \pm\frac{1}{2} \end{cases}, \tag{II.14}$$

where $m_{hh} = m/(\gamma_1 - 2\gamma_2)$ and $m_{lh} = m/(\gamma_1 + 2\gamma_2)$. Eqn. (II.14) describes two doubly degenerate subbands with the effective mass m_{hh} and m_{lh} respectively in the vicinity of the band edge. The subband with the larger effective mass m_{hh} is referred as the heavy hole (hh) band and the subband with the smaller effective mass m_{lh} is referred as the light hole (lh) band. Therefore, the degeneracy of the valance band originated from the quadruplet is lifted for finite $|\mathbf{k}|$ by the different effective mass as shown in Fig. II.1. In Table. II.1, the effective mass (bulk value) of the heavy hole and light hole band is listed for several relevant bulk material of III-V compounds.

II.A.2 Vertical confinement

The eigenstates in the quantum well is obtained based on the envelope function approach [41]. The method requires that the A and B materials constituting the quantum well structures are well lattice matched and they crystallize with the same crystallographic structure which are well satisfied for the GaAs/AlGaAs and GaAs/InAs heterostructures.

In the envelope function model, the key assumption is to write the heterostructure wavefunction as,

$$\psi(\mathbf{r}) = \sum_n f_n^{(A,B)}(\mathbf{r}) u_{n0}(\mathbf{r}), \tag{II.15}$$

where the band edge Bloch functions are assumed to be the same in each kind of layer that constitutes the quantum well structure. The objective is to determine $f_n^{(A,B)}(\mathbf{r})$. Since $u_{n0}(\mathbf{r})$ are linearly independent, the continuous condition for the wavefunction at $z = z_0$ gives

$$f_n^{(A)}(\mathbf{r}_\perp, z_0) = f_n^{(B)}(\mathbf{r}_\perp z_0), \tag{II.16}$$

where $\mathbf{r}_\perp$ is a two-dimensional position vector perpendicular to the growth direction (z direction). The lattice match condition ensures the heterostructure to be translationally invariant in the layer plane. Therefore, f_n can be further factorized into,

$$f_n^{(A,B)}(\mathbf{r}) = \frac{1}{\sqrt{S}} \exp(i\mathbf{k}_\perp \cdot \mathbf{r}_\perp) \chi_n^{(A,B)}(z), \tag{II.17}$$

where S is the sample area and $\mathbf{k}_\perp = (k_x, k_y)$ is the in plane wavevector.

The relevant heterostructure states are constructed from the host states near the zone center which are well described by the $\mathbf{k} \cdot \mathbf{p}$ method in II.A.1. We further take the *Ben Daniel-Duke Model* [41] which assumes the heterostructure state is built from host states that belongs

to a single band. This model works qualitatively well for the lowest conduction states of GaAs-Ga(Al)As heterostructures with GaAs layer thickness larger than ~ 100 $\mathring{A}$ and for the heavy hole levels at $\mathbf{k}_\perp = 0$ in any heterostructure. Since most of the physics can be made transparent within this simple model, we will apply it for calculation of the quantum well confinement for the conduction band state and also use the model as the starting point for the discussion of the confined heavy hole and light hole valance band states.

We first look at the conduction band. The effective masses will be denoted by $m_A^*(m_B^*)$ and the energy of conduction band edge by $\varepsilon_c^{A(B)}$ in the A(B) layers. We have [41],

$$\left[\varepsilon_c(z) + \frac{\hbar^2 k_\perp^2}{2\mu(z)} - \frac{\hbar^2}{2}\frac{\partial}{\partial z}\frac{1}{\mu(z)}\frac{\partial}{\partial z}\right]\chi(z) = \varepsilon\chi(z) \tag{II.18}$$

where $\mu(z) = m_A^*$ (m_B^*) and $\varepsilon_c(z) = \varepsilon_c^A$ (ε_c^B) if z corresponds to layer A (B). The boundary conditions at the A-B interfaces are such that $\chi(z)$ and $\frac{1}{\mu(z)}\frac{d\chi}{dz}$ both being continuous. The difference in energy of the conduction band edge of the two materials form a one-dimensional potential trap for the conduction band electron (see Fig. II.4). The energy scale of this trap is $\sim 0.1 - 1$ eV which is a rather strong confinement. The effective mass mismatch also contributes to the total confining barrier by a term which is $k_\perp$ dependent. This term is small in most instances, e.g., conduction states in GaAs/Al_xGa_{1-x}As. If we further neglect this effective mass mismatch by assuming $m_A^* = m_B^* = m^*$, Eqn. (II.18) reduces to the quantum mechanics textbook problem of a particle confined in a one-dimensional square well.

To have a qualitative picture of the trapped states in this square well potential, we first estimate the energy levels for an infinite potential well problem,

$$E_n(k_x, k_y) = \frac{\hbar^2}{2m_A^*}\left[(\frac{n\pi}{d})^2 + k_x^2 + k_y^2\right] \quad n = 1, 2, 3, \cdots$$

At $k_x = k_y = 0$, the energy levels are equal to $E_l = \frac{\hbar^2}{2m^*}(\frac{l\pi}{d})^2$. The quantum well structure for the GaAs fluctuation quantum dot under investigation has a thickness d ranges from $\sim 3 - 6$ nm [30, 37]. By plug in this number and the effective mass of the conduction band electron (see Table. II.1), we have the ground state energy $E_1 \sim 0.1$ eV which is in the same order of magnitude as the confinement potential. Therefore, we conclude that while the quantum well potential in the growth direction is sufficient to hold several energy levels confined in growth direction, in the real situation, the potential is not sufficiently strong to confine the electron entirely in the GaAs layer and a portion of it will evanescently penetrate into the AlGaAs layer. This could lead to the large deviation of the heterostructure electron g-factor from the bulk value in GaAs [45] (note the sign and magnitude difference in the bulk g-factor of GaAs and AlGaAs materials in Table. II.1). The lift of the energy of the conduction band electron by this quantum well confinement from the bulk band edge is ~ 0.1 eV.

For the confinement of holes in quantum well, it is convenient to use the Luttinger Hamiltonian of Eqn. (II.8) to which we add the confinement potential due to the difference in energy of the band edge of host material A and B. For simplicity, we also neglect the non-spherical term in the Luttinger Hamiltonian and further assume that the Kohn-Luttinger parameters are identical in the layers A and B. We denote the energy of the valance band edge by $\varepsilon_c^{A(B)}$ in the A(B) layers. The hole Hamiltonian in the quantum well becomes [40],

$$\mathcal{H} = \frac{\hbar^2}{2m}\left[(\gamma_1 + \frac{5\gamma_2}{2})\nabla^2 - 2\gamma_2(\mathbf{J}\cdot\boldsymbol{\nabla})^2\right] + \varepsilon_v(z) \tag{II.19}$$

where $\boldsymbol{\nabla}$ act on the envelope part of the hole wave function, and $\varepsilon_v(z) = \varepsilon_v^A$ (ε_v^B) if z corresponds to layer A (B). The Hamiltonian of Eqn. (II.19) is non-separapable because of the terms like $J_xJ_z(\partial/\partial x)(\partial/\partial z))$ (the off-diagonal term S in the matrix form of Eqn. (II.9)). These "off-diagonal" term will have negligible effect for small in plane $k_\perp$ but could induce band anti-crossing for large $k_\perp$. Here we first neglect these "off-diagonal" terms and consider their effects later.

If we choose the quantization axis of the angular momentum $\mathbf{J}$ along the growth direction (z direction), the Hamiltonian for motion in the z direction becomes,

$$\mathcal{H} = \frac{\hbar^2}{2m}\left[(\gamma_1 + \frac{5\gamma_2}{2}) - 2\gamma_2 J_z^2\right]\left(\frac{\partial}{\partial z}\right)^2 + \varepsilon_v(z) \tag{II.20}$$

For $J_z = 3/2$ state, the above Hamiltonian is a one-dimensional square potential for a particle with mass equal to the heavy hole effective mass $m_{hh} = m/(\gamma_1 - 2\gamma_2)$ in the bulk. Similarly, $J_z = 1/2$ state acts as if it had the light hole effective mass $m_{lh} = m/(\gamma_1 + 2\gamma_2)$ in the bulk. Therefore, the confinement energy is larger for the $J_z = 1/2$ state than the heavy $J_z = 3/2$ state, as illustrated in Fig. II.3(a). This lifts the degeneracy of the $J_z = 3/2$ band and $J_z = 1/2$ and the energy spacing of the ground states of confinement of the two bands can be estimated by assuming the infinite potential well: $E_{J_z=3/2} - E_{J_z=1/2} \sim -\frac{\hbar^2}{2m_{hz}}(\frac{\pi}{d})^2 + \frac{\hbar^2}{2m_{lz}}(\frac{\pi}{d})^2 \sim 0.1$ eV.

The Hamiltonian for the in plane motion is given by,

$$\mathcal{H} = \frac{\hbar^2}{2m}\left[(\gamma_1 + \frac{5\gamma_2}{2}) - 2\gamma_2 J_x^2\right]\left(\frac{\partial}{\partial x}\right)^2 \tag{II.21}$$

As we have chosen the quantization of angular momentum $\mathbf{J}$ to be along the z direction, we shall evaluate J_x^2 in the z basis. We have the expectation values,

$$\begin{aligned}\langle J = 3/2, J_z = \pm 3/2|J_x^2|J = 3/2, J_z = \pm 3/2\rangle &= 3/4\\ \langle J = 3/2, J_z = \pm 1/2|J_x^2|J = 3/2, J_z = \pm 1/2\rangle &= 7/4\end{aligned}$$

Plug into Eqn. (II.21), we find that the $J_z = \pm 3/2$ bands behaves as if it had the in-plane mass $m_{hx} = m/(\gamma_1 + \gamma_2)$ while the $J_z = \pm 1/2$ states had the in-plane mass $m_{lx} = m(\gamma_1 - \gamma_2)$. Therefore, the $J_z = \pm 3/2$ states has a smaller in-plane mass than the $J_z = \pm 1/2$ states. This

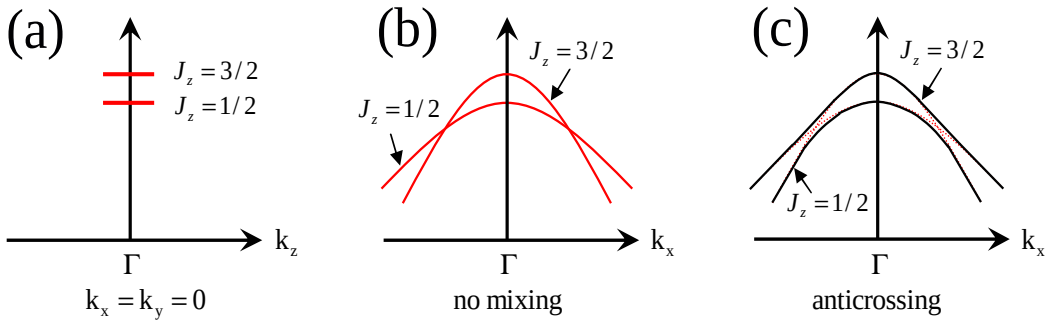

Figure II.3 Dispersion relation of the $J_z = 3/2$ and $J_z = 1/2$ valence bands in quantum well [40]. (a) Energy shift due to the confinement in the growth direction. (b) In plane dispersion of the two valance bands when the "off-diagonal" terms are neglected (without mixing). (c) Level anti-crossing when "off-diagonal" terms are included.

phenomenon is referred as mass reversal in the literature. In absence of the off-diagonal terms (S and R in Eqn. (II.9)), the two bands $J_z = 3/2$ and $J_z = 1/2$ will cross each other due to the mass reversal as illustrated in Fig. II.3(b). The off-diagonal terms lead to the mixing (anti-crossing) of the two bands $J_z = \pm 3/2$ and $J_z = \pm 1/2$ at large $k_\perp$ as shown in Fig. II.3(c). Nonetheless, the terms "heavy hole" and "light hole" will be used, as in the literature [40], to designate the subbands in quantum well arising from the $J_z = \pm 3/2$ and $J_z = \pm 1/2$ band edge states respectively. The heavy hole subband will be of our interest for optical control of quantum dynamics in the dot.

II.A.3 Lateral confinement

Electron and hole confinement within the plane of the quantum well (in the x and y direction) is made possible by the fact that the quantum well thickness is not uniform. Fig. II.4 show schematically how monolayer-size fluctuations in the quantum well can give rise to the localized $\varphi(\mathbf{r}_\perp)$ part of the envelope function. We focus on the conduction band electron and the "heavy hole" valance band. The energy lift by the quantum confinement in the z direction can be roughly estimated by $\frac{\hbar^2}{2m^*}(\frac{\pi}{d})^2$ for the lowest energy state. This energy lift is larger where the quantum well is thinner and therefore provide lateral confinement where the quantum well has an island (see Fig.II.2(a)). The energy scale of this lateral confinement is typically of several to several tens meV in GaAs fluctuation dot. GaAs fluctuation dot with lateral size ~ 40 nm can hold several localized energy levels for electron and hole. Since the lateral length scale is also larger than the exciton Bohr diameter (~ 23 nm in GaAs), the localized electrons and holes will bind together to form excitons in the fluctuation island.

In InAs self-assembled quantum dot, the lateral confinement is much stronger due to

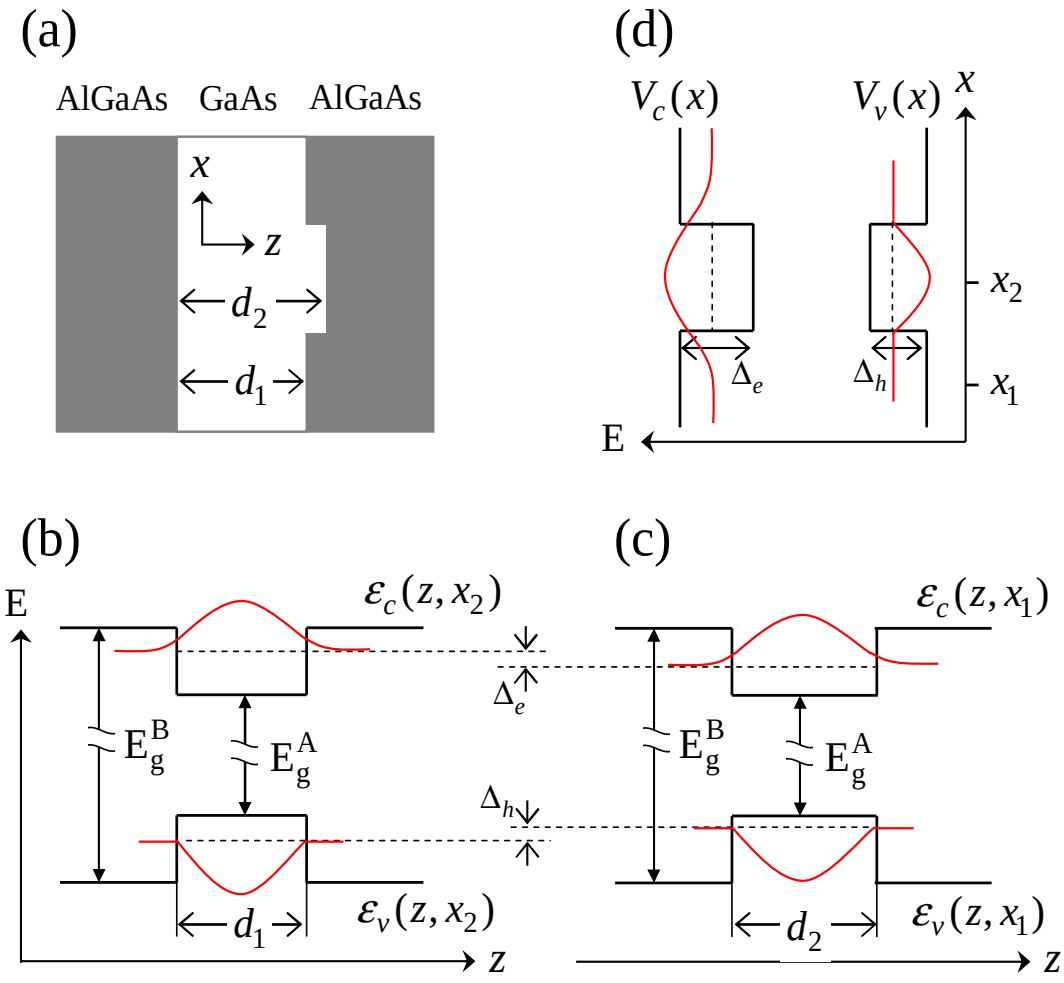

Figure II.4 Schematics of the three-dimensional confinement of electrons and holes in a GaAs fluctuation quantum dot [46]. (a) Interface fluctuation, typically of one monolayer, form a fluctuation dot. The bright region is the GaAs material and the dark region is AlGaAs. (b) Vertical confinement for electrons and holes in the growth direction (z direction) at $x = x_1$ where the quantum well is thinner $d = d_1$. (c) Vertical confinement in the growth direction at $x = x_2$ where the quantum well is one monolayer thicker $d = d_2$. (d) The difference of the energy lift by vertical confinement in regions of different thickness form a lateral confinement for the electrons and holes.

its pyramid structure as shown in Fig. II.2(b).

II.A.4 Hole-mixing

The "off-diagonal" terms S and R of the Luttinger Hamiltonian (Eqn. (II.9)) will couple the heavy hole and light hole subbands for non-zero $k_\perp$ (see also Fig. II.3). For quantum dot with inversion symmetry in the growth direction, the expectation value of k_z in the envelope function of the lowest confined states vanishes and therefore, S will have a negligible effect. In this case, the dominant contribution to heavy hole light hole mixing comes from R. In presence of hole mixing, the states that originate from the $J_z = 3/2$ heavy hole state can be generally written as: $(1, \eta_2^+, \eta_1^+, 0)$ with normalization understood. The basis set is $|J = 3/2, J_z = 3/2\rangle$, $|J = 3/2, J_z = 1/2\rangle$, $|J = 3/2, J_z = -1/2\rangle$ and $|J = 3/2, J_z = -3/2\rangle$. Similarly, the state originate from $J_z = -3/2$ state is: $(0, \eta_1^-, \eta_2^-, 1)$. $\eta_1^\pm$ and $\eta_2^\pm$ are typically small in GaAs fluctuation dot ($\eta_1^\pm$ can be of several percent and $\eta_2^\pm$ usually negligible) and can be taken as real numbers.

In InAs self-assembled quantum dot, due to stronger lateral confinement, the confined states will have larger values of $k_\perp$ and therefore, hole-mixing effect can be larger in these dots.

II.B Optical properties

II.B.1 Light-exciton interaction in quantum dot

We review here the exciton-light interaction in the quantum dot [46]. The wavelength of the optical field ($\lambda \sim \ \mu$m) is typically much larger than the dimension of the quantum dot, therefore, the light-matter interaction Hamiltonian can be written in the electric dipole approximation

$$H_i(t) = -\mathbf{P} \cdot \mathbf{E}(\mathbf{r}_0, t), \tag{II.22}$$

where $\mathbf{P} = -e\mathbf{r}$ is the polarization operator and $\mathbf{r}_0$ is the central position of the quantum dot. We first derive below the second quantized form for this polarization operator. The second quantized field operator for the electron in the quantum dot can be expressed as,

$$\psi(\mathbf{r}) = \sum_{m,\sigma} F_{c,m}(\mathbf{r}) u_{c,0}(\mathbf{r}) \chi(\sigma) a_{c,m,\sigma} + \sum_{m,l,\sigma} F_{v,m}(\mathbf{r}) u_{v,l,0}(\mathbf{r}) \chi(\sigma) a_{v,m,l,\sigma} \tag{II.23}$$

where $F(\mathbf{r})$ is the envelope function, $u(\mathbf{r})$ is the band edge Bloch function and c (v) denotes the conduction (valance) band respectively. We have limited the expansion to the lowest conduction band and the heavy hole subband of the top valance band. All the rest bands are far off-resonance from the frequency of the optical field we will be using. m denotes the quantum number in the quantum dot confinement and for the same reason, we have also limited the expansion in m to

cover only the lowest several confined states (all with the lowest quantum number in the vertical confinement, but excited states in the lateral confinement can sometimes be involved due to the smaller energy spacing ∼meV). $l = \pm 1$ is the orbital angular momentum of the heavy hole valance states (notice that $J_z = 3/2$ $(-3/2)$ is formed by the orbital angular momentum state $l = 1$ (-1) with spin on state $\uparrow$ $(\downarrow)$). $\chi(\sigma)$ are the spin wavefunction,

$$\chi(\uparrow) = \begin{bmatrix} 1 \\ 0 \end{bmatrix}, \quad \chi(\downarrow) = \begin{bmatrix} 0 \\ 1 \end{bmatrix} \tag{II.24}$$

The second quantized form of the polarization operator can be written as,

$$\begin{aligned} \mathbf{P} &= \int d^3\mathbf{r}\psi^\dagger(\mathbf{r})\mathbf{r}\psi(\mathbf{r}) \qquad \text{(II.25)} \\ &= \int d^3\mathbf{r} \sum_{m,\sigma;m',\sigma',l} F^*_{c,m}(\mathbf{r})u^*_{c,0}(\mathbf{r})\mathbf{r}F_{v,m'}(\mathbf{r})u_{v,l,0}(\mathbf{r})\delta_{\sigma,\sigma'}a^\dagger_{c,m,\sigma}a_{v,m',l,\sigma'} \\ &\quad + \int d^3\mathbf{r} \sum_{m,\sigma;m',\sigma',l} F_{c,m}(\mathbf{r})u_{c,0}(\mathbf{r})\mathbf{r}F^*_{v,m'}(\mathbf{r})u^*_{v,l,0}(\mathbf{r})\delta_{\sigma,\sigma'}a^\dagger_{v,m',l,\sigma'}a_{c,m,\sigma} \\ &= \mathbf{P}^\dagger_- + \mathbf{P}_- + \mathbf{P}^\dagger_+ + \mathbf{P}_+ \end{aligned}$$

The four components are respectively

$$\begin{aligned} \mathbf{P}^\dagger_- &\equiv \sum_{m,m'} \mu\hat{\epsilon}_+\mathcal{P}_{c,m;v,m'}a^\dagger_{c,m,\uparrow}a_{v,1,m',\uparrow} \qquad \text{(II.26)} \\ \mathbf{P}_- &\equiv \sum_{m,m'} \mu\hat{\epsilon}_-\mathcal{P}^*_{c,m;v,m'}a^\dagger_{v,1,m',\uparrow}a_{c,m,\uparrow} \\ \mathbf{P}^\dagger_+ &\equiv \sum_{m,m'} \mu\hat{\epsilon}_-\mathcal{P}_{c,m;v,m'}a^\dagger_{c,m,\downarrow}a_{v,\bar{1},m',\downarrow} \\ \mathbf{P}_+ &\equiv \sum_{m,m'} \mu\hat{\epsilon}_+\mathcal{P}^*_{c,m;v,m'}a^\dagger_{v,\bar{1},m',\downarrow}a_{c,m,\downarrow} \end{aligned}$$

where

$$\mathcal{P}_{c,m;v,m'} \equiv \int d^3\mathbf{r}F^*_{c,m}(\mathbf{r})F_{v,m'}(\mathbf{r}), \tag{II.27}$$

and

$$\mu \equiv \frac{1}{\Omega}\int_{cell} d^3\mathbf{r}u_{c,0}(\mathbf{r})xu_{v,x,0}(\mathbf{r}) = \frac{1}{\Omega}\int_{cell} d^3\mathbf{r}u_{c,0}yu_{v,y,0} = \frac{1}{\Omega}\int_{cell} d^3\mathbf{r}u_{c,0}zu_{v,z,0}, \tag{II.28}$$

are both real numbers by our convention. The polarization vector $\hat{\epsilon}_\pm$ has the properties:

$$\hat{\epsilon}_\pm = \hat{\epsilon}^*_\mp \equiv \frac{\hat{x} \pm i\hat{y}}{\sqrt{2}}, \quad \hat{\epsilon}_\pm \cdot \hat{\epsilon}^*_\pm = 1, \quad \hat{\epsilon}_\pm \cdot \hat{\epsilon}^*_\mp = 0. \tag{II.29}$$

In the last step of Eqn. (II.25), we have used,

$$u_{v,\pm 1,0}(\mathbf{r}) = \frac{u_{v,x,0}(\mathbf{r}) \pm iu_{v,y,0}(\mathbf{r})}{\sqrt{2}} \tag{II.30}$$

We have also used the property that the envelope function $F_{c,m}(\mathbf{r})$ and $F_{v,m}(\mathbf{r})$ are slowly varying within a unit cell so that,

$$\begin{aligned} & \int d^3\mathbf{r} \sum_{m,\sigma;m',\sigma'} F^*_{c,m}(\mathbf{r}) u^*_{c,0}(\mathbf{r}) \mathbf{r} F_{v,m'}(\mathbf{r}) u_{v,l,0}(\mathbf{r}) \\ = & \sum_i F^*_{c,m}(\mathbf{R}_i) F_{v,m'}(\mathbf{R}_i) \int_{cell} d^3\mathbf{r} u^*_{c,0}(\mathbf{r}) \mathbf{r} u_{v,l,0}(\mathbf{r}) \\ = & \int d^3\mathbf{R} F^*_{c,m}(\mathbf{R}) F_{v,m'}(\mathbf{R}) \frac{1}{\Omega} \int_{cell} d^3\mathbf{r} u^*_{c,0}(\mathbf{r}) \mathbf{r} u_{v,l,0}(\mathbf{r}) \end{aligned} \tag{II.31}$$

where Ω is the unit cell volume and the integral $\int_{cell}$ runs over the unit cell. The normalization condition is such that,

$$\int d^3\mathbf{R} F^*_{c(v),m}(\mathbf{R}) F_{c(v),m}(\mathbf{R}) = 1, \quad \int_{cell} d^3\mathbf{r} u^*_{c(v),0}(\mathbf{r}) u_{c(v),0}(\mathbf{r}) = \Omega \tag{II.32}$$

The electric field of the $\sigma\pm$ circular polarized light propagating in the z-direction has the form,

$$\begin{aligned} \mathbf{E}_\pm(z,t) &= E_\pm \left(\hat{x}\cos(kz-\omega t+\phi) \mp \hat{y}\sin(kz-\omega t+\phi)\right) \\ &= \frac{E_\pm}{\sqrt{2}} \left(\hat{\epsilon}_\pm e^{i\phi} e^{i(kz-\omega t)} + \hat{\epsilon}^*_\pm e^{-i\phi} e^{-i(kx-\omega t)}\right), \end{aligned} \tag{II.33}$$

The positive and negative frequency part of $\mathbf{E}_\pm(z,t)$ can be separated,

$$\mathbf{E}^{(+)}_\pm(z,t) = \frac{E_\pm}{2}(\hat{x} \pm i\hat{y}) e^{i\phi} e^{i(kz-\omega t)} = \frac{E_\pm}{\sqrt{2}} \hat{\epsilon}_\pm e^{i\phi} e^{i(kz-\omega t)} \tag{II.34}$$

$$\mathbf{E}^{(-)}_\pm(z,t) = \frac{E_\pm}{2}(\hat{x} \mp i\hat{y}) e^{-i\phi} e^{-i(kz-\omega t)} = \frac{E_\pm}{\sqrt{2}} \hat{\epsilon}^*_\pm e^{-i\phi} e^{-i(kz-\omega t)} \tag{II.35}$$

Therefore, the light-exciton Hamiltonian with polarization operation expressed in the second quantized form is,

$$\begin{aligned} H_i &= \mathbf{E}\cdot\mathbf{P} = (\mathbf{P}^\dagger_- + \mathbf{P}_- + \mathbf{P}^\dagger_+ + \mathbf{P}_+) \cdot (\mathbf{E}^{(+)}_- + \mathbf{E}^{(-)}_- + \mathbf{E}^{(+)}_+ + \mathbf{E}^{(-)}_+) \\ &= (\mathbf{P}^\dagger_- + \mathbf{P}_+) \cdot (\mathbf{E}^{(+)}_- + \mathbf{E}^{(-)}_+) + (\mathbf{P}_- + \mathbf{P}^\dagger_+) \cdot (\mathbf{E}^{(-)}_- + \mathbf{E}^{(+)}_+) \end{aligned} \tag{II.36}$$

where in the last step we have used the properties of $\hat{\epsilon}_\pm$ in Eqn. (II.29)

From now on, we will work with the rotating wave approximation (RWA). In this approximation, terms in a Hamiltonian which oscillate rapidly are neglected. This is a valid approximation when the applied optical field is near resonance with the transition in quantum dot, and the intensity is low. Explicitly, terms in the Hamiltonian which oscillate with frequencies $\omega + E$, are neglected while terms which oscillate with frequencies $\omega - E$ are kept, where ω is the

light frequency, and E is a transition frequency. The Hamiltonian in RWA is therefore,

$$\begin{aligned} H_{\text{RWA}} &= \mathbf{P}_-^\dagger \cdot \mathbf{E}_-^{(+)} + \mathbf{P}_+ \cdot \mathbf{E}_+^{(-)} + \mathbf{P}_- \cdot \mathbf{E}_-^{(-)} + \mathbf{P}_+^\dagger \cdot \mathbf{E}_+^{(+)} \\ &= \sum_{m,m',i} \frac{\Omega_{i,-}^{m,m'}}{2} e^{i\phi_i} e^{i(k_i z_0 - \omega_i t)} a_{c,m,\uparrow}^\dagger a_{v,1,m',\uparrow} \\ &\quad + \sum_{m,m',i} \frac{\Omega_{i,+}^{m,m'}}{2} e^{i\phi_i} e^{i(k_i z_0 - \omega_i t)} a_{c,m,\downarrow}^\dagger a_{v,\bar{1},m',\downarrow} \\ &\quad + \sum_{m,m',i} \frac{\Omega_{i,-}^{m,m'}}{2} e^{-i\phi_i} e^{-i(k_i z_0 - \omega_i t)} a_{v,1,m',\uparrow}^\dagger a_{c,m,\uparrow} \\ &\quad + \sum_{m,m',i} \frac{\Omega_{i,+}^{m,m'}}{2} e^{-i\phi_i} e^{-i(k_i z_0 - \omega_i t)} a_{v,\bar{1},m',\downarrow}^\dagger a_{c,m,\downarrow} \end{aligned} \tag{II.37}$$

where

$$\Omega_{i,\sigma}^{m,m'} \equiv \sqrt{2}\mu \mathcal{P}_{c,m;v,m'} E_{i,\sigma}, \tag{II.38}$$

usually referred as the **Rabi frequency** in the literature. z_0 is the central coordinate of quantum dot in the growth direction and $E_{i,\sigma}$ denotes the amplitude of the σ circularly polarized component of the ith optical field.

Eqn. (II.37) describes the interaction of quantized mode of electrons and holes with classical electromagnetic field. As the interaction of quantum dot with quantized mode of electromagnetic field is also involved in our work, we provide the form of the Hamiltonian where the electromagnetic field operator is quantized,

$$\mathbf{E}_\pm^{(+)}(\mathbf{r}) = i \sum_j \sqrt{\frac{\hbar\omega_j}{2\epsilon}} \hat{\epsilon}_\pm v_j(\mathbf{r}) b_{j,\pm} \tag{II.39}$$

where $b_{j,\sigma}$ is the photon annihilation operator of a photon in mode j with polarization σ, frequency ω_j and spatial profile $v_j(\mathbf{r})$. Similarly, $\mathbf{E}_\pm^{(-)}$ is the sum of the $b_j^\dagger$ terms with,

$$\mathbf{E}_\pm^{(-)}(\mathbf{r}) = \left[\mathbf{E}_\pm^{(+)}(\mathbf{r})\right]^\dagger \tag{II.40}$$

H_{RWA} in the second quantized form is therefore,

$$\begin{aligned} H_{\text{RWA}} &= i \sum_{m,m',j} \mu \mathcal{P}_{c,m;v,m'} \sqrt{\frac{\hbar\omega_j}{2\epsilon}} v_j(\mathbf{r}_0) a_{c,m,\uparrow}^\dagger a_{v,1,m',\uparrow} b_{j,-} \\ &\quad + i \sum_{m,m',j} \mu \mathcal{P}_{c,m;v,m'} \sqrt{\frac{\hbar\omega_j}{2\epsilon}} v_j(\mathbf{r}_0) a_{c,m,\downarrow}^\dagger a_{v,\bar{1},m',\downarrow} b_{j,+} \\ &\quad - i \sum_{m,m',j} \mu \mathcal{P}_{c,m;v,m'}^* \sqrt{\frac{\hbar\omega_j}{2\epsilon}} v_j^*(\mathbf{r}_0) a_{c,m,\uparrow} a_{v,1,m',\uparrow}^\dagger b_{j,-}^\dagger \\ &\quad - i \sum_{m,m',j} \mu \mathcal{P}_{c,m;v,m'}^* \sqrt{\frac{\hbar\omega_j}{2\epsilon}} v_j^*(\mathbf{r}_0) a_{c,m,\downarrow} a_{v,\bar{1},m',\downarrow}^\dagger b_{j,+}^\dagger \end{aligned} \tag{II.41}$$

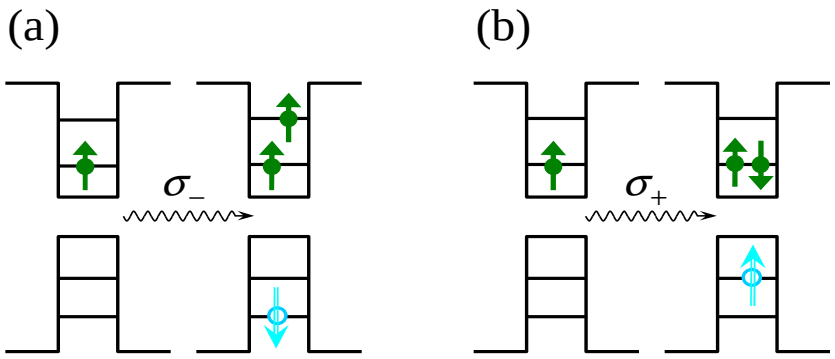

Figure II.5 Schematic illustration of the creation of trion states in quantum dot. The quantum dot initially holds a single conduction band electron with spin up in the lowest state of the confinement potential. (a) Due to the Pauli exclusion law, a $\sigma-$ circularly polarized light can only create an exciton on the excited state of the quantum dot confinement. (b) $\sigma+$ polarized light can create the lowest energy trion state with two electrons forming a singlet and a hole in the spin up state.

The physical interpretation of Eqn. (II.41) is transparent. By absorption of a $\sigma-$ polarized photon (therefore annihilate it), a spin up electron can be promoted from the heavy hole valance band with orbital angular momentum +1 to the conduction band. Alternatively, we can also say that absorption of a $\sigma-$ polarized photon will create an exciton consist of a $J_z = 1/2$ electron and a $J_z = -3/2$ heavy hole. The term with $\sigma+$ polarized photon has a similar interpretation. The conjugate term just describes the conjugate process: annihilation of an exciton accompanied by the photon emission. The neglected terms by the RWA is also easily understood, it just describes the process that an exciton and a photon are annihilated together or created together both of which are extremely unfavorable in energy.

II.B.2 Optical transition selection rules

If an optical field is in resonance with one of transitions, e.g., $(c, m) \rightarrow (v, m')$, and the bandwidth and Rabi frequency of this field is much smaller than the energy spacing between the quantized states by the lateral confinement ($\sim 1 - 10$ meV), it is then well justified to assume that only the electrons $a_{c,m,\sigma}$ and $a_{v,\pm 1,m',\sigma}$ are involved in interaction with this optical field. This is usually the situation in this study. Without causing confusion, we are going to use below the $e^\dagger_\pm$ to denote the creation of an conduction band electron of $J_z = \pm 1/2$ with the quantum number m in the confinement potential understood and similarly $h^\dagger_\pm$ to denote the creation of a heavy hole with $J_z = \pm 3/2$ (annihilation of an electron in the heavy hole valance band with $J_z = \mp 3/2$).

In the most cases of interest, the GaAs fluctuation dot or InAs self-assembled dot is

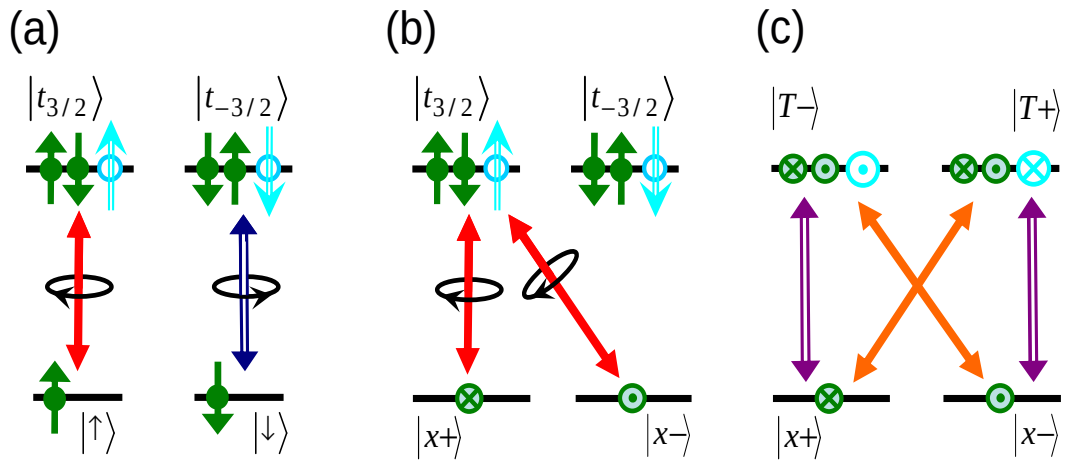

Figure II.6 Optical transition selection rules in quantum dot illustrated in various basis sets. (a) The basis being eigenstates of $\hat{J}_z$. Red single solid line denotes σ_+ polarized light and blue double solid line denotes σ_- polarized light. (b) The two electron spin states are transformed to the basis in x direction: $|x\pm\rangle \equiv (|\uparrow\rangle \pm |\downarrow\rangle)/\sqrt{2}$. Red single solid line denotes σ_+ polarized light. (c) The two trion states are also transformed to the basis in x direction: $|T\pm\rangle \equiv (|t_{\frac{3}{2}}\rangle \pm ||t_{-\frac{3}{2}}\rangle)/\sqrt{2}$. Purple double solid line denotes X-polarized light and orange single solid line denotes Y-polarized light.

charged with one extra electron in the conduction band, e.g., by modulation Si doping in the barrier. Optical field with $\sigma\pm$ polarization can create charged exciton state (also known as trion) as illustrated in Fig. II.5. Due to the coulomb interaction, the spatial part of the wavefunction of exciton in presence of the extra electron could be slightly modified, leading to quantitative change in the envelop part of the transition dipole moment $\mathcal{P}_{c,m;v,m'}$. The energy of the excitonic states can also be affected by the coulomb binding energy. Nonetheless, we can expect that the form of the light-matter interaction will NOT be changed qualitatively by the presence of the single electron. Trion states can be created in two types of configurations as illustrated in Fig. II.5. We are interested in the lowest trion states which correspond to the configuration in Fig. II.5(b): the two electrons form a spin singlet and the hole spin can be up and down and both the electrons and hole are in the lowest energy states of quantum dot confinement. In this case, the four states that are involved in the interaction with light are the two single electron states and two trion states. In the eigenbasis of $\hat{J}_z$, they are respectively: $|\uparrow\rangle \equiv e_+^\dagger|G\rangle$, $|\downarrow\rangle \equiv e_-^\dagger|G\rangle$, $|t_{\frac{3}{2}}\rangle \equiv e_+^\dagger e_-^\dagger h_+^\dagger|G\rangle$ and $|t_{-\frac{3}{2}}\rangle \equiv e_+^\dagger e_-^\dagger h_-^\dagger|G\rangle$ where $|G\rangle$ denote an empty conduction band and full valence band. We have neglected the heavy hole light hole mixing for the moment. The transition selection rule between these four states is shown Fig. II.6(a). The transition selection rule represented in other basis sets are also useful in our study. In Fig. II.6(b) and (c), we have changed the basis for the spin states and the trion states respectively so that they are eigenstates of the total angular momentum in the x direction $\hat{J}_x$. The selection rule can also be represented with the linearly

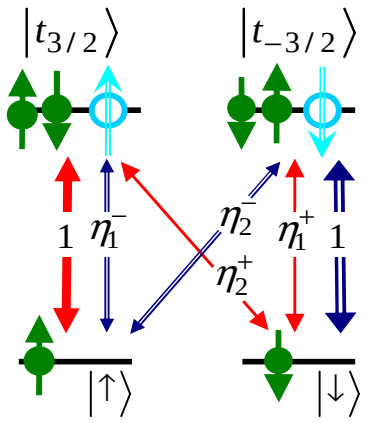

Figure II.7 Imperfect transition selection rule in the growth direction in presence of heavy hole-light hole mixing. Red single solid line denotes σ_+ polarized light and blue double solid line denotes σ_- polarized light.

polarized basis for the optical field as shown in Fig. II.6(c).

II.B.3 Control of spin qubit in quantum dot via the optical Raman process

In our system, the qubit is encoded in the spin 1/2 subspace of the quantum dot single electron in the conduction band. The localized single electron has the advantage of long spin coherence time (a detailed investigation of this is the subject of chapter VII). Arbitrary control of the spin, i.e., rotation from an arbitrary initial state $\alpha|\uparrow\rangle + \beta|\downarrow\rangle$ to an arbitrary final state $\mu|\uparrow\rangle + \nu|\downarrow\rangle$ in the spin subspace, is realized through an optical Raman process via the intermediate trion states. As shown in previous section, optical field can create or annihilate an electron-hole pair in the quantum dot, coupling the single electron spin states to the trion states. Depending on the polarization and frequency of the optical field, various optical paths can be established to realize the rotation of the spin via the Raman scheme. For example, if we select the optical field to be $\sigma+$ circularly polarized, as shown in Fig. II.6(b), then the $|t_{-\frac{3}{2}}\rangle$ trion state is decoupled from optical field and not involved in the dynamics. Therefore, we obtained a Λ like three level system. A scheme for arbitrary rotations in the spin subspace via an optical Raman transition through the intermediate trion state $|t_{\frac{3}{2}}\rangle$ has been proposed in [17] and serves as the main method for single qubit control. In this scheme, rotations of spin are realized with pulse shaped single laser field with $\sigma+$ polarization. Alternatively, the two arms of the Raman transition in the Λ system can be coupled independently by two different optical fields. This could be realized by applying a strong magnetic field, e.g. in the x direction, to

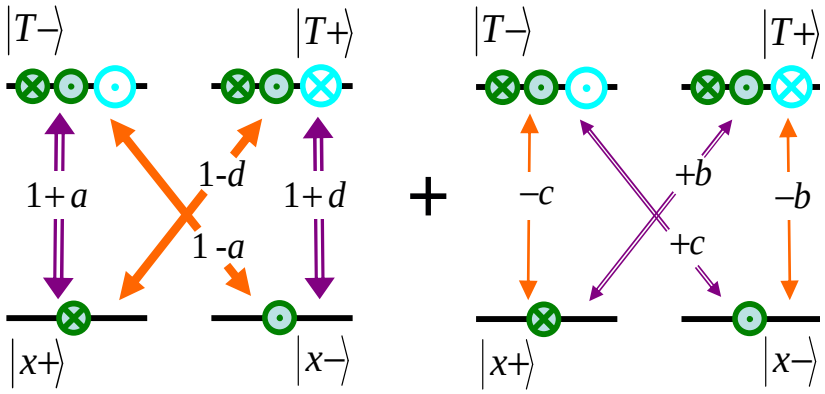

Figure II.8 Imperfect transition selection rule in the x basis. Purple double solid line denotes X-polarized light and orange single solid line denotes Y-polarized light. The left part shows the major selection rules with each transitions denoted by thick solid lines and the right part denotes the small corrections due to hole mixing with each transitions denoted by thin solid lines. The coefficients are respectively:$a \equiv (\eta_1^+ + \eta_2^+ + \eta_1^- + \eta_2^-)/2; b \equiv (-\eta_1^+ + \eta_2^+ + \eta_1^- - \eta_2^-)/2; c \equiv (-\eta_1^+ - \eta_2^+ + \eta_1^- + \eta_2^-)/2; d \equiv (\eta_1^+ - \eta_2^+ + \eta_1^- - \eta_2^-)/2$.

split the spin states $|x\pm\rangle$. Due to the vanishing g factor of holes in the x direction, the two trion states $|T\pm\rangle$ will remain degenerate. By having a X-polarized optical field with frequency near the resonance of $|x+\rangle \rightarrow |T-\rangle$ transition and a Y-polarized field with frequency near the resonance of $|x-\rangle \rightarrow |T-\rangle$ transition, the transition to trion state $|T+\rangle$ is off-resonance with both fields and therefore negligible as compared to the doubly resonant Raman transition between the rest three states and a desired Raman configuration is obtained. As shown in later chapters, the optical Raman process will play a central role in control of spin and photon dynamics in the quantum dot.

II.B.4 Optical transition selection rules with imperfections

In presence of the heavy hole-light hole mixing, we still use $|t_{\frac{3}{2}}\rangle$ to denote the mixed state trion which has the general form of the coefficients of the hole components: $(1, \eta_2^+, \eta_1^+, 0)$ in the basis with hole spin on $|J = 3/2, J_z = 3/2\rangle$, $|J = 3/2, J_z = 1/2\rangle$, $|J = 3/2, J_z = -1/2\rangle$ and $|J = 3/2, J_z = -3/2\rangle$ state respectively and its time reversed components as $|t_{-3/2}\rangle$ with the corresponding components $(0, \eta_1^-, \eta_2^-, 1)$ (see the discussion in section II.A.4). $\eta_1^\pm$ and $\eta_2^\pm$ are typically small ($\eta_1^\pm$ can be of several percent and $\eta_2^\pm$ usually negligible) and can be taken as real numbers. The imperfect transition selection rule in the growth direction is shown in Fig. II.7.

By a transform to the basis $\{|T_\pm\rangle \equiv (|t_{3/2}\rangle \pm |t_{-3/2}\rangle)/\sqrt{2}, |x_\pm\rangle \equiv (|\uparrow\rangle \pm |\downarrow\rangle)/\sqrt{2}\}$, the corresponding transition selection rules are obtained as shown in Fig. II.8. At zero magnetic field, there is time reversal symmetry between the two sets of states $\{|t_{3/2}\rangle, |\uparrow\rangle\}$ and $\{|t_{-3/2}\rangle, |\downarrow\rangle\}$

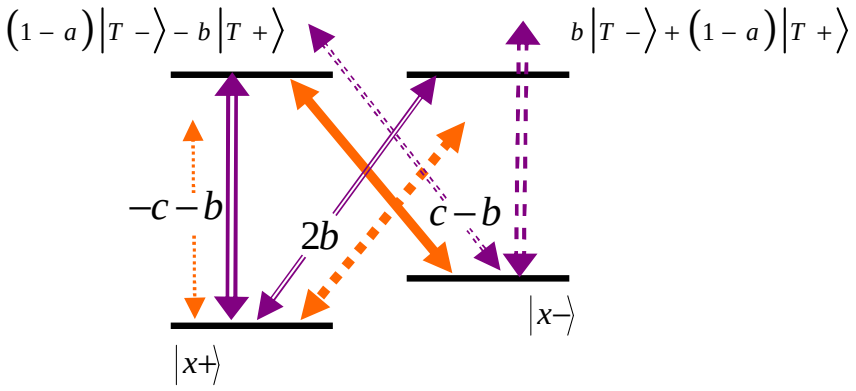

Figure II.9 Level schemes and transition selection rule in the x basis under a magnetic field in the x direction. Solid line are used to denote on-resonance transitions and dotted lines for off-resonance transitions. Purple double line denotes X-polarized light and orange single line denotes Y-polarized light.

in the growth direction, thus we have $\eta^{+}_{1,2} = \eta^{-}_{1,2}$ so that b and c vanishes in Fig. II.8. The transition selection rules in the x basis are thus purely the left part of Fig. II.8. In this case, the imperfection in transition selection rules in the growth direction is eliminated in the x basis and the coefficients a, d only contribute to a small modification of the transition strength which can be characterized in experiments.

b and c can have small but non zero values in a magnetic field and the right part of Fig. II.8 contributes to the imperfections in optical transitions. Nonetheless, the facts that trion states only play a role as intermediate states and that the two trion states $|t_{\pm 3/2}\rangle$ have degenerate energies allow the Raman schemes to be further protected automatically against this small imperfections. Fig. II.9 shows the transition selection rules with a basis transform in the subspace of the two trion states. The desired Raman path with Y-polarized light coupling the $|x-\rangle \leftrightarrow (1-a)|T-\rangle - b|T+\rangle$ transition and X-polarized light coupling the $|x+\rangle \leftrightarrow (1-a)|T-\rangle - b|T+\rangle$ transition are dominant with strong transition strength and double resonances while all undesired Raman pathes are either of weak transition strength in the order of $b(c)$ or far detuned or both. Thus, we still obtained a three level Λ system with desired Raman transitions as a good approximation.

II.C Chapter summary

We have reviewed in the chapter the electronic and optical properties of quantum dot formed in the III-V compounds. As a summary, we will first draw below an analogy between an electron in the crystal periodic potential under the single particle effective mass approximation

and a bare electron in free space. First of all, the envelope part of the wavefunction is analogous to the spatial wavefunction of a bare electron and the band edge Bloch function $|u_{n,0}\rangle$ (where spin-orbit coupling has been considered) is analogous to the spin wavefunction. In kinetics, the effective mass m^* replaces the free mass of a bare electron m and the crystal momentum $\hbar\mathbf{k}$ (or $-i\hbar\boldsymbol{\nabla}$ acting on the envelop function in the coordinate representation) replaces the momentum of the bare electron. In response to the external magnetic field, the effective g-factor will play the role of the g-factor ($g_0 = 2$) of a bare electron. For interband optical transitions with the light propagating in the growth direction, a similar "selection rule" can be applied here: for allowed transitions, we require $\Delta J_z = \pm 1$ for the band edge Bloch function while for the envelope part of the wavefunction, we require $\Delta L_z = 0$ if there is rotational symmetry in the x-y plane or a non-vanishing overlap between the envelop function of initial and final states in the broader case. The quantum dot confinement is also well understood in analogy to a single particle confined in quantum box, i.e., the band edge energy mismatch of different materials offers the three-dimensional confinement potential that can be plugged into the Schrödinger equation for the envelope wavefunction. This confinement leads to discrete quantized energy levels. Indeed, with all these properties, the quantum dots behave very much like "artificial atoms" with well defined optical transition selection rules. The discrete energy levels have been confirmed from the photoluminescence (PL) or photoluminescence excitation (PLE) spectrum in various types of quantum dot systems [12, 13, 14, 15, 31, 32, 33, 34, 35, 36, 38]. Quantum Dots are particularly significant for optical applications due to their large optical dipole moment. Coherent Rabi oscillations of single exciton have been observed in GaAs flucution dot [2] and In(Ga)As self assembled dot [47, 48]. Coherent oscillations between exciton to biexciton transitions have also been experimentally demonstrated in GaAs fluctuation dot [3, 4].

III

Single Photons in Optical Micro-Cavities and Waveguides: A Brief Review

In this chapter, we briefly review the confinement of photons in semiconductor microstructures, i.e., optical micro-cavities and waveguides.

III.A Single photon as carrier of quantum bit

We have mentioned in the previous chapter that the spin of the electrons in quantum dots is an excellent candidate as the carrier of qubit. As the electrons are confined to a definite spatial region, the spin qubit belongs to the type which is usually referred as the stationary qubit. Alternatively, if the carrier qubit can move freely from one region of the space to another, it is referred as the flying qubit. A canonical example for the flying qubit is the photon wavepacket which is widely used for photonic quantum computation with linear optics elements [49] and quantum cryptography [50, 51]. As the photon can have many degrees of freedom, there are more than one ways to encode the quantum information. We show below several examples.

Polarization qubit. Here the quantum information is encoded in the polarization subspace. For example, for photon in free space, we can use the basis of linear polarization,

$$|\psi\rangle = a|X\rangle + b|Y\rangle \tag{III.1}$$

or the basis of circular polarization,

$$|\psi\rangle = a|\circlearrowleft\rangle + b|\circlearrowright\rangle \tag{III.2}$$

The requirement is that the different polarization components have an identical spatial wavefunction so that they can not be distinguished unless polarization degrees are measured (no leakage of quantum information outside the polarization subspace). Single qubit rotation can be easily achieved, e.g., with wave plate.

Number qubit. Here the quantum information is encoded in the photon number subspace, e.g.,

$$|\psi\rangle = a|vac\rangle + b|\alpha\rangle \tag{III.3}$$

where $|vac\rangle$ denote the vacuum and $|\alpha\rangle$ denote a single photon wavepacket $|\alpha\rangle \equiv \int dk\alpha_k|k\rangle$ where $|k\rangle$ represents plane waves. Single qubit ration for this type of number qubit is not easy. Nonetheless, they can be used in the intermediate step of a quantum operation, e.g., for transfer of quantum information [52].

Photon propagation in free space is subjected to attenuation and decoherence. A more ideal propagation channel for photons are provided by optical fiber [53, 54] or optical waveguides which can be etched on semiconductor structures [55] or formed in line defects in photonic crystals [56, 57]. In optical fiber or waveguides, number qubit can be similarly defined as in free space. Propagation modes with orthogonal polarization but degenerate in energy also exists in fiber and waveguides and therefore polarization qubit can be defined in a similar way, e.g., in the basis of TE and TM modes or alternatively in the linearly polarized basis of LP modes [53, 54].

III.B Confinement of single photons in micro-cavities

Stationary spin qubit in quantum dot has the advantage of addressability, stability and integrability. Single photon travels at the speed of light and therefore is an ideal candidate for quantum communication between spatially separated regions. Flying photon qubit and stationary spin qubit are complementary to each other in their advantages. In order to integrate the dynamics of photonic qubit with spin qubit in quantum dot and utilize the advantages of both, we need the single photon to interact appreciably with the electronic states in a single quantum dot. From the light-matter interaction Hamiltonian Eqn. (II.41), as the quantum dot has a fixed optical transition dipole moment which is limited by its size, one way to have strong interaction is to make the spatial wavefunction of the photon having a large amplitude ($v(r_0)$ in Eqn. (II.41)) in the quantum dot vicinity. This can be achieved by confining photons in optical micro-cavity structures [58].

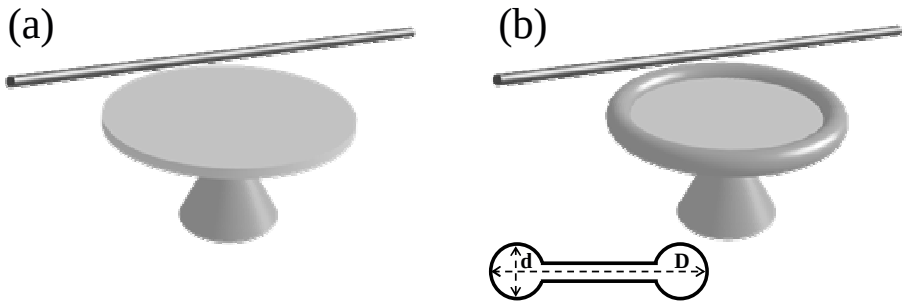

Figure III.1 Fiber coupled micro-cavities. (a) Micro-disk cavity. (b) Micro-toroid cavity. D denotes principal diameter and d denotes minor diameter [59].

III.B.1 Micro-cavities in semiconductor structures

Optical cavity refers to the resonant structures for light confinement. The principle of cavity can be illustrated with two parallel dielectric mirrors. Light is reflected back and forth in the region between the two mirrors and if the distance between mirrors satisfy: $d = n\lambda/2$ where λ is the wavelength of light and n is a integer, a standing wave cavity mode can be formed in the intermirror region. This type of cavity is usually referred as the Fabry-Perot cavities in the literature and has been widely used in the study of quantum coherent dynamics in atomic physics experiments [60].

For the purpose of strong interaction of single photons with single quantum dot, the critical properties for an optical cavity is the quality factor Q and the mode volume V.

The quality factor of a cavity mode is defined as: $Q \equiv \frac{\lambda}{\delta\lambda}$ where $\delta\lambda$ is the uncertainty of the wavelength due to the imperfections of cavity confinement. Interband transitions in semiconductor quantum dot usually occurs at the energy scale $\sim$eV and therefore, cavity modes with $\lambda_0 \sim \mu$m is of interest. For a high-Q cavity, we can also express $Q \equiv \frac{\lambda}{\delta\lambda} = \frac{\omega}{\delta\omega}$ where ω is the frequency of the mode and $\delta\omega$ is its broadening in spectrum. Obviously, the life time of the cavity mode is proportional to Q. A cavity with high Q-factor allows light to be confined in the quantum dot vicinity for sufficient long time for interaction with the electronic states. Finesse $\mathcal{F} \equiv \frac{\Delta\lambda}{\delta\lambda}$ is also used in complementary with the Q-factor to characterize the cavity property. Here $\Delta\lambda$ is the separation in wavelength between adjacent cavity modes (also known as free spectral range (FSR)). Finesse tells how well each cavity modes can be distinguished from each other and it has an intuitive interpretation of how many times light can be reflected between the mirrors before it escapes the cavity region. For low order cavity mode, Q is in the same order of $\mathcal{F}$.

A cavity with small mode volume allows a strong electric field from a single photon and

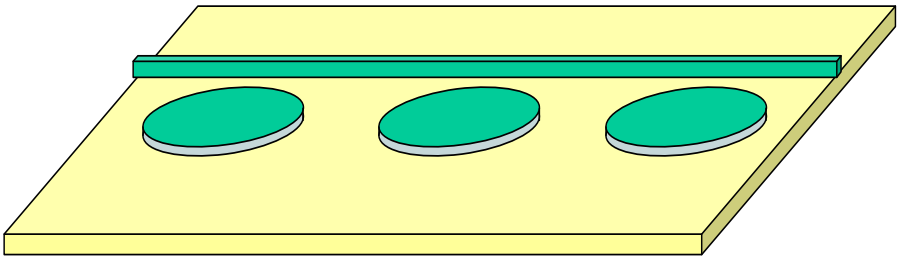

Figure III.2 Waveguide coupled micro-disk cavity on chip.

hence the strong coupling with the quantum dot. We have the relation,

$$\int d\mathbf{r} 2\epsilon E_{cav}^{(+)}(\mathbf{r}) E_{cav}^{(-)}(\mathbf{r}) = \hbar\omega \tag{III.4}$$

where $E_{cav}(\mathbf{r})$ is the electric field of the cavity mode and the integration runs over the whole cavity region. Therefore, the electric field is inverse proportional to $\sqrt{V}$.

In conventional Fabry-Perot cavity, ultra high finesse $\mathcal{F} \sim 5 \times 10^5$ has been achieved through improvement of the dielectric mirror [58]. But as the cavity mode is not well confined in the two directions that is parallel to the mirror surface, the mode volume can not be made too small. The state of art mode volume that can be achieved is $\sim \mathrm{O}(10^3)\mu\mathrm{m}^3$ [58].

Semiconductor micro-structure offers a good chance to achieve optical cavities with high-Q and small V (see [58] for a review of the progress in this field). These micro-structures are usually referred as micro-cavities for their small size. Light is confined by total internal reflection (TIR) in the inner wall of the micro-cavities (see Fig. III.4(a) for illustration). Micro-cavities can be realized in a number of ways in semiconductor structures. In Fig. III.1 and III.2, we show several examples of the micro-cavities etched on semiconductor surfaces. Two dimensional photonic bandgap crystals is also an ideal structure to form a cavity resonator [56, 57]. Propagation of light in the plane has a forbidden bandgap for carefully designed periodical arrays of air-holes drilled on the 2-D slab. As shown in Fig. III.3, by forming a point defect in the 2D arrays of air holes, the light can be almost perfectly confined in the plane of the slab if its frequency lies in the forbidden bandgap. The vertical confinement, achieved by total internal reflection at the slab semiconductor - air interfaces, is imperfect, in that light with small in-plane wavevectors can leak out of the top and bottom. Vertical leakage can also be greatly limited by proper engineering of the defect [61, 62]. We listed below the critical properties of several micro-cavities structures.

Silicon microsphere: Q exceeding 10^8, $V \sim 10^3\mu\mathrm{m}^3$ [63] [64].

Microdisk: $Q \sim \mathrm{O}(10^4)$ in III-V materials and $Q \sim \mathrm{O}(10^5)$ in polymer; $V \sim 6(\lambda_0/n)^3$ where n is the refractive index of the material and λ_0 the wavelength of cavity mode [58].

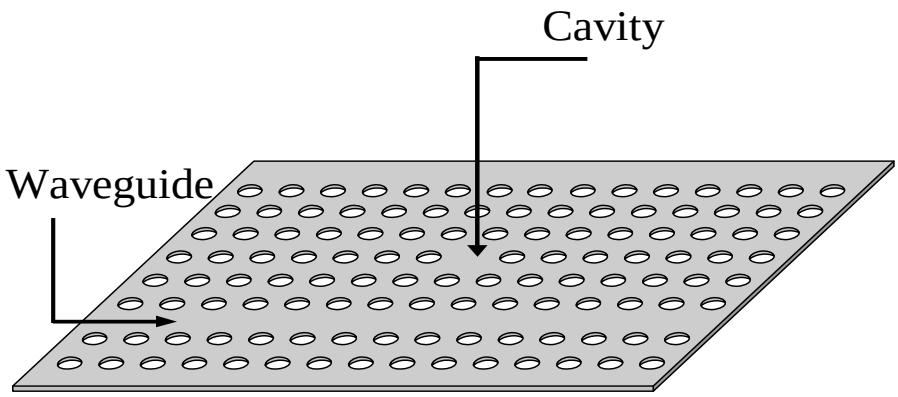

Figure III.3 Coupled cavity and waveguide structure formed by point and line defects in 2D photonic crystals.

Microtoroid: $Q \sim 10^8$ achieved with principle diameter $D \sim 100$ μm and minor $d \sim$ O(1) μm (see Fig. III.1(b) for the definitions of D and d) [59] . Theoretical analysis shows the possibility of realizing micro-toroid with intrinsic Q-factor exceeding 10^8 and mode volume $\sim$ O(10) μm^{-3} [65].

Defect cavity in 2D PC: $Q \sim 6 \times 10^5$, $V \sim 1.2(\lambda_0/n)^3 \sim 0.072$ μm^3 achieved [61, 62]. Theoretically analysis show that Q-factors greater than 2×10^7 may be obtained when optimizing the structure [62]. The matrix of the 2D photonic crystal can either be silicon or III-V compounds [66].

III.B.2 Whispering gallery mode

The cavity mode that is confined by the various types of micro-cavities discussed in III.B.1 all belongs to the same class which is usually referred as the whispering gallery mode (WGM). WGMs occur at particular resonant wavelengths of light confined to a spherical or cylindrical volume with an index of refraction greater than that surrounding it. At these wavelengths, the light undergoes total internal reflection at the volume surface and becomes trapped inside the volume (see Fig. III.4(a)). Ideal dielectric spheres have modes characterized by four indices (n, l, m, p), where (n, l, m) are radial and angular indices while p designates either TE (transverse electric) or TM (transverse magnetic) polarization. The mode number n tells the number of wavelengths around the circumference of the cavity (see Fig. III.4(b)) and the mode order l denotes the number of maxima in the radial dependence of the electromagnetic field within the cavity (see Fig. III.4(c)). In the ideal sphere each (n, l, m) subspace is $2l + 1$ degenerate. Actual resonators exhibit slight eccentricity which splits the resonant frequencies into $2l + 1$ distinct values associated with the index m. Beyond the Q and V properties discussed in III.B.1,

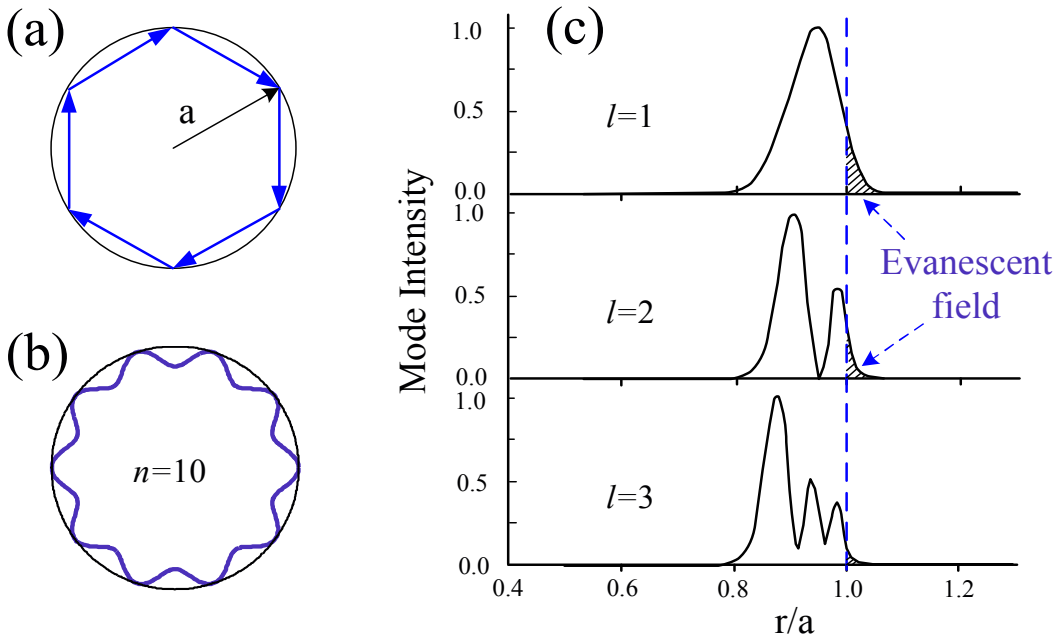

Figure III.4 Whispering gallery mode (WGM) in a micro-sphere cavity [67]. (a) Illustration of photon confinement by total internal reflection on the cavity wall. (b) WGM with mode number $n = 10$. (c) Mode intensity as a function of radial coordinate r for WGMs with the lowest several mode order l.

the spacing of cavity modes in frequency is also an important properties for applications. In a silica microsphere with diameter ~ 100 μm, the spacing in energy between modes with different n and l quantum number is larger or in the order of $\sim$meV. The splitting of modes with different m in the same (n, l) subspace due to the eccentricity is typically one fold smaller, e.g. ~ 100 μeV for a microsphere with diameter of 35μm with 2% deformation. Therefore, if coupling with a single cavity mode is desired, silica microsphere of this size is suitable for use with system where the relevant energy scales $\ll 100$ μeV, e.g., diamond nano-crystals with NV centers [20, 21, 22].

Modes with different polarizations, TE and TM, have very different electric and magnetic field profile [68]. The TE modes have no electric field amplitude in the radial direction and the electric field is in-plane along the azimuthal direction in the equator plane. The TM modes have no in-plane electric field components in the equator plane and outside the equator plane, there is a predominantly radial electric field vector.

The different geometric shape of micro-disk and micro-toroid cavities can affect the energies distributions and field profiles of the WGMs. But qualitatively, we still have quantized cavity modes characterized by the (n, l, m, p) quantum numbers which are well separated in energies. p quantum number again distinguishes TE and TM modes. For example, for micro-disk cavity, the TE modes have the electric field parallel to the disk plane; while for the TM

modes, the electric field is perpendicular to the disk plane [69].

Defect cavities formed in 2D photonic bandgap crystals lacks the cylindrical or spherical symmetry. However, the cavity modes are still referred as whispering gallery modes and denoted using the quantum numbers mentioned above. WGMs of interests here are those of the lowest several n quantum number. These modes have the smallest mode volume (in the order of cubic of half the wavelength, which is the ultimate value that can be achieved). Again, they are divided to TE type and TM type depending on the electric and magnetic field profile. Because of the strong confinement in the extreme small volume, the spacing of the cavity modes in energy is very large in this type of cavities. For the state of art micro-cavity achieved in Noda's group [61, 62], the measured spectrum shows a single resonant peak in a spectral range of $\sim$ 100meV. So this type of cavity is ideal for cavity QED applications with quantum dot where a single cavity mode is desired.

III.B.3 Strong coupling of single cavity photon with quantum dot

The strong confinement of light in an extremely small region allows the **strong coupling regime** between a single quantum of photon and a single excitation of matter. Strong coupling regime in cavity QED is defined for which the coupling energy g_{cav} between a single quantum of cavity photon and a single excitation of matter becomes larger than $\max(\gamma_{cav}, \gamma_t)$ where γ_{cav} is the cavity leakage rate and γ_t is the relaxation rate of the energy excitation of matter. Strong coupling regime is signatured, e.g. in the photoluminescence spectrum, by the observation of vacuum Rabi splitting [60]. Strong coupling regime has been achieved in several different cavity - quantum dot (nano-crystal) systems as briefly mentioned below and efforts are still being made in many other systems.

In order for the quantum dot to interact with the cavity photon, they have to be spatially arranged in the cavity field. Various arrangement is possible depending on the types of cavity we will be using.

Layers of quantum dots can be embedded in the matrix slab where the 2D photonic crystal with point defects are formed. Quantum dot sitting inside the defects at the mode maxima can have the strongest coupling with the cavity mode. Strong coupling of the defect cavity in 2D GaAs photonic crystal with the self-assembled InAs quantum dot has already been achieved [66] which is one of the first demonstration of strong coupling for single quantum dot cavity QED. Achieved simultaneously is the strong coupling of self-assembled InGaAs quantum dot with micro-pillar cavities [70]. The coupling strength $g_{cav} \sim 0.1$meV in both cases.

Micro-disk cavities can be used for coupling with III-V quantum dots. Quantum dots can be embedded inside the micro-disk so that those sitting in the mode maxima will have

the strongest possible couplings with the WGMs. Strong coupling regime for GaAs fluctuation quantum dot embedded in micro-disk structure similar to the illustration of Fig. III.1(a) has been recently achieved [71]. Due to the large dipole moment of the fluctuation dot, the coupling strength $g_{cav} \sim 0.2$meV from the measurement. For the micro-disk structures shown in Fig. III.2, quantum dot can also sits outside of the cavity in the evanescence field of WGM..

For the silicon micro-sphere cavities, nano-crystals are usually used for coupling with the cavity photons. These includes the CdSe-Cds core-shell nano-crystals [63] and diamond nano-crystals with nitrogen vacancy (NV) centers. The nano-crystals can be deposited on the surface of the micro-sphere and they sit in the evanescence field of WGMs (shaded area shown in Fig. III.4(c)).

The development in this field is so rapid that our knowledge needs to be refreshed frequently.

III.B.4 Dot-cavity-waveguide coupled structure for interplay between flying photon and stationary spin

Here we come back to the original motivation for the investigation of cavity QED: the coupled dynamics between flying photons and stationary spins.

For all applications involved in this study, only one cavity mode is involved. Therefore, the cavity shall be sufficiently small so that the mode separation in energy is much larger than all relevant energy scales and all other cavity modes can be neglected due to far detuning. For coupling to a III-V quantum dot, the micro-disk cavities and the defect cavities in 2D PBC well satisfy this condition. Micro-sphere cavities might be used together with nano-crystals (as mentioned in III.B.3) in which the excitation can be predominantly coupled to a single WGM. The inclusion of multi-cavity modes, on one hand might add to the complexity of the dynamics, and on the other hand, may provide more freedoms in dynamical control which will be the topics for future study.

For the definiteness of the transition selection rules, we may want the cavity mode have a well defined electric field direction in the vicinity of the quantum dot. Whether TE or TM mode shall be used depends on the specific spatial arrangement and the quantum operation.

The cavity-dot coupling allows the interplay between the excitation in single quantum dot with single photon confined in cavities. As we shall see in the succeeding chapters, useful applications is possible by further integration of micro-cavities with fibers or waveguides as shown in Fig. III.1, III.2 and III.3 for the various systems. The electric field of the propagating mode in fiber or waveguides overlaps with the evanescence part of the cavity field and the coupling is controllable by tuning of the distance in design. Through this coupling, a confined cavity photon

can be interconverted with a propagating single photon wavepacket in the fiber or waveguide. The selected cavity mode with the specific polarization configuration may have non-zero couplings *only* with propagation mode with a particular polarization in the fiber or waveguide. Notice that with the fiber or waveguide attached to the cavity, the total Q-factor may drop. But what is of importance is the intrinsic Q-factor in absence of the fiber or waveguide. The coupling to a highly directional out coupling channel is by design and is an important ingredient in the desired quantum dynamics as we will show in the next several chapters.

The dot-cavity-waveguide coupled structure has integrated the photonic, electronic and spintronic components in the semiconduct structures. Implementation of these coupled structures for quantum information processing will be the theme of the following chapters.

IV

Solid State Phase Gate and Quantum Entanglement for Single Photon Pairs

Entangled photon pairs are the main stay of quantum information processing [26] and the controlled gate which conditions the dynamics of one photon on the state of the other also enables a key logic operation for quantum computation. There are two approaches to realize such gates: (1) linear optics with projective measurements [49]; (2) nonlinear optics at the single photon level. Photon gate can be realized with linear optics elements, e.g., phase plate and beam splitters, facilitated by post selection based on measurement of ancillary photons. Therefore, the gate operation based on linear optics elements is probabilistic and conditioned on the measurement results. The prototype two photon gate by nonlinear optics for universal quantum information processing is the nonlinear phase gate [72]. Due to the Kerr-type nonlinearity, the presence of a second photon can induce a conditional phase shift on the other photon. A two qubit phase gate with nonlinear shift π can be shown to be equivalent to a CNOT gate facilitated by single qubit rotations and is therefore a universal two qubit gate.

The logic gate working with few-photon nonlinear optics requires impractical interaction length (e.g. several meters) in conventional Kerr media [72]. To obtain giant optical nonlinearity for a two-photon logic gate, novel schemes have been demonstrated, e.g. the atom-cavity QED [73], or proposed, e.g. slow light in a coherently prepared atomic gas exhibiting electromagnetically induced transparency (EIT) [74]. In these schemes, prior preparation of the atom media is needed. Furthermore, the interacting photons are in free space and in practical application,

collection into optical fiber or waveguide for propagation is needed. The collection processes can lower appreciably the quantum efficiency of the whole operation.

For the sake of stability and integrability, a solid state quantum phase gate for single photons is highly desirable. Calculation shows that with moderate system parameters achievable in experiments, a quantum dot embedded micro-cavity exhibit giant third order optical nonlinearity, promising for a conditional phase shift of O(π) [75, 76]. Here we propose a solid state phase gate based on the dot-cavity-waveguide coupled system. The quantum dot coupled microcavities act as a scattering center with the desired large nonlinearity for photons propagating in the optical fibers. The unique fiber-cavity structure circumvents the problem of photon collection. The photon scattering at the phase gate have inevitably some unwanted dynamics such as polarization-dependent reflection and motion-polarization entanglement. By relying on the transmission probability, the gate has some inevitable probabilistic nature as the linear optics procedure. The essential distinction lies in our use of the strong nonlinearity to provide definite interaction dynamics in the cavities versus the entanglement generated by the projective measurement. The probabilistic nature arises from the coupling of the photons to the solid state system, which is unavoidable in any system, but its effect can be ameliorated. Our solution is two pronged: to eliminate the linear reflection by EIT and to minimize motion-polarization entanglement by pulse shaping and system design.

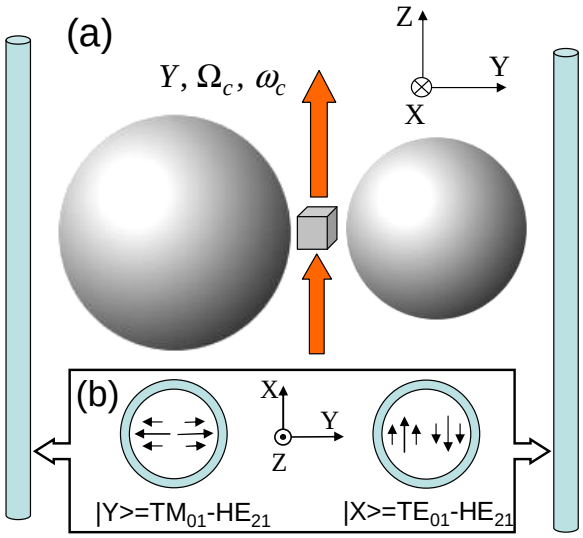

Figure IV.1 Dot-cavity-fiber coupled system as a solid state gate for single photon pairs.

IV.A System configuration

The arrangement of our proposed device is given in Fig. IV.1(a). Two photons travelling along two optical fibers receive their interaction by coupling to two silicon microsphere cavities which are joined by a doped quantum dot. The dot provides in theory [75] a strong third-order optical nonlinearity which is essential for a controlled interaction between two photons. Two cavities of different resonant frequencies are needed to afford control of coupling to either photon. They also act as an in-situ energy filter preventing two photons ending in the same fiber.

A strong magnetic field is applied in the x direction and a classical pump field propagating in the z direction with Y polarization is shinning on the quantum dot. Their effects on the system dynamics is explained in the succeeding sections.

The two LP_{11} modes in a step index optical fiber [53, 54] are chosen as the two polarization states $|X\rangle$ and $|Y\rangle$ for the qubits (see Fig. IV.1(b)). The relevant modes in the microcavities are chosen to be the TM modes resonant with the quantum dot transitions while the other TM modes and all TE modes are tuned far off-resonant for a small cavity ($\sim \mu$m) [77]. The TM cavity mode can be excited only by an $|X\rangle$ photon in the fiber, whose coupling strength to the cavity on the left (right), $\kappa_{L(R)}$, are designed by adjusting the distance between the cavity and the fiber [78]. $|Y\rangle$ photon has zero coupling with the selected cavity mode due to their orthogonal electric field configuration. Thus, only in the $|XX\rangle$ state do the two incoming photons interact via the cavity-dot coupling system, resulting a conditional phase-shift.

The spatial configuration of the cavity-dot structure is such that the TM cavity modes are predominantly X-polarized at the site of the quantum dot. Therefore, the cavity field does not couple to the quantum dot transition where Y-polarized field is needed (see Fig. II.6(c) for optical transition selection rules expressed with optical field in linear polarized basis).

We shall emphasize that the above choices of the system configuration is not the only possibility. Other configuration, e.g, by making use of the TE cavity mode instead and (or) with

Table IV.1 Truth table for the phasegate operation in the ideal case. $\phi^L_{R(L)}$ denotes the linear phaseshift of X-polarized photon in right (left) channels and ϕ^{NL} denotes the nonlinear phaseshift.

	$\|XX\rangle$	$\|XY\rangle$	$\|YX\rangle$	$\|YY\rangle$
$\|XX\rangle$	$\exp(i\phi^{NL} + i\phi^L_L + i\phi^L_R)$	0	0	0
$\|XY\rangle$	0	$\exp(i\phi^L_R)$	0	0
$\|YX\rangle$	0	0	$\exp(i\phi^L_L)$	0
$\|YY\rangle$	0	0	0	1

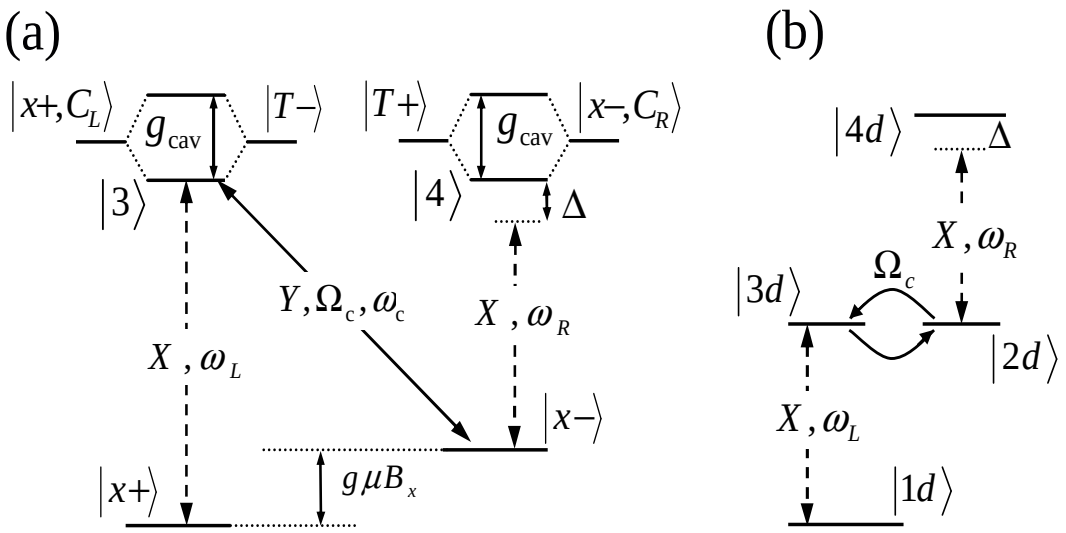

Figure IV.2 Optical processes of the phase gate operation. (a) The energy structure. (b) The dressed energy states.

flying photon qubit defined by the TE and TM propagating mode in fiber, is possible and could be more suitable depending on the experimental realization. The only objective here is to realize the truth table in the form as shown in Table. IV.1.

IV.B Nonlinearity, EIT, and laser cooling

The strong photon-photon interaction induced by the dot-coupled cavities is favored by both the small cavity-mode volume and the large dipole moment of the quantum dot transitions. The quantum dot which contains a single active electron plays an essential role. The basic nonlinear optical process is illustrated with the aid of the energy structures in Figure IV.2(a). The strong magnetic field applied along the x direction produce non-degenerate transitions from the electron spin states to the charged exciton states (trions), which are tuned respectively in resonance with the two cavity modes. The two split electron states are $|x\pm\rangle \equiv (1/\sqrt{2})(e_+^\dagger \pm e_-^\dagger)|G\rangle$, and the two degenerate trion states are $|T\pm\rangle \equiv (1/\sqrt{2})(e_+^\dagger e_-^\dagger h_-^\dagger \pm e_+^\dagger e_-^\dagger h_+^\dagger)|G\rangle$, where $e_\pm^\dagger$ and $h_\pm^\dagger$ create electron and hole spin states along the z axis. The transition selection rules are: $|x\pm\rangle \leftrightarrow |T\mp\rangle$ via the X-polarized field and $|x\pm\rangle \leftrightarrow |T\pm\rangle$ via the Y polarized field (see Fig. II.6(c) of Chapter II). Therefore, these transitions are coupled by selected TM cavity mode. The strong coupling between the trion state $|T-\rangle$ and the cavity-dot state $|x+,C_L\rangle$ (or between $|T+\rangle$ and the cavity-dot state $|x-,C_R\rangle$) mixes each pair into two split trion-polariton states, where $C_{L(R)}$ denotes the left (right) cavity mode. We denote the lower polariton states as $|3\rangle$ and $|4\rangle$, respectively. The four states, $|x+\rangle$, $|x-\rangle$, $|3\rangle$, and $|4\rangle$, form the level structure for the optical

nonlinearity and all other states are assumed far off resonance. This situation is well satisfied by the cavity-dot coupling $g_{cav} \sim 0.5$ meV, cavity decay rate into the fiber ~ 0.1 meV, and Zeeman splitting $g\mu_B B_x \sim 1$ meV. The large value of g_{cav} is not critical provided that it is much larger than the cavity decay rate.

To induce an interaction between the photons from the left and right channels, a strong Y-polarized pump pulse is applied to resonantly couple the states $|x-\rangle$ and $|3\rangle$. We consider the effect of this classical field in the dressed basis: $|1d\rangle \equiv |x+\rangle |N\rangle$, $|3d\rangle \equiv |3\rangle |N\rangle$, $|2d\rangle \equiv |x-\rangle |N+1\rangle$, and $|4d\rangle \equiv |4\rangle |N+1\rangle$, where the Y-polarized coherent field is approximated by the Fock state $|N\rangle$ with large N. Fig. IV.2(b) shows how the two X photons on separate fibers, which affect separately the modes in the left and right cavities, are coupled by the Y pump. In these dressed state picture, the X-polarized single photons in the left fiber couples the two states $|1d\rangle$ and $|3d\rangle$ and the X-polarized single photons in the right fiber couples $|2d\rangle$ and $|4d\rangle$. $|2d\rangle$ is coupled to $|3d\rangle$ by the Y-polarized classical field. The coupling strength Ω_c between $|3d\rangle$ and $|2d\rangle$ is proportional to the electric field strength. Thus, the nonlinear optical coupling is readily manipulated by switching on and off the pump pulse. With the pump field on, nonlinear scattering with one photon in each channel is established in the sense that left channel photon can populate the initial state $|2d\rangle$ for right channel photon scattering while right channel photon may deplete the final state $|3d\rangle$ for the left channel photon scattering.

The classical pump field also increases the efficiency of the operation by eliminating the linear reflection through the electromagnetical induced transparency (EIT) effect [74, 79, 80] and the laser cooling process as explained below. With the pump field resonantly coupling the $|x-\rangle \leftrightarrow |3\rangle$ transition, the linear reflection of the left fiber photon is significantly suppressed if its frequency is tuned in resonant with the $|x+\rangle \leftrightarrow |3\rangle$ transition, which results from the destructive interference between the damped polariton state $|3d\rangle$ and the meta-stable state $|2d\rangle$ coupled by the classical pump field (this will be evidenced in the linear scattering T matrix for left fiber photon, Eq. (IV.2) in the next section). The linear reflection of the X-polarized photons from the right channel is eliminated since the initial state of the system has been prepared in $|1d\rangle$ by the laser cooling cycle: the classical pulse pumps the ground state $|x-\rangle$ to $|3\rangle$, and then the polariton state relax to $|x+\rangle$ through the cavity-to-fiber leakage. The reduction of the linear reflection in both fibers brings to prominence the third order terms which are responsible for the gate operation.

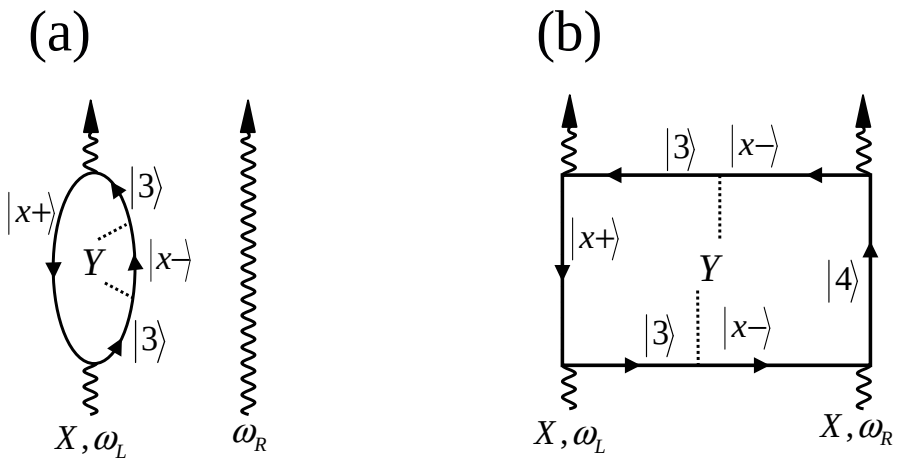

Figure IV.3 Feynman diagrams for the scattering processes. (a) The linear scattering. (b) The nonlinear scattering. Note that both are shown only with the lowest order diagram in terms of the coupling by the Y-polarized pump field.

IV.C Two photon scattering process

The transformation of the polarization state of two photons is carried out by scattering theory. In the momentum space, the two photon scattering matrix is given by,

$$S_{k'_L\sigma,k'_R\sigma';k_L\sigma,k_R\sigma'} = \delta_{k_L,k'_L}\delta_{k_R,k'_R} - 2\pi i\delta\left(\hbar\omega'_L + \hbar\omega'_R - \hbar\omega_L - \hbar\omega_R\right)\left(T^{(1)}_{fi} + T^{(3)}_{fi}\right) \tag{IV.1}$$

where the δ function signatures energy conservation. The linear scattering T matrix

$$\begin{aligned} T^{(1)}_{fi} &= \delta_{\sigma_L,X}\delta_{k_R,k'_R}\frac{|\kappa_L|^2}{2} \\ &\times\frac{E_{1d} + \hbar ck_L - E_{2d}}{\left(E_{1d} + \hbar ck_L - E_{3d} + i\Gamma_3/2\right)\left(E_{1d} + \hbar ck_L - E_{2d}\right) - \Omega_c^2}, \end{aligned} \tag{IV.2}$$

and the nonlinear scattering T matrix

$$\begin{aligned} T^{(3)}_{fi} &= \frac{\delta_{\sigma_L,X}\kappa_L\Omega_c/\sqrt{2}}{\left(E_{1d} + \hbar ck_L - E_{3d} + i\Gamma_3/2\right)\left(E_{1d} + \hbar ck_L - E_{2d}\right) - \Omega_c^2} \\ &\times\frac{\delta_{\sigma_R,X}\left|\kappa_R\right|^2/2}{E_{1d} + \hbar ck'_L + \hbar ck'_R - E_{4d} + i\Gamma_4/2} \\ &\times\frac{\delta_{\sigma_L,X}\kappa^*_L\Omega^*_c/\sqrt{2}}{\left(E_{1d} + \hbar ck'_L - E_{3d} + i\Gamma_3/2\right)\left(E_{1d} + \hbar ck'_L - E_{2d}\right) - \Omega_c^2}, \end{aligned} \tag{IV.3}$$

are obtained from non-perturbative calculation [81]. $\Gamma_{3(4)}$ is the decay rate of the polariton states $|3\rangle$ (or $|4\rangle$). In silicon microspheres, the whispering gallery modes can have Q-factor as high as $\sim 10^8$ [82], so the intrinsic decay of the cavity modes can be neglected. The relaxation rate of trions is of the order of μeV, much less than the cavity-to-fiber loss. Thus, the decay of the trion polaritons is dominated by the leakage of the cavity modes into the fiber modes. The decay rates thus can be approximated as $\Gamma_{3(4)} \approx \left|\kappa_{L(R)}\right|^2/c$.

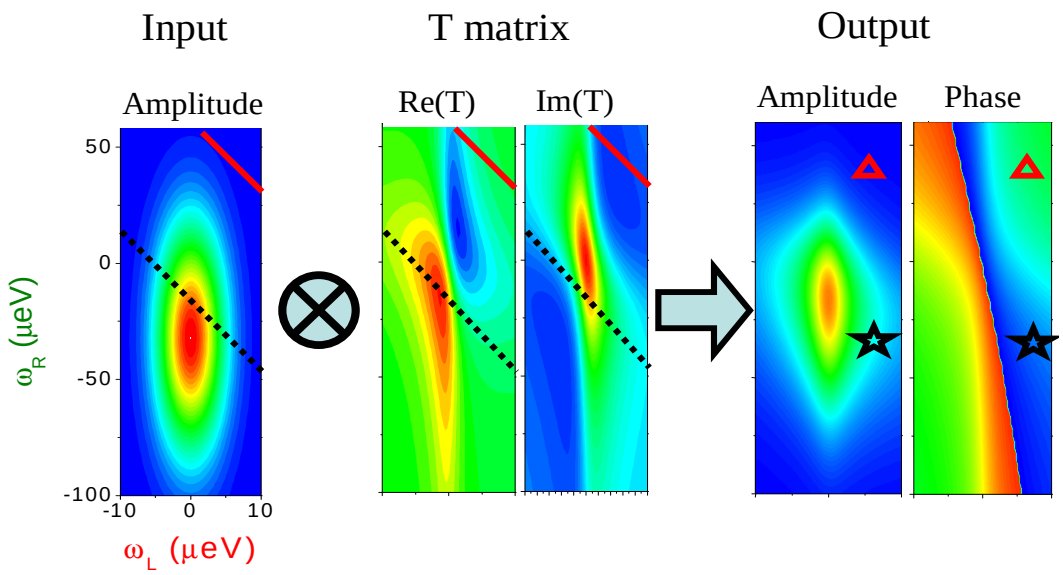

Figure IV.4 Schematic illustration of phase and amplitude modulation effect on the transmitted photons due to the convolution of the incoming photons with the scattering matrix. The incoming wavefunctions are assumed real. Red triangle-shaped and black start-shaped dots indicate two component of the transmitted two photon wavefunctions that is differently modulated due to the different integration length (shown by the solid red line and the dotted black line respectively).

The Y-polarized photons are not scattered as they are not coupled to the cavities by design. The linear term in Eq. (IV.2) contributes to the reflection of the X-polarized photon from the left channel. EIT effect is evident from the vanishing of $T_{fi}^{(1)}$ when the incoming photon is in resonance with the $|1d\rangle \rightarrow |3d\rangle$ transition. The linear reflection of the X-polarized photons from the right channel is absent since the initial state of the system has been prepared in $|1d\rangle$ by the laser cooling cycle as mentioned in Section IV.B. The linear scattering processes for X-polarized photons in left and right channels are shown schematically with the lowest order feynman diagram in Fig. IV.3(a). Notice the linear scattering T matrix of Eq. (IV.2) and hence the phenomena of EIT is actually a non-perturbative results in terms of the coupling by the Y-polarized pump field.

The nonlinear scattering matrix in Eq. (IV.3), with one photon in each channel, is composed of three fractions corresponding to three processes: the excitation of the trion-polariton by the left-channel photon, the induced scattering of the right-channel photon, and the emission of the left-channel photon by the polariton recombination. Again, the nonlinear scattering T matrix of Eq. (IV.3) is a non-perturbative results in terms of the strong coupling by the pump field. The nonlinear scattering processes are shown schematically with the lowest order feynman diagram in Fig. IV.3(b).

The two photon outgoing wave function is a convolution of the incoming wave function

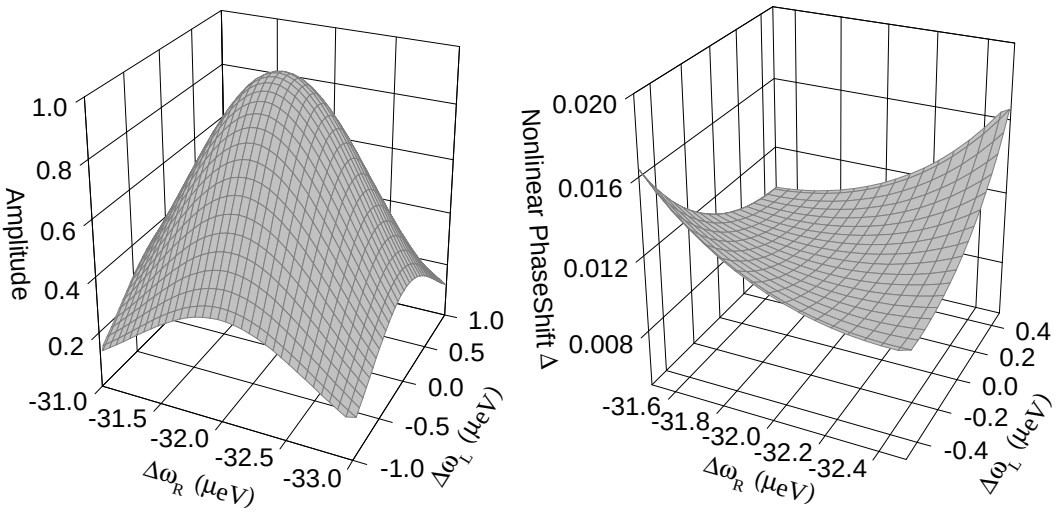

Figure IV.5 The amplitude and nonlinear phaseshift of the transmitted two-photon wavefunction as functions of the detuning for the incoming photons being Gaussian wavepackets of equal width in spectrum.

with the S Matrix,

$$\Psi^{out}\left(k'_L,\sigma;k'_R,\sigma'\right)=\sum_{k_L,k_R}S_{k'_L\sigma,k'_R\sigma';k_L\sigma,k_R\sigma'}\Psi_L^{in}\left(k_L,\sigma\right)\Psi_R^{in}\left(k_R,\sigma'\right) \tag{IV.4}$$

Due to the resonance features in the T-matrix, the transmission coefficient $t_{XX}=fe^{-i\phi}$, where f and ϕ are in general functions of the wavevectors, can cause the amplitude and phase modulation of the transmitted wave since the incoming photons are in wave packets. The modulation by the resonance structure in linear and nonlinear T matrix might be suppressed either by using pulses with longer duration in time or by working in far off-resonance region. However, there is an extra source of amplitude and phase modulation of the transmitted photon wavepactets which is specific to the nonlinear scattering only. By the δ function in the S matrix Eqn. (IV.1), the $|k'_L,X;k'_R,X\rangle$ component of the outgoing wavefunction has a contribution from all incoming components $|k_L,X;k_R,X\rangle$ where $k'_L+k'_R=k_L+k_R$ is satisfied, which corresponds to the integration over a straight line in the momentum space, as shown schematically in Fig. IV.4. Different components of the outgoing wavefunction may corresponds to different integration length and hence subject to different nonlinear phaseshift and reflection.

We can generally express the transmitted part of the two photon outgoing wave function in $|XX\rangle$ configuration as,

$$\Psi^{out}\left(k'_L>0,k'_R>0\right)=e^{i\Delta\phi\left(k'_L,k'_R\right)}\left(\Psi_L^{out}\left(k'_L\right)\Psi_R^{out}\left(k'_R\right)+B\left(k'_L,k'_R\right)\right) \tag{IV.5}$$

where $\Psi_L^{out}\left(k'_L\right)(\Psi_R^{out}\left(k'_R\right))$ are the transmitted part of the linearly scattered wave function cor-

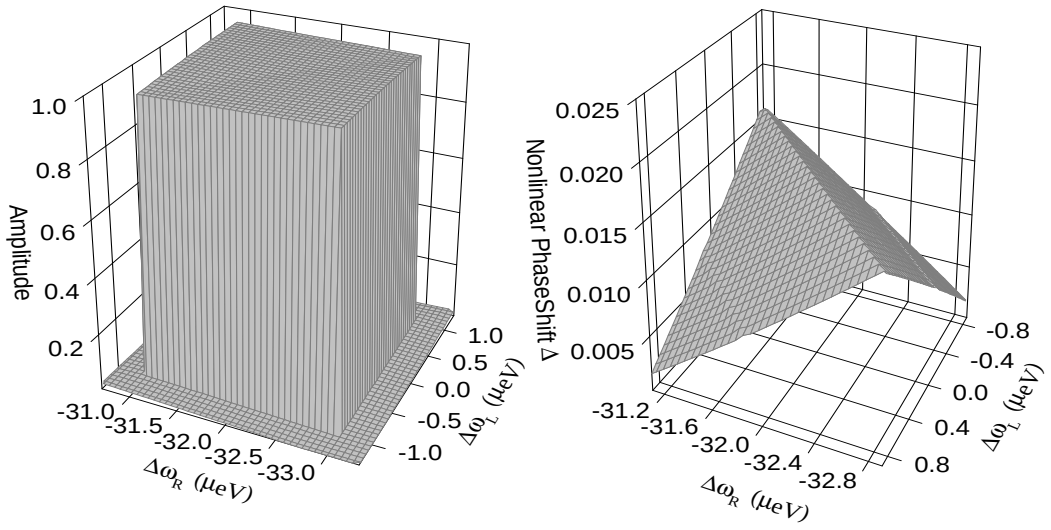

Figure IV.6 The amplitude and nonlinear phaseshift of the transmitted two-photon wavefunction as functions of the detuning for the incoming photons being square wavepackets of equal width in spectrum.

responding to the incoming wave function $\Psi_L^{in}(k_L)(\Psi_R^{in}(k_R))$. $\Delta\phi(k'_L, k'_R)$ correspond to the nonlinear phase shift. $B(k'_L, k'_R)$ is the nonlinear correction to amplitude and is typically small compared to $\Psi_L^{out}(k'_L)\Psi_R^{out}(k'_R)$ if the detuning Δ, of the right channel photon frequency from the $|x-\rangle \leftrightarrow |4\rangle$ transition energy (see Fig. IV.2(b)), is large. In principle, $\Delta\phi(k'_L, k'_R)$ is a function of k'_L, k'_R resulted from the convolution form of Eqn. (IV.4) and a global nonlinear phase shift is not well defined as illustrated in Fig. IV.5 for incoming photon wavepackets both in gaussian shape and Fig. IV.6 for incoming photon wavepackets both in square shape in spectrum.

Although often overlooked in the literature, the phase-variation effect results in distortion of the pulse shape and entanglement of the motion and polarization of the photons.

IV.D Pulse shaping for suppression of the phase variation effect

Since the qubit is encoded in the polarization subspace of the single photon, we have the freedom to choose the shape of its spatial wavefunction. We show how the carefully selected shapes of the input single photon wavepackets leads to reduction of the output pulse deformation.

The guideline for pulse shape selection is listed below. (1) As a consequence of the EIT effect induced by the optical coupling between the $|3d\rangle$ and $|2d\rangle$ states, the choice of the left input photon to be within $\pm\Omega_c$ of being in resonance with the $|1d\rangle \rightarrow |3d\rangle$ transition, the

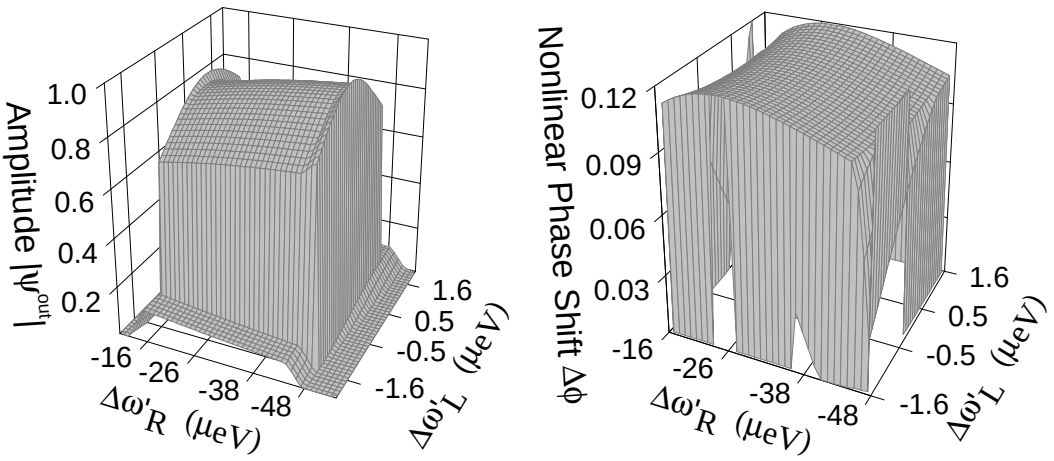

Figure IV.7 Optimized phase gate operation with the incoming photons in selected shapes I. Left (right) part is the amplitude (nonlinear phaseshift) of the transmitted two-photon wavefunction as functions of the detuning $\Delta\omega_L \equiv \hbar c k'_L - (E_{3d} - E_{1d})$ and $\Delta\omega_R \equiv \hbar c k'_R - (E_{4d} - E_{2d})$. The parameters are: $\Gamma_3 = \Gamma_4 = 60$ μeV, $\Omega_c = 8$ μeV; $g_{cav} = 0.5$ meV. The input wavefunction is such that $\Psi^i(k_L, k_R) = \theta(48 + \Delta\omega_R)\theta(-16 - \Delta\omega_R)\theta(1.6 + \Delta\omega_L)\theta(1.6 - \Delta\omega_L)$ with arguments in units of μeV.

linear reflection is reduced and the first factor on the right side of Eq. (IV.3) will yield a strong third-order transmission. (2) To diminish the pulse shape distortion due to the sharp resonant structure around the $|2d\rangle \rightarrow |4d\rangle$ transition, the right-channel photon is detuned about $\sim \Gamma_4/2$ below the transition where the real part (corresponding to the nonlinear phaseshift) of $T^{(3)}$ is large and flat while the imaginary part (corresponding to the reflection) has decreased to a small value. (3) To minimize the pulse broadening and distortion resulted from the convolution of the input pulses with the S matrix, we choose the two input pulses to have sqaure-shaped spectra with much different widths. In our design, $\Gamma_4/2$ is much larger than Ω_c, so the right-channel pulse is set the wider in frequency. Such a choice will allow a uniform integration length (which may be inferred from Fig. IV.4 if the area is further elongated vertically) for almost all components of the transmitted two photon outgoing wavefunction.

Figure IV.7 presents the transmitted wavefunction (k'_L, $k'_R > 0$) for incoming photons in square pulses with the polarization state $|XX\rangle$. Though visible, the pulse distortion and broadening and the inhomogeneity in nonlinear phase-shift $\Delta\phi\,(k'_L, k'_R)$ is quite small. A nonlinear phaseshift of $\pi/29$ is obtained with a two photon transmission probability of $f = 0.72$ where $f \equiv \int_0^\infty dk'_L \int_0^\infty dk'_R \left|\Psi^{out}\,(k'_L, k'_R)\right|^2$.

The loss in transmission and the pulse distortion in Fig. IV.7 result mainly from the imperfect EIT when the photon is off-resonant with the $|1d\rangle \rightarrow |3d\rangle$ transition. Improvement of both the pulse shape and transmission is effected by increasing the pump power Ω_c (in order

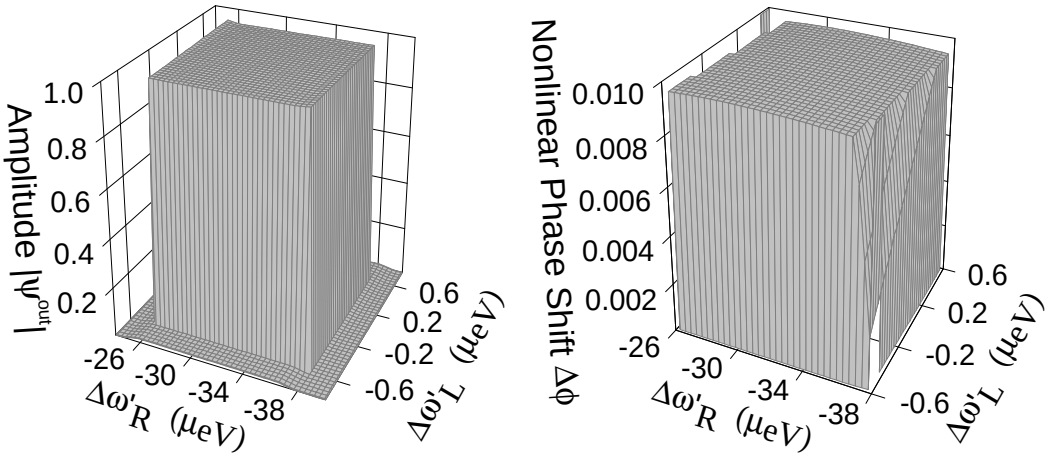

Figure IV.8 Optimized phase gate operation with the incoming photons in selected shapes II. The plot is the same as Fig. IV.7 except that the parameters are: $\Gamma_3 = 45$ μeV, $\Gamma_4 = 60$ μeV; $\Omega_c = 15$ μeV; $g_{cav} = 0.5$ meV and $\Psi^i(k_L, k_R) = \theta(38 + \Delta\omega_R)\theta(-26 - \Delta\omega_R)\theta(0.6 + \Delta\omega_L)\theta(0.6 - \Delta\omega_L)$.

to open a larger EIT window) and by using narrower bandwidth pulses at the expense of a weak nonlinear phase shift. An example is shown in Fig. IV.8, in which a nonlinear phase shift $\sim \pi/330$ is obtained almost without pulse-shape change or reflection loss, shown by the computed transmission probability of $f \sim 0.982$.

IV.E Gate operations

The suppression of the phase-variation effects allows the well defined conditional phase-shift on photon polarization qubit. The efficiency of gate operation is analyzed here. The qubit is specified to be the polarization state of single photon pulse of the designated shape, e.g., the selected shapes discussed in section IV.D. Any distortion of the spatial wavefunction is considered as a leakage out of the qubit subspace.

The initial state is specified by the density matrix ρ_i in the basis set of the direct products of the polarization states, $|\sigma_L\sigma_R\rangle$ with $\sigma = X$ or Y, and of the wave vector states $|k_L, k_R\rangle$. For characterizing gate operations, we take the initial state to be $\frac{1}{\sqrt{2}}(|X\rangle_L + |Y\rangle_L) \otimes \frac{1}{\sqrt{2}}(|X\rangle_R + |Y\rangle_R)$ with the spatial part having the selected shapes understood. So ρ_i in the polarization subspace is,

$$\rho_i = \frac{1}{4}\begin{bmatrix} 1 & 1 & 1 & 1 \\ 1 & 1 & 1 & 1 \\ 1 & 1 & 1 & 1 \\ 1 & 1 & 1 & 1 \end{bmatrix} \tag{IV.6}$$

The transmitted state ρ_f is given by the normalized $t\rho_i t^\dagger$, where t is the transmission matrix.

By design, t is diagonal in the polarization states. The final density matrix of the two-photon polarizations is obtained by tracing ρ_f over the wave vectors of the photons [83]. We assume the linear part of the phaseshift is always compensated, e.g., by passing the photon through some dispersive media and we do not consider this effect on the transmitted wavepackets.

In the ideal phase gate operation with conditional phaseshift ϕ, we have

$$t = \begin{bmatrix} e^{i\phi} & 0 & 0 & 0 \\ 0 & 1 & 0 & 0 \\ 0 & 0 & 1 & 0 \\ 0 & 0 & 0 & 1 \end{bmatrix} \tag{IV.7}$$

so

$$\rho_t^{ideal} = \frac{1}{4} \begin{bmatrix} 1 & e^{i\phi} & e^{i\phi} & e^{i\phi} \\ e^{-i\phi} & 1 & 1 & 1 \\ e^{-i\phi} & 1 & 1 & 1 \\ e^{-i\phi} & 1 & 1 & 1 \end{bmatrix} \tag{IV.8}$$

Considering the reflection and pulse distortion, both effects will result in the leakage out of the qubit subspace and therefore,

$$t = \begin{bmatrix} f_1 e^{i\phi} & 0 & 0 & 0 \\ 0 & f_2 & 0 & 0 \\ 0 & 0 & 1 & 0 \\ 0 & 0 & 0 & 1 \end{bmatrix} \tag{IV.9}$$

Therefore, ρ_t is,

$$\rho_t = \frac{1}{f_1^2 + f_2^2 + 2} \begin{bmatrix} f_1^2 & f_1 f_2 e^{i\phi} & f_1 e^{i\phi} & f_1 e^{i\phi} \\ f_1 f_2 e^{-i\phi} & f_2^2 & 1 & 1 \\ f_1 e^{-i\phi} & 1 & 1 & 1 \\ f_1 e^{-i\phi} & 1 & 1 & 1 \end{bmatrix} \tag{IV.10}$$

Fidelity $Tr\left[\rho_t^{ideal}\rho_t\right]$ is a quantity for characterizing the gate efficiency. As the input state in the current discussion is a pure state and the ideal gate transform preserve the pure state properties, the purity $Tr[\rho_t^2]$ is another quantity for characterizing the gate operations. In addition, the measure of the deterministicity of the gate is given by the normalization factor $\frac{f_1^2+f_2^2+2}{4}$.

We take the two examples of pulse shaping in the previous section and characterize their gate operations.

In the first case (Fig. IV.7),

$$\rho_t = \frac{1}{3.557}\begin{bmatrix} 0.7027 & 0.7698+0.0824i & 0.8308+0.0890i & 0.8308+0.0890i \\ 0.7698-0.0824i & 0.8543 & 0.9220 & 0.9220 \\ 0.8308-0.0890i & 0.9220 & 1 & 1 \\ 0.8308-0.0890i & 0.9220 & 1 & 1 \end{bmatrix} \tag{IV.11}$$

while the corresponding target state with the same amount of nonlinear phase shift ($\sim \pi/29$) is given by,

$$\rho_t^{ideal} = \frac{1}{4}\begin{bmatrix} 1 & \frac{0.8308+0.0890i}{0.835554} & \frac{0.8308+0.0890i}{0.835554} & \frac{0.8308+0.0890i}{0.835554} \\ \frac{0.8308-0.0890i}{0.835554} & 1 & 1 & 1 \\ \frac{0.8308-0.0890i}{0.835554} & 1 & 1 & 1 \\ \frac{0.8308-0.0890i}{0.835554} & 1 & 1 & 1 \end{bmatrix} \tag{IV.12}$$

The purity of the state after the gate transform,

$$Tr[\rho_t^2] = 0.997089$$

and the fidelity of the gate,

$$Tr\left[\rho_t^{ideal}\rho_t\right] = 0.9935$$

In the second case (Fig. IV.8),

$$\rho_t = \frac{1}{3.9804}\begin{bmatrix} 0.9816 & 0.9901+0.0092i & 0.9907+0.0092i & 0.9907+0.0092i \\ 0.9901-0.0092i & 0.9988 & 0.9994 & 0.9994 \\ 0.9907-0.0092i & 0.9994 & 1 & 1 \\ 0.9907-0.0092i & 0.9994 & 1 & 1 \end{bmatrix} \tag{IV.13}$$

while the corresponding target state with the same amount of nonlinear phase shift is given by,

$$\rho_t^{ideal} = \frac{1}{4}\begin{bmatrix} 1 & \frac{0.9907+0.0092i}{0.990735} & \frac{0.9907+0.0092i}{0.990735} & \frac{0.9907+0.0092i}{0.990735} \\ \frac{0.9907-0.0092i}{0.990735} & 1 & 1 & 1 \\ \frac{0.9907-0.0092i}{0.990735} & 1 & 1 & 1 \\ \frac{0.9907-0.0092i}{0.990735} & 1 & 1 & 1 \end{bmatrix} \tag{IV.14}$$

The purity of the state after the gate transform,

$$Tr[\rho_t^2] = 0.999999$$

and the fidelity of the gate,

$$Tr\left[\rho_t^{ideal}\rho_t\right] = 0.99998$$

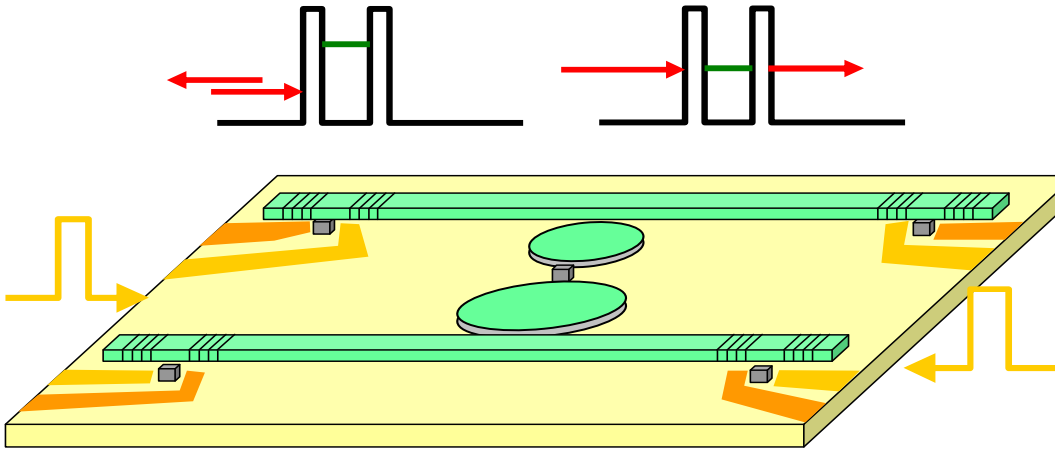

Figure IV.9 Proposed structure for realizing multi-shot phase gate operations to accumulate nonlinear phase shift. The four legs of the gate are controlled by the Fabri-Perot structures. One quantum dot is coupled to each structure and polariton state is formed. These structures act as double barrier tunnelling potentials (shown on top) for photons. By tuning the resonance energy of the polariton state via DC electric field, single photon can either tunnel through or get reflected by these structures. After the incoming single photons enter into the phase gate region, the Fabri-Perot structures are set on "close" positions so that photons are reflected about the phase gate structure to accumulate the nonlinear phaseshift. The single photons can leave the phase gate if the Fabri-Perot structures are set on "open" positions.

Phase gate may be used to generate entangled photon pairs. An ideal phase gate transform with π nonlinear phase shift will produce fully entangled pairs of photons for the initial state of Eqn. (IV.6). We may examine the amount of entanglement generated by the gate operations in the two examples of pulse shaping.

To calculate the entanglement of formation [84], we define,

$$\tilde{\rho}_t = (\sigma_{1y} \otimes \sigma_{2y})\, \rho_t^* \,(\sigma_{1y} \otimes \sigma_{2y}) \tag{IV.15}$$

where ρ_t^* is the complex conjugate of ρ_t and σ_{1y}, σ_{2y} are pauli matrix acting on left and right photon qubit respectively.

We label the eigenstates of $\rho_t \tilde{\rho}_t$ as $\lambda_1, \lambda_2, \lambda_3, \lambda_4$ in decreasing order. The concurrence is then defined by,

$$C \equiv \max\{0, \sqrt{\lambda_1} - \sqrt{\lambda_2} - \sqrt{\lambda_3} - \sqrt{\lambda_4}\} \tag{IV.16}$$

The Entanglement of Formation is related to the concurrence by:

$$E\,(C) = h\left(\frac{1+\sqrt{1-C^2}}{2}\right) \tag{IV.17}$$

where,

$$h\,(x) = -x \log_2 x - (1-x) \log_2 (1-x) \tag{IV.18}$$

Table IV.2 n+n gates with parameters: $\Gamma_3 = 0.06$ meV, $\Gamma_4 = 0.5$ meV $\Omega_c = 6.2$ μeV. The left- and right-channel Gaussian pulses with FWHM 7.5 μeV and 50 μeV are resonant with the left and right polariton transitions, respectively. The parameters are optimized for the largest nonlinear reflection. C denotes the concurrence and $E(C)$ the entanglement of formation.

n	Transmission Probability	Fidelity	Purity	C	$E(C)$
2	0.1165	0.8638	0.9591	0.7277	0.6272
4	0.02074	0.9758	0.9850	0.9515	0.9306

We may verify that a fully entangled pure state, e.g., $\frac{1}{\sqrt{2}}(|XX\rangle + |YY\rangle)$, corresponds to $C = 1$ and $E(C) = 1$.

By taking the initial state given by Eqn. (IV.6), and passing through the phase gate with pulse shaping of Fig. IV.7, we have the final state Eqn. (IV.11) and the computed concurrence $C = 0.0717$ and entanglement of formation $E(C) = 0.0142$. For comparison, the corresponding quantities for the ideal gate transform with the same amount of nonlinear phase shift (Eqn. (IV.12)) are: $C = 0.0533$ and $E(C) = 0.0087$.

For the second example of pulse shaping of Fig. IV.8, we have the final state Eqn. (IV.13) and the computed concurrence $C = 0.0064$ and entanglement of formation $E(C) = 0.00018$. For comparison, the corresponding quantities for the ideal gate transform with the same amount of nonlinear phase shift (Eqn. (IV.14)) are: $C = 0.0046$ and $E(C) = 0.0001$.

The examples above show that reduction of the reflection and distortion of the photon pulses diminishes the gate phase and the entanglement. A small entanglement is still useful for some quantum information purposes [85]. Moreover, a large phase-shift can be accumulated, either by passing a photon pair many times through the phase gate (see Fig. IV.9), or by using a series of many identical gates integrated into a single chip. With modern fabricating techniques, the integrated quantum gates can be constructed either with micro-disks and wave guides etched on semiconductor heterostructures [55] or with point- and line-defects engineered in photonic lattices [56, 57] (see illustrations in Fig. IV.10).

IV.F Nonlinear reflection and photon entanglement

To use the system to produce an entangled photon pair rather than to perform a controlled phase operation, we optimize the entanglement by a different procedure. The nonlinear reflection which is a deleterious factor in the phase gate operation might be utilized for entanglement generation. First the input state is prepared as the equal linear combination of the four polarization states of the two photons $\frac{1}{2}(|XX\rangle + |XY\rangle + |YX\rangle + |YY\rangle)$. Then the state is passed n times through the coupled system. Due to the nonlinear reflection, the amplitude on

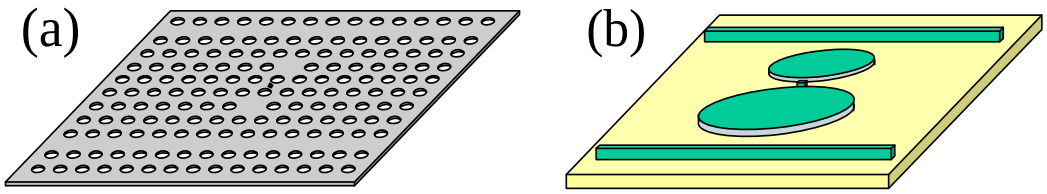

Figure IV.10 Solid state phase gate on chip. (a) Realization in 2D photonic crystals. (b) Etched on surface.

the $|XX\rangle$ component is suppressed after projection onto the two photon transmission subspace which results in $\frac{1}{\sqrt{3}}(|XY\rangle + |YX\rangle + |YY\rangle)$. By single bit operation swapping the $|X\rangle$ and $|Y\rangle$ states in both photons, the above state is transformed to $\frac{1}{\sqrt{3}}(|YX\rangle + |XY\rangle + |XX\rangle)$ and is then passed through the phase gate n more times and we obtain the final state in the two photon transmission subspace as $\frac{1}{\sqrt{2}}(|YX\rangle + |XY\rangle)$. By this procedure, we obtain fully polarization entangled photon pairs which is a probabilistic process. While the quantum phase gate operation is favored by maximizing the transmission, the entanglement is favored maximizing the nonlinear reflection and symmetrizing the two photons for maximal projection of the polarization degrees of freedom.

Table V.2 shows the calculated results for 2+2 and 4+4 gates. The transmission probabilities are much lower than for the phase operation. The quantitative measures of the operation including fidelity $\mathrm{Tr}\left[\rho_t \rho_{ideal}\right]$ towards the maximally entangled state $\frac{1}{\sqrt{2}}(|XY\rangle + |YX\rangle)$, the purity $\mathrm{Tr}\left[\rho_t^2\right]$, the concurrence C and the entanglement of formation $E(C)$ [84], all show excellent entanglement.

IV.G Chapter summary

In summary, we have proposed a solid-state controlled phase gate for two photons. The flying qubits are conducted through fibers coupled to scattering centers composed of microcavities connected by a doped semiconductor quantum dot. This allows a fiber implementation of quantum information processor. Calculated results show that the system is flexible as a phase gate as well as producing strong entanglement. The obtained single photon nonlinearity may be implemented in photon based quantum information processing. It is recently recognized that linear optical elements combined with some nonlinear effects may appreciably improve the efficiency of photonic quantum computation [86]. The trions in doped quantum dot used for nonlinear interaction here can be replaced by other electronic systems, such as biexcitons in an undoped quantum dot (results will be published elsewhere), states in nanoclusters, or even some strong transitions in rare-earth impurities, e.g., the 4d-5f transition in Er^{2+}. The microcavity may be

micro-disks or defects in photonic lattices (see Fig. IV.10). The structure has unique features, such as small size, integrability, and stability, useful for quantum information and for scalable quantum computing.

IV.H Acknowledgements

The text of chapter IV, in part, is a reprint of the material as it appears in Wang Yao, Ren-Bao Liu, and L. J. Sham, *Nanodot-Cavity Electrodynamics and Photon Entanglement*, Phys. Rev. Lett **92**, 217402, © 2004 The American Physical Society, where the dissertation author was the first author. The co-authors in this publication directed, supervised, and co-worked on the research which forms the basis of this chapter.

V

Control of Spin-Photon Interface for Quantum Networks

Quantum networks composed of local nodes which are connected by quantum channels are essential for quantum communication and desirable for scalable and distributed quantum computation [23, 87]. The local nodes consist of clusters of stationary qubits and can be operated in parallel. Flying qubits in the quantum channel can take quantum information from one cluster to another when necessary. The stationary qubit can be provided by stable levels of atoms, quantum dots or impurity centers in solid state structures. Photon wavepacket will be an ideal carrier for flying qubit with either the photon number states or the polarization forming the qubit. The key part here is the quantum interface that allows deterministic interplay between stationary and flying qubits. The ability for faithful mapping between the two types of qubit is essential towards the scalability of the distributed quantum computer [23].

The prototype quantum interface for this purpose was proposed by Cirac *et al.* [88] which is composed of a cavity coupled to a three-level Λ system. Through the cavity assisted Raman process, the stationary qubit formed by stable levels of atoms and the flying qubit formed by number states of photon wavepacket can be inter-converted. Via similar cavity assisted Raman process, schemes for mapping between motional states of single trapped atom [89] or collective excitation of atomic ensembles [90, 91] and the quantum states of single photons are also proposed. Proper dynamic control is essential for implementing desired functions of the quantum network. Previously available controls include the time symmetric scheme [88] and the adiabatic scheme [90, 91, 92], with which useful network operations such as deterministic state transfer can be performed. However, both schemes are subject to some constraints, not fully utilizing the

potential of the quantum interface.

In this chapter, we discuss a most general form of the control of this prototype quantum interface [93, 94]. The time symmetric scheme of [88] and the adiabatic scheme of [90, 91, 92] form special and approximate cases. The constraints imposed by these two schemes can be shown to be unnecessary, greatly saving the physical resources and improving the time efficiency for implementing the quantum network. We show that the dot-cavity-waveguide coupled system is a very promising structure for the physical realization of the quantum interface.

V.A Survey of previous work

Illustration of this prototype quantum interface is shown in Fig. V.1. The two ground states, $|g\rangle$ and $|e\rangle$, of the three level system form the stationary qubit. State $|g\rangle$ is coupled to the intermediate state $|t\rangle$ by the cavity mode and $|e\rangle$ to $|t\rangle$ by classical light. Direct excitation of cavity by classical light is assumed absent. The cavity is coupled to the electromagnetic continuum outside which forms a photonic channel. A Raman path from $|e\rangle$ to $|g\rangle$ through the intermediate state $|t\rangle$ is thus formed. If the three level system is initially on state $|e\rangle$, the classic light can bring it to state $|t\rangle$ by a π rotation which can then relax to state $|g\rangle$ by spontaneous emission of a cavity photon. The cavity photon can then leak into the photonic channel forming a single photon wavepacket. If the three level system is initially on state $|g\rangle$, it will remain on this state provided the cavity is in its vacuum. The qubit of information carried by the three level system can thus be mapped onto a flying qubit in the photonic channel whose number states form the qubit and the sending function of this node is completed,

$$(C_g|g\rangle + C_e|e\rangle) \otimes |\text{vac}\rangle \rightarrow |g\rangle \otimes [C_g|\text{vac}\rangle + C_e|\alpha_{\text{out}}\rangle] \,. \tag{V.1}$$

where $|\alpha\rangle$ denotes a single photon wavepacket in the photonic channel and $|\text{vac}\rangle$ the channel vacuum. The receiving function is the mapping of flying qubit to the stationary qubit and can be considered as the time reversal of the above process,

$$|g\rangle \otimes (C_g|\text{vac}\rangle + C_e|\alpha_{\text{in}}\rangle) \rightarrow (C_g|g\rangle + C_e|e\rangle) \otimes |\text{vac}\rangle. \tag{V.2}$$

With the output of the sending node directed as the input of the receiving node (see Fig. V.1), transfer of qubit between the two distant nodes can be performed.

The difficulty in realizing the network lies in the receiving end. Instead of being absorbed by the three level system, the single photon pulse can be reflected by the cavity mirror unless the pulse shape of the classic control light matches the single photon pulse exactly. However, it has been considered to be a difficult problem as the classic control light has a functional dependence on the single photon wavepacket. A way to get around this difficulty was provided in [88]. The

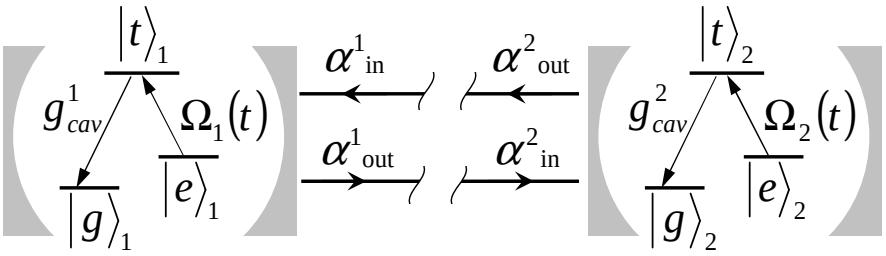

Figure V.1 Schematic illustration of the quantum network. The node is composed of cavity coupled to three level Λ system. The two ground states $|g\rangle$ and $|e\rangle$ of the three level system form the Hilbert space for the stationary qubit. State $|g\rangle$ is coupled to the intermediate $|t\rangle$ by the cavity mode with strength g_{cav} and $|e\rangle$ to $|t\rangle$ by classical light with Rabi frequency $\Omega(t)$. Direct excitation of cavity by classical light is assumed absent. The cavity itself is coupled to the continuum outside which forms a photonic channel. Two nodes are connected by the photonic channel in the following way: the output of node 1 is directed to node 2 as its input and vice versa.

central idea is that if the quantum interface can be controlled to generate an outgoing photon wavepacket of a time symmetric shape, by setting the classic control at the receiving node just the time reversal of that at the sending node, the time reversal symmetry will guarantee the photon wavepacket to be completely absorbed at the receiving node. A solution for this time symmetric operation was also provided in [88].

Many atom CQED based experiments have been stimulated by this proposal in the past several years, e.g., by Kuhn *et al.* [95], McKeever *et al.* [96] and Keller *et al.* [97]. When atoms are used as stationary qubit, its center of mass dynamics can be deleterious to the quantum interface operations. In the two latest experiments [96, 97], efforts were made to trap atoms or ions inside the optical cavity so that the uncertainty in position is greatly reduced and the interface functions in a rather deterministic way. The dependence in shape of the generated single photon wavepacket on the classic control light has also been demonstrated in [97].

There has been development on the control scheme as well. The original proposal by Cirac *et al.* requires the sending and receiving node to be identical and operated in a time symmetric way. This would impose a great demand on the physical resource to build a quantum network. Later, Lukin *et al.* [90, 91] showed that if the this quantum interface is operated in the adiabatic regime, the driving field for generation of a single photon wavepacket of arbitrary shape can be found. However, the operation has to be slow enough to guarantee the adiabaticity.

V.B Exact solution of the quantum interfacing dynamics

In this section, we will present the general and exact solution for the dynamics of this prototype quantum interface, based on which is a new control scheme without any constraint of time reversal symmetry or adiabaticity. We will show that both the sending and receiving processes can be independently controlled by designing the laser pulses. The controllability are two-folded: First, the single-photon pulse shape, provided smooth enough, can be arbitrarily specified; Second, the Raman process can be operated as a partial cycle, in which arbitrary amount of entanglement between the stationary qubit and the flying qubit can be created on demand. This second controllability makes possible a new scheme to deterministically create non-local entanglement between distant nodes in the quantum network. The time symmetric scheme of [88] is a special case of our scheme operated as a full cycle and the adiabatic scheme of [90, 91, 92] forms the approximation of our scheme in the slow operation regime.

For the quantum interface shown in Fig. V.1, the Hamiltonian describing the interaction of the single mode cavity with the three level system and with the channel continuum is,

$$\begin{aligned} H &= \omega_c a^\dagger a + \omega_t \left|t\right\rangle \left\langle t\right| + \omega_e \left|e\right\rangle \left\langle e\right| + \int_0^\infty d\omega \omega b_\omega^\dagger b_\omega + g_{cav} \left(i \left|t\right\rangle \left\langle g\right| a + H.c.\right) \\ &\quad + \frac{1}{2}\left[i\Omega\left(t\right) e^{-i\omega_L t} \left|t\right\rangle \left\langle e\right| + H.c.\right] + \int_0^\infty d\omega \left(i\sqrt{\gamma/2\pi} b_\omega^\dagger a + H.c.\right) \end{aligned} \tag{V.3}$$

where b_ω is the annihilation operator for the mode of frequency ω in the channel continuum and a is the annihilation operator for cavity mode. The energy of state $\left|g\right\rangle$ is set as zero. $\left|g\right\rangle \rightarrow \left|t\right\rangle$ transition is coupled to cavity mode with strength g_{cav}. $\left|e\right\rangle \rightarrow \left|t\right\rangle$ transition is coupled by classic control light of time dependent Rabi frequency $\Omega(t)$ and central frequency ω_L. The coupling of the cavity mode to the channel continuum is assumed constant:$\sqrt{\gamma/2\pi}$. An ideal situation is assumed neglecting photon leakage into free space through intermediate state $\left|t\right\rangle$ or the cavity wall.

We note that the system described by this Hamiltonian, under the optical excitation and the cavity-dot and cavity-channel interaction, has two invariant Hilbert subspaces, with the basis $\{\left|g,0\right\rangle \left|\text{vac}\right\rangle\}$ and $\{\left|e,0\right\rangle \left|\text{vac}\right\rangle, \left|t,0\right\rangle \left|\text{vac}\right\rangle, \left|g,1\right\rangle \left|\text{vac}\right\rangle, \left|g,0\right\rangle \left|\omega\right\rangle\}$, respectively (where in $\left|s,n\right\rangle$, $s = g, e, t$ or $\bar{t}$ denotes the state of three level system and n denotes the number of photons in the single cavity mode, $\left|\omega\right\rangle$ denotes the one-photon Fock state of the channel mode of frequency ω). So the evolution of the system can be generally described by the state $C_g \left|g,0\right\rangle \left|\text{vac}\right\rangle + C_e \left|\Psi^e\left(t\right)\right\rangle$ in the interaction picture, where

$$\left|\Psi^e\left(t\right)\right\rangle = \beta_e\left(t\right)\left|e,0\right\rangle \left|\text{vac}\right\rangle + \beta_t\left(t\right)\left|t,0\right\rangle \left|\text{vac}\right\rangle + \beta_c\left(t\right)\left|g,1\right\rangle \left|\text{vac}\right\rangle + \int_0^\infty d\omega_\omega \alpha_\omega\left(t\right)\left|g,0\right\rangle \left|\omega\right\rangle . \tag{V.4}$$

The time evolution of the amplitudes in the interaction picture is described by the following

Schrödinger equations,

$$\dot{\beta}_e = -\frac{\Omega_1^*}{2} e^{-i(\omega_t-\omega_L-\omega_e)t}\beta_t \tag{V.5a}$$

$$\dot{\beta}_t = g_{cav} e^{i(\omega_t-\omega_c)t}\beta_c + \frac{\Omega}{2} e^{i(\omega_t-\omega_L-\omega_e)t}\beta_e \tag{V.5b}$$

$$\dot{\beta}_c = -g_{cav} e^{-i(\omega_t-\omega_c)t}\beta_t - \sqrt{\gamma/2\pi}\int_0^\infty d\omega e^{-i(\omega-\omega_c)t}\alpha_\omega \tag{V.5c}$$

$$\dot{\alpha}_\omega = \sqrt{\gamma/2\pi} e^{i(\omega-\omega_c)t}\beta_c \tag{V.5d}$$

From Eq. (V.5d), α_ω can be formally expressed as,

$$\alpha_\omega(t) = \alpha_\omega(t_0) + \sqrt{\gamma/2\pi}\int_{t_0}^{t} dt' e^{i(\omega-\omega_c)t'}\beta_c(t') \tag{V.6}$$

or

$$\alpha_\omega(t) = \alpha_\omega(t_1) - \sqrt{\gamma/2\pi}\int_{t}^{t_1} dt' e^{i(\omega-\omega_c)t'}\beta_c(t') \tag{V.7}$$

where $t_0 \to -\infty$ and $t_1 \to +\infty$ represents the remote past and remote future respectively when the incoming/outgoing photon wave-packet are in the far field not interacting with the quantum interface. By substituting Eqs. (V.6) and (V.7) into Eq. (V.5c), the Schrödinger equations become,

$$\dot{\beta}_e = -\frac{\Omega_1^*}{2} e^{-i(\omega_t-\omega_L-\omega_e)t}\beta_t \tag{V.8a}$$

$$\dot{\beta}_t = g_{cav} e^{i(\omega_t-\omega_c)t}\beta_c + \frac{\Omega}{2} e^{i(\omega_t-\omega_L-\omega_e)t}\beta_e \tag{V.8b}$$

$$\dot{\beta}_c = -g_{cav} e^{-i(\omega_t-\omega_c)t}\beta_t - \sqrt{\gamma}\alpha_{in}(t) - \frac{\gamma}{2}\beta_c \tag{V.8c}$$

$$= -g_{cav} e^{-i(\omega_t-\omega_c)t}\beta_t - \sqrt{\gamma}\alpha_{out}(t) + \frac{\gamma}{2}\beta_c \tag{V.8d}$$

where,

$$\alpha_{\rm in}(t) \equiv \int d\omega \alpha_\omega(t_0) e^{-i(\omega-\omega_c)t}/\sqrt{2\pi}$$

with $t_0 \to -\infty$ and,

$$\alpha_{\rm out}(t) \equiv \int d\omega \alpha_\omega(t_1) e^{-i(\omega-\omega_c)t}/\sqrt{2\pi}$$

with $t_1 \to +\infty$ are the incoming and outgoing pulse of the photon in the quantum channel, respectively. Eqs. (V.8c) and (V.8d) are obtained within the Weisskopf-Wigner approximation [98]. The quantum fluctuation caused by the quantum channel is on the order of $\gamma/\omega_c \ll 1$ (which is the typical situation for both atom-CQED system and solid state systems) and thus the Weisskopf-Wigner approximation is well justified here. Although Eqs. (V.8c) and (V.8d) contain terms which yield exponential dependence on time, they are time reversible with each other. Thus, Eqs. (V.8) describe a reverable quantum evolution.

Below, we will show that, from Eqs. (V.8), the amplitudes $\beta_e(t)$, $\beta_c(t)$ and $\beta_t(t)$ as well as the Rabi frequency $\Omega(t)$ of the control field can be expressed in terms of $\alpha_{\rm in}$ and $\alpha_{\rm out}$. Thus

the desired operation, with $\alpha_{\rm in}$ and $\alpha_{\rm out}$ arbitrarily specified, can be generated on demand as long as the normalization of the wavefunction of Eq. (V.4) is not violated.

First, we note that $\beta_c(t)$ is immediately available from Eqs. (V.8c) and (V.8d),

$$\sqrt{\gamma}\beta_c\left(t\right)=\alpha_{\rm out}\left(t\right)-\alpha_{\rm in}\left(t\right) \tag{V.9}$$

which is an instantaneous map of the difference between the input and output in the photonic channel. From Eq. (V.8c), $\beta_t(t)$ is also readily expressible in terms of $\alpha_{\rm in}$ and $\alpha_{\rm out}$ as,

$$\begin{aligned}\beta_t &= \frac{-\dot{\beta}_c-\sqrt{\gamma}\alpha_{in}\left(t\right)-\frac{\gamma}{2}\beta_c}{g_{cav}}e^{i(\omega_t-\omega_c)t} \\ &= \frac{-(\dot{\alpha}_{\rm out}-\dot{\alpha}_{\rm in})/\sqrt{\gamma}-(\alpha_{\rm in}(t)+\alpha_{\rm out}(t))\sqrt{\gamma}/2}{g_{cav}}e^{i(\omega_t-\omega_c)t}\end{aligned} \tag{V.10}$$

From Eq. (V.8a) and (V.8b), we can solve for the amplitude of $\beta_e(t)$,

$$\frac{d}{dt}\left|\beta_e\right|^2=-\frac{d}{dt}\left|\beta_t\right|^2+g_{cav}(\beta_c^*\beta_t e^{-i(\omega_t-\omega_c)t}+\beta_c\beta_t^* e^{i(\omega_t-\omega_c)t}) \tag{V.11}$$

and the phase,

$$\frac{d}{dt}\arg(\beta_e)=\frac{1}{2i}\left|\beta_e\right|^{-2}\left(\dot{\beta}_t\beta_t^*-\beta_t\dot{\beta}_t^*\right)+\frac{g_{cav}}{2i}\left|\beta_e\right|^{-2}\left(\beta_t\beta_c^* e^{-i(\omega_t-\omega_c)t}-\beta_c\beta_t^* e^{i(\omega_t-\omega_c)t}\right) \tag{V.12}$$

And finally, from Eq. (V.8b), we can express $\Omega(t)$ in terms of the amplitudes that have been solved above,

$$\Omega\left(t\right)=2\frac{\dot{\beta}^t-g_{cav}\beta^c}{\beta^e} \tag{V.13}$$

The normalization condition can also be obtained from Eqs. (V.9), (V.10) and (V.11),

$$\frac{d}{dt}(\left|\beta_e\right|^2+\left|\beta_t\right|^2+\left|\beta_c\right|^2)=\left|\alpha_{in}\right|^2-\left|\alpha_{out}\right|^2 \tag{V.14}$$

The functions of this quantum interface can be classified into three types: (I) there is no incoming photon and the quantum interface generates an outgoing photon wavepacket of a specified shape; (II) there is an incoming photon wavepacket of a specified shape and it is completely absorbed by the quantum interface; (III) there is an incoming photon wavepacket of a specified shape, and the quantum interface generates an outgoing photon wavepacket of another specified shape. The first two type of controls form the basis for the quantum network operation. With control of type III, the quantum interface can act as a controllable scatter or pulse shaper for single photon wavepacket. This control can also be considered as the combination of consecutive controls of type II and I. In the following, we will discuss in more details the first two types of controls.

The sending node of the quantum network is operated with control of type I. The initial conditions are: $\alpha_{\rm in}(t)=0$, $\beta_c(t_0)=0$, $\beta_e(t_0)=1$ and $\beta_t(t_0)=0$. The integral form of Eq. (V.14) becomes,

$$\left|\beta_e\right|^2=1-\sin^2\theta\int_{t_0}^{t}\left|\tilde{\alpha}_{\rm out}\left(\tau\right)\right|^2d\tau-\left|\beta_c\right|^2-\left|g_{\rm cav}\right|^{-2}\left|\dot{\beta}_c+\gamma\beta_c/2\right|^2, \tag{V.15}$$

where $\tilde{\alpha}_{\rm out}$ is the normalized wavepacket of the emitted photon, and $\sin^2\theta$ is the average photon number. For a photon number and a pulse shape arbitrarily specified, the amplitude of the cavity mode is determined by Eq. (V.9) as $\beta_c = \tilde{\alpha}_{\rm out}\sin\theta\left(\sqrt{2\pi\kappa}\right)$. If we pose the problem of finding the optical control to produce a specified shape of the outgoing photon wavepacket, the fact that the right-hand side of Eq. (V.15) is positive requires the specified output pulse be sufficiently smooth, i.e., the pulse generation process be slower than the cavity-channel and the dot-cavity tunnelling rate (with timescales γ^{-1} and $g_{\rm cav}^{-1}$, respectively). At the remote future time $t_1 \to +\infty$, the photon emission process is completed, i.e., $\beta_c(t_1) = \dot{\beta}_c(t_1) = 0$, so $\beta_e(t_1) = e^{i\phi}\cos\theta$ with the controllable phase ϕ given by Eq. (V.12). The most general form of the photon generation process can be expressed as,

$$(C_g|g\rangle + C_e|e\rangle)\otimes|{\rm vac}\rangle \stackrel{\Omega(t)}{\to} C_g|g\rangle\otimes|{\rm vac}\rangle + C_e\left[e^{i\phi}\cos\theta|e\rangle\otimes|{\rm vac}\rangle + \sin\theta|g\rangle\otimes|\tilde{\alpha}_{\rm out}\rangle\right] \quad \text{(V.16)}$$

When the full Raman transition is completed, $\theta = \pi/2$ and $\beta_e(t_1) = 0$, Eq. (V.16) is reduced to,

$$(C_g|g\rangle + C_e|e\rangle)\otimes|{\rm vac}\rangle \stackrel{\Omega}{\to} |g\rangle\otimes(C_g|{\rm vac}\rangle + C_e|\tilde{\alpha}_{\rm out}\rangle)\,, \quad \text{(V.17)}$$

which corresponds to mapping of the stationary qubit onto the flying qubit. If initially the three level system is entirely in state $|e\rangle$, this mapping operation can function as deterministic generation of a single-photon wavepacket with any desired pulse shape $\tilde{\alpha}_{\rm out}$. If the Raman cycle is controlled to be partially completed ($\theta < \pi/2$), the state initially in $|e\rangle\otimes|{\rm vac}\rangle$ is transformed into an entangled state of the stationary spin and the flying photon

$$e^{i\phi}\cos\theta|e\rangle\otimes|{\rm vac}\rangle + \sin\theta|g\rangle\otimes|\tilde{\alpha}_{\rm out}\rangle. \quad \text{(V.18)}$$

The entanglement entropy $E = -\cos^2\theta\log_2\cos^2\theta - \sin^2\theta\log_2\sin^2\theta$ can be set any value between 0 and 1 depending on the rotating angle θ.

The receiving node is operated with control of type II, typically as a full Raman cycle, in the quantum network scheme. It is basically the time-reversal of the full-cycle sending process. With the three level system initially on state $|g\rangle$ and the incoming photon $C_g|{\rm vac}\rangle + C_e|\alpha_{\rm in}(t)\rangle$, the mapping transformation is

$$|g\rangle\otimes(C_g|{\rm vac}\rangle + C_e|\alpha_{\rm in}\rangle) \stackrel{\Omega}{\to} (C_g|g\rangle + C_e|e\rangle)\otimes|{\rm vac}\rangle. \quad \text{(V.19)}$$

As in the sending process, the incoming photon pulse $\alpha_{\rm in}(t)$ can be arbitrarily specified, provided that it is smooth enough, and that the photon can be absorbed without reflection. As the stationary qubit converted from the photon state can be read out non-destructively (this will be discussed in chapter VI), the receiving node can also act as an efficient photon detector which measures the photon number state when the photon pulse shape is known.

By combining the sending and receiving processes, the transfer of a qubit from one node to another can be easily implemented, with the outgoing photon from the sending node directed as the incoming photon for the receiving node. Obviously, when two state-transfer operations with opposite directions are combined together, the two qubits are swapped. For swap operations, the waveguide connecting the two nodes should be long enough to make the photon travelling time longer than the operation time.

If the operation at the sending node has been designed to produce an entangled state of the stationary and the flying qubit, the mapping process at the receiving node will just produce a non-locally entangled state of the two nodes by the transformation

$$\begin{aligned} |e\rangle_1|g\rangle_2 \otimes |\mathrm{vac}\rangle \quad &\stackrel{\Omega_1}{\rightarrow} \quad e^{i\phi}\cos\theta|e\rangle_1|g\rangle_2 \otimes |\mathrm{vac}\rangle + \sin\theta|g\rangle_1|g\rangle_2 \otimes |\tilde{\alpha}_{\mathrm{out}}\rangle \\ &\stackrel{\Omega_2}{\rightarrow} \quad \left[e^{i\phi}\cos\theta|e\rangle_1|g\rangle_2 + \sin\theta|g\rangle_1|e\rangle_2\right] \otimes |\mathrm{vac}\rangle. \end{aligned} \tag{V.20}$$

We end this section with a summary of the essential quantum network functions enabled by the exact solution: (i) It can send a flying quantum state and can also function as a deterministic source of single-photons with arbitrary pulse shape and controllable photon number. (ii) It can receive a flying quantum state, being an efficient single-photon detector provided that the incoming photon pulse shape is known. (iii) The sending and receiving processes combined transfer a state from one node to another. (iv) An incoming flying qubit may be swapped with a stationary qubit which enables the swap of two remote qubits. (v) An entangled state of the stationary and flying qubits is produced in a partial Raman cycle. (vi) Two stationary qubits separated far away are entangled when the photon state generated by the partial Raman cycle is mapped into a stationary qubit.

V.C Dot-cavity-waveguide realization of the quantum interface

Here we discuss a physical structure that is well suited for the realization of the quantum interface discussed in the previous section. The basis for our proposed physical implementation of a node is formed by a substantial list of recent experimental advances on optical manipulation of excitons in single nanodots [4], nanodot-microsphere coupling [63], cavity-fiber coupling [58], fabrication of high-quality microcavities and waveguides, both on semiconductor surfaces [58] and in photonic crystals [56, 61] and especially the very recent findings of vacuum Rabi splitting of nanodot embedded in such cavities [66, 70, 71]. The duration of a typical operation in the node is of the order 100 ps, consistent with the theoretical estimates of optical operations on spin qubits in dots for network purposes [8, 17, 18]. The speed and pulse shaping may well be within

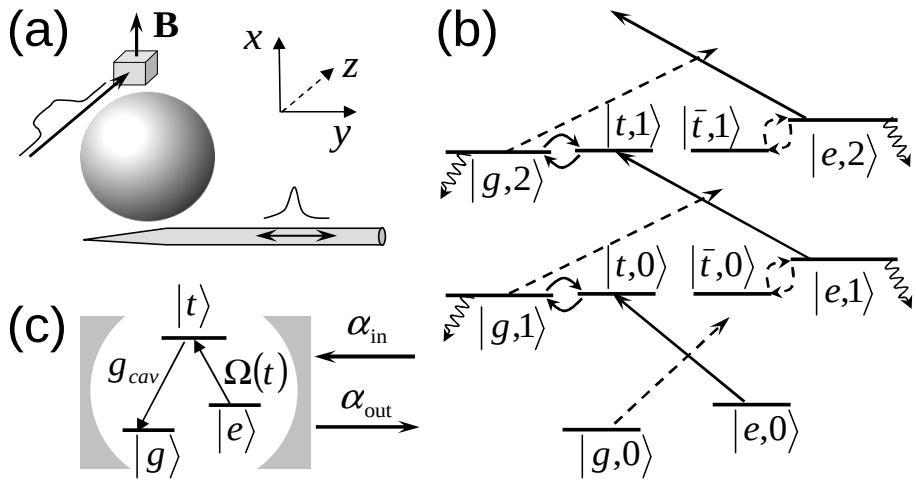

Figure V.2 Dot-cavity-waveguide structure as a quantum interface: system configuration and energy level schemes. (a) A high-Q micro-sphere coupling a 'tapered' waveguide and a doped quantum dot. (b) The level diagram and optical process. In $|s,n\rangle$, $s = g, e, t$ or $\bar{t}$ denotes an electronic state in the dot and n denotes the number of photons in the single cavity mode. Straight, curved, and wavy arrows represent the laser excitation, dot-cavity coupling, and cavity-fiber tunnelling, respectively. The resonant and off-resonant processes are represented by solid and dashed lines, respectively. (c) The simplified cavity-assisted Raman process.

the capability of the existing ultrafast optics.

The quantum interface is made up of a high-Q microcavity coupling a quantum dot and an optical waveguide (or a fiber), such as the cartoon shown in Fig. V.2(a). Lowering of the Q of the cavity due to the strong coupling with the waveguide is part of the process and has no deleterious effect on the quantum operation. The detailed optical process is depicted in Fig. V.2(b). The qubit is represented by the two spin states $|g\rangle$ and $|e\rangle$ which have split energies ω_g and ω_e in a static magnetic field normal to the optical axis of the dot. The lowest two optically excited states are the trion states $|t\rangle$ and $|\bar{t}\rangle$, with energies ω_t and $\omega_{\bar{t}}$ respectively. If we choose the active cavity mode of an electric field in the Y-direction at the vicinity of the dot and the control laser of X-polarization, the states $|g\rangle$, $|e\rangle$, $|t\rangle$ and $|\bar{t}\rangle$ then corresponds respectively to the electron spin states $|x+\rangle$, $|x-\rangle$ and the trion states $|T+\rangle$, $|T-\rangle$ defined in Chapter II. The cavity mode of frequency ω_c couples with strength $g_{\rm cav}$ only to the transitions $|g\rangle \rightarrow |t\rangle$ and $|e\rangle \rightarrow |\bar{t}\rangle$, and the controlling laser of central frequency ω_L and complex Rabi frequency $\Omega(t)$ couples only to the cross transitions $|g\rangle \rightarrow |\bar{t}\rangle$ and $|e\rangle \rightarrow |t\rangle$. The laser light and cavity mode satisfy the resonance condition: $\omega_L + \omega_e = \omega_c + \omega_g = \omega_t$. By the Zeeman splitting and the selection rules, the trion state $|\bar{t}\rangle$ is off-resonant to the laser light and the cavity mode (shown by dashed lines in Fig. V.2(b)). The cavity mode is coupled to the waveguide continuum by the coupling constant κ.

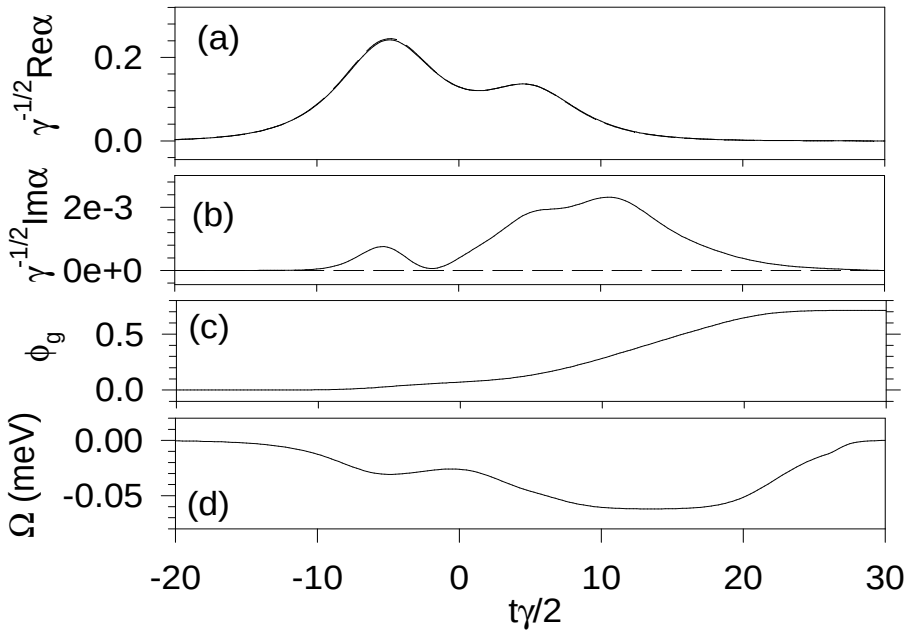

Figure V.3 Numerical simulation of generation of a single photon pulse with double sech shape from the dot-cavity-waveguide structure. (a) Real part of the dimensionless amplitude of the simulated photon pulse (solid line) as a function of the dimensionless time $\gamma t/2$. The deviation from the target pulse is not visible. (b) Imaginary part of the simulated pulse (solid line) and the target pulse (dashed line). (c) Phase drift of the state $|g,0\rangle$. (d) Rabi frequency of the control laser. The trion decay rate is set at $\Gamma = 3\mu$eV, and the intrinsic loss rate of cavity mode is assumed to be $\gamma' = 0.1$ μeV. The cavity-fiber tunnelling rate is chosen to be $\gamma = 0.2$ meV and the dot-cavity coupling constant $g_{\rm cav} = 0.1$ meV.

At a sending node, the Raman process consists in first the laser field resonantly exciting the spin state $|e,0\rangle$ to the trion state $|t,0\rangle$, then the trion state resonantly coupled to the cavity state $|g,1\rangle$ which finally is rotated to the spin state $|g,0\rangle$ forming a photon wave packet in the waveguide. The receiving mode is just the time-reversed process. Undesirable dynamics involving the state $|\bar{t}\rangle$ is eliminated by making the Zeeman splitting sufficiently larger than the cavity-dot coupling and the Rabi frequency. The resultant optical process is the cavity-assisted resonant Raman process in a Λ-type three-level system shown in Fig. V.2(c). Then for any shape of the single-photon wave packet in the waveguide, an analytical solution of the pulse shape of the laser field may be found based on the derivation of section V.B. With this analytically obtained laser pulse shape as the controlling input, numerical calculations including the non-resonant transitions and realistic decoherence have been performed and high efficiency of desired operations at the quantum interface is demonstrated.

Error of the quantum operations described above is estimated in terms of fidelity by numerical simulations including the undesired non-resonant dynamics and unavoidable decoher-

ence. The main source of decoherence is the trion decay by spontaneous emission and the cavity mode leakage other than the dynamics accounted above. The fiber loss and the spin relaxation are negligible on the time-scale of 100 ps and the distance-scale of 1 cm of relevance here [1]. The trion decay rate, based on experiment [99], is set at $\Gamma = 3\mu$eV, and the intrinsic loss rate of a high-Q cavity excluding coupling to the dot and the fiber is assumed to be $\gamma' = 0.1$ μeV (corresponding to a Q-factor $\sim 10^7$). The cavity-fiber tunnelling rate is chosen to be $\gamma = 0.2$ meV and the dot-cavity coupling constant $g_{\rm cav} = 0.1$ meV taken from state of art experiments [66, 70, 71]. The remaining sources of error are the non-resonant excitation of the multi-photon states and AC Stark shift of the energy levels. The latter induces a deterministic phase drift between $|g\rangle$ and $|e\rangle$, which is independent of the coefficients $C_{g(e)}$ as the two excitation pathways starting respectively from $|g\rangle$ and $|e\rangle$ are independent of each other (see Fig. V.2 (b)), and thus can be compensated by a single-qubit operation. Leakage out of the qubit subspace by the non-resonant excitation to multi-photon states is greatly suppressed by a 1 meV Zeeman splitting (can be achieved at less than 10 T magnetic field for InAs dots), which is much larger than the Rabi frequency and the cavity-dot coupling.

In practical operation, we may take the strategy to design the shape $\Omega(t)$ of the control field from the ideal set of Eqs. (V.8), and use this designed $\Omega(t)$ to drive the system dynamics which is subject to decoherence processes and the undesired dynamics as shown in Fig. V.2(b). We present in Fig. V.3 the simulation result of mapping a spin state to a flying photon wavepacket with the pulse shape targeted as a superposition of two sech-functions as $\alpha_{\rm out}^{\rm ideal}(t) = {\rm sech}(\gamma t/6 + 5) + 0.5{\rm sech}(\gamma t/6 - 5)$, with normalization understood.

The fidelity of the photon pulse generation $|\langle\alpha_{\rm out}^{\rm ideal}|\alpha_{\rm out}\rangle| \approx 0.9912$. Because of the non-adiabatic optical pumping and dot-cavity coupling, the whole mapping process can be completed within 300 ps. The simulation of the photon absorption process shows an overall fidelity greater than 0.99 as well. Indeed, the dot-cavity-waveguide structure well promises the realization of a high efficiency quantum interface for spins and photons.

V.D Pulse shaping study for the optimized efficiency in presence of imperfections

For a quantum network function, the control scheme allows an arbitrary shape of the intermediate single photon wavepacket, and therefore offers great flexibility in the physical im-

[1] With this quantum interface, we are aiming at the construction of a solid state quantum network on chip for distributed quantum computation. See the discussion of section IX.D in the final chapter.

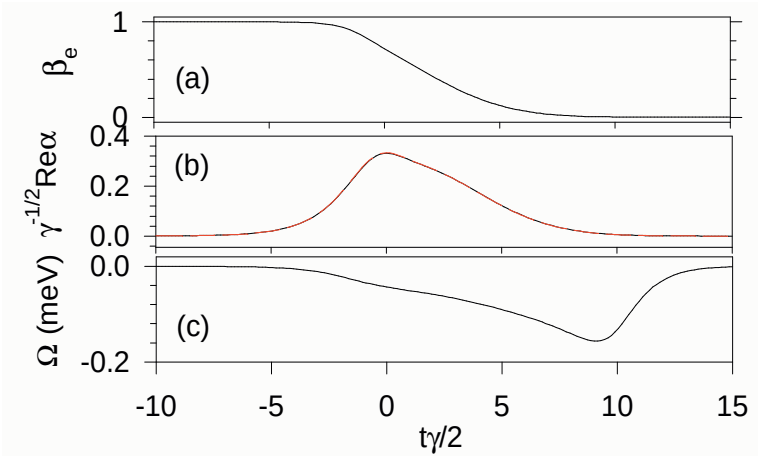

Figure V.4 Generation of single photon pulse of a target shape of a sech ram-up and a Gaussian decay: $(1-\tanh(\gamma t/4))\mathrm{sech}(0.35\gamma t)+(1+\tanh(\gamma t/4))\exp(-\gamma^2t^2/100)$. The relevant parameters are: $\gamma = 0.1$meV, $g_{cav} = 0.1$meV, $\gamma_t = 3\mu$eV, $\gamma' = 0.05\mu$eV. (a) Amplitude of the state β_e. (b) Generated single photon wavepacket (solid line). The dashed line shows the target shape. The difference is not visible in this case. (c) The Rabi frequency of the driving field.

plementation. For example, if for some technique reason, the sending or receiving node is only capable with some fixed shapes of the single photon wavepacket, the control design at the other node by the exact solution may well enable the network function. While both the sending and receiving node are controllable, we have the freedom to choose an arbitrary intermediate photon wavepacket. Yet in presence of the undesired dynamics, e.g., to the $|\bar{t}\rangle$ state in the proposed dot-cavity-waveguide structure, different intermediate single wavepacket may result in different efficiency. Here we investigate the network operation with various shapes of the intermediate single photons and show that some straightforward pulse-shaping may improve the efficiency for some of them. As a demonstration, we focus our discussion on the Gaussian shapes and exponential shapes as the tail and (or) ram-up of single photon pulse.

The undesired dynamics in the dot-cavity-waveguide realization is suppressed by applying the external magnetic field to detune the energy of the unwanted transitions from the

Table V.1 Merits of entanglement creation numerically simulated for the dot-cavity-waveguide system with various photon pulse shape, normalization understood. $g^{1,2}_{\mathrm{cav}} = 0.1$ meV and $\gamma^{1,2} = 0.2$ meV.

$\alpha(t)$	$\mathrm{sech}(\gamma t/6)$	$\exp(-\gamma^2t^2/128)$	$\frac{1+\tanh(\gamma t/8)}{\cosh(\gamma t/6)}+\frac{1-\tanh(\gamma t/8)}{\exp(\gamma^2t^2/128)}$
Fidelity	0.9912	0.9908	0.9906
$E(\rho_{qubit})$	0.9995	0.9995	0.9994
P_{leak}	0.0173	0.0182	0.0184

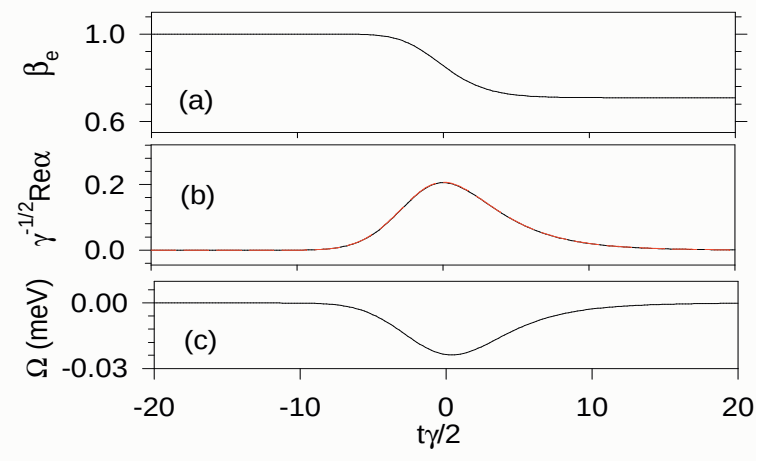

Figure V.5 Creation of entanglement between the stationary and flying qubit with the target state: $(|e\rangle \otimes |\text{vac}\rangle + |g\rangle \otimes |\tilde{\alpha}_{\text{out}}\rangle)/\sqrt{2}$. The desired single photon pulse shape has a Gaussian ram-up followed by a sech decay: $(1+\tanh(\gamma t/4))\text{sech}(0.15\gamma t) + (1-\tanh(\gamma t/4))\exp(-\gamma^2 t^2/64)$. The parameters are: $\gamma = 0.1$meV, $g_{cav} = \gamma$, $\gamma_t = 3\mu$eV, $\gamma' = 0.05\mu$eV. (a) Amplitude of the state β_e. Notice that the amplitude ends with $1/\sqrt{2}$ here in stead of 0 in the state transfer case. (b) Generated single photon wavepacket (solid line). The dashed line shows the target shape. The difference is not visible in this case. The integration of the pulse area is 1/2 for this entanglement creation case instead of 1 in the state transfer. (c) The Rabi frequency of the driving field.

frequency of the laser field. To have the undesired dynamics well suppressed, a natural expectation is that the system shall not be driven too hard, i.e., the Rabi frequency $\Omega(t)$ being much smaller than the detuning energy (electron zeeman splitting in the magnetic).

The exact solution to Rabi frequency $\Omega(t)$ of the driving field for several different target photon pulse shapes for various network operations are shown in Fig. V.4,V.6 and V.5. The fast diminishing tails of the Gaussian pulse tends to require higher peak value of $\Omega(t)$ than the exponential tails of the Sech pulse. In presence of the undesired coupling to the trion state $|\bar{t}\rangle$, the Gaussian shapes causes more non-resonant excitations than the exponential ones. Therefore, single photon pulse with ram-up and tail both of an exponential shape, e.g., the ones shown in Fig. V.3 and V.5, is advantageous for mediating network operations.

On the other hand, deviation from target shape at the tail region of the single photon pulse has a negligible effect on the fidelity of interface operations as compared to non-resonant excitation, thus tuning down $\Omega(t)$ at the tail region can make the Gaussian pulse more efficient for achieving fidelity. Table V.3 shows the results of a comparative study of the merits of the photon pulse in the Sech shape, the Gaussian, and an asymmetric shape with exponential shape on the rise and Gaussian on the fall, mediating entanglement of two spin qubits to the Bell state $e^{i\phi}|g\rangle_1|e\rangle_2 + |e\rangle_1|g\rangle_2$. The merits calculated are the fidelity, the entanglement of formation $E(\rho_{qubit})$ in the subspace of the two spin qubits and the probability of leakage out of this subspace,

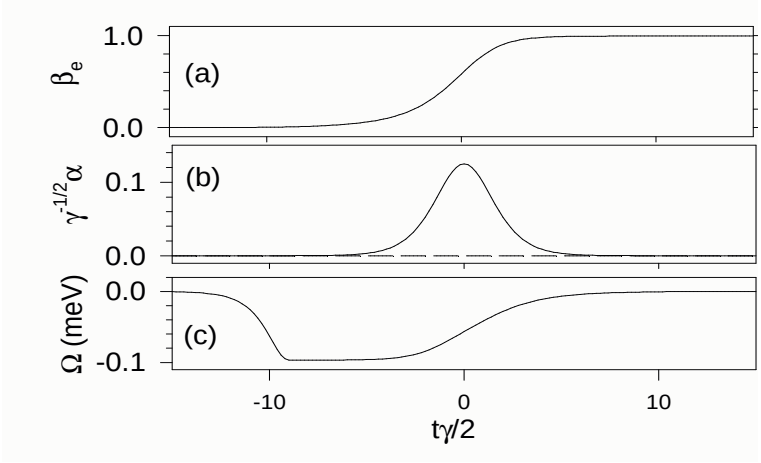

Figure V.6 Absorption of a single photon wavepacket of shape sech($\gamma t/4$). The parameters are $\gamma = 0.1$meV, $g_{cav} = \gamma$, $\gamma_t = 3\mu$eV, $\gamma' = 0.05\mu$eV. (a) Amplitude of the state β_e. (b) Solid line shows the incoming single photon wavepacket and the dashed line shows the reflected photon wavepacket. (c) The Rabi frequency of the driving field.

P_{leak}. We can see that after pulse shaping for the driving field by smoothly tuning it down at the tail region, the operations mediated by single photon pulse of Gaussian shapes may have comparable efficiency as compared to that mediated by the single photon of Sech shape.

V.E Error analysis and fault tolerance

In the above discussions, exact knowledge of the coupling strength g_{cav}, γ and $\Omega(t)$ are assumed. But in general, there could be various errors on parameters due to imperfect characterization of the system. Here we discuss the robustness of our scheme in presence of unknown system parameter errors.

For generality, the discussion in this section is for the genuine three level model in

Table V.2 Fidelity of the entanglement creation and state transfer scheme in the presence of various system parameter errors. The Rabi frequencies $\Omega_{1(2)}(t)$ are analytically designed for a target Bell state $(|g\rangle_1|e\rangle_2 + |e\rangle_1|g\rangle_2)/\sqrt{2}$ in the former scheme and for transferring $(|g\rangle + |e\rangle)/\sqrt{2}$ state in the latter both with carrier shape sech($\frac{\gamma t}{6}$), assuming $g_{cav}^{1,2} = 0.1$ meV and $\gamma^{1,2} = 0.2$ meV. The evolutions are then simulated by adding $+(-)10\%$ to $g_{cav}^{1(2)}$, $\gamma^{1(2)}$ or $\Omega_{1(2)}(t)$ at node 1(2) respectively. The operation fidelity with no parameter error are listed for comparison. Photon leakage rates γ_t and γ' are set as 3μeV and 0.05μeV respectively in all cases.

	no error	10% g error	10% γ error	10% $\Omega(t)$ error
Entangle	0.9922	0.9881	0.9905	0.9870
Transfer	0.9922	0.9891	0.9911	0.9901

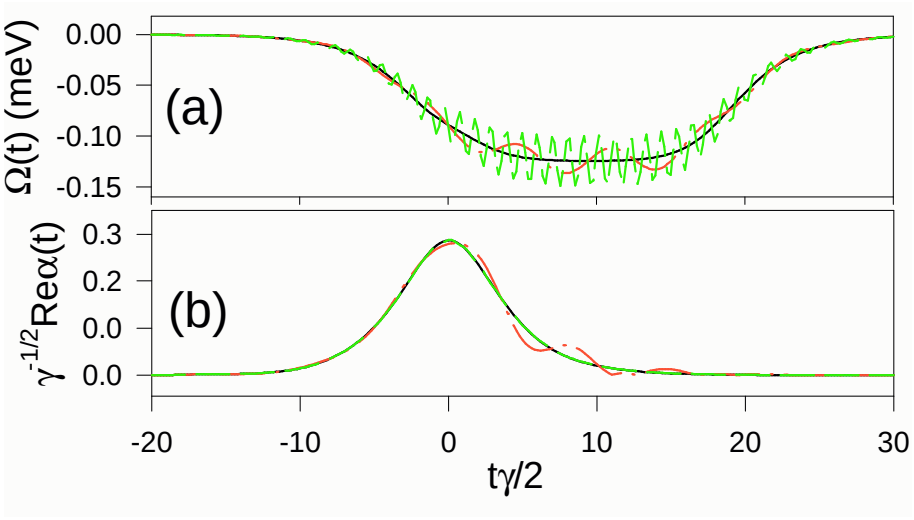

Figure V.7 State transfer of $((|g\rangle+|e\rangle)/\sqrt{2})$ in presence of shape fluctuations of the control pulses. (a) The designed control pulse at the sending node (black solid line) and the applied control pulse with slow fluctuations (red dashed dot line) and fast fluctuations (green solid line). The control pulse at the receiving node has a similar error applied. (b) The generated intermediate single photon wavepacket. The black solid lines shows the target shape. Deviation of the generated single photon wavepacket is invisible in the fast fluctuation case. The fidelity of the transfer is 0.9912 with the slow shape fluctuations and 0.9922 with the fast shape fluctuations. The parameters used are: $\gamma = 0.2$meV, $g_{cav} = \gamma/2$, $\gamma_t = 3\mu$eV, $\gamma' = 0.05\mu$eV.

Fig. V.1. Non-ideality including the photon leakage into free space through cavity wall (the intrinisic cavity leakage with rate γ') and from intermediate state $|t\rangle$ (with rate γ_t) is taken into account by adding decoherence terms to Eq. (V.8),

$$\dot{\beta}_e = -\frac{\Omega_1^*}{2} e^{-i(\omega_t-\omega_L-\omega_e)t}\beta_t \tag{V.21a}$$

$$\dot{\beta}_t = g_{cav} e^{i(\omega_t-\omega_c)t}\beta_c + \frac{\Omega}{2} e^{i(\omega_t-\omega_L-\omega_e)t}\beta_e - \frac{\gamma_t}{2}\beta_t \tag{V.21b}$$

$$\dot{\beta}_c = -g_{cav} e^{-i(\omega_t-\omega_c)t}\beta_t - \sqrt{\gamma}\alpha_{in}(t) - \frac{\gamma}{2}\beta_c - \frac{\gamma'}{2}\beta_c \tag{V.21c}$$

$$= -g_{cav} e^{-i(\omega_t-\omega_c)t}\beta_t - \sqrt{\gamma}\alpha_{out}(t) + \frac{\gamma}{2}\beta_c - \frac{\gamma'}{2}\beta_c \tag{V.21d}$$

For proper accounting of the effect of the "unknown" systematic errors in the numerical simulation, we design the Rabi frequency $\Omega(t)$ of the control field from the ideal set of Eqs. (V.8) using the assumed value of g_{cav} and γ. And then in the numerical simulation, the dynamics is driven by $\Omega'(t)$, g'_{cav} and γ' which contains errors (deviation from the assumed value g_{cav}, γ and the solved $\Omega(t)$) plus the extra decoherence terms. The resonance conditions of the Raman process is assumed: $\omega_t = \omega_c = \omega_L + \omega_e$.

We listed in Table. V.2 the effect of the unknown errors in the various parameters on

the fidelity of entanglement to $e^{i\phi}|g\rangle_1|e\rangle_2 + |e\rangle_1|g\rangle_2$ and transfer of the state $|g\rangle + |e\rangle$ state both with the photon pulse shape sech($\frac{\gamma t}{6}$). Our system shows a surprising robustness: 10% unknown errors on g_{cav}, γ or $|\Omega(t)|$ only reduce the fidelity by less than 1%.

The $|\Omega(t)|$ error studied in Table. V.2 is a global one on the amplitude, e.g. induced by the stationary qubit being slightly out of focus from the classic control field. We also studied the efficiencies of network operations in presence of the control field shape errors, i.e., temporal fluctuations in amplitude. Surprisingly, the control scheme is found immune against fast fluctuations (see Fig. V.7). This robustness is due to the finite bandwidth of the quantum interface, i.e., the coupling strength between the cavity and the three level system and also the cavity waveguide tunneling rate, which forbid the single photon pulse shape to follow any fast changes in the control. Any temporal fluctuations in the control field with the frequency higher than the interface bandwidth are effectively averaged out. The time independent amplitude error discussed in Table. V.2 may be considered as a special shape error which is actually the most deleterious scenario for the network operation.

$\Omega(t)$ can also have unknown phase error due to laser phase fluctuation which can be considered static in the time scale of our operation. We show below that what matters in two node operations is the relative phase between $\Omega_1(t)$ and $\Omega_2(t-\tau)$ where τ is the propagation delay.

Assume that the classic driving field at the sending node has a unknown phase of φ_1 and, hence, the Rabi frequency is now $\Omega_1(t)\, e^{i\varphi_1}$. From the form of the coupling term that involves the classical field in the Hamiltonian Eq. (V.3), the unknown phase factor can be absorbed by redefining the state $|\tilde{e}\rangle_1 \equiv e^{-i\varphi_1}|e\rangle_1$, so that,

$$\frac{1}{2}\left[i\Omega_1(t)e^{i\varphi_1}e^{-i\omega_L t}|t\rangle_{11}\langle e| + H.c.\right] \equiv \frac{1}{2}\left[i\Omega_1(t)e^{-i\omega_L t}|t\rangle_{11}\langle\tilde{e}| + H.c.\right] \tag{V.22}$$

and we can make the same transform at the receiving node. Starting from a general state $(C_g|g\rangle_1 + C_e|e\rangle_1)\,|g\rangle_2 \otimes |\text{vac}\rangle \equiv C_g|g\rangle_1|g\rangle_2 \otimes |\text{vac}\rangle + C_e e^{i\varphi_1}|\tilde{e}\rangle_1|g\rangle_2 \otimes |\text{vac}\rangle$, two-node operations in the presence of laser phase fluctuation can be generally expressed as,

$$\begin{aligned}
& C_g|g\rangle_1|g\rangle_2 \otimes |\text{vac}\rangle + C_e e^{i\varphi_1}|\tilde{e}\rangle_1|g\rangle_2 \otimes |\text{vac}\rangle \qquad \text{(V.23)}\\
\xrightarrow{\Omega_1(t)} \quad & C_g|g\rangle_1|g\rangle_2 \otimes |\text{vac}\rangle + C_e e^{i\varphi_1}\left[e^{i\phi}\cos\theta|\tilde{e}\rangle_1|g\rangle_2 \otimes |\text{vac}\rangle + \sin\theta|g\rangle_1|g\rangle_2 \otimes |\tilde{\alpha}_{\text{out}}\rangle\right]\\
\xrightarrow{\Omega_2(t-\tau)} \quad & \left[C_g|g\rangle_1|g\rangle_2 + C_e e^{i\varphi_1}\left(e^{i\phi}\cos\theta|\tilde{e}\rangle_1|g\rangle_2 + \sin\theta|g\rangle_1|\tilde{e}\rangle_2\right)\right] \otimes |\text{vac}\rangle
\end{aligned}$$

The final state is equivalent to,

$$\left[c_g|g\rangle_1|g\rangle_2 + c_e\left(e^{i\phi}\cos\theta|e\rangle_1|g\rangle_2 + e^{i\varphi_1}e^{-i\varphi_2}\sin\theta|g\rangle_1|e\rangle_2\right)\right] \otimes |\text{vac}\rangle$$

If the classic driving fields at the two nodes can be phase locked in a delayed manner so that

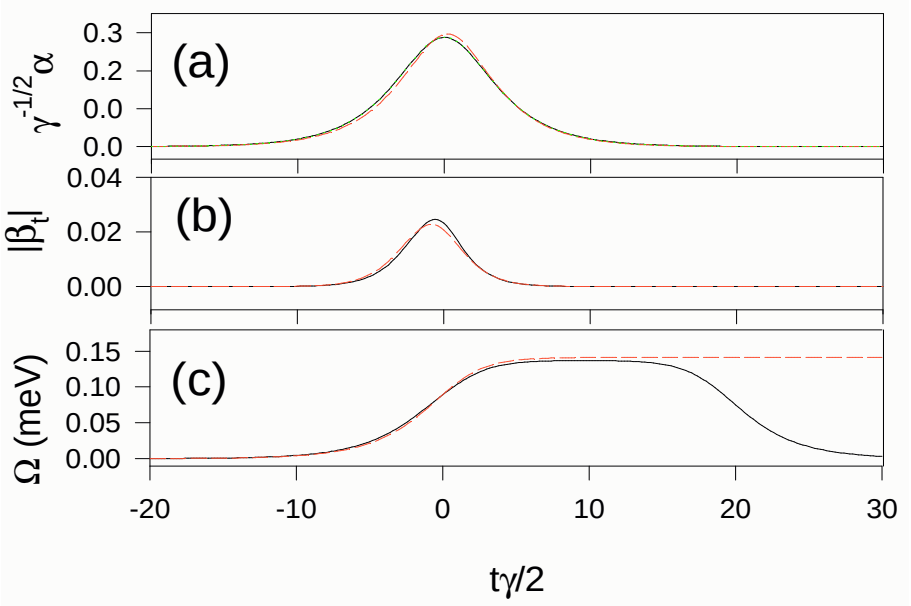

Figure V.8 Compare of the single photon generation by the adiabatic scheme and the exact solution I. The target single photon wavepacket is of shape sech($\gamma/6t$), with normalization understood. The parameters are $\gamma = 0.2$meV, $g_{cav} = \gamma$, $\gamma_t = 3\mu$eV, $\gamma' = 0.05\mu$eV. (a) The generated single photon wavepacket using the adiabatic scheme(dashed line) and the exact solution(solid line). The dotted line shows the target pulse shape. (b) The occupation of the intermediate state $|\beta_t|$. (c) The Rabi frequency of the driven field from adiabatic design(dashed line) and the exact solution(solid line).

there is a certain relative phase between $\Omega_1(t)$ and $\Omega_2(t-\tau)$, the two node operation is well protected from laser phase fluctuations.

Photon loss in the propagation is also deleterious to quantum network applications. However, for applications where the spatial dimension of the quantum network system is not large, i.e., in distributed quantum computations, photon propagation in optical fibers or waveguides is almost decoherence free. Moreover, error correction schemes dealing with this propagation loss is available [100]. When long distance quantum state transfer is desired, the idea of quantum repeaters [101] might be incorporated into the quantum network design for protection against the photon propagation loss.

V.F Comparison with other schemes

In this section, we discuss the link of our scheme to other schemes that were previously proposed, specifically, the time symmetric scheme of [88] and the adiabatic scheme of [90, 91, 92].

The solution provided in [88] is obtained in the perturbative regime for a detuned Raman process. While detuning can suppress photon leakage into free space through the intermediate

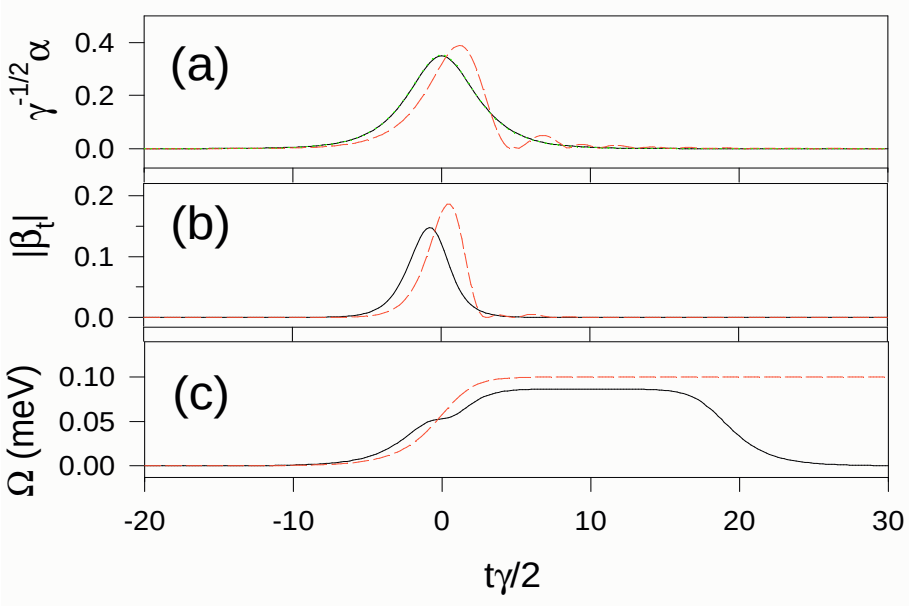

Figure V.9 Compare of the single photon generation by the adiabatic scheme and the exact solution II. The plot is the same as Fig. V.8 except that the target pulse shape is $sech(\gamma/4t)$ and the parameters are: $\gamma = 0.2$meV, $g_{cav} = \gamma/2$, $\gamma_t = 3\mu$eV, $\gamma' = 0.05\mu$eV.

state, this photon leakage is shown, by the numerical simulations in the previous sections, to be negligible when γ_t is much smaller than any other energy scales of the system. Such could be the typical situation in solid state system composed of a quantum dot coupled to microcavity [93]. The controlling scheme we presented here can be used to design both detuned and resonant Raman process. The resonant Raman process utilizes fully the coupling between the cavity and the three level system and thus allows the generation and absorption of ultrafast pulses.

We have compared the adiabatic scheme of [90, 91, 92] with our exact solution in various parameter regimes for the genuine three level model (Fig. V.1). In Table. V.2, we show the comparison results for the fidelity of state transfer operation mediated by a sech target pulse of various duration. The adiabatic scheme works well when the duration of the incoming/outgoing single photon pulse is much longer than the maximum of γ^{-1} and g_{cav}^{-1}. When our scheme is operated in this regime, the occupation of the intermediate state $|t\rangle$ is found very small and the system indeed evolve adiabatically. We illustrate in Fig. V.8 an example of the operation in this regime. From Fig. V.8(c), we can see that the design of the Rabi frequency $\Omega(t)$ using the adiabatic scheme is almost identical to that given by our exact solution (the noticeable difference in $\Omega(t)$ at the tail region of the photon wavepacket has negligible effect on the fidelity as both $|t\rangle$ and $|e\rangle$ states have already been depleted at the moment). Both schemes give fidelity close to perfect.

Table V.3 Compare of the fidelity of state transfer operation using the adiabatic scheme and the exact solution both with the same target pulse of a sech shape. We fix the cavity coupling to the photonic channel $\gamma = 0.2$meV, the relaxation of the intermediate state into free space $\gamma_t = 3\mu$eV and the cavity leakage into free space $\gamma' = 0.05\mu$eV.

g_{cav}	γ	γ	$\gamma/2$	$\gamma/2$	$\gamma/2$
target pulse	sech($\gamma t/6$)	sech($\gamma t/4$)	sech($\gamma t/6$)	sech($\gamma t/4$)	sech($\gamma t/2.4$)
F_{exact}	0.9959	0.9957	0.9844	0.9837	0.9815
F_{adia}	0.9936	0.9896	0.9206	0.8194	0.5547

As can be expected, the adiabatic schemes is shown to fail in generation or absorption of fast single photon pulses. While the fidelity of our scheme remains high in these fast operation regimes, the fidelity of adiabatic scheme drops appreciably as shown in Table. V.3. We illustrate also in Fig. V.9 a comparison of design using the two schemes in this regime. The occupation of the intermediate state $|t\rangle$ is found not negligible as can be seen from Fig. V.9(b). Since in the adiabatic scheme, the three level system is assumed always in the dark state composed of only $|e\rangle$ and $|g\rangle$, the scheme gives a poor design of the Rabi frequency $\Omega(t)$ in the active time period as can be seen in Fig. V.9(c). As a consequence, the pulse generated from the adiabatic design has an appreciable deviation from the target shape (see Fig. V.9(a)).

V.G Chapter summary

We have discussed a general and exact solution to the dynamics of a quantum interface composed of a three level system coupled to a continuum through a cavity, which yields a controlling scheme for arbitrary operations on the stationary qubit and the flying qubit. The scheme enables an number of quantum network operations including sending, receiving, swapping as well as a new way of deterministically entangling qubit between distant nodes. The removal of the constraints of time symmetry can greatly save the cost of resource for physical implementation of quantum network. The removal of adiabaticity allows ultra-fast operations. The exact solution also allows learning studies on the system parameters by trial and error, while the intrinsic robustness against unknown parameter errors paves the way for further exploration of quantum feedback control [102, 103] for this system. The quantum interface with the sending and receiving operation can also be considered, respectively, as single photon source and detector for a wavepacket of arbitrary shape and might find its use in quantum computation and quantum information with linear optics devices.

This control scheme is applicable to a wide range of physical implementation of the quantum interface including atom-CQED and solid state systems. With the advances in fabrica-

tion of coupled structures of solid state micro-cavities, waveguides and quantum dots [58, 66, 70], solid state implementation can be of particular interest [93]. Apart from the stability and integrability of the solid state structure, the strong coupling of quantum dot embedded in semiconductor micro-cavity recently achieved in lab [70, 66, 71] makes them very desirable as components of the quantum interface. The state of art dot-cavity coupling allows operations with bandwidth of ~ 0.1meV, about 2 orders faster than the major decoherence rate in this solid state system. As shown in the numerical simulations, such a parameter regime make possible using resonant Raman process for ultra-fast operations of $\sim$ 100ps while maintaining fidelity over 99%. The absence of unwanted center of mass dynamics of the stationary qubit is another merit of solid state system.

V.H Acknowledgements

The text of chapter V, in part, is a reprint of the material as it appears in Wang Yao, Ren-Bao Liu, and L. J. Sham, *Theory of Control of the Spin-Photon Interface for Quantum Networks*, Phys. Rev. Lett **95**, 030504, © 2005 The American Physical Society, where the dissertation author was the first author, and Wang Yao, Ren-Bao Liu, and L. J. Sham, *Theory of Control of the Dynamics of the Interface between Stationary and Flying Qubits*, J. Opt. B.: Quant. Semiclass. Opt. **7**, S318, © 2005 IOP Publishing Ltd, where the dissertation author was the first author. The co-authors in these publications directed, supervised, and co-worked on the research which forms the basis of this chapter.

VI

Ultra-fast Initialization and Quantum Non-Demolition Measurements of Single Spins

Initialization or cooling in ultrafast timescales is a prerequisite for coherent optical control of single spins, especially for quantum computation which requires continuous reset of qubits for quantum error correction [23]. On the other hand, the quantum measurement of single electron spins is notoriously difficult. The existing schemes of single-spin measurement [104, 105, 106, 107, 108] are mostly based on electrical measurement via spin-charge conversion and thus is incompatible with ultrafast optical control of spins.

Quantum non-demolition (QND) measurement is also a critical element for scalable quantum computation. In quantum computation, the final state before measurement is in general a superposition of the basis states, written as $\sum C_x|x\rangle$, and a measurement in the basis gives an output x from which the result is derived. In practice, to establish statistical confidence or accumulate signal strength by imperfect detection, the measurement should be repeated to have a certain x observed at least twice. In a destructive measurement, each cycle has to be started with a fresh preparation of the final state and could result in any possible output x, which amounts to measuring an ensemble of identical quantum states (similar to identical molecules used in liquid NMR-based quantum computation [109, 110]). When the number of qubits (problem size) increases, the number of basis states $|x\rangle$ in the superposition could increase exponentially, as in the famous Shor algorithm for factorization [111], thus the physical resources, being the number of repeated cycles or the ensemble size, would scale up exponentially. By contrast, in a QND

measurement, a state collapses into a basis state and remains in it for the repeated cycles, thus the signal strength can be accumulated with a limited number of repetitions, similar to cycling transitions used for single ions [112, 113, 114].

In this chapter, we illustrate the idea of using single-shot coherent quantum evolution to realize ultrafast cooling and QND measurement of single electron spins, in the coupled system of a doped quantum dot, a microcavity, and a waveguide. The directed one-dimensional photon continuum and coherent optical control of the cavity-QED provide the means of manipulating irreversible photon-emission processes for the purpose of spin initialization and readout. The study outlines a new direction for current research on cavity QED of single solid-state systems such as quantum dots and impurities.

VI.A System configuration

The basic idea of controlling cavity QED is depicted in Fig. VI.1 which is of the same configuration as the spin-photon interface described in the previous chapter for the quantum network. A high-quality cavity coupled to a nanodot modifies the electromagnetic vacuum in the vicinity of the n-doped dot via the coupling between the whispering-gallery-modes in the cavity and the electronic transitions in the dot. A waveguide coupled to the cavity [78] acts as a quantum channel into which the cavity photon can escape rapidly to a designated destination such as a detector.

The qubit is represented by the electron spin states $|\pm\rangle$ split by a static magnetic field in the x direction. The operations are mediated by the two degenerate trion states $|T\mp\rangle$ with the hole spin in $\mp x$ direction respectively (see chapter II). Thus an X- or Y-polarized tipping pulse will flip $|\pm\rangle$ to $|T\mp\rangle$ or $|T\pm\rangle$, respectively (see the discussion of optical selection rules in II.B.2). The trion states are, by design, off-resonant from the cavity modes to avoid cavity-induced optical decoherence during quantum operations of the spin. When the nanodot-cavity coupling is desired, the trion transitions and the cavity mode $|C\rangle$ may be driven by a laser pulse into resonance via the AC Stark effect. The active cavity mode is chosen to have X-polarization in the vicinity of the nanodot, so that when brought within resonance, the trion states $|T\pm\rangle$ and the cavity states $|\mp, C\rangle$ are coupled into two split trion-polariton states, respectively. This provides a fast decay of the trion to a spin state by emitting a photon into the quantum channel. A choice of the polarization of the tipping pulse can either (1) use the quantum channel as an entropy dump for the process of cooling the spin to the ground state, or (2) entangle the spin qubit with a photon qubit in the quantum channel, thus enabling the QND measurement of the spin qubit via photon detection.

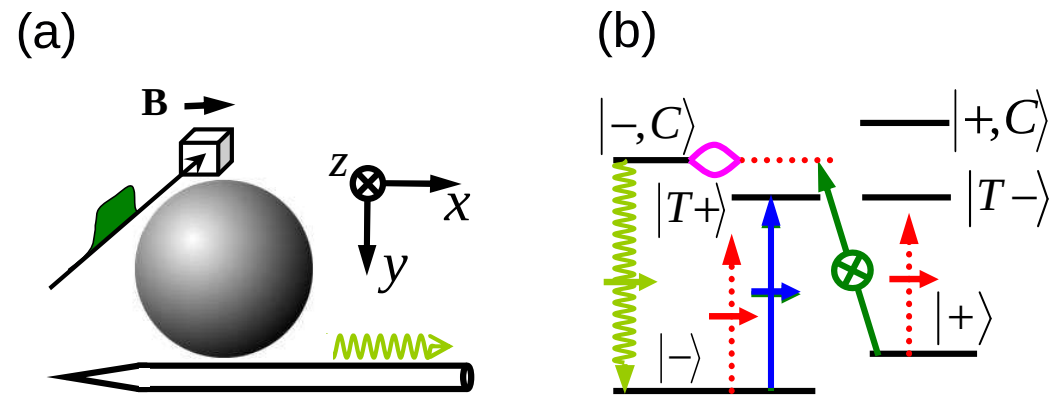

Figure VI.1 (a) Schematics of the dot-cavity-waveguide coupled structure. (b) Basic optical processes for cooling and measuring a spin state. The dotted, solid, and wavy arrows represent the AC Stark pulse, the tipping pulse, and the spontaneous emission, respectively. X and Y polarizations are indicated by horizontal arrows and circled cross, respectively.

Error sources which cause the most concern in solid-state quantum computation, specifically in optically controlled quantum-dot systems, are irreversible photon emission during qubit operations, non-resonant excitation of unwanted levels, imperfect selection rules, and system parameter uncertainty. The idea of suppressing such errors by shaping the controlling laser pulse will be demonstrated here through two examples: On-demand switch of dot-cavity coupling by AC Stark effect can avoid spontaneous emission during qubit operations, and chirped pulses can perform Rabi flops robust against parameter uncertainty.

VI.B Initialization cycle

The detailed optical processes of cooling a spin qubit are illustrated in Fig. VI.2 (a). To be general, we assume that the doped electron spin is initially in an unpolarized state, i.e., $\hat{\rho}(-\infty) = 0.5|-\rangle\langle -| + 0.5|+\rangle\langle +|$. A cooling cycle consists of four basic steps: (1) An X-polarized AC Stark pulse is adiabatically switched on, bringing the states $|T+\rangle$ and $|-,C\rangle$ into resonance; (2) A Y-polarized tipping pulse flips the spin up state $|+\rangle$ to the polariton states formed by $|T+\rangle$ and $|-,C\rangle$; (3) The polariton states relax to the spin down state $|-\rangle$ rapidly by emitting a photon into the waveguide, dumping the spin entropy to the environment; (4) The AC Stark pulse is adiabatically switched off. No photon-generation or spin-flip would take place if the initial spin state were $|-\rangle$. Thus ideally, after the cooling cycle, the spin is fully polarized with the entropy mapped into the quantum channel, and the final density matrix becomes $|-\rangle\langle -| \otimes (0.5|0\rangle\langle 0| + 0.5|1\rangle\langle 1|)$, where $|n\rangle$ is the n-photon waveguide state.

The cooling process has been simulated by numerically solving the master equation of

the dot-cavity system

$$\partial_t\hat{\rho} = -i\left[\hat{H},\hat{\rho}\right] - \frac{\gamma+\gamma'}{2}\mathcal{L}_{\hat{a}}\hat{\rho} - \frac{\Gamma}{2}\sum_{s,s'=\pm}\mathcal{L}_{|s\rangle\langle Ts'|}\hat{\rho}, \tag{VI.1}$$

$$\begin{aligned}\hat{H} &\equiv \Omega_C\hat{a}^\dagger\hat{a} \pm \frac{\omega_L}{2}|\pm\rangle\langle\pm| + \Omega_T|T\pm\rangle\langle T\pm| + g_{\rm cav}|T\pm\rangle\langle\mp|\hat{a} + \text{H.c} \\ &+ [\chi_t(t)\boldsymbol{\epsilon}_t + \chi_p(t)\boldsymbol{\epsilon}_p]\cdot\boldsymbol{\epsilon}_X\left(|T\pm\rangle\langle\mp| + r_C\hat{a}^\dagger\right) + \text{H.c} \\ &+ [\chi_t(t)\boldsymbol{\epsilon}_t + \chi_p(t)\boldsymbol{\epsilon}_p]\cdot\boldsymbol{\epsilon}_Y|T\pm\rangle\langle\pm| + \text{H.c},\end{aligned} \tag{VI.2}$$

$$\mathcal{L}_{\hat{o}}\hat{\rho} \equiv 2\hat{o}\hat{\rho}\hat{o}^\dagger - \hat{o}^\dagger\hat{o}\hat{\rho} - \hat{\rho}\hat{o}^\dagger\hat{o}, \tag{VI.3}$$

where γ is the cavity-waveguide escape rate, γ' is the cavity-free-space loss rate, Γ is the trion decay rate due to spontaneous emission into free-space, $\hat{a}$ annihilates a cavity photon, r_C is the ratio of pump strength of the cavity mode to that of the trions by control pulses, the subscripts t and p denote the tipping and AC Stark pulses, respectively. $\boldsymbol{\epsilon}_{X(Y)}$ denote the polarization along $X(Y)$ direction and $\boldsymbol{\epsilon}_{t(p)}$ are the polarization of the tipping (ac Stark) pulse. Realistic parameters have been chosen as follows: The Zeeman splitting $\omega_L = 1$ meV, $\gamma = 0.2$ meV, $\gamma' = 0.045$ μeV (corresponding to an intrinsic Q-factor $\sim 3\times10^7$), the dot-cavity coupling $g_{\rm cav} = 0.1$ meV, the cavity-trion detuning $\Omega_C - \Omega_T - \omega_L/2 = 0.5$ meV, $\Gamma = 1$ μeV, and $r_C = 0.3$.

The control of the nanodot-vacuum coupling is provided by shaping the pump and tipping pulses. The AC Stark pulse has an almost-square profile as

$$\chi_p(t) = \chi_p e^{-i\Omega_p t}\left[\text{erf}\left(\sigma_p(t-t_1)\right) - \text{erf}\left(\sigma_p(t-t_2)\right)\right],$$

(see Fig. VI.2 (b)) and is X-polarized ($\boldsymbol{\epsilon}_p = \boldsymbol{\epsilon}_X$). The spectral width ($\sigma_p = 0.354$ meV) is set much smaller than the detuning ($\Omega_T + \omega_L/2 - \Omega_p = 5.5$ meV), so that the effect due to non-adiabatic switch-on and off is negligible. For the parameters given above, the trion state $|T+\rangle$ and the cavity state $|-,C\rangle$ are brought into resonance when the pump strength ($2\chi_p$) reaches the value 1.21 meV. As the pump pulse maintains the resonant cavity-dot tunnelling which facilitates the photon escape to the quantum channel, the trion state relaxes very fast (on the time-scale of $g_{\rm cav}^{-1}$ and γ^{-1}, ~ 10 ps). A duration of the pump pulse $t_2 - t_1 = 70$ ps is found sufficient for the total dissipation of the photon. The tipping pulse ideally should be a π-pulse for Rabi-oscillation between $|+\rangle$ and $|T+\rangle$. Due to the dynamical nature of the states (dressed by the AC Stark pulse) and the rather small polariton splitting (~ 0.1 meV), a perfect π-rotation requires an extremely long pulse. The solution is to shape a chirped pulse as $\chi_t(t) = \chi_t e^{-i\phi(t)-i\Omega_t t}\text{sech}\left(\sigma_t(t-t_t)\right)$ with the phase sweeping rate $\dot{\phi}(t) = -\sigma_c\tanh\left(\sigma_t(t-t_t)\right)$ [115]. The frequency of the pulse now will sweep from σ_c above Ω_t to σ_c below. When the sweeping range $[\Omega_t - \sigma_c, \Omega_t + \sigma_c]$ covers both of the trion-polariton states, the initial spin state $|+\rangle$ will be left adiabatically in a superposition of the two polariton states, which relaxes rapidly to the target spin state $|-\rangle$. In simulation,

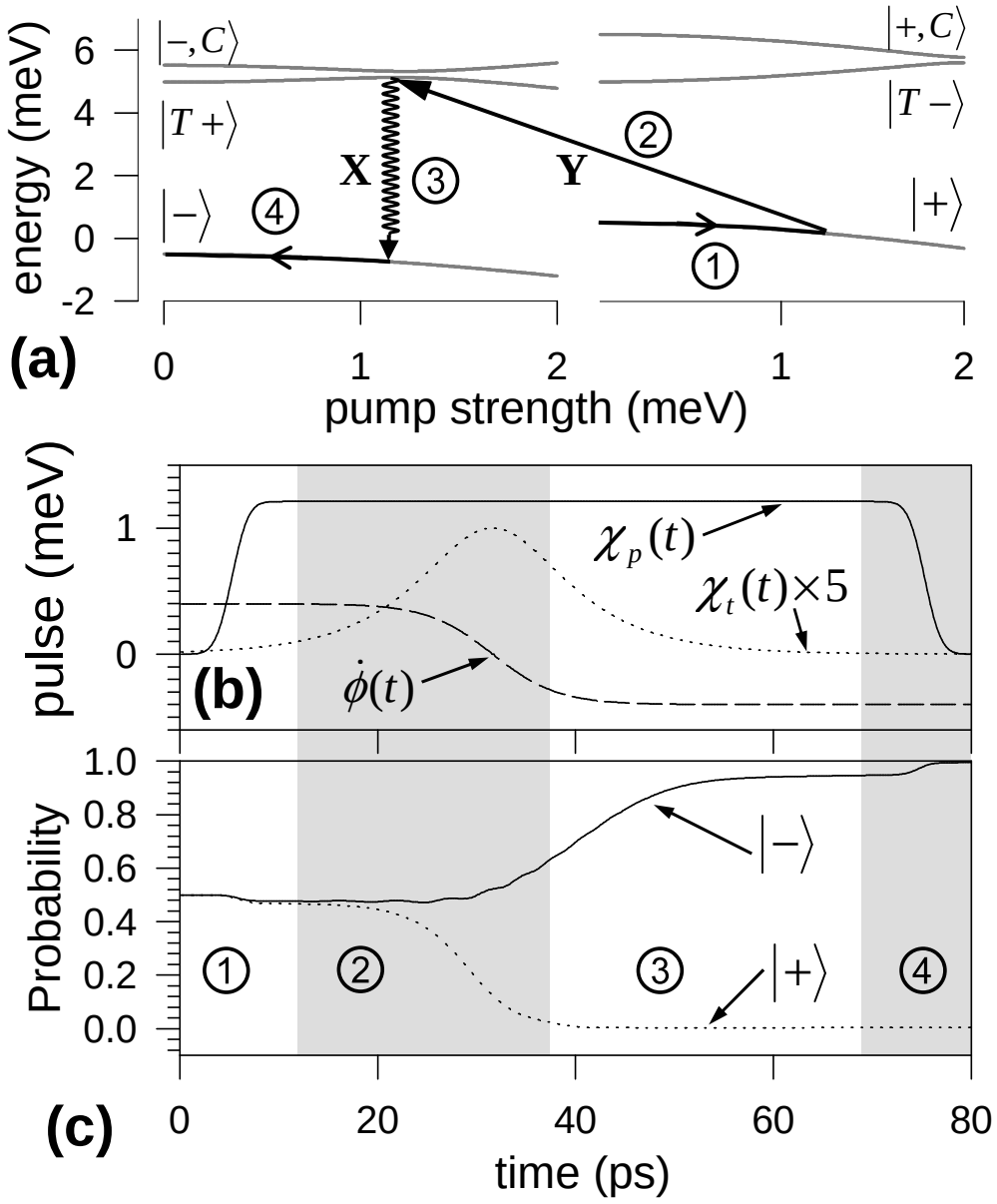

Figure VI.2 Ultrafast initialization of single electron spin in quantum dot. (a) Detailed optical process for spin initialization. The grey curves are the energies of different states versus the Rabi frequency of the AC Stark pulse, in the rotating frame. (b) The Rabi frequencies of the AC Stark pulse and the tipping pulse (amplified by a factor 5), and the sweeping frequency of the tipping pulse. (c) Probabilities of spin down and up. Different steps of the cooling cycle, indicated by ①-④, are distinguished by shadowed areas in (b) and (c).

the tipping pulse, with frequency sweeping range $\sigma_c = 0.4$ meV, strength $\chi_t = 0.2$ meV, and duration $1/\sigma_t = 6.58$ ps, flips the spin state $|+\rangle$ to the polariton states with negligible error. Such a geometrical flip is insensitive to transition frequency and strength [115], and thus can tolerate to some degree laser fluctuations and uncertainty in dipole moment, transition energy, and selection rules.

Figure VI.2 (c) shows that a single cooling cycle completed within 80 ps produces an almost 100% polarized spin from a maximally mixed state. The multi-photon cavity states were included in the numerical calculation, as they renormalize the AC Stark shift (the real excitation of multi-photon states is negligible due to the off-resonance condition). Inclusion of up to 3-photon states was found sufficient to obtain converged results. The density matrix at the end of the cycle is $\hat{\rho} = 0.9945|-\rangle\langle-| + 0.0040|+\rangle\langle+| + \hat{\rho}_{\rm err}$, where $\hat{\rho}_{\rm err}$ is the probability ($\approx$0.15%) of the system remaining in the trion states which results mainly from the non-adiabatic switching of the AC Stark pulse. The decay of the trion and the cavity modes by emitting photons into free-space constitute the main error source ($\approx 0.4\%$), as the trion state relaxes to different spin states depending on the polarization of the emitted free-space photon.

VI.C Measurement cycle

A mere switch of the polarizations of the tipping and pump pulses from (Y, X) to (X, Y), respectively, changes the "cooling" operation to a "measurement" one. The measurement cycle includes four basic steps (see Fig. VI.3 (a)): (1) An X-polarized tipping pulse flips the spin state $|+\rangle$ to the trion state $|T-\rangle$; (2) A Y-polarized AC Stark pulse adiabatically switched on drives the trion state into resonance with the cavity state $|+, C\rangle$; (3) The trion state resonantly tunnels into the cavity state and relaxes rapidly back to the spin state $|+\rangle$, leaving a photon emitted into the quantum channel; (4) The AC Stark pulse is adiabatically switched off. Suppose that the spin state to be measured is $\alpha|+\rangle + \beta|-\rangle$ and the channel is initially in the vacuum state $|0\rangle$. The measurement process will ideally transform the system into the entangled state $\alpha|+\rangle|1\rangle + \beta|-\rangle|0\rangle$, so that the detection of the photon projects the electron into a spin eigenstate, providing a QND measurement of the spin.

Note that the pulse timing for measurement is different from that for cooling (cf. Fig. VI.3 (b) and Fig. VI.2 (b)). The measurement sequence has been designed to minimize the real excitation of the multi-photon states, while the cooling sequence has been designed to minimize the emission of free-space photons by the trion states. In measurement, the Rabi flop between the spin state and the trion is well separated in frequency from the cavity mode so that chirping the pulse is unnecessary. Instead, a simple Gaussian π pulse $\chi_t(t) = \chi_t e^{-\sigma_t^2(t-t_t)^2/2 - i\Omega_t t}$

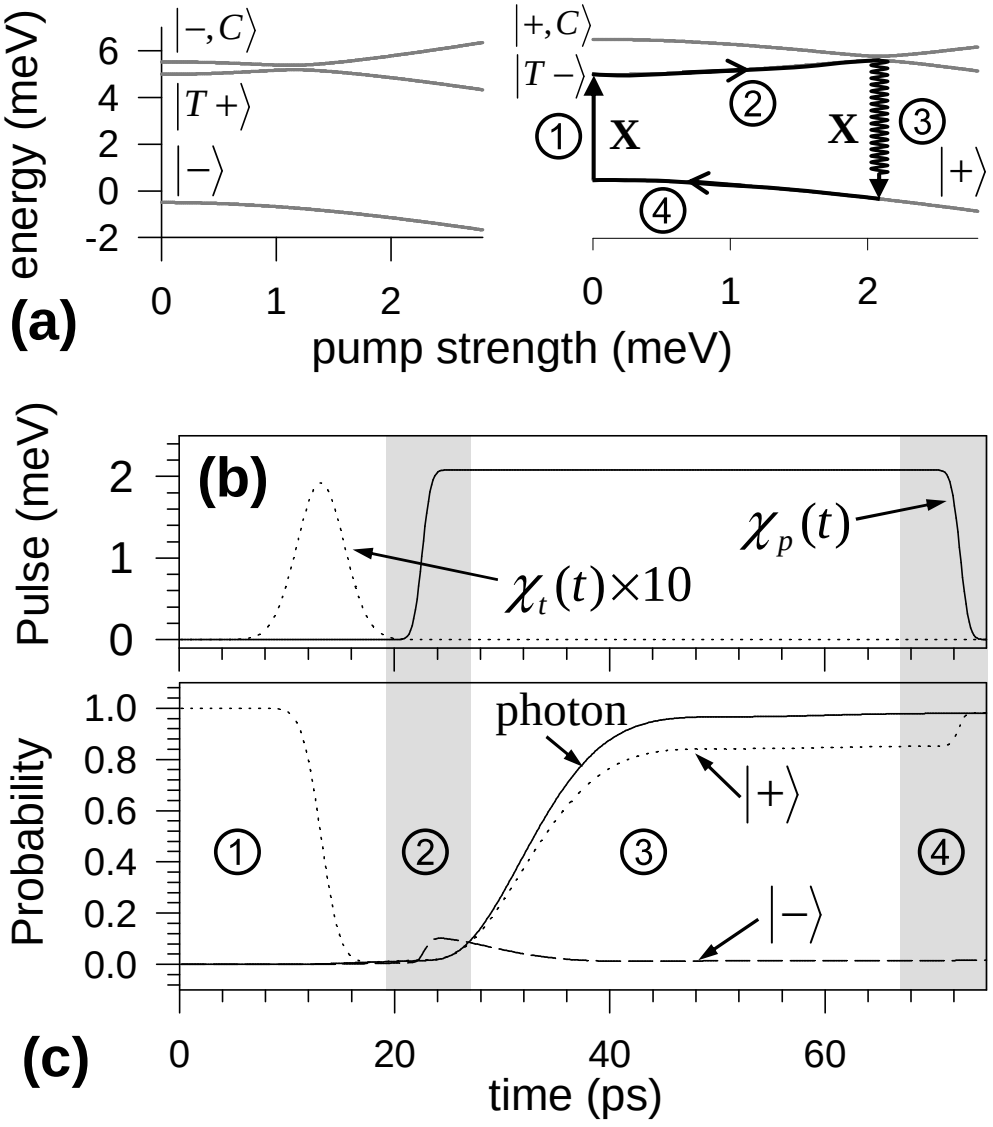

Figure VI.3 QND measurement of single electron spin in quantum dot. (a) Detailed optical process for the measurement cycle. (b) The Rabi frequencies of the AC Stark pulse and the tipping pulse (amplified by a factor 10). (c) Probabilities of spin down and up, and the number of waveguide photons, for a spin initially polarized up.

is used. The AC Stark pulse is chosen Y-polarized to avoid direct excitation of the cavity mode.

The measurement cycle has been numerically simulated for the same structure as in Fig. VI.2. The number of photons emitted into the waveguide is calculated with $\partial_t n = \gamma\langle\hat{a}^\dagger\hat{a}\rangle$. The tipping and the AC Stark pulses are set such that $1/\sigma_t = 2.19$ ps, $\chi_t = 0.192$ meV, $\Omega_t = \Omega_T - \omega_L/2$, $\sigma_p = 0.707$ meV, $2\chi_p = 2.08$ meV, $\Omega_T + \omega_L/2 - \Omega_p = 5.5$ meV, and the duration of the pump pulse $t_2 - t_1 = 50$ ps. After a single cycle of measurement, an initial state $\hat{\rho}_0 = |+\rangle\langle+|$ results in the final state $\hat{\rho}_1 = 0.0161|-\rangle\langle-| + 0.9824|+\rangle\langle+| + \hat{\rho}_{\rm err}$ with the number of photon emitted into the waveguide $n = 0.9806$ (see Fig. VI.3 (c)), while an initial state $\hat{\rho}_0 = |-\rangle\langle-|$ results in the final state $\hat{\rho}_1 = 0.9955|-\rangle\langle-| + 0.0040|+\rangle\langle+| + \hat{\rho}_{\rm err}$ with $n = 0.0015$ (not shown). The photon emitted into the waveguide can be detected with high efficiency [116, 117]. If the detector has zero dark-count rate and efficiency of 50%, the POVM (positive operator-valued measures [6]) for the measurement process can be defined as $\hat{P}_0 \equiv 0.9992|-\rangle\langle-| + 0.5097|+\rangle\langle+|$ and $\hat{P}_1 \equiv 0.0008|-\rangle\langle-| + 0.4903|+\rangle\langle+|$. Here operator $\hat{P}_1$ is associated with the outcome of a photon detection event at the detector, and $\hat{P}_0 \equiv 1 - \hat{P}_1$ is associated with non-detection of any photons. The physical meaning is transparent by noting that the probability of outcome $m = 0, 1$ is given by $p(m) = \langle\psi|\hat{P}_m|\psi\rangle$. Within a 5-cycle measurement [1], the spin state can be measured with accuracy higher than 97%, and the back-action noise to the spin is less than 10%, while the time duration is less than 0.4 ns, much shorter than the spin decoherence time.

VI.D Chapter summary

In summary, the coupling between the electromagnetic fields and the nanodot can be customized both by spatially assembling micro-resonators and quantum channels in the vicinity of the dot and by temporal design of the control optical pulses. Such a control can speed up the spontaneous decay of the excited state in the dot leading to ultrafast cooling and QND measurement of a single electron spin. As the bandwidth of the desired quantum pathway from dot to cavity to waveguide may be engineered much larger than those undesired ones, e.g., leakage into free space, the initialization and measurement cycle may be realized in a timescale under which those leakage errors are negligibly small. Therefore, the coupled system of dot-cavity-waveguide considered as a whole evolves unitarily under the pulse control. The cooling and measurement, as unitary quantum transformations, conserve the entropy or quantum information, which is essential for quantum error diagnosis and quantum feedback control. For example, in the initialization

[1] The distinct probability of the outcome $m = 1$ if $|\psi\rangle = |+\rangle$ or $|\psi\rangle = |-\rangle$ permits a simple criterion for identifying the spin states in the multi-cycle measurement, with the detection of one or more photons, we declare the electron as in 'spin-up' state, and, with non-detection of photon in all cycles, we declare the electron as in 'spin-down' state.

cycle, not only the spin is "refreshed" as desired, the original state of the spin qubit is mapped onto the photon state of the photonic channel which may be analyzed for information.

Cooling and measurement via single-shot quantum evolution should be the ultimate paradigm of controlling the interaction between macroscopic environments (or instruments) and microscopic quantum systems, which is central to nanosciences, especially in molecular electronics and quantum computation. The unitary transformation, involving the controllable 'environment' (photons in the waveguide), is significantly different from the quantum jumps proposed for spin-qubit readout [118, 119].

The specific micro-ring-waveguide structure may be replaced by equivalent waveguide-resonator systems such as microsphere-fiber structures [78] and line- and point-defects engineered in photonic crystals [61, 62, 120]. In the numerical simulations, we attempted to take care of the primary sources of errors, including the optical decoherence, unintended dynamics involving states not desired, either by stating their estimated size if not negligible or by designing the processes to limit their effect. The strong electron-cavity photon coupling assumed in the numerical simulations of the initialization and measurement operations turns to be reasonable by the new findings [70, 66]. Moreover, efficiency reduction as a consequence of lower Q values can be tolerated by recycling the operations a few times. The schemes proposed here may also be adapted to monitor and control the spin state of a single molecule [121] adsorbed on a cavity-waveguide structure.

VI.E Acknowledgements

The text of chapter VI, in part, is a reprint of the material as it appears in Ren-Bao Liu, Wang Yao, and L. J. Sham, *Coherent Control of Cavity Quantum Electrodynamics for Quantum Nondemolition Measurements and Ultrafast Cooling*, Phys. Rev. B **72**, 081306(R), © 2005 The American Physical Society, where the dissertation author was the second author. The co-authors in this publication directed, supervised, and co-worked on the research which forms the basis of this chapter.

VII

Quantum Theory of Electron Spin Decoherence by Interacting Nuclear Spins in a Quantum Dot

In the previous chapters, we have discussed quantum logic operations on the spin and photon qubits in the coupled dot-cavity-waveguide system. The efficiency of quantum operations relies critically on the coherence property of the system. While the optical relaxation due to spontaneous emission has been considered and the effect efficiently ameliorated in the design, we have not yet included the decoherence of the electron spin qubit in the quantum dot. As the operations need finite amount of time $T_{\rm op} \sim 10-100$ ps, to be able to correct the errors generated by various noises and systematic errors, the qubit coherence time has to be sufficiently long to allow the informatics approach of quantum error correction to be implemented [24, 25, 26, 27, 28, 29]. The critical quantity here is the ratio of the qubit coherence time and the operation time, $T_{\rm coh}/T_{\rm op}$. It has been shown in theory that when this quantity becomes larger than some fault-tolerant threshold value, scalable quantum computation becomes possible with quantum error correction schemes. The current threshold value for $T_{\rm coh}/T_{\rm op}$ is $\sim 10^3 - 10^4$ depending on the physical systems and the details of operations [29]. People have been working hard to seek for error correction scheme with lower fault-tolerant threshold. Meantime, theoretical and experimental efforts are being made for characterization of the various error sources, in particular, the inevitable decoherence processes in various physical systems. In addition to the informatics approach of quantum error correction, physical methods for mitigation of these decoherence are being steadily pursued.

While the quantum dot electron spin possessed the advantages of stability and scalability for quantum computation, a major concern is the spin decoherence time might be fast in the solid state systems. At low temperature and in a strong external magnetic field, which are typical experimental conditions for quantum logic controls in QD systems [45, 107], consensus holds that the coupling to lattice nuclear spins is the dominant cause for the electron spin decoherence. In this chapter, we will present a quantum theory to this nuclear induced decoherence of the electron spin, which posts the ultimate limit on quantum applications with quantum dot electrons. We demonstrate with numerical calculations performed on GaAs quantum dot.

VII.A Spin decoherence of localized electrons in semiconductors

Understanding of the decoherence properties of a localized spin in a solid state environment is of fundamental interest as well as practical significance for applications in quantum information science and nanotechnology. Example of such systems include electron spin confined in III-V quantum dot and around donor impurities in Silicon. Decoherence of the electron spin results from the contact with its environments, e.g., phonons, lattice nuclear spins, or fluctuations of external field.

We first recapitalize the concept of decoherence of a two level quantum system (i.e., spin 1/2) in contact with environment, and show how decoherence can arise out of the quantum mechanical description [122, 123, 124]. We take the initial state of the electron spin to be in a coherent superposition of the spin up and down states $|\pm\rangle$ in an external magnetic field $|\phi^s(0)\rangle = C_+|+\rangle + C_-|-\rangle$, which together with the environment state at that instant forms a single-product, or *unentangled* state, $|\Psi(0)\rangle = |\phi^s(0)\rangle \otimes |J\rangle$. The state of the coupled system of the spin plus environment evolves over time t to $|\Psi(t)\rangle = C_+(t)|+\rangle \otimes |J^+(t)\rangle + C_-(t)|-\rangle \otimes |J^-(t)\rangle$ which is *entangled*, i.e., no longer a single-product state when the environment states $|J^{\pm}(t)\rangle$ are not the same. Any physical observable of the electron spin is determined by the reduced density matrix which is obtained by tracing over the environment states $\rho^s_{\sigma,\sigma'}(t) = C^*_{\sigma'} C_\sigma \langle J^{\sigma'}(t)|J^\sigma(t)\rangle$. The diagonal element of the reduced density matrix $\rho^s_{\sigma,\sigma}$ gives the probability of finding the spin in state $|\sigma\rangle$. Either off-diagonal element is a measure of the coherence of the electron spin. The environment-driven shifting of the probability between the spin states is known as longitudinal relaxation, the timescale of which is denoted as T_1. The decay of off-diagonal element $\rho^s_{+,-}$ is known as spin decoherence. Longitudinal spin relaxation also results in the lost of spin coherence. For the purpose of technological applications, the longitudinal relaxation can be virtually suppressed by tuning the eigenenergy splitting of the spin to be much larger

than the dominant excitation energies in the environment and the system-bath coupling strength [125, 126, 127, 128, 129, 130]. Thus the key issue for quantum information processing is the so-called pure dephasing, i.e., the decoherence in absence of longitudinal relaxation. When the cause of spin flip is removed, the reduced Hamiltonian of the whole system is of the diagonal form in spin, $\hat{H} = |+\rangle\langle+| \otimes \hat{H}^+ + |-\rangle\langle-| \otimes \hat{H}^-$. The environment, depending on the spin in state $|+\rangle$ or $|-\rangle$, evolves under the Hamiltonian $\hat{H}^\pm$ into separate pathways $|J^\pm(t)\rangle \equiv e^{-i\hat{H}^\pm t}|J\rangle$ in the Hilbert Space. Pure decoherence, also known as pure transverse decoherence, is then measured by $\mathcal{L}^s_{+,-}(t) = |\langle J|e^{i\hat{H}^- t}e^{-i\hat{H}^+ t}|J\rangle|$. The timescale $\mathcal{L}^s_{+,-}(t)$ decays is referred as the single spin pure dephasing time T_2.

The physical observable of an ensemble of spins is described by the ensemble averaged reduced density matrix $\sum_i p_i \rho^i_{\sigma,\sigma'}$ where p_i is the probability of having the ith member. Ensemble spin decoherence is measured by the decay of $\sum_i p_i \rho^i_{+,-}$, the timescale of which is denoted as T_2^*. In addition to the entanglement with environment illustrated in the previous paragraph, ensemble spin dynamics is also subjected to the inhomogeneous broadening of the spin resonance energy. As a consequence, T_2^* is in general several orders shorter than T_2. $\pi/2 - \tau - \pi - \tau -$ echo spin echo sequence has been a standard techniques in NMR experiments [131, 132, 133, 134, 135] and ESR experiments [136, 137, 138] to eliminate the dephasing due to ensemble inhomogeneous broadening. Spin echo magnitude decreases with the increase of the echo delay time τ. This timescale is usually referred as the spin echo decay time T_H. It is generally believed that ensemble spin echo decay time T_H gives a measure of the single spin T_2.

While electrons localized by donor impurities in silicon have been well studied in the past decades in ESR experiments [136, 137, 138], the same experimental technique is not applicable to III-V system [1]. With the emerging potential in quantum applications, the decoherence processes of the electron spin in III-V quantum dot are being intensively studied. For GaAs and InAs quantum dot placed in strong magnetic field of $\sim 1 - 10$ T, the experimentally measured value $T_1 \sim 10^{-4} - 10^{-2}$ s [107, 127, 130] is in good agreement with the theoretical estimation of the phonon-induced longitudinal relaxation [125, 126, 139]. Theoretical studies also suggests that the pure dephasing due to phonon is well suppressed at temperature $\lesssim 1$ k [140, 141]. However, recent advances in measurements on GaAs quantum dots shows decoherence time that is much faster than the spin relaxation time. Ensemble decoherence time $T_2^* \sim 1 - 10$ ns were experimentally established either from measurement on a spatial ensemble of GaAs dots [45] or from time-ensemble measurement of single GaAs dot [11, 142, 143]. Spin echo type of measurement was also performed on the electric gate defined GaAs dot [144] which shows an echo decay time of

[1] Due to the large inhomogeneous broadening of the electron zeeman energy in the nuclear Overhauser field in III-V material, a simultaneous π-rotation for all spins in the ensemble is very difficult to implement.

$T_H \sim 1\mu$s. Both T_2^* and T_H are orders faster than the longitudinal relaxation time T_1. These are strong evidences that some mechanism other than phonon leads to this faster transeverse decoherence and the cause is believed to be the nuclear spins sitting on the lattice sites.

There has been a rich literature on the nuclear induced electron spin decoherence. The effect of direct electron-nuclear flip-flops due to the hyperfine interactions have been studied in [145, 146, 147, 148, 149, 150, 151]. While this process can dominate at low magnetic field, it is well suppressed at magnetic field of several Tesla or higher which are typically required by many current schemes of using localized electron spin for quantum information processing [9, 17, 93, 152, 153]. The electron spin decoherence under strong magnetic field was first formulated in the semiclassical framework of spectral diffusion theory [154, 155, 156, 157]. The quantum dot electron spin decoherence was interpreted as a consequence of the stochastic evolution of the nuclear Overhauser field due to the nuclear spin flip-flops driven by dipolar interaction [150, 151].

Full quantum mechanical study of the problem is stimulated by the need of decoherence characterization in quantum information science [158, 159, 160, 161]. Quantum solution to the problem can provide the basis for efficient methods to ameliorate the decoherence. In what follows, we will present a quantum theory to the electron spin transverse decoherence induced by interacting nuclear spins in quantum dot. The decoherence is explained in terms of quantum entanglement of the electron with the pair-flip excitations in the nuclear bath driven by the various nuclear-nuclear interactions. The nuclear interaction mediated by the virtual spin-flip of the electron, usually overlooked in the literature, is shown to play an important role in single electron spin free-induction decay. The spin-echo pulse not only recovers the coherence lost by inhomogeneous broadening but also eliminates the decoherence due to the electron-mediated nuclear pair-flips. Therefore, single spin T_2 time is significantly different from ensemble spin echo decay T_H, counter to the usual expectations. The observation that nuclear pair-correlation plays the dominant role in determining the electron spin coherence is in agreement with the parallel work of Witzel, deSousa and Das Sarma [158] in which the ensemble spin echo behavior was calculated for the phosphors impurities in silicon based on a quantum cluster expansion methods.

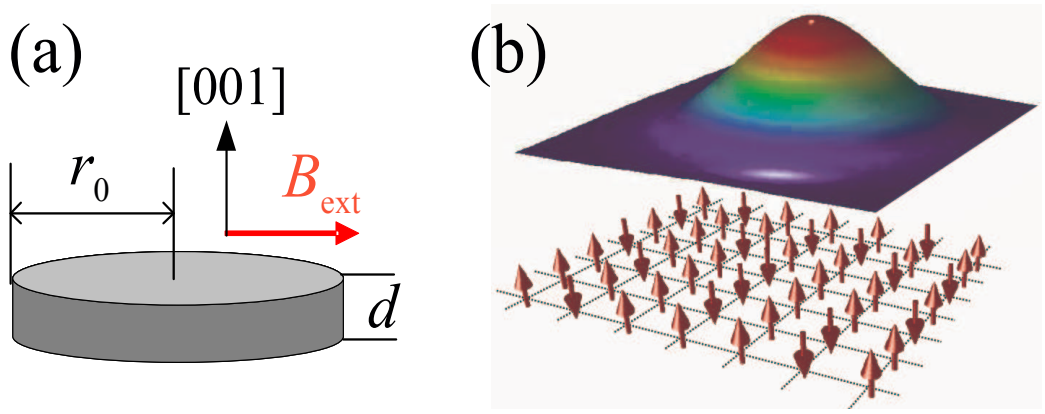

Figure VII.1 Schematic illustration of a quantum dot containing one electron and many nuclear spins. (a) A GaAs quantum dot with thickness d in growth direction [001] and lateral Fork-Darwin radius r_0, in an external magnetic field B_{ext}. (b) Illustration of an electron confined in the quantum dot containing many nuclear spins of a random configuration. The hyperfine interaction between the electron spin and the nuclear spins is determined by the electron's orbital wavefunction.

VII.B Model

VII.B.1 First-principle Hamiltonian

Mesoscopic bath of nuclear spins for the electron

The GaAs material has the Zincblende lattice structure, with Ga and As ions located in two interpenetrating face-centered cubic lattices. The natural abundance of the isotopes in GaAs materials is 100%, 60.4% and 39.6% for ^{75}As, ^{69}Ga, and ^{71}Ga, respectively. All the isotopes have non-zero nuclear spin moments $j = 3/2$. The geometry of the QD and the electron-nuclear spin system are schematically plotted in Fig. VII.1.

The electron spin has moment $S = 1/2$. The orbital motion of the electron is quantized due to the confinement of the QD and we assume the electron in the ground orbital state with the wavefunction $\Psi(\mathbf{r})$. In general, the electron wavefunction depends critically on the shape and size of the QD and on the external magnetic field. The large sizes of the QDs considered here well justifies the envelope function approximation in which the wavefunction can factorized into the band-edge Bloch wavefunction $u_c(\mathbf{r})$ and a slow-varying envelope function $f(\mathbf{r})$ as discussed in Chapter II. Without loss of generality, the fluctuation GaAs quantum dot under typical growth condition is assumed under a hard-wall confinement along the growth direction [001] and a parabolic in-pane confinement. Neglecting the field-dependence of the electron orbital states,

the envelope wavefunction of the ground state can be written as

$$f(\mathbf{r}) = \sqrt{\frac{2}{d}}\cos(\frac{\pi}{d}z)\theta\left(\frac{d}{2}-|z|\right)\frac{1}{\sqrt{\pi}r_0}\exp(-\frac{x^2+y^2}{2r_0^2}) \tag{VII.1}$$

where d is the thickness in the growth direction [001] as schematically shown in Fig. VII.1(a) and r_0 is the Fock-Darwin radius in plane.

The relevant nuclear bath for the electron spin decoherence consists of all lattice nuclei that is in direct contact with the electron [2]. For typical GaAs fluctuation dot, the total number of relevant nuclei is $N \sim 10^5 - 10^6$, of a mesoscopic size. These nuclei inside the dot also couples to the outside nuclei, e.g., through the dipole interactions, but the coupling is weak. Within timescale of interest, the electron spin decoherence solely arises from the coupled dynamics with the mesoscopic number of nuclei inside the dot. We will approach the decoherence problem by solving the coupled dynamics of one electron spin and N ($\sim 10^5 - 10^6$) nuclear spins. Such identification of the mesoscopic bath is further justified by numerical test which shows no noticeable modification of the electron spin decoherence when the bath is made larger by including nuclei out of the QD.

The total Hamiltonian of the electron and nuclear spins consists of the Zeeman energy $\hat{H}_0$ under the strong external magnetic field, the hyperfine interaction between the electron and the nuclear spins $\hat{H}_{\rm eN}$, and the nuclear-nuclear spin interaction $\hat{H}_{\rm NN}$, which are to be discussed term by term below.

Zeeman energy

Unless specified otherwise, the magnetic field is assumed to be along the [110] direction. With the magnetic field direction designated to be the z-axis, the Zeeman energy is given by

$$\hat{H}_{\rm e} = -\gamma_e^* B_{\rm ext}\hat{S}_e^z \equiv \Omega_e \hat{S}_e^z, \tag{VII.2a}$$

$$\hat{H}_{\rm N} = -\sum_{n,\alpha}\gamma_\alpha B_{\rm ext}\hat{J}_{n,\alpha}^z \equiv \sum_{n,\alpha}\omega_\alpha \hat{J}_{n,\alpha}^z, \tag{VII.2b}$$

where $\hat{\mathbf{S}}_e$ denotes electron spin operator and $\hat{\mathbf{J}}_{n,\alpha}$ denotes the operator for the nuclear spin at position n of the isotopic type α (^{75}As, ^{69}Ga, or ^{71}Ga). γ_e^* is the effective gyromagnetic ratio of the electron which is determined by the quantum dot effective Landé g-factor, $\gamma_e^* \equiv -\mu_B g^*/\hbar$. In GaAs fluctuation dot, g^* has been measured to be ~ 0.13 [45]. We note that in reality, the electron effective g-factor depends dramatically on the size, shape, element composite, and environment of the dot, and also varies with the external magnetic field. For very large dot in cases of the gate confined dot in GaAs, we may expect that the g-factor will approach its bulk

[2] These include all nuclei in the effective volume of the quantum dot, i.e., all lattice sites covered by the electron envelope wavefunction.

value of 0.44 (a value of 0.34 has been reported from preliminary experiments in the electric gate defined GaAs dot [143]). γ_α are the gyromagnetic ratios of the nuclear spins available from standard NMR handbooks. Typically, γ_α is 2 orders smaller than γ_e^*.

Hyperfine interaction

The hyperfine interaction between the electron and the nuclear spins consists of the isotropic Fermi contact interaction $\hat{H}_{\rm eN,i}$, and the anisotropic dipole-dipole interaction $\hat{H}_{\rm eN,a}$. The isotropic part can be written as

$$\hat{H}_{\rm eN,i} = \sum_{n,\alpha} a_{n,\alpha} \hat{\mathbf{S}}_e \cdot \hat{\mathbf{J}}_{n,\alpha}, \tag{VII.3a}$$

$$a_{n,\alpha} = \frac{\mu_0}{4\pi} \gamma_e \gamma_\alpha \frac{8\pi}{3} \left|\Psi\left(\mathbf{R}_{n,\alpha}\right)\right|^2, \tag{VII.3b}$$

where μ_0 is the vacuum magnetic permeability, γ_e is the electron gyromagnetic ratio (note that here the free electron g-factor $g_0 = 2.0023$ should be used, $\gamma_e \equiv -\mu_B g_0/\hbar$), and $\mathbf{R}_{n,\alpha}$ denotes the coordinates of the nth α-type ion. Thus the coefficient of the contact Fermi hyperfine interaction can be expressed as

$$a_{n,\alpha} = \frac{2\mu_0}{3} \gamma_e \gamma_\alpha d_\alpha \frac{a_0^3}{4} \left|f\left(\mathbf{R}_{n,\alpha}\right)\right|^2 \equiv A_\alpha \frac{a_0^3}{4} \left|f\left(\mathbf{R}_{n,\alpha}\right)\right|^2, \tag{VII.4}$$

where a_0 is the lattice constant, and $d_\alpha \equiv \left|u_c\left(\mathbf{R}_{n,\alpha}\right)\right|^2$ is the charge density of conduction band electron at the α-type nuclei. The electron densities at Ga and As ions is taken from Ref. [162].

There is also dipolar hyperfine interaction between the electron and nuclei spins, which has the anisotropic form as

$$\hat{H}_{\rm eN,a} = -\sum_{n,\alpha} \frac{\mu_0}{4\pi} \gamma_e \gamma_\alpha \int \left|\Psi\left(\mathbf{r}\right)\right|^2 \left\{ \frac{\hat{\mathbf{S}} \cdot \hat{\mathbf{J}}_{n,\alpha}}{\left|\mathbf{r} - \mathbf{R}_{n,\alpha}\right|^3} - \frac{3\hat{\mathbf{S}}_e \cdot \left(\mathbf{r} - \mathbf{R}_{n,\alpha}\right)\left(\mathbf{r} - \mathbf{R}_{n,\alpha}\right) \cdot \hat{\mathbf{J}}_{n,\alpha}}{\left|\mathbf{r} - \mathbf{R}_{n,\alpha}\right|^5} \right\} d\mathbf{r}. \tag{VII.5}$$

It can be shown that for s-type Bloch states and slow-varying envelope functions, the dipolar hyperfine interaction is much weaker than the contact Fermi interaction. The dipolar coupling becomes important only when the electron Bloch state is of the p-type (and thus the Fermi contact interaction vanishes). Considering the fact that the electron wavefunction is dominated by the s-orbit states for large III-V quantum dots, the dipolar hyperfine coupling will not be included at present study, while our theory can readily include its contribution where necessary.

Intrinsic nuclear spin interactions

The interaction between nuclear spins have been intensively studied in sophisticated NMR experiments and in theories. Various mechanisms have been established to account for the

width and shape of the NMR resonances, including the direct dipole-dipole interaction $\hat{H}^{d}_{\rm NN}$, the indirect pseudo-exchange interaction $\hat{H}^{\rm ex}_{\rm NN}$, the indirect pseudo-dipolar interaction $\hat{H}^{\rm ps}_{\rm NN}$, and the intra-nuclear quadrupole interaction $\hat{H}^{q}_{\rm NN}$.

The direct interaction between the nuclei is due to the dipole-dipole interaction and has the form as

$$\hat{H}^{d}_{\rm NN} = \sum_{n,\alpha<m,\beta} \frac{\mu_0}{4\pi} \frac{\gamma_\alpha \gamma_\beta}{R^3_{n\alpha;m,\beta}} \Big(\hat{\mathbf{J}}_{n,\alpha} \cdot \hat{\mathbf{J}}_{m,\beta} - \frac{3\hat{\mathbf{J}}_{n,\alpha} \cdot \mathbf{R}_{n\alpha;m,\beta} \mathbf{R}_{n\alpha;m,\beta} \cdot \hat{\mathbf{J}}_{m,\beta}}{R^2_{n\alpha;m,\beta}} \Big), \tag{VII.6}$$

with $\mathbf{R}_{n,\alpha;m,\beta} \equiv \mathbf{R}_{n,\alpha} - \mathbf{R}_{m,\beta}$.

The indirect nuclear interaction is mediated by the virtual excitation of the electron-hole pairs by the electron-nuclear hyperfine interaction [163, 164, 165, 166]. When the virtual excitation is caused by the Fermi-contact hyperfine interaction, a group-theory analysis can show that the indirect coupling has the form of isotropic exchange interaction as

$$\hat{H}^{\rm ex}_{\rm NN} = - \sum_{n,\alpha<m,\beta} B^{\rm ex}_{n,\alpha;m,\beta} \hat{\mathbf{J}}_{n,\alpha} \cdot \hat{\mathbf{J}}_{m,\beta}, \tag{VII.7}$$

which is thus named pseudo-exchange interaction in literature [163, 165]. The specific expression of the exchange coefficient $B^{\rm ex}_{n,\alpha;m,\beta}$ is determined by the band structure of the material and generally is very complicated. The leading contribution of the pseudo-exchange interaction for near neighbors, however, can be expressed as

$$B^{\rm ex}_{n,\alpha;m,\beta} = \frac{\mu_0}{4\pi} \frac{\gamma^{\rm ex}_\alpha \gamma^{\rm ex}_\beta}{R^3_{n\alpha;m,\beta}} \frac{a_0}{R_{n\alpha;m,\beta}}, \tag{VII.8}$$

where $\gamma^{\rm ex}_\alpha$ is the effective gyromagnetic ratio determined by the renormalized charge density of the s-orbit electron [165]. The experimental characterization of the pseudo-exchange interaction is still incomplete and the only available data for the GaAs material are the coupling coefficients $B^{\rm ex}_{n,\alpha;m,\beta}$ between Ga and As ions at shortest bonds, with the absolute sign undetermined. To proceed without the exact form of the exchange interaction, we will just use the formula in Eq. (VII.8) and derive the effective gyromagnetic ratios from Ref. [166].

When the virtual excitation of electron-hole pairs involves both the Fermi-contact and the dipolar hyperfine interactions, the indirect nuclear spin coupling due to the second order process has been shown by Bloembergen and Rowland to have the form of classical dipolar interaction, and is named as pseudo-dipolar coupling [164]. The pseudo-dipolar coupling can be written as

$$\hat{H}^{\rm ps}_{\rm NN} = - \sum_{n,\alpha<m,\beta} b^{\rm ps}_{n,\alpha;m,\beta} \frac{\mu_0}{4\pi} \frac{\gamma_\alpha \gamma_\beta}{R^3_{n,\alpha;m,\beta}} \Big(\hat{\mathbf{J}}_{n,\alpha} \cdot \hat{\mathbf{J}}_{m,\beta} - \frac{3\hat{\mathbf{J}}_{n,\alpha} \cdot \mathbf{R}_{n\alpha;m,\beta} \mathbf{R}_{n\alpha;m,\beta} \cdot \hat{\mathbf{J}}_{m,\beta}}{R^2_{n\alpha;m,\beta}} \Big), \tag{VII.9}$$

where $b^{\rm ps}_{n,\alpha;m,\beta}$ is a dimensionless function of the distance between the nuclei. The experimental characterization of the pseudo-dipolar coupling is, however, rather limited. Considering the

pseudo-dipolar coupling has the same form as the direct dipolar coupling and the numerical evaluations are still subjected to uncertainty in other parameters such as the indirect exchange coupling, the pseudo-dipolar interaction will not be included in our numerical calculations.

Bloembergen and Rowland have also shown that the dipolar hyperfine interaction alone can induce the indirect coupling via the virtual excitation of electron-hole pairs, which, according to the group-theory analysis, has the form as a sum of a pseudo-exchange and a pseudo-dipolar contribution, and thus can be absorbed into the indirect interactions discussed above.

Lattice distortion can also result in local electric field gradient near quantum dot, inducing intra-nuclear quadrupole interaction for nuclear spins with moment greater than 1/2. The quadrupolar interaction can be written as

$$\begin{aligned} \hat{H}^{q}_{\mathrm{NN}} &= \sum_{n,\alpha} \frac{eQ_\alpha}{2J_\alpha(2J_\alpha-1)} \hat{\mathbf{J}}_{n,\alpha} \cdot \overleftrightarrow{V}(n,\alpha) \cdot \hat{\mathbf{J}}_{n,\alpha} \\ &\equiv \sum_{n,\alpha} \sum_{i,j=x,y,z} \hat{J}^{i}_{n,\alpha} \Theta_{ij}(n,\alpha) \hat{J}^{j}_{n,\alpha}, \end{aligned} \tag{VII.10}$$

where Q_α is the quadrupole moment of the α-type nuclear spin, and $\overleftrightarrow{V}(n,\alpha)$ is the symmetric and traceless gradient tensor of the local electric field at position $\mathbf{R}_{n,\alpha}$. The quadrupole interaction contributes only to the energy cost of the nuclear spin flips. The field gradient depends critically on the specific growth condition of the QD. Since we are not aware of any reliable characterization of the quadrupole interaction in the QD systems in question, this interaction will not be included in the numerical calculation in this work.

Summary of the microscopic model

In summary, the quantum dynamics of the electron-nuclear spin system in the QD is determined by the Hamiltonian

$$\hat{H} = \hat{H}_{\mathrm{e}} + \hat{H}_{\mathrm{N}} + \hat{H}_{\mathrm{eN,i}} + \hat{H}_{\mathrm{eN,a}} + \hat{H}^{d}_{\mathrm{NN}} + \hat{H}^{\mathrm{ex}}_{\mathrm{NN}} + \hat{H}^{\mathrm{ps}}_{\mathrm{NN}} + \hat{H}^{q}_{\mathrm{NN}}. \tag{VII.11}$$

In typical III-V compound semiconductors such as InAs, GaAs, and InP, it has been demonstrated that the four different types of the nuclear spin interaction are of the same order of magnitude. While there is no difficulty to include all these interactions in the theoretical framework to be presented here, we will neglect the dipolar hyperfine interaction $\hat{H}_{\mathrm{eN,a}}$ since it is much weaker than the contact hyperfine interaction $\hat{H}_{\mathrm{eN,i}}$, and omit the pseudo-dipolar coupling and the quadrupole interaction due to the lack of characterization of these two interactions in literature. The indirect exchange interaction is assumed a simplified form, without loss of generality. These approximations in modelling the spin interactions, the simplified assumptions on the QD shape, the electron wavefunction, and the g-factor, and the inadequacy in characterization of material parameters (especially those for the nuclear spin interactions), all these limitations, while

immaterial to our theoretical formalism, will render the numerical evaluations presented here a semi-quantitative nature. The calculation, however, can be easily performed to quantitatively predict experimental results once the relevant parameters are determined.

VII.B.2 Reduced Hamiltonian in strong magnetic field

Following the discussion in VII.B.1, the first principle Hamiltonian we consider for the electron nuclear spin system is,

$$\begin{aligned}
\hat{H} &= \hat{H}_0 + \hat{H}_1 + \hat{H}_2 \qquad \text{(VII.12)}\\
\hat{H}_0 &= \hbar\Omega_e \hat{S}_e^z + \sum_{n,\alpha} \hbar\omega_\alpha \hat{J}_{n,\alpha}^z \\
\hat{H}_1 &= \sum_{n,\alpha} A_{n,\alpha} \frac{1}{2}\left(\hat{J}_{n,\alpha}^+ \hat{S}_e^- + \hat{J}_{n,\alpha}^- \hat{S}_e^+\right) \\
\hat{H}_2 &= \sum_{(n,\alpha)\neq(m,\beta)} b_{n,\alpha;m,\beta}(\hat{J}_{n,\alpha}^+ \hat{J}_{m,\beta}^- + \hat{J}_{n,\alpha}^- \hat{J}_{m,\beta}^+) - \sum_{(n,\alpha)\neq(m,\beta)} 4b_{n,\alpha;m,\beta}\hat{J}_{n,\alpha}^z \hat{J}_{m,\beta}^z \\
&\quad + \sum_{(n,\alpha)\neq(m,\beta)} d_{n,\alpha;m,\beta}(\hat{J}_{n,\alpha}^+ \hat{J}_{m,\beta}^- + \hat{J}_{n,\alpha}^- \hat{J}_{m,\beta}^+) + \sum_{(n,\alpha)\neq(m,\beta)} 2d_{n,\alpha;m,\beta}\hat{J}_{n,\alpha}^z \hat{J}_{m,\beta}^z \\
&\quad + \sum_n \bar{A}_n \hat{J}_n^z \hat{S}_e^z
\end{aligned}$$

We have grouped the full Hamiltonian $\hat{H}$ into three parts: (1) $\hat{H}_0$ with Ω_e and ω_α being the zeeman frequency of the electron spin and nuclear spin of isotope α respectively in the external magnetic field; (2) $\hat{H}_1$, which is the off diagonal part of the electron-nuclear hyperfine coupling (with coefficient $A_n \sim 0.1 - 1$MHz); (3) $\hat{H}_2$, which contains the nuclear-nuclear dipolar couplings (with coefficient $b_{n,\alpha;m,\beta} \sim 0.1$kHz), the nuclear-nuclear indirect exchange interaction (with coefficient $d_{n,\alpha;m,\beta} \sim 0.1$kHz), and the diagonal part of the electron-nuclear hyperfine coupling (with coefficient $\bar{A}_n$, and $\bar{A}_n = A_n$ if we only keep the dominant isotropic Fermi contact hyperfine part). With the effect of $\hat{H}_1$ overlooked in the literature, $\hat{H}_0 + \hat{H}_2$ is the model Hamiltonian typically used for the study of nuclear induced electron spin decoherence [150, 158]. Pair-wise nuclear spin flip-flops resulted from dipolar couplings are known to be responsible for the electron spin decoherence. In a magnetic field of several Tesla or higher, the real process of electron spin flip induced by $\hat{H}_1$ is forbidden due to the large energy cost. However, it can be problematic to simply neglect $\hat{H}_1$ since it can still affect the electron nuclear spin dynamics through higher order processes, e.g., in the form of flip-flop of nuclear spin pair (n, m) realized by two successive virtual transitions of $\hat{J}_{n,\alpha}^+ \hat{S}^-$ and $\hat{J}_{m,\beta}^- \hat{S}^+$, an effect similar to that induced by direct nuclear

dipolar coupling. Thus, it is favorable to remove $\hat{H}_1$ to first order by a canonical transform [167],

$$\begin{aligned} e^{-i\hat{s}}\hat{H}e^{i\hat{s}} &= \hat{H}_0+\hat{H}_2-\frac{1}{2}i\left[\hat{s},\hat{H}_1\right]-i[\hat{s},\hat{H}_2]- \\ &\quad \left(\frac{1}{2!}-\frac{1}{3!}\right)\left[\hat{s},\left[\hat{s},\hat{H}_1\right]\right]-\frac{1}{2!}\left[\hat{s},\left[\hat{s},\hat{H}_2\right]\right]+\cdots \end{aligned} \tag{VII.13}$$

where the Hermitian operator $\hat{s}$ is determined by the condition $\hat{H}_1=[i\hat{s},\hat{H}_0]$ and cancellation in consequence has been performed on right hand side of Eqn. (VII.13). The omitted terms are of order $\hat{s}^3$ or more. The leading correction in the expansion is of interest,

$$\begin{aligned} [i\hat{s},\hat{H}_1] &= \sum_{n\neq m}\frac{A_nA_m}{2\left(\hbar\omega_n-\Omega_e\right)}(\hat{J}_n^-\hat{J}_m^++\hat{J}_n^+\hat{J}_m^-)\hat{S}^z \\ &\quad +\sum_n\frac{A_nA_n}{\Omega_e-\omega_n}\left(\hat{J}_n^z\left(S^2-\hat{S}_z^2\right)-\left(j^2-\hat{J}_n^{z2}\right)\hat{S}^z\right) \end{aligned} \tag{VII.14}$$

The first term is the electron mediated [3] nuclear spin flip-flop and the last terms are just the stark shift to the second order of the electron and nuclear spin zeeman frequency. The next correction $[i\hat{s},\hat{H}_2]$ contains electron spin flip terms, in a similar form to $\hat{H}_1$, however with the magnitude reduced by the factor $\Gamma/\hbar\Omega_e$ (Γ being the inhomogeneous broadened linewidth of electron zeeman frequency due to the nuclear Overhauser field) which ranges from 10^{-2} to 10^{-3} for GaAs dot in a magnetic field of $1-10$ T. Since the effect must come in squared, this term in the Hamiltonian is negligible. The next term in the expansion is found $[\hat{s},[\hat{s},\hat{H}_2]]\sim\Gamma/\hbar\Omega_e[\hat{s},\hat{H}_1]$. Again, its effect on electron spin coherence is reduced by $(\Gamma/\hbar\Omega_e)^2$ as compared to $[\hat{s},\hat{H}_1]$, as it is the spectral weight of the flip-flop excitations that comes in. The rest terms in the expansion of Eqn. (VII.13) can be found to be either $[\hat{s},\hat{H}_1]$ like or $\hat{H}_1$ like but with magnitude reduced by higher powers of $\Gamma/\hbar\Omega_e$. Thus, the effect of $\hat{H}_1$ on the electron spin coherence is well incorporated in the effective Hamiltonian expressed in the rotating frame,

$$\begin{aligned} \hat{H}_{\text{eff}} &\equiv e^{i\hat{H}_0t}\left(\hat{H}_2-\frac{1}{2}i[\hat{s},\hat{H}_1]\right)e^{-i\hat{H}_0t} \\ &= \sum_{n,\alpha}\bar{A}_{n,\alpha}\hat{J}_{n,\alpha}^z\hat{S}_e^z-\sum_{(n,\alpha)\neq(m,\beta)}4b_{n,\alpha;m,\beta}\hat{J}_{n,\alpha}^z\hat{J}_{m,\beta}^z+\sum_{(n,\alpha)\neq(m,\beta)}2d_{n,\alpha;m,\beta}\hat{J}_{n,\alpha}^z\hat{J}_{m,\beta}^z \\ &\quad +\sum_{n,\alpha}\frac{A_{n,\alpha}A_{n,\alpha}}{2\hbar(\Omega_e-\omega_{n,\alpha})}\left(\hat{J}_{n,\alpha}^z/2-\left(15/4-\hat{J}_{n,\alpha}^{z2}\right)\hat{S}^z\right) \\ &\quad +\sum_{n\neq m)}b_{n,\alpha;m,\alpha}(\hat{J}_{n,\alpha}^+\hat{J}_{m,\alpha}^-+\hat{J}_{n,\alpha}^-\hat{J}_{m,\alpha}^+)+\sum_{n\neq m)}d_{n,\alpha;m,\alpha}(\hat{J}_{n,\alpha}^+\hat{J}_{m,\alpha}^-+\hat{J}_{n,\alpha}^-\hat{J}_{m,\alpha}^+) \\ &\quad +\sum_{n\neq m}\frac{A_{n,\alpha}A_{m,\alpha}}{4\hbar\left(\Omega_e-\omega_{n,\alpha}\right)}(\hat{J}_{n,\alpha}^-\hat{J}_{m,\alpha}^++\hat{J}_{n,\alpha}^+\hat{J}_{m,\alpha}^-)\hat{S}^z \end{aligned} \tag{VII.15}$$

where we have further neglected the flip-flop terms between nuclei of different isotope type due to the large difference in the gyromagnetic ratio. $\hat{H}_{\text{eff}}$ is diagonal in terms of the electron spin

[3] As the origin of this electron mediated nuclear interaction is the off-diagonal electron-nuclear hyperfine interaction, we sometimes also refer it as hyperfine mediated nuclear interaction.

operator and can be formally expressed as $\hat{H}_{\rm eff} \equiv |+\rangle\langle +|\hat{H}^+ + |-\rangle\langle -|\hat{H}^-$ where $\hat{H}^\pm$ drives the nuclear spin dynamics conditioned on the electron spin state.

The transformation e^{is} also rotates the state vector by the amount of $\Gamma/\hbar\Omega_e$ in angle. This rotation of the wavefunction is responsible for the visibility loss in the measurement of electron spin coherence, which comes in square of the rotation angle. In what follows, we will neglect this visibility loss of $\sim (\frac{\Gamma}{\hbar\Omega_e})^2$ as well.

Since the effective Hamiltonian is diagonal in the electron spin states, the evolution of the reduced electron density matrix for the electron spin and the nuclear environment starting from a separable state $\rho^{\rm e}(0) \otimes \rho^{\rm N}$ can be expressed as $\rho^{\rm e}_{\mu,\nu}(t) = \mathcal{L}_{\mu,\nu}(t)\rho^{\rm e}_{\mu,\nu}(0)$ $(\mu,\nu = \pm)$, where the correlation matrix is given by

$$\mathcal{L}_{\mu,\nu}(t) = e^{-i(\mu-\nu)\Omega_{\rm e}t/2}{\rm Tr}_N\{\rho^{\rm N}e^{i\hat{H}^\nu t}e^{-i\hat{H}^\mu t}\}. \tag{VII.16}$$

The diagonal correlation $\mathcal{L}_{\mu,\mu}(t) = 1$ since no longitudinal spin relaxation is present. The spin decoherence is governed by $\mathcal{L}_{+,-}(t)$. A natural basis set for the nuclear bath is the product states $|J\rangle \equiv \bigotimes_n |j_n\rangle$ which are eigenstates of all the spin components along the magnetic field [145]. As the temperature that can be practically reached ranges from ~ 10 mk to $\sim$ K which is high temperature for nuclear spins, the nuclear bath is of high entropy. Two scenarios for the initial state of the nuclear bath will be considered here. First, the decoherence due to the quantum fluctuation from a pure nuclear state $|J\rangle$ of the typical configuration could be of ultimate interest for quantum application [145]. The typical nuclear bath state $|J\rangle$ will be of a random configuration. This ensure a sufficiently large number of decoherence channels in the bath for the quantum evolution to be a real irreversible dynamics (the period of a Poincáre cycle virtually goes to infinity). The electron spin decoherence due to the quantum fluctuation from the pure bath state $|J\rangle$ corresponds to the single spin T_2 time. Second, we shall also consider the effect of the thermal fluctuation in an ensemble of bath states. This corresponds to the ensemble experiments capable by current technologies, performed either on a spatial dot ensemble or with repeated measurements on single dot. Ensemble spin echo decay time T_H will be discussed under this second scenario. Under both scenarios, we may approach formally with the initial density matrix of the nuclear bath $\rho^N = \sum'_J p'_J|J'\rangle\langle J'|$, with $p'_J = \delta_{J,J'}$ for the first case and p'_J being nearly identical for all J' in the second case. $\mathcal{L}_{\mu,\nu}(t)$ then becomes,

$$\mathcal{L}_{\mu,\nu}(t) = \sum_J p_J e^{-i\phi_J(t)} \left|\langle J^-(t)|J^+(t)\rangle\right| \tag{VII.17}$$

where $|J^\pm(t)\rangle \equiv e^{-i\hat{H}^\pm t}|J\rangle$. In the above expression, we have separated, in the contribution from each ensemble member J, the amplitude $|\langle J^-(t)|J^+(t)\rangle|$ and the phase factor $e^{-i\phi_J(t)}$. The phase factor turns out to be a trivial one which is due to the free evolution of the electron spin

in the external magnetic field plus a nuclear Overhauser field, $E_J = \sum_n j_n a_n$, related to the initial configuration $|J\rangle$. And $\phi_J(t) = (\Omega_e + E_J)t$ for free induction decay. Different nuclear configurations will correspond to vary different $E_J = \sum_n j_n a_n$. The inhomogeneous broadening of the electron spin zeeman frequency in the local Overhauser field (i.e., the hyperfine energy E_J) will dominate the FID in ensemble dynamics as $\sum_J p_J e^{-i\phi_J(t)} = e^{-i\Omega_e t-(t/T_2^*)^2}$, with the dephasing time $T_2^* \sim \sqrt{N}\left(\sum_n a_n\right)^{-1} \sim 10$ ns [11, 45]. In case of spin echo, the electron is flipped at time τ so $\phi_J(t) = (\Omega_e + E_J)\left[\tau_1 - (t-\tau_1)\right]$. If the spin coherence is observed at time 2τ, $\phi_J(2\tau) = 0$ and we then have,

$$\mathcal{L}_{\mu,\nu}(2\tau) = \sum_J p_J \left|\langle J^-(2\tau)|J^+(2\tau)\rangle\right| \tag{VII.18}$$

Therefore, the nontrivial part is to solve for $|\langle J^-(t)|J^+(t)\rangle|$ for all possible nuclear configurations, which determines electron spin decoherence behavior when inhomogeneous broadening is not present, i.e., either in case of ensemble spin echo or the single spin dynamics . As we will establish in the rest of this chapter, this magnitude, within relevant timescale of interest, is determined by the spectrum of excitations (in the form of nuclear pair-wise flip-flops) that is associated with the initial configuration $|J\rangle$. By the central limit theorem, for a quantum dot with N nuclear spins, the excitation spectrum is identical up to a relative error $\sim 1/\sqrt{N}$ for almost all possible state $|J\rangle$ in the ensemble. As number of nuclei is large, $N \sim 10^6$, the difference is negligibly small. Thus the correlation function can be factorized into a pure state dynamics part associated with the typical nuclear configuration $|J\rangle$, which is of a random configuration, and an ensemble factor as

$$\mathcal{L}_{+,-}(t) = \mathcal{L}^{\rm s}_{+,-}(t) \times \mathcal{L}^{(0)}_{+,-}(t), \tag{VII.19a}$$

$$\mathcal{L}^{\rm s}_{+,-}(t) \equiv \left|\langle J^-(t)|J^+(t)\rangle\right|, \tag{VII.19b}$$

$$\mathcal{L}^{(0)}_{+,-}(t) \equiv \sum_J P_J^{-i\phi_J(t)}, \tag{VII.19c}$$

$$\phi_J(t) = E_J\left[\tau_1 - (\tau_2-\tau_1) + \cdots + (-1)^n(t-\tau_n)\right] \tag{VII.19d}$$

Above, we have assumed a general scenario where electron spin is flipped at time τ_1, τ_2, ..., and τ_n respectively.

VII.C Theory

VII.C.1 Pseudo-spin model

The solution to the pure state evolution $|J^\pm(t)\rangle \equiv e^{-i\hat{H}^\pm t}$ relies on the pair-correlation approximation as explained below. From Eqn. (VII.15), the nuclear Hamiltonian $\hat{H}^\pm$, conditioned

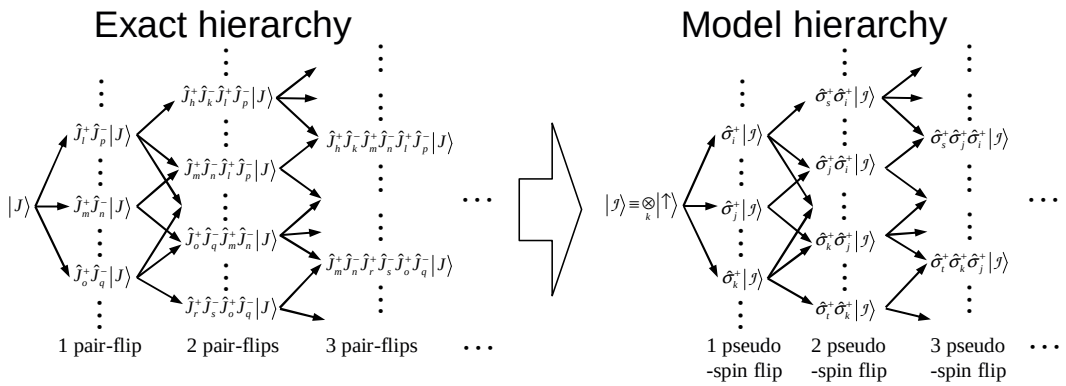

Figure VII.2 Hierarchy of the nuclear spin dynamics.

on the electron spin states $|\pm\rangle$, can be grouped into four terms $\hat{H}^{\pm} = \pm\hat{H}_A + \hat{H}_B + \hat{H}_D \pm \hat{H}_E$

$$\hat{H}_A = {\sum_{n\neq m}}' \frac{a_n a_m}{4\Omega} \hat{J}_n^+ \hat{J}_m^- \equiv {\sum_{n\neq m}}' A_{n,m} \hat{J}_n^+ \hat{J}_m^-, \tag{VII.20a}$$

$$\hat{H}_B = {\sum_{n\neq m}}' B_{n,m} \hat{J}_n^+ \hat{J}_m^- \tag{VII.20b}$$

$$\hat{H}_D = \sum_{n<m} D_{n,m} \hat{J}_n^z \hat{J}_m^z \tag{VII.20c}$$

$$\hat{H}_E = \sum_n (a_n/2)\, \hat{J}_n^z \equiv \sum_n E_n \hat{J}_n^z, \tag{VII.20d}$$

where the summation with a prime runs over only the homo-nuclear pairs, the subscript A denotes the hyperfine mediated nuclear-nuclear interaction, B the off-diagonal part of the direct nuclear-nuclear interaction, D the diagonal part of the direct nuclear-nuclear interaction, and E the diagonal part of the contact electron-nuclear hyperfine interaction. The hyperfine energy, determined by the electron orbital wavefunction, has a typical energy scale $E_n \sim a_n \sim \frac{\mathcal{A}}{N} \sim 10^6\ \mathrm{s}^{-1}$ for a dot with about 10^6 nuclei [162], where $\mathcal{A}$ is the hyperfine constant depending only on the element type. The direct nuclear-nuclear interaction, which is "short-ranged" (referred here as decaying no slower than dipolar), has the near-neighbor coupling $B_{n,m} \sim D_{n,m} \sim b \sim 10^2\ \mathrm{s}^{-1}$. The hyperfine mediated interaction, which couples any two nuclear spins that are in contact with the electron and is associated with opposite signs for opposite electron spin states, has an energy scale dependent on the field strength, $A_{n,m} \sim \frac{\mathcal{A}^2}{N^2\Omega}$1–10 s^{-1} for field $\sim$ 40–1 T. This hyperfine mediate interaction is differentiated from the "short-range" direct nuclear-nuclear interaction by the qualifier "infinite-range". We work in the interaction picture defined by $\hat{H}_e$ and $\hat{H}_N$ in which the dynamics are determined by $\hat{H}^{\pm}$.

We take the basis set of the bath as eigenstates of $\hat{H}_N = \sum_{n,\alpha} \hbar\omega_n \hat{J}_n^z$: $\bigotimes_n |j_n\rangle$. In Eqn. (VII.20), $\hat{H}_D$ and $\hat{H}_E$ are diagonal in this basis. The off-diagonal terms $\hat{H}_A$, $\hat{H}_B$ are weak perturbations that will excite the bath initially on an arbitrary configuration $|J\rangle \equiv |j_1\rangle \cdots |j_N\rangle$.

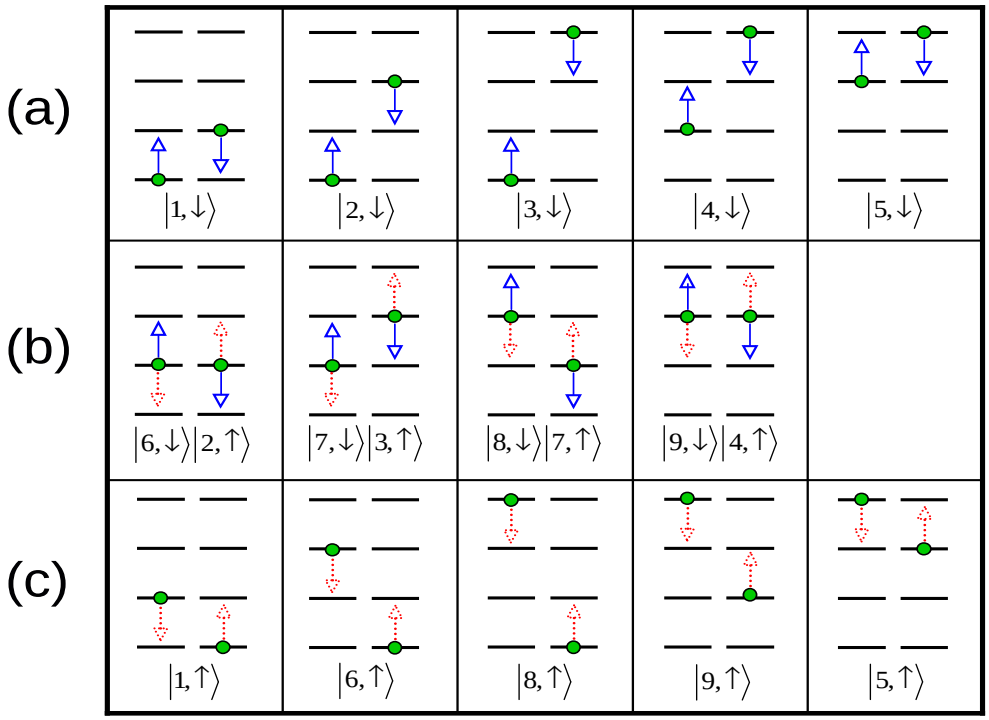

Figure VII.3 Illustration of mapping from pair states to pseudo-spin states for nuclei of spin 3/2. The green dots show state $|j_m\rangle|j_n\rangle$. The state vector show the mapped state $|k,\sigma\rangle$. The blue solid arrows between lines show to which state the operator $\hat{J}_m^+\hat{J}_n^-$ would lead and the red dotted arrows show to which state $\hat{J}_m^-\hat{J}_n^+$ would lead. (a)Monogamy states with pseudo-spin down. (b)Bigamy states which are mapped to two pseudo-spins with one up and one down respectively. (c) Monogamy states with pseudo-spins up.

The elementary excitations in the nuclear spin bath are pair-flip excitations created by operators $\hat{J}_m^+\hat{J}_n^-$ in the reduced Hamiltonian. Starting from any initial nuclear configuration, the evolution of the nuclear spin states by these elementary excitations is of the hierarchy as shown in the left side of Fig. VII.2. We can regard the zeroth layer of this hierarchy, the initial state, as the 'vacuum' of the pair-flip excitations and layer n corresponds to n pair-flip excitations have been created. The state at time t is a linear superposition of all possibilities:

$$|J(t)\rangle = C_J(t)|J\rangle + \sum_{m,n} C_{m,n}(t)\hat{J}_m^+\hat{J}_n^-|J\rangle + \sum_{l,p,m,n} C_{l,p,m,n}(t)\hat{J}_l^+\hat{J}_p^-\hat{J}_m^+\hat{J}_n^-|J\rangle + \cdots . \quad \text{(VII.21)}$$

where the summation over the indexes $m,n,l,p,\ \ldots$ are defined such that $|J\rangle$, $\hat{J}_m^+\hat{J}_n^-|J\rangle$, $\hat{J}_l^+\hat{J}_p^-\hat{J}_m^+\hat{J}_n^-|J\rangle$, $\ldots$ denote different eigenstates of $\hat{H}_N$ orthogonal to each other.

We solve this dynamics in the nuclear spin bath based on a pseudo-spin model as described below. We have on sites labelled $n = 1,\ldots,N$ the nuclear spin states $|j_n\rangle$ with $-j \le j_n \le j$ for nuclei of spin j. As the elementary excitations are pair dynamics driven by $\hat{J}_m^+\hat{J}_n^-$, we first sort out the pair states $|j_n\rangle|j_m\rangle$. These pair states are divided into three

categories:

1. *Down States*: A down state $|j_n\rangle|j_m\rangle$ has a partner $|j_n+1\rangle|j_m-1\rangle$ created by

$$\hat{J}_n^+\hat{J}_m^-|j_n\rangle|j_m\rangle = \sqrt{(j+j_n+1)(j-j_n)}\sqrt{(j-j_m+1)(j+j_m)}|j_n+1\rangle|j_m-1\rangle$$

A down state must have $(j_n < j, j_m > -j)$. There are $(2j)^2$ down states for each bond.

2. *Up States*: An up state $|j_n\rangle|j_m\rangle$ has a partner $|j_n-1\rangle|j_m+1\rangle$ created by $\hat{J}_n^-\hat{J}_m^+|j_n\rangle|j_m\rangle$. The up state must have $(j_n > -j, j_m < j)$. There are $(2j)^2$ up states for each bond.

3. *Single States*: A single pair state has no partners connected by $\hat{J}_n^-\hat{J}_m^+|j_n\rangle|j_m\rangle$ or its Hermitian conjugate, i.e., $j_n = j_m = j$ or $j_n = j_m = -j$.

The single states may be mapped to pseudo-spin 0 states. Since they are scalar states, their Hamiltonian terms will commute with every other operators, they can only contribute to the phase factor in the electron spin coherence through the Overhauser field, causing inhomogeneous broadening.

We shall find by an explicit construction that the up and down states can be paired to provide states of $(2j)^2$ spin 1/2 - the pseudo-spin states. These states are divided into:

1. *Monogamy States*: Each state belongs to only one pseudo-spin although its partner may be a bigamist. These states are edge states in that at least one of the two spin quantum numbers (j_n or j_m) equal to $\pm j$ but they cannot both be equal to j or to $-j$. Half of them ($4j-1$ states) are down states, $|j_n = -j\rangle|j_m > -j\rangle$ or $|j_n < j\rangle|j_m = j\rangle$, see Fig. VII.3(a). The other $4j-1$ states, $|j_n > -j\rangle|j_m = -j\rangle$ or $|j_n = j\rangle|j_m < j\rangle$, see Fig. VII.3(c).

2. *Bigamy States*: Each belongs to two different pseudo-spins. They are interior states: $-j < j_n < j$ and $-j < j_m < j$. There are $(2j-1)^2$ of them, see Fig. VII.3(b).

The mapping to pseudo-spins is carried out by labelling the set of down monogamy and bigamy states, $p(j_n, j_m) = 1, \ldots, (2j)^2$. Note that p depends only on the spin quantum numbers. The state mapping for the down states is,

$$|j_n\rangle|j_m\rangle \rightarrow |p(j_n, j_m)\downarrow\rangle.$$

Next, we match from each $|j_n\rangle|j_m\rangle$ of the above set, the partner state $|j_n+1\rangle|j_m-1\rangle$, which will be a member of either the up monogamy or the bigamy set. Thus,

$$|j_n+1\rangle|j_m-1\rangle \rightarrow |p(j_n, j_m)\uparrow\rangle.$$

These two steps are illustrated for $j = 3/2$ in Fig. VII.3. Notice that by the above mapping to the pseudo-spins, each bigamy state has been mapped to the product of an up state of one pseudo-spin and a down state of another,

$$|j_n\rangle|j_m\rangle \rightarrow |p(j_n, j_m)\uparrow\rangle \otimes |p'(j_n, j_m)\downarrow\rangle.$$

as shown in Fig. VII.3(b)

For any initial configuration $|J\rangle$, the relevant set of pseudo-spins $\mathcal{G}_J$ is determined by examining every possible nuclear spin pair (m,n). Each pair will contribute 0, 1 or 2 pseudo-spins if $|j_m\rangle|j_n\rangle$ is in the single state, Monogamy state or Bigamy state configuration (see Fig. VII.3). The many nuclear spin initial state $|J\rangle$ is then mapped to,

$$|J\rangle \equiv |j_1\rangle \cdots |j_N\rangle \Rightarrow |\mathcal{J}\rangle \equiv \bigotimes_{k\in\mathcal{G}_J} |k\sigma\rangle \tag{VII.22}$$

where k labels both the nuclear pair (m,n) and the pseudo-spin type $p(j_n,j_m)$. $\sigma =\uparrow$ or $\downarrow$ depending on whether k is mapped from up or down Monogamy or Bigamy state. Different initial nuclear configurations will result in different sets of pseudo-spins. For a randomly chosen initial configuration $|J\rangle$, the number of pseudo-spins is given by $M \sim (\frac{2j}{2j+1})^2 ZN$ where N is the total number of nuclear spins and Z the number of neighboring nuclei coupled to a particular nuclear spin by the nuclear-nuclear interaction. For short ranged direct interaction, $Z \sim O(10)$ and for the infinite-ranged hyperfine mediated interaction $Z = N$. The factor $(\frac{2j}{2j+1})^2$ arises as the single state, Monogamy state and Bigamy state are contributing 0, 1 and 2 pseudo-spins respectively. For convenience, when the set $\mathcal{G}_J$ is determined from the $|J\rangle$, we redefine the pseudo-spin up and down states, i.e. $|k,\sigma\rangle \rightarrow |k,-\sigma\rangle$, for those pseudo-spins in set $\mathcal{G}_J$ so that the initial state $|\mathcal{J}\rangle$ in this new definition corresponds to all pseudo-spins pointing 'up': $\bigotimes_k |\uparrow\rangle_k$. The redefinition is conditioned on the initial nuclear configuration $|J\rangle$.

The original Hamiltonian $\hat{H}^{\pm}$ is mapped to the pseudo-spin Hamiltonian of the from,

$$\hat{H}^{\pm}_{sp} = \sum_k \hat{\mathcal{H}}^{\pm}_k \equiv \sum_k \mathbf{h}^{\pm}_{k,\alpha} \cdot \hat{\boldsymbol{\sigma}}_k/2 \tag{VII.23}$$

The effective magnetic field $\mathbf{h}^{\pm}_k$ on the pseudo-spins, conditioned on the electron spin state, are to be determined by reproducing the matrix elements, $\langle J|\hat{J}^+_m\hat{J}^-_n\hat{H}^{\pm}\hat{J}^+_n\hat{J}^-_m|J\rangle - \langle J|\hat{H}^{\pm}|J\rangle$ and $\langle J|\hat{H}^{\pm}\hat{J}^+_n\hat{J}^-_m|J\rangle$, namely the energy cost and transition amplitude for nuclear pair-flips.

The pseudo-spin model for characterizing the nuclear spin bath dynamics is to approximate the exact evolution of Eqn. (VII.21) by the independent evolution of all pseudo-spins in $\mathcal{G}_J$,

$$|\mathcal{J}(t)\rangle = \bigotimes_{k\in\mathcal{G}_J} |\psi^{\pm}_k(t)\rangle = C_{\mathcal{J}}(t)|\mathcal{J}\rangle + \sum_{k_1} C_{k_1}(t)\hat{\sigma}^+_{k_1}|\mathcal{J}\rangle + \sum_{k_1,k_2} C_{k_1,k_2}(t)\hat{\sigma}^+_{k_1}\hat{\sigma}^+_{k_2}|\mathcal{J}\rangle + \cdots . \tag{VII.24}$$

This pseudo-spin dynamics can be put into a similar hierarchy as shown in the right part of Fig. VII.2 which we will refer to as model hierarchy in contrast to the exact hierarchy.

With the mapping established for the state and the Hamiltonian, the first two layers of the exact hierarchy will be reproduced exactly by the model hierarchy, i.e., there is a one to one

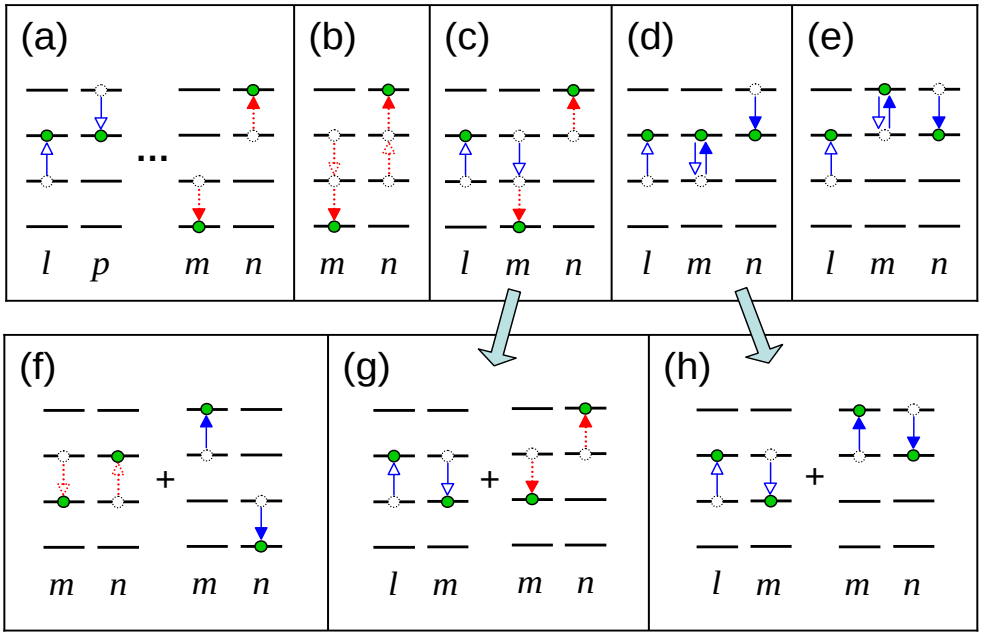

Figure VII.4 Illustration of multi pair-flip excitations in the nuclear bath. We use hollow arrowheads to indicate the first pair-flip and solid arrowheads to indicate the second pair-flip. Red dotted arrows denote the pseudo-spin flip from 'down' state to 'up' state and blue solid arrows for the inverse process (see text). (a) Independent pair flips; (b-e) Various situations of overlapping pair-flips; (f-h) Approximations in the independent pseudo-spin model.

correspondence between $\hat{J}_m^+\hat{J}_n^-|J\rangle$ and $\hat{\sigma}_k^+|\mathcal{J}\rangle$ with the energy and coupling to the initial state $|J\rangle$ ($|\mathcal{J}\rangle$) exactly reproduced.

Error arises when more than one excitations have been created in the system. In Fig. VII.4, we illustrate with the case when two pair-flip excitations have been created. If the two pair-flips do not overlap as shown in Fig. VII.4(a), their dynamics are then independent of each other and well described by the pseudo-spin model. Fig.VII.4(b-e) illustrate the various situations that the two pair-flips overlap, by sharing one or two nuclei. The flip-flop of the first nuclear pair (l, m) changes the spin configuration of both nuclear l and m and if a second flip-flop is to take place on pair (l, m) or (n, m) or (l, n), it is no longer described by the dynamics of the original pseudo-spins assigned to it. Instead, in the model hierarchy by the independent pseudo-spin model, two successive flip-flops on pair (l, m) or two successive flip-flops on pair (l, m) and (m, n) respectively are shown in Fig.VII.4(f-h). Fig. VII.4(g) can be considered as the approximate form of Fig. VII.4(c) and Fig. VII.4(h) as that of Fig. VII.4(d). The model hierarchy contains events like Fig. VII.4(f) which is absent in the exact hierarchy and events like Fig. VII.4(e) in the exact hierarchy is not contained in the model hierarchy. Therefore, on layer 2, the model hierarchy coincides with the exact hierarchy in events described by Fig. VII.4(a)

and differ by replacing the events of Fig.VII.4(b-e) with events of Fig.VII.4(f-h). The difference in a general layer can be analyzed in the same way.

By the pseudo-spin model, we are using Eqn. (VII.24) as the bath state for calculating physical properties instead of Eqn. (VII.21) at time t. The ratio of the states that differ in the exact and model hierarchies is estimated below which serves as an upper bound for error estimation (notice that the physical properties of interest are not necessarily changed by replacing events of Fig.VII.4(b-e) with events of Fig.VII.4(f-h), therefore, this error-estimation is not necessarily a tight bound). If $n-1$ pair-flip excitations have already been generated, to create the next excitation, we have M pseudo-spin to choose from and $\sim 2(n-1)Z$ of them overlap with the previous excitations. Therefore, the probability of having a new excitation without overlapping with the previous excitations is given by: $\sim \frac{M-2(n-1)Z}{M}$. By induction, the probability of creating n non-overlapping pair-flip excitations is then given by,

$$\begin{aligned} p(n) &\simeq 1 \times \frac{M-2Z}{M} \cdots \times \frac{M-2(n-1)Z}{M} \\ &\simeq \exp\left[-\frac{2Z}{M} - \cdots - \frac{2(n-1)Z}{M}\right] \\ &= \exp\left[-\frac{n(n-1)}{N}(\frac{2j+1}{2j})^2\right] \end{aligned} \tag{VII.25}$$

The second $\simeq$ holds if $2nZ \ll M$ which is always true in the timescale relevant in our study.

Comparing the model hierarchy and the exact hierarchy, we find from the above analysis that they differ in layer n with the relative amount of $1-p(n)$. This difference is negligible in the timescale relevant for our interest and therefore, the pair-correlation approximation and hence the pseudo spin model provides an excellent approximation to the exact dynamics. A detailed estimation of the error bound will be presented in section VII.E of this chapter.

VII.C.2 Single spin free induction decay and ensemble spin echo

Within the pair correlation approximation, and using the tool of the pseudo spin model, we can calculate the single spin free induction decay as well as the ensemble spin echo profile.

Given a randomly chosen initial configuration of the nuclear spin bath, the pseudo spin Hamiltonian of Eqn. (VII.23) maybe determined by brute forth counting. The pair-flip dynamics from the initial state $|J\rangle$ can be viewed as the independent rotation of the pseudo-spins initially along $+z$ axis under the effective pseudo-magnetic field $\mathbf{h}_k^{\pm} \equiv (\pm 2A_k + 2B_k, 0, D_k \pm E_k)$, where, for the electron spin state $|\pm\rangle$, $\pm A_k$ and B_k are the pair-flip transition amplitudes contributed by the hyperfine mediated coupling $\hat{H}_A$ and the intrinsic coupling $\hat{H}_B$, respectively, and D_k and $\pm E_k$ are the energy cost of the pair-flip contributed by the diagonal nuclear coupling $\hat{H}_D$ and

the hyperfine interaction $\hat{H}_E$, respectively. $\mathcal{L}^s_{+,-}(t)$ can be factorized as

$$\mathcal{L}^s_{+,-}(t) = \prod_k \left| \langle \uparrow | e^{i\mathcal{H}_k^- t} e^{-i\mathcal{H}_k^+ t} | \uparrow \rangle \right|, \tag{VII.26}$$

where $\mathcal{H}_k^{\pm}$ is the pseudo-spin Hamiltonian if the electron spin is in state $|\pm\rangle$. Here it is convenient to introduce the quantity

$$\delta_k^2 \equiv 1 - \left| \langle \uparrow | e^{i\mathcal{H}_k^- t} e^{-i\mathcal{H}_k^+ t} | \uparrow \rangle \right|^2 \tag{VII.27}$$

and we will see in the next chapter that δ_k possesses a simple geometrical interpretation as the distance between the two pseudo-spin states $e^{-i\mathcal{H}_k^+ t}|\uparrow\rangle$ and $e^{-i\mathcal{H}_k^- t}|\uparrow\rangle$ on the Bloch sphere. As in the timescale of our interest, $t \ll A_k^{-1}, B_k^{-1}$ for all pseudo spins, we always have $\delta_k \ll 1$ and therefore,

$$\mathcal{L}^s_{+,-}(t) = \prod_k \sqrt{1-\delta_k^2} \approx \prod_k e^{-\delta_k^2/2}, \tag{VII.28}$$

A couple of justified simplifications can provide an understanding of the effects of various mechanisms on the spin decoherence. First, the energy cost by the diagonal nuclear coupling (D_k) can be neglected as it is by three orders of magnitude smaller than that by hyperfine interaction (E_k). Second, for near-neighbor pair-flips, the intrinsic nuclear interaction is much stronger than the hyperfine mediated one for the field strength under consideration. Third, for non-local pair-flips, the intrinsic interaction is negligible due to its short-range characteristic. Thus we can separate the flip-pairs into one subset, $k \in K_A$, which contains $O(N^2)$ non-local flip-pairs, driven by the effective pseudo-magnetic field $\mathbf{h}_k^{\pm} \approx (\pm 2A_k, 0, \pm E_k)$ and a second subset, $k \in K_B$, which contains $O(N)$ near-neighbor flip-pairs, driven by $\mathbf{h}_k^{\pm} \approx (2B_k, 0, \pm E_k)$. The conjugate pseudo-spins will precess along opposite directions in the non-local subset K_A, and symmetrically with respect to the y-z plane in the near-neighbor subset K_B. The decoherence can be readily grouped by the two different mechanisms as

$$\mathcal{L}^{\mathrm{s}}_{+,-} \cong \prod_{k\in K_B} e^{-\frac{t^4}{2}E_k^2 B_k^2 \mathrm{sinc}^4 \frac{h_k t}{2}} \prod_{k\in K_A} e^{-2t^2 A_k^2 \mathrm{sinc}^2(h_k t)}, \tag{VII.29}$$

where $h_k = |\mathbf{h}_k^{\pm}|$. We can see that the hyperfine-mediated and the intrinsic couplings lead to the $e^{-(t/T_{2,A})^2}$ and the $e^{-(t/T_{2,B})^4}$ behavior in time shorter than the inverse pair-flip energy cost (which corresponds to the width of the excitation spectrum),

$$T_{2,B} \approx b^{-1/2}\mathcal{A}^{-1/2}N^{1/4};\ T_{2,A} \approx \Omega_e \mathcal{A}^{-2}N \tag{VII.30}$$

where b is the typical value of near neighbor intrinsic nuclear coupling strength B_k and $\mathcal{A} \equiv \sum_n a_n$ is the hyperfine constant.

In ensemble dynamics, FID will be dominated by the inhomogeneous broadening. To single out the real decoherence time from the T_2^*, spin echo pulses can be applied to eliminate the

dephasing due to the distribution of the local nuclear Overhauser field. After a π-pulse applied at τ, the inhomogeneous broadening part of the correlation $\mathcal{L}^{(0)}_{+,-}(t) = 1$ for $t = 2\tau$. Therefore, the solution to ensemble echo decay also amounts to solving the quantum dynamics $\mathcal{L}^{s}_{+,-}(t)$ which can be obtained as well with the pseudo spin model.

Under the spin echo setup where a π flip of the electron is applied at time τ, the pseudo spin evolution is given by,

$$|\psi^{\pm}_k(t)\rangle = e^{-\frac{i}{2}\mathbf{h}^{\mp}_k\cdot\hat{\boldsymbol{\sigma}}_k(t-\tau)}e^{-\frac{i}{2}\mathbf{h}^{\pm}_k\cdot\hat{\boldsymbol{\sigma}}_k\tau}|\uparrow\rangle. \tag{VII.31}$$

and therefore the electron spin coherence at 2τ is,

$$\mathcal{L}^{s}_{+,-}(2\tau) = \prod_k \left|\langle\uparrow|e^{i\mathcal{H}^{-}_k\tau}e^{i\mathcal{H}^{+}_k\tau}e^{-i\mathcal{H}^{-}_k\tau}e^{-i\mathcal{H}^{+}_k\tau}|\uparrow\rangle\right|, \tag{VII.32}$$

We now show that the echo pulse will also modify the electron spin decoherence induced by the quantum pair-flip dynamics. As the electron spin is reversed by the π-pulse, the hyperfine-mediated transition amplitude A_k and the hyperfine energy cost E_k for each pair-flip will change the sign after the pulse. Thus, the pseudo-spins driven by the hyperfine-mediated coupling (in subset K_A) will reverse their precession after the pulse and return to the origin at $t = 2\tau$, disentangling the electron spin and the pseudo-spins. So the decoherence driven by hyperfine-mediated coupling is largely eliminated in the spin-echo configuration (see Fig. VII.6). For the pseudo-spin driven by the intrinsic coupling (subset K_B), the conjugate pseudo-spins will switch their precession axis which also reverse the entanglement to some extent but no full recover can be obtained at the echo time. Finally, the electron spin coherence at the echo time can be derived as

$$\mathcal{L}_{+,-}(2\tau) \cong \prod_{k\in K_B} e^{-2\tau^4 E_k^2 B_k^2 \mathrm{sinc}^4\left(h^B_k\tau/2\right)}. \tag{VII.33}$$

Similar to the analysis for single system FID, the spin echo signal begins with $e^{-(2\tau/T_{\mathrm{H}})^4}$ short-time behavior and could crossover towards the Markovian-type exponential decay at long-time limit. There is a simple relation between the short time decoherence times $T_{\mathrm{H}} = \sqrt{2}T_{2,B}$, showing that the decoherence due to the intrinsic nuclear interaction is only partially suppressed in spin echo setup.

VII.D Numerical results

In this section, we present some calculation results for GaAs fluctuation dot.

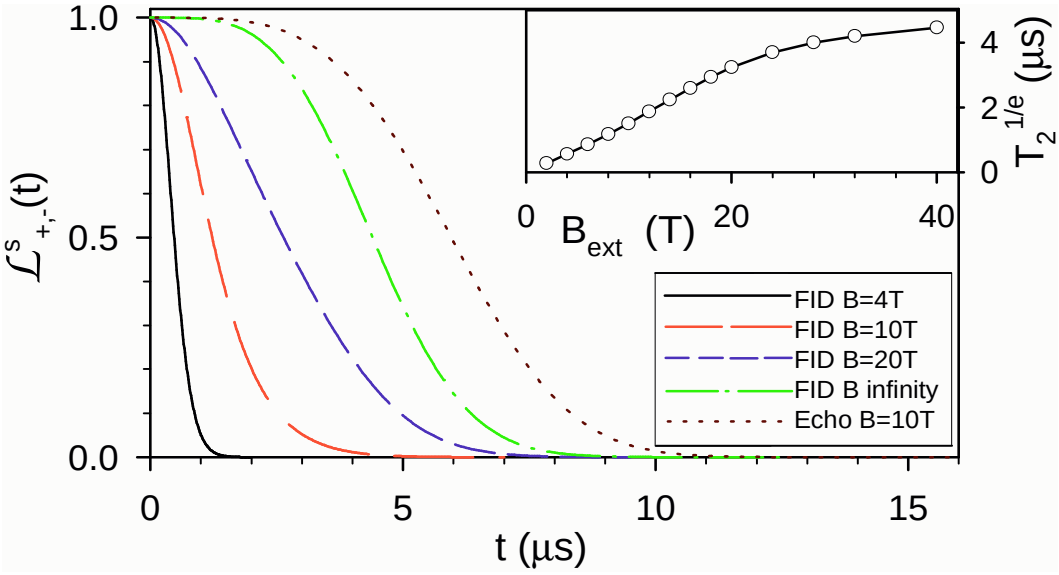

Figure VII.5 Single electron spin FID for a dot with $d = 2.8$ nm and $r_0 = 15$ nm under various field strengths. The spin echo profile as a function of $t = 2\tau$ for $B_{\text{ext}} = 10$ T is also plotted for comparison. The insets shows the field dependence of the FID decoherence time.

VII.D.1 Single spin free induction decay

We first discuss the free induction decay of single spin where the nuclear bath begins on a pure product state of random configuration.

In numerical evaluations, we assume the external magnetic field is applied along the [110] direction. For the indirect intrinsic nuclear interaction, we consider only the exchange part [164, 163, 165]. The quantum dot effective g-factor of the electron is taken as 0.13 from the experimental data for GaAs fluctuation dot [45]. The initial state $|J\rangle$ is generated by randomly setting each nuclear spin according to a "high-temperature" Boltzmann distribution ($P_J = \text{constant}$).

Figure VII.5 shows the single spin FID for a typical dot under various field strengths B_{ext}. The inset of Fig. VII.5 shows the field dependence of decoherence time $T_2^{1/e}$ which is defined as the time when the FID signal is $1/e$ of its initial value. The first important message is the strong field dependence of $T_2^{1/e}$. This shows the significance of the hyperfine mediated nuclear coupling for single spin free induction decay. The hyperfine mediate nuclear coupling is suppressed only under an extremely strong field (~ 20 T for the dot in question).

For comparison, we also show in Fig. VII.5 the ensemble spin echo signal calculated for the same dot under a field of 10 Tesla (the brown dotted line). The second important message is that the single spin FID signals have significantly different decoherence times from the spin echo signals. This counteracts the general intuition that ensemble echo decay time T_H give a measure

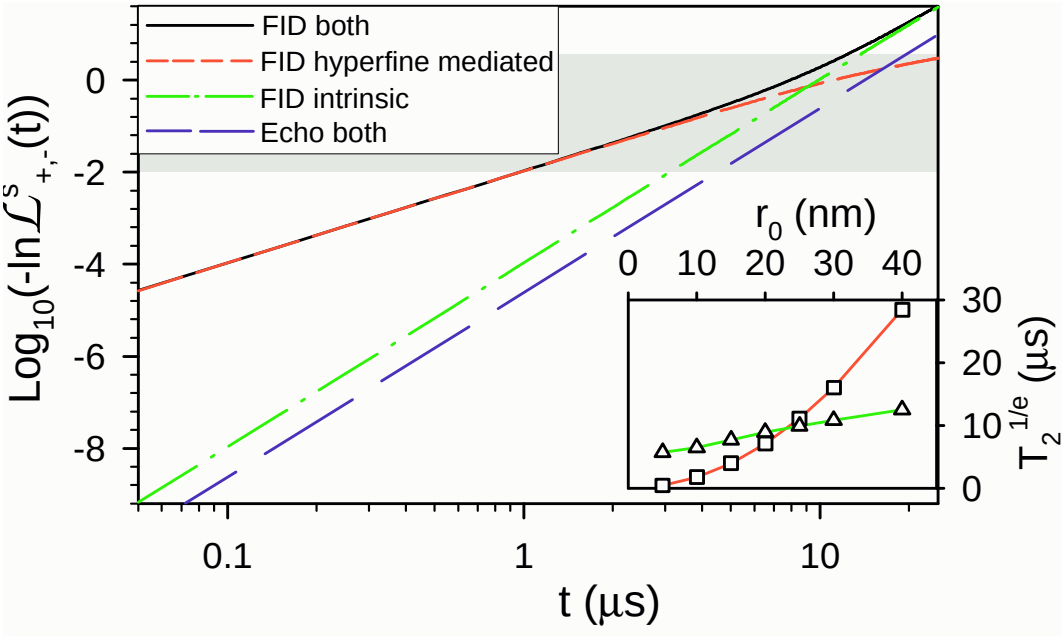

Figure VII.6 Separated contributions to the single-system FID by the hyperfine-mediated nuclear coupling, the intrinsic nuclear interaction, and both, for a dot with $d = 6.2$ nm and $r_0 = 25$ nm at $B_{\text{ext}} = 12$ T. The spin echo profile with both mechanisms is shown in comparison. The inset shows the FID decoherence times resulting from only the hyperfine-mediated interaction (square symbol) or only the intrinsic interaction (triangle symbol) as functions of r_0.

of the single spin T_2 time.

In Fig. VII.6, we looked separately at the contributions to electron spin decoherence from the hyperfine-mediated nuclear couplings and the intrinsic nuclear interactions. The results in shown in double log plot where the slope of the curve gives a direct measure of the power on the exponents. We can see the that the expected short time behavior of the $e^{-(2\tau/T_{2,\text{B}})^4}$ and $e^{-(2\tau/T_{2,\text{A}})^2}$ for the two mechanisms are indeed confirmed from this calculation. When both mechanism are comparable, the single spin FID begins with the $e^{-(2\tau/T_{2,\text{A}})^2}$ decay and may cross over to the $e^{-(2\tau/T_{2,\text{B}})^4}$ decay at longer time as shown for this quantum dot [4].

In the insets of Fig. VII.6, we also show the dot size dependence of the decoherence timescales due to the two different nuclear coupling mechanisms. We can see that for very small quantum dot, single spin FID is dominated by the hyperfine mediated nuclear coupling and for very large quantum dot, it is dominated by the intrinsic nuclear coupling. The quantum dot in the plot of main body of Fig. VII.6 actually corresponds to an intermediate size where both mechanisms are comparable and therefore, the crossover effect may be observable.

[4]The shaded area in Fig. VII.6 corresponds to the observable window in experiments, beyond which the coherence is either too close to unity to be distinguished or completely lost.

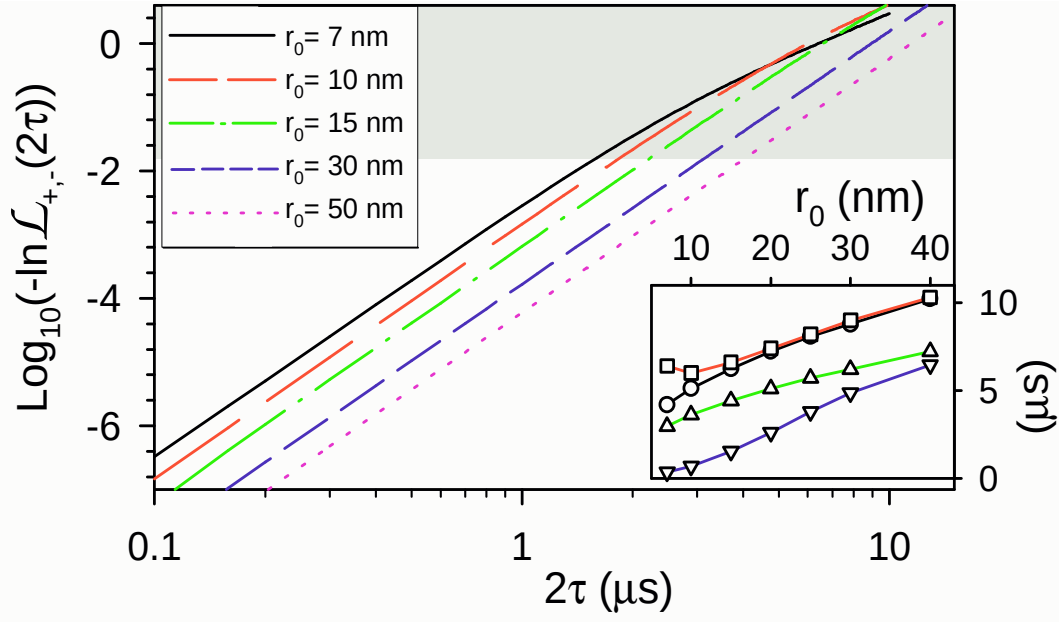

Figure VII.7 Spin echo signal for dots of $d = 2.8$ nm and various r_0 at $B_{\rm ext} = 10$T. The inset shows the size dependence of the decoherence times (see text), $T_{\rm H}$ as circles, $T_{\rm H}^{1/e}$ squares, $T_{2,B}$ triangles, $T_2^{1/e}$ inverted triangles.

VII.D.2 Ensemble spin echo decay

The ensemble spin echo profile is also calculated for quantum dot of various size Fig. VII.7. Here the dot thickness is fixed to be 3 nm and the external field in 10 Tesla. The double log plot of the spin echo profile for dot of various Fock-Darwin radius shows that the initial decay of the spin echo profile is universally described by $e^{-(2\tau/T_{\rm H})^4}$.

An interesting feature in the spin echo profile is the cross over of the decay from e^{-t^4} to lower powers on the exponent for small quantum dot (see the solid black curve in Fig. VII.7 for dot with $r_0 = 7$ nm). Such cross over behaviors can be understood by the slowly set up of the energy-conservation from the sinc function in Eqn. (VII.33). The range of the pair-excitation spectrum that is contributing to the electron spin decoherence is inverse proportional to the evolution time t due to the energy time uncertainty relation. For short time, almost all pair-excitations are contributing and electron spin sees all the non-markovian features of the environment. As the time grows beyond the inverse excitation spectrum width, the quantum kinetics becomes a stochastic Markovian process by building up the energy-conserving Fermi-Golden rule as indicated by the sinc function in Eq. (VII.33). As a consequence, the decoherence will eventually cross to exponential decay in the very long time limit. For smaller dot, the inhomogenerity of the electron wavefunction is large, so the excitation spectrum for the nuclear

spin fluctuations have a broader feature and the crossover to the Markovian regimes occurs earlier and could be observable in the proper time window. When the crossover behavior is present, two parameters are needed to characterize the spin echo profile. One is the short time parameter T_H defined in section VII.C.2. The second is the over-all decoherence time $T_H^{1/e}$ defined as the echo delay time at which the spin echo magnitude drops to 1/e of its zero delay value. If we plot the dot size dependence of these spin echo decay time, we find that the short time parameter T_H increase monotonically with the dot size, but the 1/e decay time $T_H^{1/e}$ displays a minimum due to the cross over effect. This shall be expected since $T_H^{1/e}$ is an over-all characterization of the decoherence timescale. For extremely large dot, the electron wavefunction is almost a uniform one so that the electron can not feel the fluctuation of the nuclear spin pair-flips. And for extremely small dot, very few nuclear spins are contributing to the decoherence and $T_H^{1/e}$ shall tends to infinity as the size of the dot tends to 0.

VII.D.3 Summary of results

In summary, with the pair-correlation method for the quantum dynamics of the electron-nuclear spin systems under strong magnetic field and at finite temperature, we have demonstrated the significance of the indirect nuclear coupling mediated by the virtual electron spin flips, which manifests itself in the strong field dependence of the FID in single-system dynamics. The calculated electron spin decoherence time in single-system FID varies from ~ 0.1 μs to ~ 10 μs for field strength from 1 T to 20 T, and saturates as the hyperfine mediated coupling is suppressed by stronger field. The spin-echo pulse not only recovers the coherence lost by inhomogeneous broadening but also eliminates the decoherence due to the electron-mediated nuclear pair-flips and reduces the decoherence by the intrinsic nuclear interaction, leading to an decoherence time ~ 10 μs independent of field strength in ensemble dynamics.

VII.E Error estimation

We perform a self-consistent analysis on validity of the pseudo-spin model. Here the relevant timescale plays the crucial role in determine the validity of the model. From the discussion in section VII.C.1, if only the first n layers of the hierarchy (the exact one and the model one) are involved, the error in the calculated physical properties is bounded by $1 - p(n) \ll 1$ if $n^2 \ll N$. Therefore, in the very short time limit, only the first several layers of the hierarchy can be involved and the pseudo-spin model gives an almost exact account of the dynamics. To estimate error upper bound for the longer time limit, we will calculate the number of layers involved (denoted as n) based on the model hierarchy of the pseudo-spin model. If n^2/N obtained

is small, we conclude that n also faithfully reflects the number of layers involved in the exact hierarchy. Therefore, the error estimation based on the pseudo-spin model is faithful and any physical properties calculated based on pseudo-spin model is a good approximation. Otherwise, the approximation is not self-consistent. It is established below that the condition $n^2 \ll N$ is the origin of an upper bound and a lower bound on the quantum dot size N for which our theory is able to deal with. The validity of the pair-correlation approach (pseudo-spin model) is indeed in the mesoscopic regime.

At any given time t, an average excitation number $N_{flip}(t)$ can be defined as follows based on the model hierarchy,

$$N_{flip}(t) = 1 \times \sum_{k_1} |C_{k_1}(t)|^2 + 2 \times \sum_{k_1,k_2} |C_{k_1,k_2}(t)|^2 + 3 \times \sum_{k_1,k_2,k_3} (t)\, |C_{k_1,k_2,k_3}|^2 + \cdots \qquad \text{(VII.34)}$$

and our analysis [168] shows that the layer-distribution of population in the hierarchy is of a normal distribution centered at N_{flip}, i.e. the population is distributed in layers from layer $N_{flip} - \sqrt{N_{flip}}$ to $N_{flip} + \sqrt{N_{flip}}$. Therefore, the quantity for characterizing the error upper bound is of a very simple form: $P_{err}(t) \equiv 1 - \exp(-N_{flip}^2(t)/N)$.

In the pseudo-spin model, $N_{flip}(t)$ defined in Eqn. (VII.34) has an equivalent expression which is more convenient for evaluation:

$$N_{flip}(t) = \sum_k |\langle\downarrow |U_k^{\pm}(t)| \uparrow\rangle|^2 \qquad \text{(VII.35)}$$

where $U_k^{\pm}(t) \equiv e^{-i\hat{\mathcal{H}}_k^{\pm} t}$ is the evolution operator for pseudo-spin k. The contribution can be divide into two parts:$N_{flip}\,(t) = N_{flip}^A\,(t) + N_{flip}^B\,(t)$. N_{flip}^A is the number of non-local pair-flip excitations and N_{flip}^B is the number of local pair-flip excitations that have been created. $N_{flip}^A\,(t)$ and $N_{flip}^B\,(t)$ have very different behavior and we analyze them separately. We will discuss below both the scenarios of free-induction evolution and the evolution under the control of sequences of short π-pulses applied on the electron spin. The latter scenario includes the spin echo setup and the various coherence control schemes which is the topic of the next chapter.

In free-induction evolution, the number of non-local pair-flips is given by,

$$N_{flip}^A\,(t) = \sum_k \left(\frac{2A_k}{h_k^A}\right)^2 \sin^2 \frac{h_k^A t}{2} \leq \sum_k A_k^2 t^2 \simeq \frac{\mathcal{A}^4}{N^2\Omega^2} t^2$$

where $h_k^A \equiv \sqrt{E_k^2 + 4A_k^2}$. Since the evolution of the non-local pair-correlation is completely reversed by the π pulses, the evolution of $N_{flip}^A\,(t)$ is also reversed and $N_{flip}^A = 0$ at each coherence echo time. Therefore, $N_{flip}^A\,(t)$ does not accumulate in the pulse controlled dynamics and we just need to look at the maximum value of $N_{flip}^A\,(t)$ between echoes. In all scenarios of the pulse controls discussed, in order to have the coherence well preserved or restored, the delay time τ

between echoes is limited by the order of magnitude of the single spin decoherence time induced by the intrinsic n-n coupling [159], $T_{2,B} \simeq b^{-1/2}\mathcal{A}^{-1/2}N^{1/4} \sim 10\mu s$. Therefore, N^A_{flip} at any time is bounded by $N^A_{flip}\left(\mathrm{O}(T_{2,B})\right)$ in all scenarios of our interest. A universal estimate of the bound on N imposed by N^A_{flip} for the validity of our approach is therefore possible,

$$\left(\frac{\mathcal{A}^4}{N^2\Omega^2}T^2_{2,B}\right)^2 \frac{1}{N} \sim \frac{\mathcal{A}^6}{N^4\Omega^4 b^2} \ll 1 \tag{VII.36}$$

For GaAs fluctuation dot in a 10T, the above condition is well satisfied for $N \gtrsim 10^4$.

For number of local pair-flip excitations, we have a similar expression in the free evolution,

$$N^B_{flip}(t) = \sum_k \left(\frac{2B_k}{h^B_k}\right)^2 \sin^2\frac{h^B_k t}{2} \leq \sum_k B^2_k t^2 \simeq \alpha N b^2 t^2$$

where $h^B_k \equiv \sqrt{E^2_k + 4B^2_k}$ and $\alpha \sim 10$ is determined by number of local neighbors and the nuclear spin quantum number j. In contrast to the non-local pair dynamics, the local pair dynamics is *not* reversed under the influence of the electron spin flip and $N^B_{flip}(t)$ accumulates all through the time. Nonetheless, it turns out that $N^B_{flip}(t) \leq \sum_k B^2_k t^2 \simeq \alpha N b^2 t^2$ holds for all scenarios of pulse controls being discussed. Unlike the lower bound on N set by N^A_{flip}, the condition $(N^B_{flip})^2/N \ll 1$ sets an upper bound on N: $N\alpha^2 (bt)^4 \ll 1$, which depends on the time range t we wish to explore. Alternatively speaking, $(N^B_{flip})^2/N \ll 1$ sets an upper bound on the time range t we can explore for some fixed N using the pseudo-spin model. We illustrate this bound using the following two examples.

1. If we wish to calculate the Hahn echo signal using the pseudo-spin model, we shall have $(\alpha N b^2 T^2_H)^2/N \ll 1$ where the Hahn echo decay time $T_H \approx b^{-1/2}\mathcal{A}^{-1/2}N^{1/4}$ [159]. Therefore, the upper bound on N is given by $N^2\alpha^2 b^2 \mathcal{A}^{-2} \ll 1$. For GaAs quantum dot, this condition is well satisfied for $N \lesssim 10^8$.

2. For bath of an intermediate size in the allowed region of $\min[\sqrt{N}, N^4 b^2 \Omega^4 \mathcal{A}^{-6}] \gg 1 \gg N^2 b^2 \mathcal{A}^{-2}$, e.g., a quantum dot of typical size $N \sim 10^5 - 10^6$ in our problem, $(\alpha N b^2 t^2)^2/N \ll 1$ is satisfied for a much longer time range $t \sim 10T_H \sim 100\mu s$.

As a summary of this error estimation, for the pair-correlation approximation (or pseudo-spin model) to be valid, nuclear spin dynamics of local pair-flips imposes an upper bound on N while nuclear spin dynamics of non-local pair-flips imposes a lower bound. Within this mesoscopic regime, the pair-correlation approximation is well justified. The mesoscopic regime of $10^4 \lesssim N \lesssim 10^8$ covers quantum dots of all practical size. The error estimation is based on characterizing the difference in the Hilbert space structure of the exact dynamics and that of the pseudo-spin model and assuming this difference has a full influence on the electron spin coherence calculation. Therefore, the bound is not necessarily tight and it is possible that the pulse control

methodology developed using the pseudo-spin model have actually a much larger validity regime. Investigation is underway.

VII.F Acknowledgements

The text of chapter VII, in part, is a reprint of the material as it appears in Wang Yao, Ren-Bao Liu, and L. J. Sham, *Theory of Electron Spin Decoherence by Interacting Nuclear Spins in a Quantum Dot*, arXiv preprint cond-mat/0508441, (2005), where the dissertation author was the first author. The co-authors in this preprint directed, supervised, and co-worked on the research which forms the basis of this chapter.

VIII

Coherence Control of the Electron Spin in a Nuclear Spin Bath

In the previous chapter, we have presented the quantum solution to the electron-nuclear spin dynamics in a quantum dot. The evolution of the mesoscopic nuclear bath is well described by a simple pseudo-spin model for the particle pair interaction in the bath. The electron spin decoherence is the consequence of the entanglement with the nuclear spin pair-flip excitations. This quantum picture forms the basis of a theory of coherence recovery of the electron spin by disentanglement. If at some time t, the electron spin can be disentangled from the bath, its coherence is restored. We demonstrate here how to disentangle the electron spin and the mesoscopic nuclear spin bath by maneuvering the bath evolution through simple controls of the electron spin only. This coherence protection via disentanglement is to be contrasted with the informatics approach of quantum error correction [24, 25, 26, 27, 28, 29] and with the methods of decoupling the quantum system from the environment either by limiting the quantum system to a decoherence-free subspace [169, 170, 171], or by dynamically averaging the system-bath coupling [172, 173, 174, 175, 176].

VIII.A Geometric picture for the nuclear induced electron spin decoherence

We describe first a geometric picture for the nuclear spin dynamics useful for the understanding of the decoherence behavior and the design of coherence control.

In section VII.C.2 of the chapter VII, we have discussed the various decoherence be-

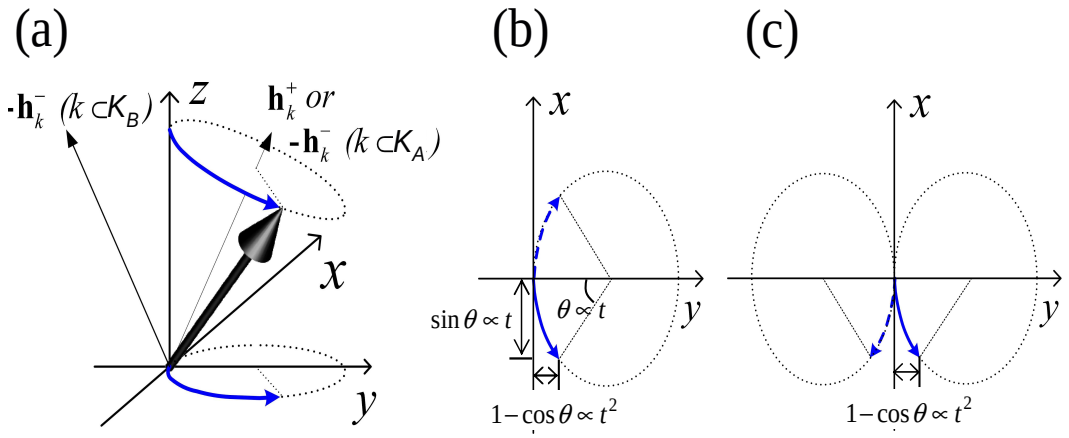

Figure VIII.1 A geometric picture for understanding the free induction decay. (a)Illustration of of the Bloch vector rotation and the projected trajectory on the x-y plane. Direction of the effective field $\mathbf{h}_k^{\pm}$ are indicated respectively for sets $\mathcal{A}$ and $\mathcal{B}$. (b) The projection of the Bloch vector trajectories to the x-y plane for pseudo-spins for non-local bath pairs. The solid (dashed) line denotes the pseudo spin evolution $|\psi_k^+(t)\rangle$ ($|\psi_k^-(t)\rangle$) conditioned on the electron spin state $|+\rangle$ ($|-\rangle$). As the rotation angle $\theta \propto t$, the distance between the conjugated vectors $\delta_k \propto t$ at short time. (c) The projection of the Bloch vector trajectories to the x-y plane for pseudo-spins for local bath pairs. The distance between the conjugated vectors $\delta_k \propto t^2$ at short time.

havior of the electron induced by the interacting nuclear spins. One pronounced feature is the universal short time behavior of $\exp(-(t/T_{2,A})^2)$ by hyperfine mediated nuclear interactions and $\exp(-(t/T_{2,B})^4)$ by direct nuclear interactions in single spin free induction decay and the $\exp(-(t/T_H)^4)$ short time behavior of ensemble spin echo decay.

Since we have mapped the pair-wise flip-flop excitations in the nuclear bath to pseudo-spins of spin 1/2, the geometric picture of Bloch sphere may be used for a pictorial understanding of these pair dynamics. The pseudo-spin states are represented by Bloch vectors, defined as $\langle\uparrow|U_k^{\pm\dagger}(t)\hat{\boldsymbol{\sigma}}_k/2U_k^{\pm}(t)|\uparrow\rangle$ depending on the electron spin state $|\pm\rangle$. The two Bloch vectors for the same pseudo spin k will be referred below as conjugation of each other. The evolution of these Bloch vectors are simply precessions about the effective magnetic field $\mathbf{h}_k^{\pm} \equiv (0, B_k \pm A_k, D_k \pm E_k)$ which is conditioned on the electron spin state. As we have discussed in VII.C.2, the dynamics of the pseudo-spins for non-local nuclear pairs is mostly determined by the dominant part of this effective field $\mathbf{h}_k^{\pm} \equiv (0, \pm 2A_k, \pm E_k)$, while the dominant part of the effective field for local nuclear pairs is $\mathbf{h}_k^{\pm} \equiv (0, 2B_k, \pm E_k)$ (see Fig. VIII.1). Under free involution, the trajectories of the two conjugated Bloch vectors for non-local bath paris are just inverse of each other as shown in Fig. VIII.1(b), while those for local bath pairs are simply mirror symmetry of each other along the pseudo x-z plane (see Fig. VIII.1(c)).

The quantity δ_k defined in Eqn. (VII.27) of the previous chapter is just the distance

between the conjugate Bloch vectors, $\delta_k^2 = 1 - |\langle\uparrow |U_k^{-\dagger}(t)U_k^{+}(t)| \uparrow\rangle|^2$, which provide a visual measure of the electron spin decoherence contributed by the kth pseudo-spin (see Eqn. (VII.28)). Based on this geometric analysis, it is straightforward to show that non-local nuclear pair dynamics contribute to the $\exp(-t^2)$ short time behavior (see Fig. VIII.1(b)) and local nuclear pair dynamics contribute to the $\exp(-t^4)$ short time behavior (see Fig. VIII.1(c)) in electron spin FID with the nuclear bath begins on a pure state $|J\rangle \equiv \bigotimes_n |j_n\rangle$.

The spin echo profile can also be understood with this geometric picture. Under the influence of the π-flip of the electron spin at $t = \tau$, the conjugate pseudo-spin Bloch vectors exchange their effective magnetic fields ($\mathbf{h}_k^+ \leftrightarrow \mathbf{h}_k^-$). For non-local bath pairs, the subsequent evolution from τ to 2τ just reverses the previous evolution from 0 to τ and, as a consequence, at the spin echo time 2τ, non-local bath pairs are not contributing to the electron spin decoherence at all. For local bath pairs, the evolution of the Bloch vectors are also affected by the electron spin flip at τ but they take different trajectories as shown in Fig. VIII.2. The two trajectories for the conjugated pseudo-spin Bloch vectors does meet some time after the electron spin flip but separate again. At the spin-echo time 2τ, their distance is of the same magnitude as in the free induction decay case, hence the spin echo decay has a similar behavior as to the free induction decay induced by the local bath pairs only and there is a universal relation between the two short time behaviors $T_H = \sqrt{2}T_{2,B}$.

VIII.B Coherence control by disentanglement in pure state dynamics

In the above analysis of spin-echo, we have seen that the flip of the electron spin can influence the evolution of the bath pairs, making possible an effective control on the nuclear spin bath dynamics. This control may lead to the restoration of the coherence of the electron spin if it can be disentangled from the bath. In this section, we consider first the scenario of pure-state dynamics where the nuclear bath begins on the pure product state $|J\rangle \equiv \bigotimes_n |j_n\rangle$ of a random configuration.

The spin-echo setup with the single π-pulse on the electron maybe considered as the prototype of such coherence control. Disentanglement of a pseudo-spin from the electron occurs when the trajectories of the two conjugated Bloch vectors meet on the Bloch sphere. For those non-local bath pairs, the dynamics are reversed under the influence of the π-pulse and are obviously disentangled from the electron spin at the spin echo time 2τ.

For local bath pairs, under the influence of the electron spin flip, the pseudo-spin can also be disentangled from the electron but at a different time. Even though different pseudo spins

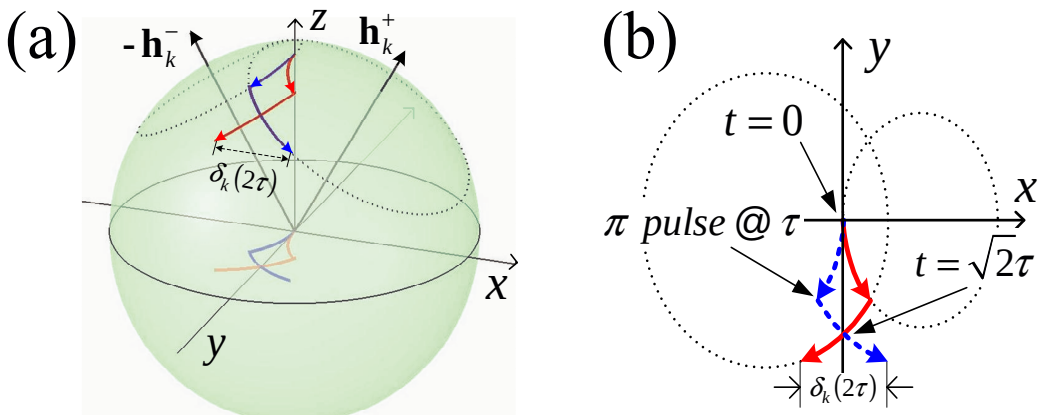

Figure VIII.2 (a) The evolution of the conjugated pseudo-spin Bloch vectors under the single-pulse control. (b) The projection of the Bloch vector trajectories to the x-y plane. Red solid (blue dashed) trajectory denotes the pseudo spin evolution $|\psi_k^+(t)\rangle$ ($|\psi_k^-(t)\rangle$).

can have very different precession frequency $h_k \equiv \sqrt{E_k^2 + 4B_k^2}$, the entanglement distance δ_k is eliminated for all pseudo spins k in the leading order of $B_k t$ at $t = \sqrt{2}\tau$ as

$$\delta_k^2 = E_k^2 B_k^2 \left(t^2 - 2\tau^2\right) + O\left(E_k^2 B_k^2 D_k^2 \tau^6\right). \tag{VIII.1}$$

Compared to the free-induction decay where $\delta_k^2 \sim E_k^2 B_k^2 t^4$ for local pair-flips (see Eqn. (VII.29)), the decoherence is reduced at the disentanglement point by a factor of $\sim D_k^2\tau^2$ ($\sim 10^{-4}$ for $\tau \sim 10\mu$s). This leads to a recovery of the electron spin coherence as is illustrated by a numerical evaluation for the electron spin in a dot of 10^6 nuclear spins which reveals the coherence revival after a π-flip of the electron spin at various τ, even when the coherence has visibly vanished (see Fig. VIII.3). In the numerical evaluation, we have chosen a large quantum dot with $d = 8.5$ nm and $r_0 = 25$ nm for which the local bath pair dynamics dominate the decoherence. For large delay times $\tau \geq T_2$, the restoration of the coherence is well pronounced at $\sqrt{2}\tau$ whereas no coherence is visible at the conventional echo time 2τ. Remarkably, even when the electron spin is flipped after the coherence has completely vanished, the coherence may be well recovered at time $\sqrt{2}\tau$.

In this pure state dynamics, the electron spin decoherence results solely from the quantum evolution induced system-bath entanglement and the coherence restoration is a consequence of the disentanglement of the electron spin and the nuclear spin bath. The disentanglement is in stark contrast to the classical phase refocus (spin echo) of an ensemble of spins with inhomogeneous broadening [131], as unambiguously evidenced by the fact that the spin echo will occur at 2τ for a π-flip applied at τ.

It should be emphasized that the dynamics of local pairs of nuclear spins is not reversed

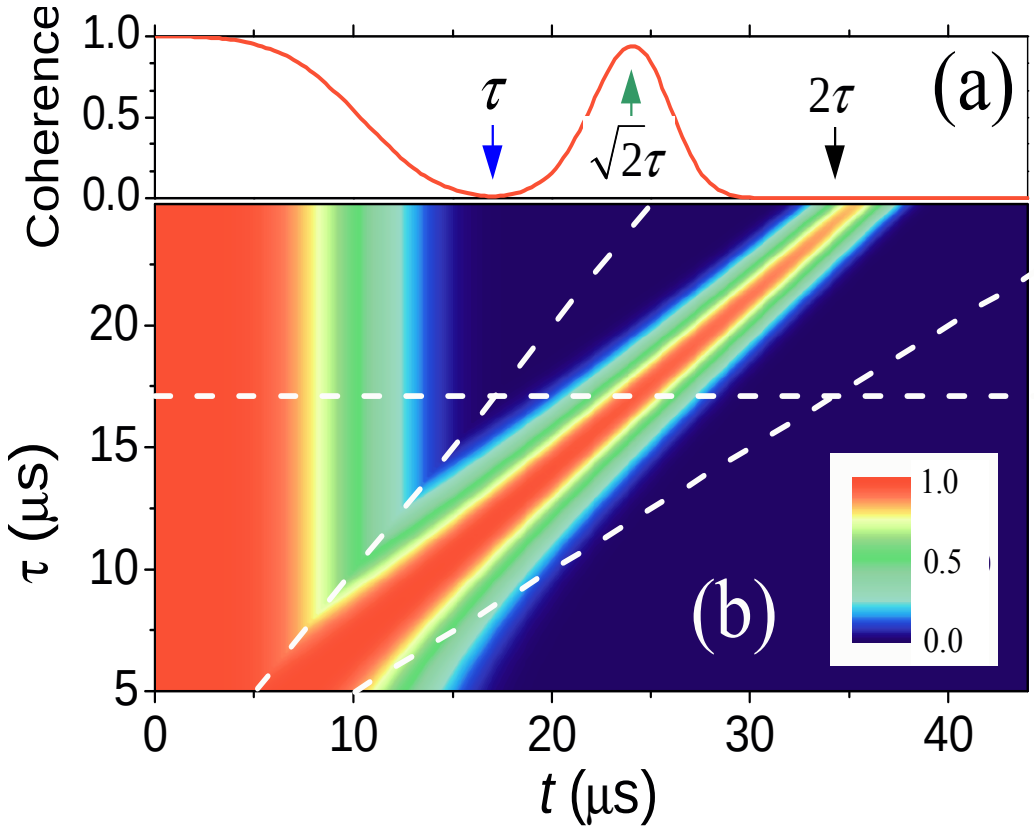

Figure VIII.3 Electron spin coherence under the single-pulse control with the nuclear bath initially on a randomly chosen unpolarized product state $|J\rangle \equiv \bigotimes_n |j_n\rangle$. (a) Electron spin coherence $\mathcal{L}^s_{+,-}$ under the control of a single flip pulse applied at $\tau = 17\mu$s. (b) The contour plot of the electron spin coherence $\mathcal{L}^s_{+,-}$ as a function of the real time t and the pulse delay time τ. The pulse time the electron spin is flipped is indicated by the left tilted dashed line. The restoration of the coherence is pronounced at $\sqrt{2}\tau$ whereas no coherence peak is visible at the conventional echo time 2τ (indicated by the right tilted dashed line). The horizontal dashed line corresponds to the cut for the curve in the top plot. The quantum dot under consideration is of the arrangement as in Fig. VII.1 of previous chapter with $d = 8.5$ nm and $r_0 = 25$ nm. $\boldsymbol{B}_{\rm ext} = 10$ T and is along the [100] direction.

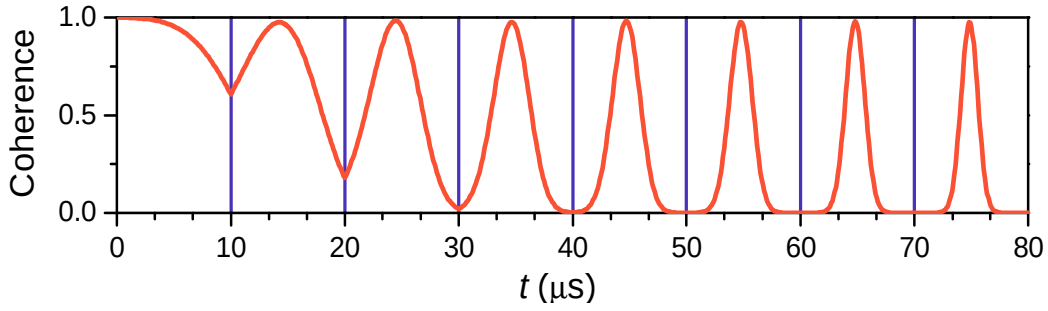

Figure VIII.4 Electron spin coherence $\mathcal{L}^s_{+,-}(t)$ with the control of a sequence of π-rotations (indicated by blue vertical lines) evenly space by $\tau = 10\mu$s. The quantum dot under consideration and the experimental conditions are the same as in Fig. VIII.3. The nuclear bath is initially on a randomly chosen unpolarized product state $|J\rangle \equiv \bigotimes_n |j_n\rangle$.

in this disentanglement process, as evidenced by the fact that the trajectory on the Bloch sphere does not return to its starting point in Fig. VIII.2.

Similar to the single-pulse control, the coherence can also be preserved by a sequence of π-rotation short pulses. It is straightforward to show that under a sequence of evenly spaced pulses with spacing time τ, the disentanglement and hence the coherence restoration will occur at $\sqrt{n(n+1)}\tau$ between the nth and the $(n+1)$th pulses. The residual decoherence, again reduced from the free-induction value by a factor $\sim D_k^2\tau^2$, is the order of $E_k^2 B_k^2 D_k^2 \tau^6$ at the disentanglement points. The coherence recovery under the control of a pulse sequence is clearly seen in the numerical evaluations presented in Fig. VIII.4.

VIII.C Coherence control in ensemble measurements with inhomogeneous broadening

The coherence restoration at the unusual time, e.g., at $\sqrt{n(n+1)}\tau$ by the control of an equally spaced pulse sequence, is observable in principle in single spin measurement with pre-determination or post-selection of bath Overhauser field through projective measurement [145], but it could be concealed by inhomogeneous broadening in ensemble measurements. In measurements performed on an ensemble of electron spins [45, 137] or the time-ensemble-averaged measurements performed on single dot electron [11, 142, 143, 144], the initial system-bath state is described by a density matrix as $(C_+|+\rangle + C_-|-\rangle)\left(C_+^*\langle +| + C_-^*\langle -|\right) \otimes \rho_N$, where the bath ensemble $\rho_N = \sum_J p_J |J\rangle\langle J|$ is in thermal equilibrium at the experimental temperature [1]. The ensemble electron spin dynamics is simply the statistical average of the pure state dynamics with

[1]The typical experiment temperature ranges from $\sim$ 10 mk to $\sim$K, low for the electron spin but appreciable for the bath nuclear spins.

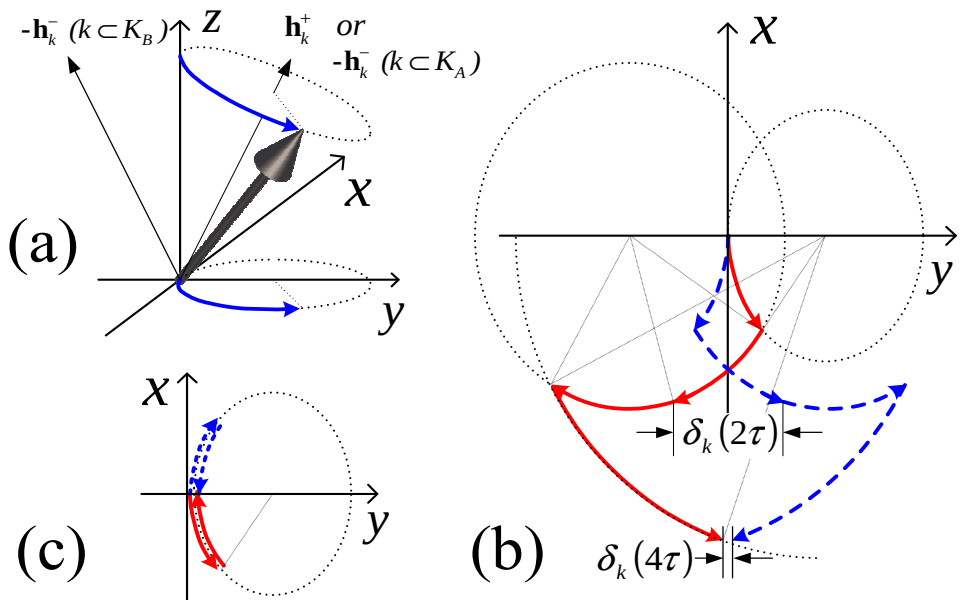

Figure VIII.5 Rotations of pseudo spin Bloch vectors under the two-pulse control. (a)Illustration of the Bloch vector rotation and the projected trajectory on the x-y plane. (b) Projected trajectory on the x-y plane for the evolution of pseudo-spin Bloch vector of local bath pairs under the influence of two π-rotations of the electron spin at time τ and 3τ respectively. (c) The same plot as (b) but for pseudo spin of non-local bath pairs. In part (b) and (c), red solid (blue dashed) trajectory denotes the pseudo spin evolution $|\psi_k^+(t)\rangle$ ($|\psi_k^-(t)\rangle$).

all possible initial nuclear bath configurations. In the pure state dynamics $C_+|+\rangle \otimes |J^+(t)\rangle + C_-|-\rangle \otimes |J^-(t)\rangle$ starting with any initial state $|J\rangle$ in the thermal ensemble, the system dynamics is affected by, in addition to the system-bath entanglement, a bath-configuration dependent local field resulting from the longitudinal electron-nuclear hyperfine coupling, i.e., the nuclear Overhauser field (see also the discussion in section VII.B.2). Denoting the electron spin splitting due to the Overhauser field as E_J, we obtain the ensemble electron spin coherence as $\rho_{+,-}(t) = C_-^* C_+ \sum_J p_J e^{-i\phi_J(t)} \mathcal{L}^s_{+,-}(t)$ where $\phi_J(t) = E_J\left[\tau_1 - (\tau_2 - \tau_1) + \cdots + (-1)^n(t-\tau_n)\right]$ under the control of a sequence of pulses applied at τ_1, τ_2, $\cdots$, and τ_n. The decoherence profile due to the quantum fluctuation (i.e., the $\mathcal{L}^s_{+,-}$ part) is insensitive, up to a factor of $1/\sqrt{N} \ll 1$, to the selection of initial bath state $|J\rangle$ [159]. This behavior is verified by numerical simulations on bath states associated with different Overhauser fields [168]. Thus, the ensemble dynamics can be factorized into a pure quantum entanglement part and a static inhomogeneous broadening part as $\rho_{+,-}(t) = C_-^* C_+ \mathcal{L}^s_{+,-}(t) \times \mathcal{L}^0_{+,-}(t)$ with the inhomogeneous dephasing $\mathcal{L}^0_{+,-}(t) \equiv \sum_J p_J e^{-i\phi_J(t)}$. In free-induction decay, $\mathcal{L}^0_{+,-}(t)$ reduces to the well-known Gaussian decay with dephasing time T_2^* [146, 147], which is usually shorter than T_2 by orders of magnitude [11, 45, 142, 143, 144]. With a sequence of flips applied on the single spin, the dephasing by inhomogeneous broadening can

be stroboscopically removed to zero at the spin-echo time t fulfilling the phase refocus condition $\tau_1 - (\tau_2 - \tau_1) + \cdots + (-1)^n(t - \tau_n) = 0$, and the width of each echo is given by T_2^*.

Since the ensemble dephasing time T_2^* ($\sim 1 - 10$ ns in GaAs dots) is much shorter than the decoherence time determined by the quantum entanglement in the single-system pure state dynamics (~ 10 μs from Fig. VIII.3), the inhomogeneous dephasing $\mathcal{L}^0_{+,-}(t)$ will virtually conceal the rich behaviors of single-system dynamics $\mathcal{L}^s_{+,-}(t)$, except for those coinciding with spin-echoes. In particular, the disentanglement at $\sqrt{n(n+1)}\tau$ under the control of n τ-spaced pulses is virtually invisible in an ensemble measurement.

To make the coherence restoration observable in these ensemble experiments, a pulse sequence can be designed to make the quantum disentanglement coincide with the spin echo. Since the disentanglement of non-local pairs always coincides with the classical phase refocus, the non-trivial job is to design a pulse sequence to disentangle the local pairs at spin-echo times. The simplest solution is a two-pulse sequence. The geometrical picture of the local pair-state evolution (see Fig. VIII.5(b)) shows that a second π-rotation pulse makes the conjugate vectors of a pseudo-spin meet again. This secondary disentanglement time in quantum evolution can indeed coincide with the secondary spin-echo time if the timing of the two flips satisfies $\tau_2/3 = \tau_1 \equiv \tau$ (see Fig. VIII.5(b)), amounting to the famous Carr-Purcell pulse sequence in NMR spectroscopies [177]. The leading contribution to the residue entanglement distance at $t = 4\tau$ under the Carr-Purcell control is

$$\delta_k^2(4\tau) \approx 16\left(E_k B_k - A_k D_k\right)^2 D_k^2 \tau^6, \tag{VIII.2}$$

in which the leading order contribution to the entanglement has been successfully eliminated. The restoration of coherence in ensemble dynamics by the two-pulse control is clearly demonstrated by numerical evaluation as shown in Fig. VIII.6. Remarkably, in ensemble experiments, the electron spin coherence can be largely recovered at 4τ by the two-pulse sequence even when the spin-echo signal at 2τ after the first pulse has completely vanished. This counteracts the intuition that the absence of spin echo means the irreversible loss of coherence. Similar phenomena have been reported in NMR experiments [178, 179].

VIII.D Concatenated design of control pulse sequence for disentanglement

Note that the pseudo-spin rotation with the Carr-Purcell control of the electron spin can be constructed recursively from the free-induction evolution as $\hat{U}_0^{\pm} = e^{-i\mathbf{h}_k^{\pm}\cdot\hat{\boldsymbol{\sigma}}_k\tau/2}$, $\hat{U}_1^{\pm} = \hat{U}_0^{\mp}\hat{U}_0^{\pm}$, and $\hat{U}_2^{\pm} = \hat{U}_1^{\mp}\hat{U}_1^{\pm}$. This observation indicates a more general pulse sequence design, i.e., the concatenated pulse sequence, which was recently developed for dynamical decoupling in quantum

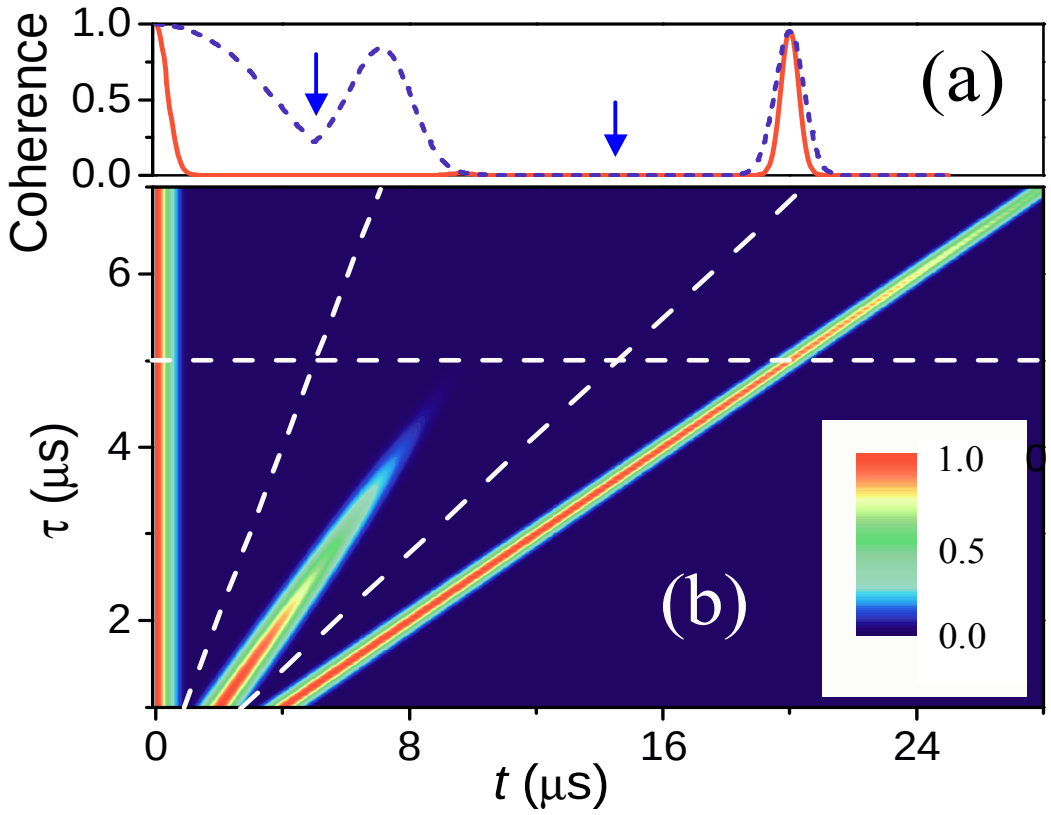

Figure VIII.6 Ensemble-averaged electron spin coherence under the two-pulse control. (a) Electron spin coherence under the control of two π-pulses applied at τ and 3τ with $\tau = 5\mu$s. The dashed blue line is the pure state dynamics part $\mathcal{L}^s_{+,-}(t)$ and the solid red line is with the inhomogeneous broadening factor included $\mathcal{L}^s_{+,-}(t) \times \mathcal{L}^0_{+,-}(t)$. The blue arrows indicate the time when the electron spin are flipped. (b) Contour plot of the ensemble-averaged electron spin coherence as a function of the real time t and the pulse delay time τ. The tilted dashed lines indicated the pulse time and horizontal dashed line corresponds to the cut for the curve in the top plot. For $\tau \geq T_2^*$, the first spin echo at 2τ becomes invisible, while the coherence restoration related to the disentanglement is well pronounced at the second spin-echo time 4τ. The quantum dot under consideration is of the arrangement as in Fig. VII.1 with $d = 2.8$ nm and $r_0 = 15$ nm. $\boldsymbol{B}_{\rm ext} = 10$ T and is along the [100] direction. The nuclear bath is initially assumed in thermal equilibrium at $T = 1$ K. In the plot, we have artificially set T_2^* in $\mathcal{L}^0_{+,-}$ to 0.5μs, about 100 times greater than its realistic value, to make the echo visible in the plot.

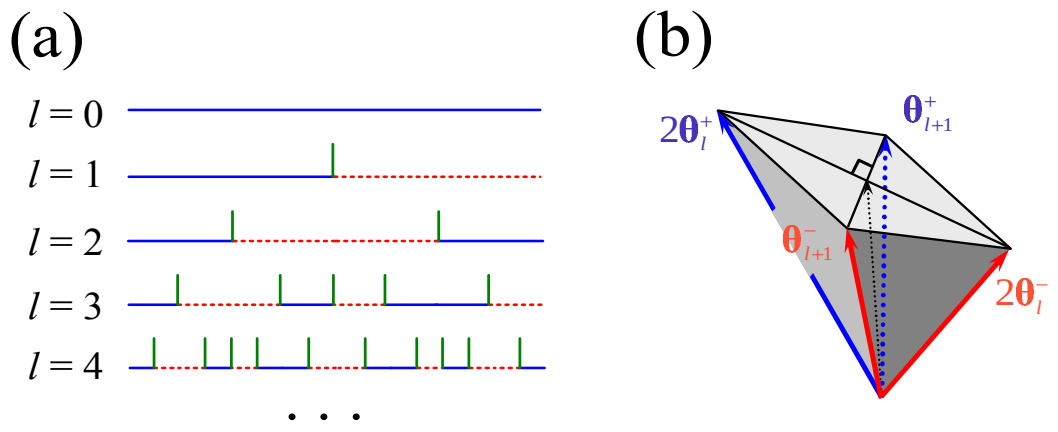

Figure VIII.7 Concatenation design of control pulse sequences. (a) Schematic illustrations of the concatenated control pulse sequences. The green spikes indicate the π-rotation pulses. Blue solid (red dashed) horizontal lines denote pseudo-spin evolution $\hat{U}_0^{\pm}$ ($\hat{U}_0^{\mp}$) respectively. The $(l+1)$the order sequence is constructed by two subsequent lth order sequences with an additional π-rotation pulse inserted only if l is even. (b) Recursive relation between the vector rotation angle $\boldsymbol{\theta}_l^{\pm}$ for a pictorial understanding of the concatenation control (see text).

computation [175]. In concatenated disentanglement, the $(l+1)$th order sequence is constructed by two subsequent lth order sequences with an additional π-rotation pulse inserted if l is even. The pseudo-spin rotation under the concatenated control can be constructed by the iteration

$$\hat{U}_l^{\pm} = \hat{U}_{l-1}^{\mp}\hat{U}_{l-1}^{\pm} \equiv e^{-i\boldsymbol{\theta}_{l-1}^{\pm}\cdot\hat{\boldsymbol{\sigma}}_k/2}. \tag{VIII.3}$$

Here we have introduced the vector rotation angle $\boldsymbol{\theta}_l^{\pm}$ for a pictorial understanding of the concatenation control. When the rotation angle $\theta_l^{\pm}$ is small, its recursion has a simple geometrical representation

$$\boldsymbol{\theta}_{l+1}^{\pm} = \boldsymbol{\theta}_l^{+} + \boldsymbol{\theta}_l^{-} \mp \boldsymbol{\theta}_l^{+} \times \boldsymbol{\theta}_l^{-}. \tag{VIII.4}$$

Thus by each level of iteration, the vector rotation angles for the conjugate pseudo-spins has the common part $\left(\boldsymbol{\theta}_l^{+} + \boldsymbol{\theta}_l^{-}\right)/2$ increased by a factor of 2 and the difference $\left(\boldsymbol{\theta}_l^{+} - \boldsymbol{\theta}_l^{-}\right)$ reduced by a factor of $\theta_l^{\pm}$ which is in the order of $2^l B_k\tau$. For $\tau \ll B_k^{-1}$, the distance δ_k under the lth order concatenation control at the spin-echo time $\tau_l \equiv 2^l\tau$ can be derived to be

$$\delta_k^2(\tau_l) \cong 4r_l^2\tau^{2l+2}2^{l(l-1)}\left(E_kB_k - A_kD_k\right)^2\left[4B_k^2\mathrm{sinc}^2\left(E_k\tau\right) + D_k^2\right]^{l-1}\mathrm{sinc}^4\frac{E_k\tau}{2}, \tag{VIII.5}$$

where $r_l^2 = 1$ for odd l and $r_l^2 = D_k^2/\left[4B_k^2\mathrm{sinc}^2\left(E_k\tau\right) + D_k^2\right]$ for even l. Thus the decoherence is reduced by an order of $\left(2^l\tau b\right)^2$ for each additional level of concatenation, until the decoherence suppression is saturated at the level $l_0 = -\log_2(b\tau)$. The decoherence profile under concatenation control is plotted in logarithm scales in Fig. VIII.8.

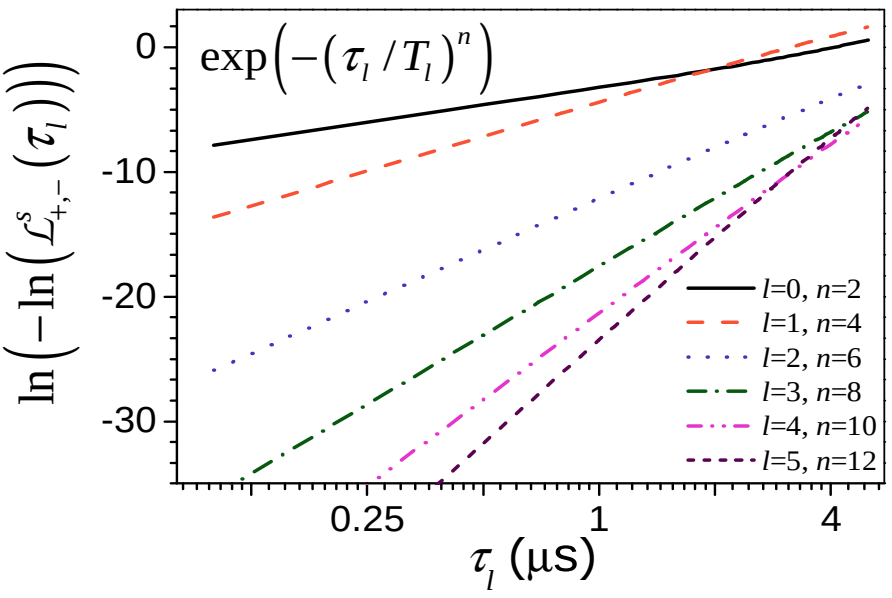

Figure VIII.8 The scaling of echo magnitude with the echo delay time $\tau_l = 2^l\tau$ by the control of concatenated pulse sequences in ensemble measurement. The quantum dot under consideration and the experimental conditions are the same as in Fig. VIII.6.

In decades of research with NMR spectroscopies, sophisticated pulse sequences have been designed to explore the coherence in complex nuclear spin systems [132, 177, 178, 180, 181]. And very recently, the concatenated pulse sequences have been proposed to protect coherence for quantum computation via dynamically decoupling the quantum system from the environment [175, 182]. In the dynamical decoupling scheme, the pulse sequences are employed to reduce the interaction Hamiltonian. Here, the disentanglement method aims directly at the mesoscopic bath dynamics. It does not seek to cancel the system-bath interaction by dynamical averaging, but instead, with the solution of bath dynamics, implements coherence control by maneuvering the bath evolution. In general, elimination of system-bath coupling is not a necessary condition for their disentanglement. For instance, at disentanglement time $\sqrt{2}\tau$ by the single pulse control, the effective system-bath interaction $\hat{S}^z \otimes \hat{H}_{\rm eff}$, defined by $e^{-i\hat{H}^{\pm}_{\rm eff}\sqrt{2}\tau} \equiv e^{-i\hat{H}^{\mp}(\sqrt{2}-1)\tau}e^{-i\hat{H}^{\pm}\tau}$ where $\hat{H}_{\rm eff} \equiv \hat{H}^{+}_{\rm eff} - \hat{H}^{-}_{\rm eff}$, does not vanish even in the first order of the object-bath coupling ($\sim \mathcal{A}/N$). As demonstrated in in Fig. VIII.4, the disentanglement times are not equally times are not equally spaced even though the controlling pulses are. In the concatenated design of control pulse sequence, under the lth order concatenated disentanglement, the effective coupling strength between the electron spin and a pseudo-spin (nuclear-spin pair-state) can be evaluated to be

$$||\hat{H}^{(l)}_{\rm eff}|| \cong \tau^l 2^{l(l-3)/2}\left|E_kB_k - A_kD_k\right|\left[4B_k^2{\rm sinc}^2\left(E_k\tau\right) + D_k^2\right]^{\frac{l-1}{2}}{\rm sinc}^2\frac{E_k\tau}{2}, \qquad \text{(VIII.6)}$$

the order of which is determined by the bath internal interaction instead of the system-bath interaction. And we have seen from Eq. (VIII.5) that the bath internal coupling strength b, rather than the system-bath coupling strength $\mathcal{A}/N$ as in dynamical decoupling [183], acts as the controlling parameter in determining the leftover decoherence. Since $b^{-1} \sim$ ms $\gg (\mathcal{A}/N)^{-1} \sim \mu$s in the nuclear spin bath, the restriction on the interpulse interval τ of control pulses is substantially relaxed. Our calculation shows that the electron spin coherence is well protected by pulse sequences with interpulse interval up to ~ 10 μs .

VIII.E Chapter summary

In summary, we have demonstrated, with a realistic system of a quantum dot containing one electron and many nuclear spins interacting with one another, the general idea of disentangling the quantum object and the mesoscopic bath and thus restoring the system coherence after it has been totally lost by the system-bath entanglement. The coherence restoration is not the reversal of the system-bath dynamics but an effective disentanglement which requires the simple control over only the quantum system instead of the enormous degree of freedom of the mesoscopic bath. The disentanglement is distinguished from the classical spin echo in inhomogeneously broadened ensemble by the coherence recovering at $t = \sqrt{2}\tau$ for a single pulse control applied at $t = \tau$. This magic time coherence restoration at $t = \sqrt{2}\tau$ is observable in principle in single-dot measurement with pre-determination or post-selection of the nuclear Overhauser field but is in general concealed by the inhomogeneous broadening in conventional ensemble experiments. To observe the coherence restoration by disentanglement in ensemble measurements, pulse sequences can be employed to control the disentanglement coincide with the spin echo. The disentanglement, realized by maneuvering the quantum evolution of mesoscopic baths, opens up an approach to coherence protection in mesoscopic systems, complementary to the dynamical decoupling scheme [175, 176, 183, 182], the quantum error correction [24, 25, 26, 27, 28], and the decoherence-free subspace method [169, 170, 171].

VIII.F Acknowledgements

The text of chapter VIII, in part, is a reprint of the material as it appears in Wang Yao, Ren-Bao Liu, and L. J. Sham, *Restoring Coherence Lost to a Mesoscopic Bath*, arXiv preprint cond-mat/0604634, (2006), where the dissertation author was the first author. The co-authors in this preprint directed, supervised, and co-worked on the research which forms the basis of this chapter.

IX

Conclusions and Future Work

In this chapter, we recapitulate the main results of this dissertation. Some relevant future directions will be mentioned along the way.

IX.A Solid-state gate for photon pairs

In Chapter IV, we have proposed a solid-state controlled phase gate for two photons. The flying qubits are conducted through fibers coupled to scattering centers composed of micro-cavities connected by a doped semiconductor quantum dot. This allows a fiber implementation of quantum information processor. The phase gate is operated under the two-photon transmission in fibers. Electromagnetical induced transparency and laser cooling effect have been incorporated in the control design to minimize the photon reflections. Pulse shape selections of single photons are discussed for optimized gate operation. Single phase gate operation allows a nonlinear phase-shift of O($\pi/10$) at the single photon level. Controlled structures for accumulation of nonlinear phaseshift by multi-operations are proposed. Calculated results also show that the system is flexible for producing strong two-photon polarization entanglement as well.

The present design implements the energy level structures of a charged quantum dot. The trion levels in charged quantum dot used for nonlinear interaction could be replaced by other electronic systems, such as biexcitons in an undoped quantum dot, states in nanoclusters, or even some strong transitions in rare-earth impurities, e.g., the 4d-5f transition in Er^{2+}. Design of control and pulse shape selection shall be individually investigated for these alternatives.

In the present study, we have assumed the point like coupling between the cavity and the fiber. In practice, this coupling depends on the details of the structures to be used. Phase-matching condition could be present if the couplings length is comparable with the photon

wavelength. The phase-matching condition could be utilized to further maximize the desired two-photon transmission. Our preliminary calculation also shows that moderate cavity-dot coupling is sufficient to offer the nonlinearity needed for single photon conditional dynamics. The strong coupling requirement may be relaxed. The present treatment should be generalized to deal with the photon scattering processes under the moderate cavity-dot coupling. In addition, the dot-cavity-fiber coupled structure may function as a novel nonlinear device working in the classical limit. Design of control in connection with the practical needs, e.g., in optical communication, could be another future direction.

IX.B Spin-photon interface

In Chapter V, we have investigated the coupled dot-cavity-waveguide structure as the spin-photon interface. The cavity assisted Raman process can be coherently controlled to establish efficient quantum pathways connecting in sequence an electron spin, a charged exciton, a cavity photon, and finally a flying photon in a quantum channel, i.e., the waveguide. Through this Raman process, the qubit initially encoded in the quantum dot electron spin can be mapped onto the photon number subspace of a single photon wavepacket with an arbitrarily designated shape. This process, together with its time reversal process at a different nodes, enables the quantum state transfer and swap between the electron spins at the two distant nodes. If the Raman process at the sending node is controlled to be a partial cycle, non-local entanglement between the two distant nodes can be created. The quantum node may also function as deterministic source and efficient detector of a single-photon wavepakcet with arbitrarily specified shape and average photon number. Numerical simulation with the inclusion of various decoherence processes shows a fidelity of 99% with parameters taken from state of art experiments. The control is also shown to be robust against various systematic errors including the mis-characterization of system parameters, phase and amplitude fluctuation of the controlling lasers.

The robustness against the systematic errors form the basis of the close-loop learning studies [103] and real-time feedback controls [102] of the spin-photon interface. Learning algorithms can be used to find the optimized manipulation of the dynamics of a complex system, through the close-loop adaptive feedback controls, without initially knowing all relevant system parameters. There has already been a great deal of success in the adaptive feedback control of quantum phenomena in atomic and molecular systems [103, 184, 185]. The implementation of learning algorithms in the quantum network operations could be an indispensable step towards efficient control of this complex system. Real-time feedback controls also share the same underlying control principles but poses more challenges since it requires the latency period of the

control loop to match the intrinsic timescale of the system. Preliminary experiments are already showing the viability of real-time feedback control in non-classical state preparation [186]. Of more interest is to look into the feasibility of tailoring the quantum dynamics of open quantum systems. Real-time quantum feedback controls of a single quantum systems is also of fundamental interest in revealing basic issues about observational back action upon the quantum dynamics. The dot-cavity-waveguide coupled structure could be an ideal platform for such studies.

In chapter VI, we have shown that the cavity assisted Raman process may also be controlled for the ultra-fast initialization and quantum non-demolition measurement of the quantum dot spin. A choice of the polarization of the control pulse can either (1) use the quantum channel as an entropy dump for the process of cooling the spin to the ground state, or (2) entangle the spin qubit with a photon qubit in the quantum channel, thus enabling the readout of the spin qubit via the photon detection. To be compatible also with the single spin rotation or the controlled two spin interaction [17, 18], the cavity can be designed off resonance from the QD transition so that cavity does not induce extra decoherence of the trion state. AC stark pulse are used to switch on the cavity-dot coupling on demand for initialization and readout purpose. Numerical simulation with the inclusion of various decoherence processes shows high efficiencies for both the initialization and measurement processes. A single cooling cycle completed within 80 ps results in 99.45% spin polarization from the originally maximally mixed state of zero spin polarization. Assuming the single photon detector of 50% efficiency and zero dark count rate, within five measurement cycles, the spin state can be measured with accuracy higher than 97%, and the back-action noise to the spin is less than 10%, while the time duration is less than 0.4 ns, much shorter than the spin decoherence time.

Monitoring of photons out coupled to optical waveguides may also provides a powerful method for continuous observation of the intracavity spin dynamics. A number of quantum measurement related studies may be performed on this structure. Interesting questions may arise when the coherently driven quantum evolutions are combined with weak and continuous quantum measurement. Future work may include the state and quantum process tomography, conditional quantum evolution of continuously and weakly observed intra-cavity spin systems.

IX.C Electron spin decoherence and coherence control in quantum dot

In Chapter VII, we present a quantum theory to the electron spin transverse decoherence induced by interacting nuclear spins in quantum dot. The decoherence is explained in terms of quantum entanglement of the electron with the pair-flip excitations in the nuclear bath driven by

the various nuclear-nuclear interactions. The nuclear interaction mediated by the virtual spin-flip of the electron, usually overlooked in the literature, is shown to play an important role in single electron spin free-induction decay. The calculated electron spin decoherence time in single-system FID varies from ~ 0.1 μs to ~ 10 μs for field strength from 1 T to 20 T, and saturates as the electron mediated coupling is suppressed by stronger field. The spin-echo pulse not only recovers the coherence lost by inhomogeneous broadening but also eliminates the decoherence due to the electron-mediated nuclear pair-flips and reduces the decoherence by the intrinsic nuclear interaction, leading to an decoherence time ~ 10 μs independent of field strength in ensemble dynamics.

In Chapter VIII, we present a coherence protection scheme to ameliorate the electron spin transverse decoherence induced by the interacting lattice nuclear spins. As the decoherence of electron spin results from the entanglement with the nuclear bath established by the coupled evolution, the disentanglement leads to the restoration of the lost electron spin coherence. Disentanglement may be realized through the implementation of sequences of short π-pulses to maneuver the nuclear bath evolution through control of the electron spin-flip. The pulse sequence design can be borrowed from the dynamical decoupling schemes in NMR spectroscopies [132] and in quantum computation [172, 173, 174, 176, 175], but the disentanglement method aims directly at the bath dynamics. It does not seek to cancel the system-bath interaction by dynamical averaging, but instead, with the solution of mesoscopic bath dynamics, implements coherence control by maneuvering the bath evolution. In general, elimination of system-bath coupling is not a necessary condition for their disentanglement. Disentanglement method leads to unique coherence recovery times, e.g., $\sqrt{2}\tau$ by the single pulse control, in the pure state dynamics which are in stark contrast to the spin echo times generally expected. The effective system-bath coupling does not vanish even in leading order at these disentanglement times. The coherence recovery at these unique times is observable in principle in single spin measurement with pre-determination or post selection of the nuclear Overhauser field, but it could be concealed by inhomogeneous broadening in ensemble measurements [11]. Complex pulse sequence control has been investigated to make the coherence recovery by disentanglement coinciding with ensemble spin echo, therefore, observable in ensemble measurements. Prediction are made for GaAs quantum dot of practical size. As the disentanglement is essentially a control of the bath dynamics rather than a control of the system-bath coupling, the controlling small parameter is the internal coupling strength within the bath rather than the system-bath coupling strength as in dynamical decoupling schemes [176]. Since the coupling between nuclear bath spins is much weaker than the electron-nuclear coupling, the restriction on the interpulse interval τ of control pulses is substantially relaxed.

The quantum theory of electron spin decoherence and the coherence control by disentanglement is based on the pair-correlation approximation. The validity of the approach depends critically on the mesoscopic size of the quantum dot and the timescale of interest. Error analysis shows that the pair-correlation method is well justified for the calculation of single spin free-induction decay and ensemble spin echo for quantum dots of all practical size. However, multi-spin correlations in the nuclear bath will gradually build up in the longer time limit, e.g., when $t \gtrsim 100$ μs for a quantum dot of typical size $N \sim 10^5 - 10^6$. Therefore, the present discussion of electron spin coherence control has been limited within this timescale, i.e., $t \lesssim 100$ μs, where the pair-correlation approximation remains valid. As the ultimate aim of the coherence control approach is to protect the electron spin coherence up to the spin T_1 timescale[1], investigation of the multi-spin correlations is of relevance. If the pulse sequence designed for the pair-correlations fails to deal with the multi-spin correlations, the search for more complex pulse sequences is needed and the ultimate limit of this coherence protect scheme by disentanglement is also of interest. In addition, the current pulse sequence design aims at the protection of spin quantum memory. Universal control of the coherence protected system will be an interesting topic [174].

The present study of the electron spin decoherence and coherence control is a time domain approach, i.e., the evolution of the initially prepared coherence is traced as a function of time. Various time domain measurements [11, 127, 130, 143] may be performed for the test of the theory. Complimentarily, optical frequency domain measurement offers a unique approach to probe the various decoherence processes in the optically controllable dots. Measurement of optical resonances with linewidth narrower than that of the laser is possible in carefully designed experiments. For example, the measurement of ultra-slow ground-state relaxation rates of ~ 10 Hz $-$kHz in various solids have been performed using the backward nearly degenerate four-wave mixing spectrum [187, 188, 189, 190]. The optical frequency domain probe of the entanglement induced electron spin decoherence process could be an interesting topic. The extension of the above mentioned techniques on the measurement of relaxation to the transverse decoherence is highly nontrivial. The observation of this slower process depends critically on the elimination of the inhomogeneous broadening of the spin resonance in the spectrum.

IX.D Distributed quantum computation on chip

The requirements for the physical implementation of quantum computation have been summarized by DiVincenzo [23]: (1) A scalable physical system with well-characterized qubits;

[1]In GaAs, the spin relaxation time $T_1 \sim$ ms has been measured for the gate defined dot [107]. For InAs self-assembled dot, spin relaxation time as long as ~ 20 ms has been observed [130].

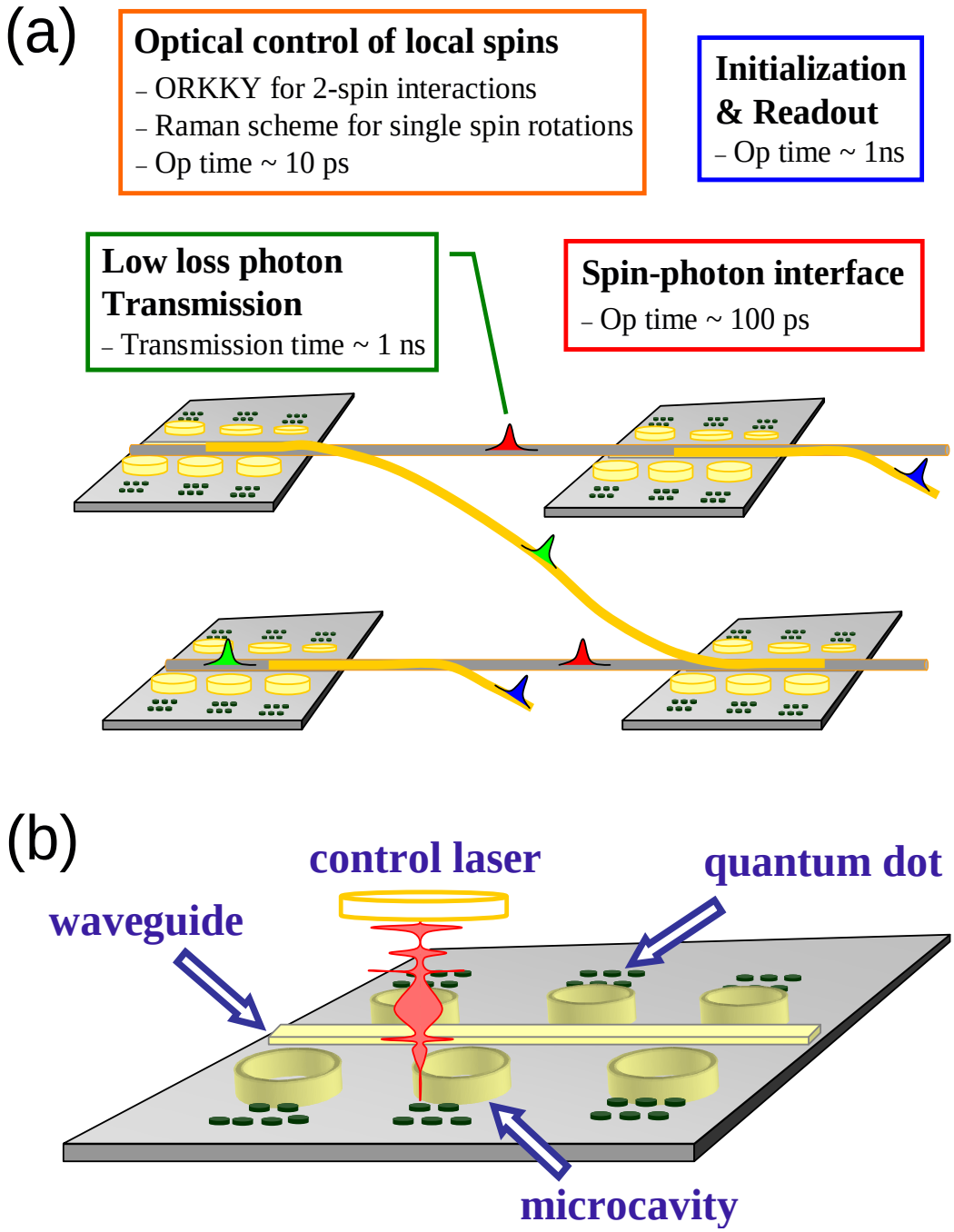

Figure IX.1 Distributed quantum information processing on chip. (a) Schematics of distributed quantum computer where communications between computation modulus are mediated by single photons in optical waveguides/fibers. (b) The spin based computation modulus on chip controlled by ultrafast optics.

(2) The ability to initialize the state of the qubits to a simple fiducial state; (3) Long relevant decoherence times, much longer than the gate operation time; (4) A "universal" set of quantum gates; (5) A qubit-specific measurement capability; (6) The ability to interconvert stationary and flying qubits; (7) The ability to faithfully transmit flying qubits between specified locations.

Our studies in this dissertation aims at realizing these criterias in the mesoscopic system of quantum dot. Together with the spin control established by previous work [8, 17, 18], now we are able to outline the construction of a solid-state quantum network for scalable and distributed processing of quantum information (see Fig. IX.1). In this network structure, a local node is formed by a cluster of charged quantum dots and quantum information is encoded on the spin of the single electron in each dot. These stationary qubits form basis for the quantum memory and quantum logic modulus. Under a strong magnetic field of 10 T and temperature of $\lesssim 1$ K, single electron spin has a free-induction decoherence time of $\sim 1 - 10$ μs by our investigation. This allows a sufficient large number of single-qubit and two-qubit operations ($T_{\rm op} \sim 10$ ps). Spin coherence may be further protected by the disentanglement method through implementation of sequences of π-rotations of electron spin.

Computation capacities could be greatly enhanced by connecting modulus via optical fibers or waveguides which act as lossless and directional quantum channels for flying photon qubit. Since it takes less than 1 ns for a photon to travel 10 cm, the quantum network can be easily scaled from nano-devices to centimeter-sized chips. The loss of photons in fibers is negligible in such a short distance. The quantum interface between stationary spin qubits and flying photon qubits are provided by the dot-cavity-waveguide coupled structure controlled by pulse shaped laser. The dot-cavity-waveguide structure also allows the ultra-fast initialization and non-destructive readout, essential for quantum error correction and scalable quantum computation.

We believe this system will be of unique potential for the realization of a scalable quantum computer.

Bibliography

[1] H. Mabuchi and A. C. Doherty, Science **298**, 1372 (2002).

[2] T. H. Stievater, X. Q. Li, D. G. Steel, D. Gammon, D. S. Katzer, D. Park, C. Piermarocchi, and L. J. Sham, Phys. Rev. Lett. **87**, 133603 (2001).

[3] G. Chen, T. H. Stievater, E. T. Batteh, X. Q. Li, D. G. Steel, D. Gammon, D. S. Katzer, D. Park, and L. J. Sham, Phys. Rev. Lett. **88**, 117901 (2002).

[4] X. Li, Y. Wu, D. Steel, D. Gammon, T. H. Stievater, D. Katzer, D. S. Park, C. Piermarocchi, and L. J. Sham, Science **301**, 809 (2003).

[5] C. J. Pethick and H. Smith, *Bose-Einstein Condensation in Dilute Gases*, 1 ed. (Cambridge University Press, Cambridge, 2002).

[6] M. A. Nielsen and I. L. Chuang, *Quantum Computation and Quantum Information* (Cambridge University Press, Cambridge, 2000).

[7] D. D. Awschalom, D. Loss, and N. Samarth, *Semiconductor Spintronics and Quantum Computing* (Springer, New York, 2002).

[8] A. Imamoğlu, D. D. Awschalom, G. Burkard, D. P. DiVincenzo, D. Loss, M. Sherwin, and A. Small, Phys. Rev. Lett. **83**, 4204 (1999).

[9] D. Loss and D. P. DiVincenzo, Phys. Rev. A **57**, 120 (1998).

[10] W. G. van der Wiel, S. De Franceschi, J. M. Elzerman, T. Fujisawa, S. Tarucha, and K. L. P., Rev. Mod. Phys. **75**, 1 (2003).

[11] A. C. Johnson, J. R. Petta, J. M. Taylor, A. Yacoby, M. D. Lukin, C. M. Marcus, M. P. Hanson, and A. C. Gossard, Nature **435**, 925 (2005).

[12] K. Brunner, U. Bockelmann, G. Abstreiter, M. Walther, G. Böhm, G. Tränkle, and G. Weimann, Phys. Rev. Lett. **76**, 3216 (1992).

[13] D. Gammon, B. V. Shanabrook, and D. S. Katzer, Phys. Rev. Lett. **67**, 1547 (1991).

[14] P. M. Petroff and S. P. DenBaars, Superlattices and Microstructures **15**, 15 (1994).

[15] N. Richard, Semicond. Sci. Tech. **11**, 1365 (1996).

[16] M. Bayer, G. Ortner, O. Stern, A. Kuther, A. A. Gorbunov, A. Forchel, P. Hawrylak, S. Fafard, K. Hinzer, T. L. Reinecke, S. N. Walck, J. P. Reithmaier, F. Klopf, and F. Schöfer, Phys. Rev. B **65**, 195315 (2002).

[17] P. Chen, C. Piermarocchi, L. J. Sham, D. Gammon, and D. G. Steel, Phys. Rev. B **69**, 075320 (2004).

[18] C. Piermarocchi, P. Chen, L. J. Sham, and D. G. Steel, Phys. Rev. Lett. **89**, 167402 (2002).

[19] L. Pang, Y. Shen, K. Tetz, and Y. Fainman, Opt. Expr. **13**, 44 (2005).

[20] F. Jelezko, T. Gaebel, I. Popa, A. Gruber, and J. Wrachtrup, Phys. Rev. Lett. **92**, 076401 (2004).

[21] C. Kurtsiefer, S. Mayer, P. Zarda, and H. Weinfurter, Phys. Rev. Lett. **85**, 290 293 (2000).

[22] A. Beveratos, R. Brouri, T. Gacoin, J. P. Poizat, and P. Grangier, Phys. Rev. A **64**, 061802 (2001).

[23] D. DiVincenzo, Fortschr. Der Physik **48**, 771 (2000).

[24] P. W. Shor, Phys. Rev. A **52**, 2493 (1995).

[25] A. M. Steane, Phys. Rev. Lett. **77**, 793 (1996).

[26] C. H. Bennett, D. P. DiVincenzo, J. A. Smolin, and W. K. Wootters, Phys. Rev. A **54**, 3824 (1996).

[27] R. Laflamme, C. Miquel, J. P. Paz, and W. H. Zurek, Phys. Rev. Lett. **77**, 198 (1996).

[28] D. Gottesman, Phys. Rev. A **54**, 1862 (1996).

[29] A. M. Steane, Phys. Rev. A **68**, 042322 (2003).

[30] T. H. Stievater, Ph.D. thesis, University of Michigan, 2001.

[31] K. Brunner, G. Abstreiter, G. Böhm, G. Tränkle, and G. Weimann, Appl. Phys. Lett. **64**, 3320 (1994).

[32] K. Brunner, G. Abstreiter, G. Böhm, G. andTränkle, and G. Weimann, Phys. Rev. Lett. **73**, 1138 (1994).

[33] A. Zrenner, L. V. Butov, M. Hagn, G. Abstreiter, G. Böhm, and G. Weimann, Phys. Rev. Lett. **72**, 3382 (1994).

[34] D. Gammon, E. S. Snow, and D. S. Katzer, Appl. Phys. Lett. **67**, 2391 (1995).

[35] D. Gammon, E. S. Snow, B. V. Shanabrook, D. S. Katzer, and D. Park, Phys. Rev. Lett. **76**, 3005 (1996).

[36] D. Gammon, E. S. Snow, B. V. Shanabrook, D. S. Katzer, and D. Park, Science **273**, 87 (1996).

[37] G. Chen, Ph.D. thesis, University of Michigan, 2002.

[38] P. M. Petroff, A. Lorke, and A. Imamoglu, Physics Today **54**, 45 (2001).

[39] J. G. Tischler, A. S. Bracker, D. Gammon, and D. Park, Phys. Rev. B **66**, 081310 (2002).

[40] P. Y. Yu and M. Cardona, *Fundamentals of Semiconductors*, 1 ed. (Springer, Berlin, 1996).

[41] G. Bastard, *Wave Mechanics Applied to Semiconductor Heterostructures* (Les Ulis, France, 1988), Chap. 3.

[42] *Landolt-Bornstein: Numerical Data and Functional Relationships in Science and Technology: Group 3: Condensed Matter: Madelung/Schulz: Semiconductors: Intrinsic Properties of Group IV Elements and III-V, II-VI and I-VII Compounds*, Vol. 22 of *Numerical Data & Functional Relationships in Science & Technology*, edited by O. Madelung, W. von der Osten, and U. Rossler (Springer-Verlag, Berlin, 1987).

[43] *Semiconductors: Data Handbook*, 3rd ed., edited by O. Madelung (Springer-Verlag, New York, 2004).

[44] D. A. Broido and L. J. Sham, Phys. Rev. B **31**, 888 (1985).

[45] M. V. Gurudev Dutt, J. Cheng, B. Li, X. Xu, X. Li, P. R. Berman, D. G. Steel, A. S. Bracker, D. Gammon, S. E. Economou, R.-B. Liu, and L. J. Sham, Phys. Rev. Lett. **94**, 227403 (2005).

[46] P. Chen, Ph.D. thesis, University of California, San Diego, 2002.

[47] H. Kamada, H. Gotoh, J. Temmyo, T. Takagahara, and H. Ando, Phys. Rev. Lett. **87**, 246401 (2001).

[48] H. Htoon, T. Takagahara, D. Kulik, O. Baklenov, A. L. Holmes, Jr., and C. K. Shih, Phys. Rev. Lett. **88**, 087401 (2002).

[49] E. Knill, R. Laflamme, and G. J. Milburn, Nature (London) **409**, 46 (2001).

[50] C. H. Bennett and G. Brassard, in *Proceedings of IEEE International Conference on Computers, Systems and signal Processing* (IEEE, New York, 1984), pp. 175 – 179.

[51] C. H. Bennett, G. Brassard, and A. K. Ekert, Sci. Am. **267**, 50 (1992).

[52] J. I. Cirac, P. Zoller, H. J. Kimble, and H. Mabuchi, Phys. Rev. Lett. **78**, 3221 (1997).

[53] G. Cancellieri, *Single-Mode Optical Fibres* (Pergamon Press, New York, 1991).

[54] P. K. Cheo, *Fiber Optics and Optoelectronics* (Prentice Hall, Englewood Cliffs, NJ, 1990).

[55] S. C. Hagness, S. T. Ho, and A. Taflove, Journal of Lightwave Techonology **15**, 2154 (1997).

[56] A. Scherer, O. Painter, J. Vuckovic, M. Loncar, and T. Yoshie, IEEE Transcations on Nanotechonology **1**, 4 (2002).

[57] L. Pang, W. Nakagawa, and Y. Fainman, Applied Optics **42**, 5450 (2003).

[58] K. J. Vahala, Nature (London) **424**, 839 (2003).

[59] D. K. Armani, T. J. Kippenberg, S. M. Spillane, and K. J. Vahala, Nature (London) **421**, 925 (2003).

[60] *Cavity Quantum Electrodynamics*, edited by P. R. Berman (Academic, San Diego, 1994).

[61] Y. Akahane, T. Asano, B.-S. Song, and S. Noda, Nature (London) **425**, 944 (2003).

[62] B.-S. Song, , S. Noda, T. Asano, and Y. Akahane, Nature Material **4**, 207 (2005).

[63] X. D. Fan, P. Palinginis, S. Lacey, H. L. Wang, and M. C. Lonergan, Opt. Lett. **25**, 1600 (2000).

[64] B. Min, T. J. Kippenberg, and K. J. Vahala, Opt. Lett **28**, 1507 (2003).

[65] S. M. Spillane, T. J. Kippenberg, K. J. Vahala, K. W. Goh, E. Wilcut, and H. J. Kimble, Phys. Rev. A **71**, 013817 (2005).

[66] T. Yoshie, A. Scherer, J. Hendrickson, G. Khitrova, H. M. Gibbs, G. Rupper, C. Ell, O. B. Shchekin, and D. G. Deppe, Nature **432**, 200 (2004).

[67] Online source: http://www.chm.bris.ac.uk/∼chjpr/Research/WGM.htm by Particle Dynamics Group, University of Bristol,.

[68] J. A. Stratton, *Electromagnetic Theory*, 1 ed. (McGraw-Hill, New York, 1941).

[69] W. Fang, D. B. Buchholz, R. C. Bailey, J. T. Hupp, R. P. H. Chang, and H. Cao, Appl. Phys. Lett. **85**, 3666 (2004).

[70] J. P. Reithmaier, G. Sek, A. Lffler, S. Hofmann, C.and Kuhn, S. Reitzenstein, L. V. Keldysh, V. D. Kulakovskii, T. L. Reinecke, and A. Forchel, Nature **432**, 197 (2004).

[71] E. Peter, P. Senellart, D. Martrou, A. Lemaître, J. Hours, J. M. Gérard, and J. Bloch, Phys. Rev. Lett. **95**, 067401 (2005).

[72] B. C. Sanders and G. J. Milburn, Phys. Rev. A **39**, 694 (1989).

[73] Q. A. Turchette, C. J. Hood, W. Lange, H. Mabuchi, and H. J. Kimble, Phys. Rev. Lett. **75**, 4710 (1995).

[74] M. D. Lukin and A. Imamo$\bar{g}$lu, Phys. Rev. Lett. **84**, 1419 (2000).

[75] W. Yao, H. Ajiki, and L. J. Sham, unpublished. (unpublished).

[76] H. Ajiki, W. Yao, and L. J. Sham, Superlattices and Microstructures **34**, 213 (2003).

[77] R. E. Benner, P. W. Barber, J. F. Owen, and R. K. Chang, Phys. Rev. Lett. **44**, 475 (1980).

[78] S. M. Spillane, T. J. Kippenberg, O. J. Painter, and K. J. Vahala, Phys. Rev. Lett. **91**, 043902 (2003).

[79] S. E. Harris, J. E. Field, and A. Imamoğlu, Phys. Rev. Lett. **64**, 11071110 (1990).

[80] H. Schmidt and A. Imamo$\bar{g}$lu, Opt. Lett. **21**, 1936 (1996).

[81] C. Cohen-Tannoudji, J. Dupont-Roc, and G. Grynberg, *Atom-Photon Interactions* (Wiley Interscience, New York, 1992).

[82] H. Wang, P. Palinginis, X. Fan, S. Lacey, and M. Lonergan, in *Proceedings of the Quantum Electronics and Laser Science Conference* (Optical Society of America, San Francisco, 2000), p. 99.

[83] N. F. Mott and H. S. Massey, *The Theory of Atomic Collisions* (Oxford University Press, London, 1965).

[84] W. K. Wootters, Phys. Rev. Lett. **80**, 2245 (1998).

[85] J. I. Cirac, W. Dür, B. Kraus, and M. Lewenstein, Phys. Rev. Lett. **86**, 544 (2001).

[86] F. Spedalieri, H. Lee, M. Florescu, K. T. Kapale, U. Yurtsever, and J. P. Dowling, Opt. Comm. **254**, 374 (2005).

[87] J. I. Cirac, A. K. Ekert, S. F. Huelga, and C. Macchiavello, Phys. Rev. A **59**, 4249 (1999).

[88] J. I. Cirac, P. Zoller, H. J. Kimble, and H. Mabuchi, Phys. Rev. Lett. **78**, 3221 (1997).

[89] A. S. Parkins and H. J. Kimble, J. Opt. B: Quant. Semiclass. Optics **1**, 496 (1999).

[90] M. D. Lukin, S. F. Yelin, and M. Fleischhauer, Phys. Rev. Lett. **84**, 4232 (2000).

[91] M. Fleischhauer, S. F. Yelin, and M. D. Lukin, Opt. Comm. **179**, 395 (2000).

[92] L.-M. Duan, A. Kuzmich, and H. J. Kimble, Phys. Rev. A **67**, 032305 (2003).

[93] W. Yao, R. B. Liu, and L. J. Sham, Phys. Rev. Lett. **95**, 030504 (2005).

[94] W. Yao, R. B. Liu, and L. J. Sham, J. Opt. B: Quant. Semiclass. Optics **7**, S318 (2005).

[95] A. Kuhn, M. Hennrich, and G. Rempe, Phys. Rev. Lett. **89**, 067901 (2002).

[96] J. McKeever, A. Boca, A. Boozer, R. Miller, J. Buck, A. Kuzmich, and H. J. Kimble, Nature **303**, 1992 (2004).

[97] M. Keller, B. Lange, K. Hayasaka, W. Lange, and H. Walther, Nature **431**, 1075 (2004).

[98] M. O. Scully and M. S. Zubairy, *Quantum Optics* (Cambridge, Cambridge, 1997).

[99] M. Bayer and A. Forchel, Phys. Rev. B **65**, 041308 (2002).

[100] S. J. van Enk, J. I. Cirac, and P. Zoller, Science **279**, 205 (1998).

[101] H. J. Briegel, W. Dür, J. I. Cirac, and P. Zoller, Phys. Rev. Lett. **81**, 5932 (1998).

[102] H. M. Wiseman and G. J. Milburn, Phys. Rev. Lett. **70**, 548 (1993).

[103] H. Rabitz, R. de Vivie-Riedle, M. Motzkus, and K. Kompa, Science **288**, 824 (2000).

[104] M. Xiao, I. Martin, E. Yablonovitch, and H. W. Jiang, Nature **430**, 435 (2004).

[105] H.-A. Engel, V. Golovach, D. Loss, L. M. K. Vandersypen, J. M. Elzerman, R. Hanson, and L. P. Kouwenhoven, cond-mat/0309023 (2003).

[106] R. Ioniciou and A. E. Poescu, quant-ph/0310047 (2003).

[107] J. M. Elzerman, R. Hanson, L. H. Willems van Beveren, B. Witkamp, L. M. K. Vandersypen, and L. P. Kouwenhoven, Nature **430**, 431 (2004).

[108] M. Friesen, C. Tahan, R. Joynt, and M. A. Eriksson, Phys. Rev. Lett. **92**, 037901 (2004).

[109] D. G. Cory, A. F. Hahmy, and T. F. Havel, Proc. Natl. Acad. Sci. USA **94**, 1634 (1997).

[110] L. M. K. Vandersypen, M. Steffen, G. Breyta, C. S. Yannoni, M. H. Sherwood, and I. L. Chuang, Nature (London) **414**, 883 (2001).

[111] P. W. Shor, SIAM J. Comput. **26**, 1484 (1997).

[112] C. A. Sackett, D. Kielpinski, B. E. King, C. Langer, V. Meyer, C. J. Myatt, M. Rowe, Q. A. Turchette, W. M. Itano, D. J. Wineland, and C. Monroe, Nature **404**, 256 (2000).

[113] A. Imamoğlu, Phys. Rev. Lett. **89**, 163602 (2002).

[114] D. F. V. James and P. G. Kwiat, Phys. Rev. Lett. **89**, 183601 (2002).

[115] D. Goswami, Phys. Report **374**, 385 (2003).

[116] S. Takeuchi, J. Kim, Y. Yamamoto, and H. H. Hogue, Appl. Phys. Lett. **74**, 1063 (1999).

[117] Y. Kang, Y. H. Lo, M. Bitter, S. Kristjansson, Z. Pan, and A. Pauchard, Appl. Phys. Lett. **85**, 1668 (2004).

[118] A. Imamoglu, Fortschr. Phys. **48**, 987 (2000).

[119] T. Calarco, A. Datta, P. Fedichev, E. Pazy, and P. Zoller, Phys. Rev. A **68**, 012310 (2003).

[120] S. Hughes and H. Kamada, Phys. Rev. B **70**, 195313 (2004).

[121] J. Wrachtrup, C. von Borczyskowski, J. Bernard, M. Orrit, and R. Brown, Nature **363**, 244 (1993).

[122] W. H. Zurek, Rev. Mod. Phys. **75**, 715 (2003).

[123] E. Joos, H. D. Zeh, C. Kiefer, D. Giulini, J. Kupsch, and I.-O. Stamatescu, *Decoherence and the Appearance of a Classical World in Quantum Theory*, 2 ed. (Springer, New York, 2003).

[124] M. Schlosshauer, Rev. Mod. Phys. **76**, 1267 (2004).

[125] A. V. Khaetskii and Y. Nazarov, Phys. Rev. B **61**, 12639 (2000).

[126] A. V. Khaetskii and Y. Nazarov, Phys. Rev. B **64**, 125316 (2001).

[127] T. Fujisawa, D. G. Austing, Y. Tokura, Y. Hirayama, and S. Tarucha, Nature **419**, 278 (2002).

[128] M. Xiao, I. Martin, E. Yablonovitch, and H. W. Jiang, Nature **430**, 435 (2004).

[129] J. M. Elzerman, R. Hanson, L. H. Willems van Beveren, B. Witkamp, L. M. K. Vandersypen, and L. P. Kouwenhoven, Nature **430**, 431 (2004).

[130] M. Kroutvar, Y. Ducommun, D. Heiss, M. Bichler, D. Schuh, D. Abstreiter, and J. J. . Finley, Nature **432**, 81 (2004).

[131] E. I. Hahn, Phys. Rev. **80**, 580 (1950).

[132] C. P. Slichter, *Principles of Magnetic Resonance*, 3rd ed. (Springer-Verlag, New York, 1992).

[133] A. Abragam, *The Principles of Nuclear Magnetism* (Oxford University Press, London, 1961).

[134] C. P. Poole and H. A. Farach, *Relaxation in Magnetic Resonance* (Academic Press, New York, 1971).

[135] W. B. Mims, in *Electron Paramagnetic Resonance*, edited by S. Geschwind (Plenum Press, New York, 1972).

[136] G. Feher and E. A. Gere, Phys. Rev. **114**, 1245 (1959).

[137] A. M. Tyryshkin, S. A. Lyon, A. V. Astashkin, and A. M. Raitsimring, Phys. Rev. B **68**, 193207 (2003).

[138] E. Abe, K. M. Itoh, J. Isoya, and S. Yamasaki, Phys. Rev. B **70**, 033204 (2004).

[139] L. M. Woods, T. L. Reinecke, and Y. Lyanda-Geller, Phys. Rev. B **66**, 161318(R) (2002).

[140] V. N. Golovach, A. Khaetskii, and D. Loss, Phys. Rev. Lett. **93**, 016601 (2004).

[141] Y. G. Semenov and K. W. Kim, Phys. Rev. Lett. **92**, 026601 (2004).

[142] A. S. Bracker, E. A. Stinaff, D. Gammon, M. E. Ware, J. G. Tischler, A. Shabaev, A. L. Efros, D. Park, D. Gershoni, V. L. Korenev, and I. A. Merkulov, Phys. Rev. Lett. **94**, 047402 (2005).

[143] F. H. L. Koppens, J. A. Folk, J. M. Elzerman, R. Hanson, L. H. W. van Beveren, I. T. Vink, H. P. Tranitz, W. Wegscheider, L. P. Kouwenhoven, and L. M. K. Vandersypen, Science **309**, 1346 (2005).

[144] J. R. Petta, A. C. Johnson, J. M. Taylor, E. A. Laird, A. Yacoby, M. D. Lukin, C. M. Marcus, M. P. Hanson, and A. C. Gossard, Science **309**, 2180 (2005).

[145] W. A. Coish and D. Loss, Phys. Rev. B **70**, 195340 (2004).

[146] A. V. Khaetskii, D. Loss, and L. Glazman, Phys. Rev. Lett. **88**, 186802 (2002).

[147] I. A. Merkulov, A. L. Elfros, and M. Rosen, Phys. Rev. B **65**, 205309 (2002).

[148] S. I. Erlingsson and Y. V. Nazarov, Phys. Rev. B **70**, 205327 (2004).

[149] N. Shenvi, R. de Sousa, and K. B. Whaley, cond-mat/0410308 (2004).

[150] R. de Sousa and S. Das Sarma, Phys. Rev. B **68**, 115322 (2003).

[151] R. de Sousa and S. Das Sarma, Phys. Rev. B **67**, 033301 (2003).

[152] R. Liu, W. Yao, and L. J. Sham, Phys. Rev. B **72**, 081306(R) (2005).

[153] W. Yao, R. Liu, and L. J. Sham, Phys. Rev. Lett. **92**, 217402 (2004).

[154] B. Herzog and E. L. Hahn, Phys. Rev. **103**, 148 (1956).

[155] J. R. Klauder and P. W. Anderson, Phys. Rev. **125**, 912 (1962).

[156] P. W. Anderson, Phys. Rev. **114**, 1002 (1959).

[157] G. M. Zhidomirov and K. M. Salikhov, Sov. Phys. JETP **29**, 1037 (1969).

[158] W. M. Witzel, R. de Sousa, and S. Das Sarma, Phys. Rev. B **72**, 161306(R) (2005).

[159] W. Yao, R. B. Liu, and L. J. Sham, cond-mat/0508441 (2005).

[160] N. Shenvi, R. de Sousa, and K. B. Whaley, cond-mat/0502143 (2005).

[161] C. Deng and X. Hu, cond-mat/0406478 (2004).

[162] D. Paget, G. Lampel, and B. Sapoval, Phys. Rev. B **15**, 5780 (1977).

[163] P. W. Anderson, Phys. Rev. **99**, 623 (1955).

[164] N. Bloembergen and T. J. Rowland, Phys. Rev. **97**, 1679 (1955).

[165] R. G. Shulman, B. J. Wyluda, and H. J. Hrostowski, Phys. Rev. **109**, 808 (1958).

[166] R. K. Sundfors, Phys. Rev. **185**, 458 (1969).

[167] J. M. Luttinger and W. Kohn, Phys. Rev. **97**, 869 (1955).

[168] W. Yao, R. B. Liu, and L. J. Sham, unpublished data. (unpublished).

[169] L. M. Duan and G. C. Guo, Phys. Rev. Lett. **79**, 1953 (1997).

[170] P. Zanardi and M. Rasetti, Phys. Rev. Lett. **79**, 3306 (1997).

[171] D. A. Lidar, I. L. Chuang, and K. B. Whaley, Phys. Rev. Lett. **81**, 2594 (1998).

[172] L. Viola and S. Lloyd, Phys. Rev. A **58**, 2733 (1998).

[173] L. Viola, E. Knill, and S. Lloyd, Phys. Rev. Lett. **82**, 2417 (1999).

[174] L. Viola, S. Lloyd, and E. Knill, Phys. Rev. Lett. **83**, 4888 (1999).

[175] K. Khodjasteh and D. A. Lidar, Phys. Rev. Lett. **95**, 180501 (2005).

[176] L. Viola, E. Knill, and S. Lloyd, Phys. Rev. Lett. **85**, 3520 (2000).

[177] H. Y. Carr and E. M. Purcell, Phys. Rev. **94**, 630 (1954).

[178] W. K. Rhim, A. Pines, and J. S. Waugh, Phys. Rev. Lett. **25**, 218 (1970).

[179] A. E. Dementyev, D. Li, K. MacLean, and S. E. Barrett, Phys. Rev. B **68**, 153302 (2003).

[180] U. Haeberlin, *High Resolution NMR in Solids: Selective Averaging* (Academic Press, New York, 1976).

[181] M. Mehring, *High Resolution NMR in Solids* (Springer-Verlag, Berlin, 1983).

[182] L. F. Santos and L. Viola, quant-ph/0602168 (2006).

[183] L. Viola and E. Knill, Phys. Rev. Lett. **94**, 60502 (2005).

[184] R. S. Judson and H. Rabitz, Phys. Rev. Lett. **68**, 1500 (1992).

[185] R. J. Levis, G. M. Menkir, and H. Rabitz, Science **292**, 709 (2001).

[186] J. M. Geremia, J. K. Stockton, and H. Mabuchi, Science **304**, 270 (2004).

[187] D. G. Steel and S. C. Rand, Phys. Rev. Lett. **55**, 2285 (1985).

[188] D. G. Steel and J. T. Remillard, Phys. Rev. A **36**, 4330 (1987).

[189] D. G. Steel, S. C. Rand, and J. Liu, J. Opt. Soc. Am. B **4**, 1794 (1987).

[190] J. T. Remillard and D. G. Steel, Opt. Lett. **13**, (1988).